



University
of Glasgow

Whyte, Griogair W.M. (2008) *Antennas for wireless sensor network applications*. PhD thesis.

<http://theses.gla.ac.uk/408/>

Copyright and moral rights for this thesis are retained by the author

A copy can be downloaded for personal non-commercial research or study, without prior permission or charge

This thesis cannot be reproduced or quoted extensively from without first obtaining permission in writing from the Author

The content must not be changed in any way or sold commercially in any format or medium without the formal permission of the Author

When referring to this work, full bibliographic details including the author, title, awarding institution and date of the thesis must be given

Antennas for Wireless Sensor Network Applications

by

Griogair W.M. Whyte

Department of Electrical and Electronic Engineering

Thesis submitted for the degree of

Doctor of Philosophy

to the

Department of Electronics and Electrical Engineering

Faculty of Engineering

University of Glasgow

© G. W. M. Whyte, 2008

Abstract

The objective of this thesis is to present an analysis of antennas, which are applicable to wireless sensor networks and, in particular, to the requirements of the Speckled Computing Network Consortium. This was done through a review of the scientific literature on the subject, and the design, computer simulation, and experimental verification, of various suitable designs of antenna

The first part of this thesis outlines what an antenna is and how it radiates. An insight is also given to the fundamental limitations of antennas. As antennas investigated in this thesis are planar-printed designs, an insight into the types of feed lines applicable, such as microstrip, CPW and slotline, is given. To help characterise the antennas investigated, the fundamental antenna analysis parameters, such as impedance bandwidth, S-parameters, radiation pattern, directivity, antenna efficiency, gain and polarisation are discussed. Also discussed is the 3D electromagnetic simulation software, HFSS, which was used to simulate the antennas in this thesis. To help illustrate the use of HFSS, a proximity-coupled patch antenna, operating at 5.8 GHz, was used as an example.

A range of antennas were designed, manufactured and tested. These used conventional printed circuit boards (PCBs) and Gallium Arsenide (GaAs) substrates, operating at a range of frequencies from 2.4 GHz to 12 GHz.

A review was conducted into relevant, suitable radio architectures such as, conventional narrowband systems, Ultra-Wide Band (UWB), and simplified radio architectures such as those based on the diode rectifier method, and Super Regenerative Receivers (SRR).

There were several UWB antennas designed, which operate over a 3.1 – 10.16 GHz operational band with a VSWR ≤ 2 . All the UWB antennas were required to transmit a UWB pulse with minimal distortion, which placed a requirement of linear phase and low values of group delay to minimise distortion on the pulse. UWB antennas investigated included a Vivaldi antenna, which was large,

directional and gave excellent pulse transmission characteristics. A CPW-fed monopole was also investigated, which was small, omni-directional and had poor pulse transmission characteristics.

A UWB dipole was designed for use in a UWB channel modelling experiment in collaboration with Strathclyde University. The initial UWB dipole investigated was a microstrip-fed structure that had unpredictable behaviour due to the feed, which excited leakage current down the feed cable and, as a result, distorted both the radiation pattern and the pulse. To minimise the leakage current, three other UWB dipoles were investigated. These were a CPW-fed UWB dipole with slots, a hybrid-feed UWB dipole, and a tapered-feed UWB dipole. Presented for these UWB dipoles are S-parameter results, obtained using a vector network analyser, and radiation pattern results obtained using an anechoic chamber.

There were several antennas investigated in this thesis directly related to the Speckled Computing Consortiums objective of designing a 5mm^3 'Speck'. These antennas were conventional narrowband antenna designs operating at either 2.45 GHz or 5.8 GHz. A Rectaxial antenna was designed at 2.45 GHz, which had excellent matching ($S_{11} = -20\text{dB}$) at the frequency of operation, and an omni-directional radiation pattern with a maximum gain of 2.69 dBi as measured in a far-field anechoic chamber. Attempts were made to increase the frequency of operation but this proved unsuccessful.

Also investigated were antennas that were designed to be integrated with a 5.8 GHz MMIC transceiver. The first antenna investigated was a compact-folded dipole, which provided an insight into miniaturisation of antennas and the effect on antenna efficiency. The second antenna investigated was a 'patch' antenna. The 'patch' antenna utilised the entire geometry of the transceiver as a radiation mechanism and, as a result, had a much improved gain compared to the compact-folded dipole antenna. As the entire transceiver was an antenna, an investigation was carried into the amount of power flow through the transceiver with respect to the input power.

“Gin a body meet a body
 Flyin' through the air,
Gin a body hit a body,
 Will it fly? and where?

Ilka impact has its measure,
 Ne'er a ane hae I,
Yet a' the lads they measure me,
 Or, at least, they try.

Gin a body hit a body
 Altogether free;
How they travel afterwards
 We do not always see.

Ilka problem has its method
 By analytics high;
For me, I ken nae ane o' them,
 But what the waur am I?”

— James Clerk Maxwell
Rigid Body Sings (l. 1–4)

Table of Contents

List of Figures	8
List of tables.....	17
Acknowledgments.....	18
Authors declaration.....	19
1. Introduction.....	20
2. An introduction to antennas	23
2.1 What is an antenna?	23
2.2 Types of antennas	26
2.2.1 Wire antennas.....	26
2.2.2 Aperture antennas	26
2.2.3 Array Antennas	26
2.2.4 Printed Antennas.....	27
2.3 Radiation Mechanism	27
2.4 The Dipole	29
2.5 Antenna Field Region	32
2.5.1 Reactive near-field region.....	32
2.5.2 Radiating near-field or Fresnel region	32
2.5.3 Radiating far-field or Fraunhofer region.....	33
2.5.4 Characteristic impedance of EM waves.....	33
2.5.5 Velocity of Propagation	34
2.6 The fields of a short electric dipole.....	35
2.7 The fields of a finite length dipole.....	45
3. Fundamental limitations of small antennas.....	51
3.1 Wheeler limit	51
3.2 Chu-Harrington Limit	52
3.3 Mclean Limit.....	55
3.4 Fundamental Limits of a 5.8 GHz antenna	56
4. Transmission lines	58
4.1 Basic transmission line theory	58
4.2 Transmission Lines	59
4.2.1 Two-wire transmission line.....	59
4.2.2 Parallel plate waveguide	60
4.2.3 Co-Axial line.....	60
4.2.4 Microstrip.....	61
4.2.5 Co-Planar Waveguide (CPW).....	63
4.2.6 Slotline	64
5. Antenna Analysis	67
5.1 Fundamental Antenna Parameters	67
5.1.1 Impedance Bandwidth	67
5.1.2 S-Parameters	68
5.1.3 Radiation Pattern.....	71
5.1.4 Directivity (D).....	72
5.1.5 Antenna Efficiency (η).....	73
5.1.6 Antenna Gain	75

5.1.7 Polarisation	76
6. Antenna design, fabrication and experimental analysis.....	79
6.1 High Frequency Simulation Software (HFSS)	79
6.1.1 Theoretical basis of HFSS	79
6.1.2 Simulating structures in HFSS.....	81
6.3 Fabrication Processes.....	86
6.4 Testing facilities.....	87
6.4.1 Near-field anechoic chamber	87
7. A proximity-coupled 5.8 GHz patch antenna	89
7.1 Background theory.....	89
7.2 Design of Patch antenna - The transmission line model.....	91
7.3 Simulated Results.....	94
7.4 Testing antenna and redesign.....	96
8. Ultra-Wide Band (UWB) Antennas.....	104
8.1 UWB Architecture	104
8.2 Key requirements for UWB antennas	105
8.3 Initial designs of UWB Antennas	107
8.3.1 UWB test system.....	107
8.3.2 The Vivaldi Antenna.....	108
8.2.2 The CPW-fed Monopole Antenna	115
8.4 Initial UWB Evaluation	121
9. A UWB channel modelling experiment.....	123
9.1 UWB test system.....	123
9.2 UWB dipole	124
9.2.1 Microstrip Edge-fed UWB dipole.....	125
9.2.1.1 Radiation pattern results	129
9.2.2 UWB dipole with slots.....	133
9.2.2.1 Effect of slots on antenna.....	133
9.2.2.2 S-parameter results for UWB dipole with slots	139
9.2.2.3 Radiation pattern results for UWB dipole with slots.....	141
9.2.3 A hybrid feed for a edge-fed UWB dipole antenna	144
9.2.3.1 S-Parameter results for hybrid feed UWB dipole	151
9.2.3.2 Radiation pattern results for hybrid feed UWB dipole	154
9.2.4 A tapered feed UWB dipole.....	157
9.2.4.1 S-parameter results for tapered feed UWB dipole.....	162
9.2.4.2 Radiation pattern results for tapered feed UWB dipole.....	166
9.3 Comparison of UWB dipoles for pulse transmission	169
9.3.1 Pulse transmission via microstrip fed UWB dipoles	172
9.3.2 Pulse transmission via CPW-fed UWB dipole with slots.....	174
9.3.3 Pulse transmission via hybrid feed UWB dipole	176
9.3.4 Pulse transmission via tapered feed UWB dipole.....	178
9.4 Evaluation of UWB dipoles	180
10. Narrowband Antenna Design.....	181
10.1 Narrowband Radio Architectures	181
10.1.1 Diode rectifier	181
10.1.2 Super Regenerative Receiver (SRR).....	182
10.1.3 Comparison of SRR link budgets at varying frequencies.....	183
10.2 The Rectaxial antenna.....	186

10.2.1	Background theory	186
10.2.2	A 2.45 GHz rectaxial antenna.....	189
10.2.3	Design of 5.8 GHz rectaxial antenna	192
10.2.4	Surface waves in a grounded dielectric	194
10.2.5	Field analysis of 5.8 GHz Rectaxial antenna.....	195
10.3	Integrated antennas at 5.8 GHz.....	201
10.3.1	Quality factor, bandwidth and efficiency.....	202
10.3.2	A compact folded dipole antenna at 5.8 GHz.....	205
10.3.2.1	Balun design.....	206
10.3.2.2	Design of compact-folded dipole antenna	209
10.3.2.2.1	Width of dipole	209
10.3.2.2.2	Printed dipole on substrate.....	211
10.3.2.2.3	Slotline-fed dipole over a ground plane.....	213
10.3.2.2.4	Folded dipole over a ground plane with transceiver.....	215
10.3.2.3	Final design of printed dipole folded around transceiver	218
10.3.2.4	Simulated and experimental results for final design.....	218
10.3.3	A 'patch' antenna at 5.8 GHz	221
10.3.4	A approximate gain measurement for integrated 5.8 GHz antennas	226
11.	Discussion and conclusions	231
12.	List of References	235
12.1	Chapter 1	235
12.2	Chapter 2	235
12.3	Chapter 3	236
12.4	Chapter 4.....	236
12.5	Chapter 5.....	237
12.6	Chapter 6.....	238
12.7	Chapter 7.....	238
12.8	Chapter 8.....	238
12.9	Chapter 9.....	239
12.10	Chapter 10.....	240

List of Figures

Figure 2.1 Antenna as a transition device.....	25
Figure 2.2 Transmission-line thevenin equivalent of antenna in transmitting mode.....	25
Figure 2.3. Charge uniformly distributed in a circular cross section cylinder wire.....	27
Figure 2.4. Oscillating electric dipole consisting of two electric charges in simple harmonic motion, showing propagation of an electric field and its detachment (radiation) from the dipole. Arrows next to the dipole indicate current (I) direction.....	30
Figure 2.5. Electric field lines for a $\lambda/2$ antenna at (a) $t = 0$, (b) $t = T/8$, (c) $t = T/4$ and (d) $t = 3T/8$	31
Figure 2.6. Field regions of an antenna.....	32
Figure 2.7. A short dipole antenna.....	35
Figure 2.8. Electric field configuration.....	36
Figure 2.9. Geometry for a short dipole.....	36
Figure 2.10. Near- and far-field patterns of E_θ and H_ϕ	44
Figure 2.11. Near-field pattern for E_r component.....	45
Figure 2.12 Approximate natural-current distribution for thin, linear, centre-fed antennas of various lengths.	46
Figure 2.13. Finite dipole geometrical arrangement for a far-field approximation.....	46
Figure 2.14. Polar plots for the radiation patterns of a dipole of length (a) 0.5λ (b) 0.75λ (c) 1λ (d) 1.25λ (e) 1.5λ (f) 1.75λ	49
Figure 3.1 Sphere enclosing an electrically small radiating element.....	51
Figure 3.2. (a) Equivalent network of a vertically-polarised omni-directional antenna (b) Equivalent circuit for N spherical modes.....	53
Figure 3.3 Fundamental limit of Q versus antenna size.....	57
Figure 4.1. Model of a section of transmission line.....	58
Figure 4.2 Parallel plate waveguide.....	60
Figure 4.3 Co-axial transmission line.....	61

Figure 4.4 Conceptual evolution of a Microstrip line from a two-wire transmission line. (a) To a two wire transmission line. (b) To a parallel-plate waveguide. (c) To a microstrip line with no dielectric (d) To a microstrip line.	62
Figure 4.5 (a) Coplanar Waveguide (CPW) geometry (b) Electric and magnetic field distributions on CPW.....	63
Figure 4.6 Slotline transmission line.....	64
Figure 4.7. Field distribution of slotline. Solid line is E-field and dashed line is H-field.	65
Figure 5.1 An N-Port network.....	69
Figure 5.2 Two port network definition.....	70
Figure 5.3 Coordinate system for antenna analysis.....	72
Figure 5.4. Schematic diagram of antenna terminated in impedance Z_T with plane wave incident on antenna (a) and equivalent circuit (b)	74
Figure 5.5. Rotation of a plane electromagnetic wave and its polarisation ellipse at $z = 0$ as a function of time.	76
Figure 6.1. 3D structure sub divided into elements.....	81
Figure 6.2. 5.8 GHz proximity coupled patch antenna	81
Figure 6.3. Wave port excitation on a SMA connector.....	82
Figure 6.4 HFSS model (a) with and (b) without radiation boundary.....	85
Figure 6.5 Solution data for seven passes.....	85
Figure 6.6. Layout of chamber. $R =$ probe to centre of AUT =111.5 cm.....	88
Figure 7.1. Representative shapes of microstrip patch antennas.....	89
Figure 7.2. (a) Microstrip antenna (b) side view.....	90
Figure 7.3. Physical and effective lengths of rectangular microstrip patch.....	92
Figure 7.4. HFSS model of 5.8 GHz patch antenna with final dimensions.....	95
Figure 7.5 Simulated results for (a) S_{11} and (b) 3D E-field.....	96
Figure 7.6. Simulated (blue) and experimental (red) results for S_{11}	97
Figure 7.7. 5.8 GHz patch antenna with 10 cm SMA cable.....	97
Figure 7.8. Surface current on 5.8 GHz patch antenna with 10 cm SMA cable...98	
Figure 7.9. Simulated (blue) and experimental (red) results for S_{11}	99
Figure 7.10 Geometrical layout of 5.8 GHz patch antenna with short circuit stub.....	99
Figure 7.11. Effect of varying short circuit stub length on S_{11} The length is varied from 8.5mm to 9.5mm.....	100

Figure 7.12. Simulated (blue), $L=8.5\text{mm}$, and experimental (red) results for S_{11}	100
Figure 7.13. Simulated results for 5.8 GHz antenna with short circuit stub. ($L=8.5\text{mm}$) (a) Surface current (b) 3D E-field pattern.....	101
Figure 7.14. Experimental radiation plots (a) horizontal cuts; red = principle cut; blue = simulated (b) vertical cuts; red = principle cut; blue = simulated.....	102
Figure 8.1 Comparison of (a) Narrowband and (b) UWB architectures.....	105
Figure 8.2 Basic block diagram of the test system.....	107
Figure 8.3 (a) Output waveform from 4015C pulser with 10x attenuation (b) Output waveform after the impulse forming network stage.....	108
Figure 8.4. (a) Schematic of Vivaldi antenna designed in this project schematic. Length = 292.1mm, Width = 203.2 mm. (b) Magnified view of transition.....	109
Figure 8.5. Plan view of Vivaldi Antenna showing the magnitude of the E-field (V/m)	110
Figure 8.6. Simulated (blue) and experimental (red) S_{11} for Vivaldi antenna...	110
Figure 8.7. Transmission response (S_{21}) for Vivaldi. Distance between antennas =20 cm.....	111
Figure 8.8. (a) Experimental group delay for Vivaldi antenna (b) magnified view for group delay. Distance between antennas = 20 cm.....	112
Figure 8.9. Vivaldi simulated antenna 3D radiation (Gain (dB)) patterns for (a) 3 GHz (b) 6 GHz and (c) 9 GHz	114
Figure 8.10. Received pulse for Vivaldi antenna.....	115
Figure 8.11. The CPW-fed monopole.....	116
Figure 8.12. (a) Simulated (red) and (b) experimental (blue) S_{11} results for CPW-fed monopole.....	117
Figure 8.13. Transmission response (S_{21}) for CPW-monopole. Distance between antennas =20 cm.....	118
Figure 8.14. Experimental (blue) results for Group delay Vs frequency.....	119
Figure 8.15. Simulated radiation patterns for (a) 3 GHz (b) 6 GHz and (c) 9 GHz.....	120
Figure 8.16. Pulse received by CPW-fed monopole.....	121
Figure 9.1 Block diagram for Strathclyde UWB test system.....	124
Figure 9.2. Elliptical dipole element with suggested feeding points (a) centre (b) bottom and (c) edge.	124

Figure 9.3. Microstrip edge-fed UWB dipole with taper. The brown element is the 'GND' for the microstrip feed.....	126
Figure 9.4. Simulated (blue) and experimental (red) results for S_{11} Vs. Frequency.....	127
Figure 9.5. Microstrip-fed UWB dipole S_{11} phase results (i) simulated (blue) (ii) experimental (red)	128
Figure 9.6. Transmission response (S_{21}) for Microstrip-fed UWB dipole. Distance between antennas =20 cm.	128
Figure 9.7. Experimental group delay for microstrip edge-fed UWB dipole. Distance between antennas = 20 cm.	129
Figure 9.8. Orientation of antenna with respect to coordinate system used for measurements.....	129
Figure 9.9. Microstrip edge-fed UWB dipole simulated 3D E-field radiation patterns for (a) 3 GHz (b) 6 GHz and (c) 9 GHz.....	131
Figure 9.10 Microstrip-fed UWB dipole simulated (blue) and experimental (red) horizontal and vertical cuts for (a) 3GHz (b) 6 GHz and (c) 9 GHz.....	132
Figure 9.11. CPW-fed dipole with slots.....	133
Figure 9.12. Current flow around the antenna at the cpw to co-axial interface...134	
Figure 9.13. Comparison of CPW-fed dipole antenna (a) with and (b) without slots.....	135
Figure 9.14 Analysis of leakage current using E-field vector plot.....	135
Figure 9.15. Simulated S_{11} results for the increasing slot length; blue = 6mm, red = 8mm, green = 10mm, magenta = 12mm, black = 17mm.....	136
Figure 9.16. (a) Real and (b) Imaginary input impedance versus frequency for increasing slot length; blue = 6mm, red = 8mm, green = 10mm, magenta = 12mm, black = 17mm.....	137
Figure 9.17. (a) Vector surface current plots (a) 2.32 GHz and (b) 3 GHz The slot = 17 mm for both plots.	138
Figure 9.18. Simulated (blue) and experimental (red) results for S_{11}	139
Figure 9.19. UWB dipole with slots S_{11} phase results (i) simulated (blue) (ii) experimental (red)	140
Figure 9.20. Transmission response (S_{21}) for CPW-fed UWB dipole with slots. Distance between antennas =20 cm.	140

Figure 9.21. Experimental group delay for UWB dipole with slots. Distance between antennas = 20 cm.	141
Figure 9.22. Orientation of antenna with respect to coordinate system used for measurements.....	141
Figure 9.23. Simulated 3D E-field radiation patterns for (a) 3 GHz (b) 6 GHz and (c) 9 GHz.....	143
Figure 9.24 CPW-fed UWB dipole with slots simulated (blue) and experimental (red) horizontal and vertical cuts for (a) 3GHz (b) 6 GHz and (c) 9 GHz.....	144
Figure 9.25. Hybrid-feed UWB dipole.....	145
Figure 9.26. HFSS model for parallel plate interaction with metal (a) GND clear (b) signal clear.....	146
Figure 9.27. S_{11} and S_{22} for sub thickness = 2.286 mm; Blue (S_{11}) and Red (S_{22}) belong to signal clear (Figure 6.22 (b)); Green (S_{11}) and Magenta (S_{22}) belong to GND clear (Figure 6.22 (a)).	147
Figure 9.28 Insertion Loss for sub thickness = 2.286 mm – GND clear (blue), Signal clear (red).....	147
Figure 9.29. Balanced feed UWB dipole (a) top view (b) underside view (c) 3D see-through view.....	149
Figure 9.30 Comparison of leakage current at 3 GHz on UWB dipole antennas (a) CPW feed with slots (b) balanced feed.....	150
Figure 9.31 Far-field pattern for hybrid feed UWB dipole connected to co-axial cable.....	151
Figure 9.32. S_{11} for simulated (blue) and practical (red)	152
Figure 9.33 Simulated (blue) and experimental (red) results for phase.....	152
Figure 9.34. Transmission response (S_{21}) for hybrid fed UWB dipole. Distance between antennas =20 cm.....	153
Figure 9.35. Experimental group delay for hybrid fed UWB dipole. Distance between antennas = 20 cm.....	153
Figure 9.36. Orientation of antenna with respect to coordinate system used for measurements.....	154
Figure 9.37. Simulated 3D E-field radiation patterns for hybrid fed UWB dipole at (a) 3 GHz (b) 6 GHz and (c) 9 GHz.....	155
Figure 9.38 Hybrid feed UWB dipole simulated (blue) and experimental (red) horizontal and vertical cuts for (a) 3GHz (b) 6 GHz and (c) 9 GHz.....	156

Figure 9.39. Layout of microstrip to parallel-plate tapered line balun. Overall dimensions - length = 71.6mm, width = 9.52mm.....	157
Figure 9.40. Surface current plot for balun at 3 GHz.....	158
Figure 9.41 Simulated S-parameter results for balun. S_{21} = Green; S_{11} = Blue; S_{22} = Red.....	159
Figure 9.42 Geometrical layout of tapered feed UWB antenna. $W = 30.875\text{mm}$; $L = 38.35\text{mm}$	160
Figure 9.43 Analysis of surface current on tapered feed antenna connected to co-axial cable.....	160
Figure 9.44. Comparison of 3D e-field patterns connected to a co-axial cable for (a) Hybrid feed UWB dipole and (b) Tapered feed UWB dipole.....	161
Figure 9.45. Tapered-feed UWB dipole S_{11} results for simulated (blue) and experimental (red)	162
Figure 9.46. E-field at 10.16 GHz for (a) Tapered feed UWB dipole (b) half-wavelength dipole.....	163
Figure 9.47. Simulated (blue) and experimental (red) results for phase.....	164
Figure 9.48. Transmission response (S_{21}) for tapered feed UWB dipole. Distance between antennas =20 cm.....	165
Figure 9.49. Experimental group delay for tapered feed UWB dipole. Distance between antennas = 20 cm.....	165
Figure 9.50. Orientation of antenna with respect to coordinate system used for measurements.....	166
Figure 9.51. Simulated 3D E-field radiation patterns for tapered feed UWB dipole at (a) 3 GHz (b) 6 GHz and (c) 9 GHz.....	167
Figure 9.52 Tapered feed UWB dipole simulated (blue) and experimental (red) horizontal and vertical cuts for (a) 3GHz (b) 6 GHz and (c) 9 GHz.....	168
Figure 9.53. Comparison of theoretical (blue) and experimental (red) results for a 100 ps pulse.....	169
Figure 9.54. 1 st derivative of Gaussian function experimental (red) and theoretical (blue) results.....	170
Figure 9.55. 2 nd derivative of Gaussian function.....	171
Figure 9.56. Pulse received using microstrip-fed UWB dipole with filter (red) and without filter (blue)	172

Figure 9.57. Pulse received using CPW-fed UWB dipole with slots with filter (red) and without filter (blue)	174
Figure 9.58. Pulse received using hybrid feed UWB dipole with filter (red) and without filter (blue)	176
Figure 9.59. Pulse received using tapered-feed UWB dipole with filter (red) and without filter (blue)	178
Figure 10.1. Diode rectifier circuit.....	182
Figure 10.2. Block diagram of complete narrowband transceiver.....	182
Figure 10.3. Output voltage vs. Input power for diode rectifier and SRR.....	183
Figure 10.4 Basic block diagram illustrating Friis equation.....	184
Figure 10.5. (a) Helix and associated dimensions (b) Relationship between circumference, spacing, turn length, and pitch angle of a helix.	187
Figure 10.6. Dimensions and coordinates for (a) helix (b) loop and (c) dipole. (d) Helix as a succession of loops and dipoles (e) Helix for normal mode calculations.....	188
Figure 10.7. Schematic of rectaxial antenna.....	189
Figure 10.8. Diagram of rectaxial antenna with dimensions.	190
Figure 10.9 Return Loss (RL) results for both simulation (a) and measured (b) results.	191
Figure 10.10. Normalised radiation patterns obtained by both simulation and measurement.....	192
Figure 10.11. Schematic of 5.8 GHz rectaxial antenna.....	192
Figure 10.12. Return loss for 5.8 GHz rectaxial antenna.....	193
Figure 10.13. (a) E-field for 2.45 GHz rectaxial antenna. (b) E-field for 5.8 GHz rectaxial antenna.....	193
Figure 10.14. Comparison of surface currents on the ground planes. (a) 2.45 GHz rectaxial antenna (b) 5.8 GHz rectaxial antenna.....	194
Figure 10.15. Geometry of a grounded dielectric slab.....	194
Figure 10.16 E-field vector plot of substrate.....	195
Figure 10.17 Vector surface current plot on the ground plane.....	196
Figure 10.18. Surface current plot (a) with and (b) without rectaxial element.....	197
Figure 10.19. Simulated plots for (a) 3D E-field (b) 3D Gain (dBi) (c) x - y cut of E-field.....	198

Figure 10.20. (a) Rectaxial antenna with small ground plane (b) x - y cut of Electric far-field radiation pattern.....	199
Figure 10.21 x - y cuts for (a) 5.8 GHz rectaxial antenna and (b) pattern multiplication of Figure 8.15 (c) and Figure 8.16 (b)	200
Figure 10.22. A 5.8 GHz MMIC Transceiver. Maximum dimensions, length = 6.2; width = 2.25 mm.....	201
Figure 10.24. Folded dipole with transceiver attached.....	205
Figure 10.25. A CPW-to-slotline transition.....	206
Figure 10.26. Simulated results for S_{21} (green), S_{11} (blue) and S_{22} (red). Stub length=5mm.....	207
Figure 10.27. Smith chart showing S_{11} at 5.8 GHz for increasing length of Slotline termination.....	208
Figure 10.28. Smith chart showing S_{11} at 5.8 GHz for CPW-to-slotline transition for increasing length of stub.....	209
Figure 10.29. Half-wavelength dipole showing current distribution. Width = 0.4mm.....	210
Figure 10.30. Input resistance (Ω) with width variation of 50 μm (blue), 100 μm (red), 200 μm (green), 300 μm (magenta), 400 μm (black)	210
Figure 10.31. Input reactance (Ω) with width variation of 50 μm (blue), 100 μm (red), 200 μm (green), 300 μm (magenta), 400 μm (black)	211
Figure 10.32. Half-wavelength dipole placed on GaAs substrate.....	212
Figure 10.33. Input resistance (Ω) with width variation of 50 μm (blue), 100 μm (red), 200 μm (green), 300 μm (magenta), 400 μm (black)	212
Figure 10.34. Input reactance (Ω) with width variation of 50 μm (blue), 100 μm (red), 200 μm (green), 300 μm (magenta), 400 μm (black)	213
Figure 10.35. Possible configuration of Speck (a) side view (b) plan view.....	214
Figure 10.36. Slotline-fed dipole antenna over ground plane.....	214
Figure 10.37. Results for real (red) and imaginary (blue) input impedance for a printed dipole antenna over a ground plane.....	215
Figure 10.38. Layout for a slotline-fed folded dipole with the transceiver body.....	216
Figure 10.39. Results for real (red) and imaginary (blue) input impedance for a printed dipole antenna over a ground plane.....	216

Figure 10.40. Far-field gain (dB) plots for (a) Folded dipole over a ground plane with transceiver (b) Slotline fed dipole over a ground plane.....	217
Figure 10.41. Schematic of folded dipole over ground plane with CPW-slotline transition.....	218
Figure 10.42. Simulated (blue) and experimental (red) results for S_{11}	219
Figure 10.43. Simulated input resistance (red) and reactance (blue). Experimental input resistance (magenta) and reactance (green)	220
Figure 10.44. Simulated 3D Gain plot for folded dipole.....	220
Figure 10.45. Schematic of ‘patch’ antenna with main dimensions outlined....	221
Figure 10.46. Vector plots for 5.8 GHz ‘patch’ antenna (a) E-field (b) Vector surface current.....	222
Figure 10.47. Simulated (blue) and experimental (green) S_{11} results for ‘patch’ antenna.....	223
Figure 10.48. Simulated 3D gain plot for ‘patch’ antenna.....	224
Figure 10.49. Transceiver body highlighted for Poynting vector calculation....	225
Figure 10.50. Simulated surface loss density on 5.8 GHz transceiver body.....	226
Figure 10.51. Experimental setup for gain measurement.....	227
Figure 10.52. Experimental results for S_{21} for 5.8 GHz proximity-coupled patch antenna with separations of 14.5cm (blue), 20cm (red), 25cm (green), 30cm (magenta), and 40cm (black)	228

List of tables

Table 8.1 Antenna performance table. CG = Constant Gain.....	122
Table 9.1. Performance comparison of UWB dipoles.....	180
Table 10.1 Power link budget for 2.45 GHz.....	185
Table 10.2 Power link budget for 5.8 GHz.....	185
Table 10.3 Power link budget for 5.8 GHz.....	185
Table 10.4 Calculated values for average gain at 5.5 GHz and 5.92 GHz.....	228
Table 10.5. Folded dipole - Signal received on spectrum analyser via patch antenna for various separations with the calculated value of gain.....	229
Table 10.6. 'Patch' antenna - Signal received on spectrum analyser via patch antenna for various separations with the calculated value of gain.....	229

Acknowledgments

I would like to thank all the staff and students at Glasgow University who have helped me during my time and made it a very enjoyable stay.

In particular, I would like to thank my supervisor Prof. Iain Thayne for letting me do the PhD in the first place. His door was always open and he was willing to listen and give advice. I would also like to give a big thanks to Ian McGregor for his help with a multitude of topics and the always enjoyable afternoon coffee conversations with him. Special mentions to Khaled Elgaid and Edward Wasige who were part of the Specknet group. Even though he has departed Glasgow, I should give a special thanks to Harold Chong who I constantly harassed about fabricating my designs in the clean room. Special thanks go to the rest of the Ultrafast Systems group and the Speckled Computing Consortium, who I have enjoyed working / socialising with.

I would also like to give a big thanks to the technical staff on level seven for their help, in particular Stuart Fairbairn for his rapid fabrication of my antenna designs and to Chris Hardy for the use of his desk and tools.

Thanks go to Faisal Darbai and Prof. Ian Glover of Strathclyde University for letting me use their equipment whenever I wanted

Very special thanks go to my father, for his encouragement and advice on writing reports, which helped me, not just throughout the course of this PhD, but my entire academic career to date.

Lastly and by no means least I would like to give a very special thanks to my girlfriend, Kirsty, as she has somehow managed to put up with me for very a long time.

This thesis is dedicated to the memory of my grandfather James 'Jimmy' Marshall.

Authors declaration

I, Griogair Whyte, declare that the work contained within this thesis is solely mine, except where acknowledged.

1. Introduction

Autonomous distributed wireless sensor networks such as those being investigated by the Speckled Computing Consortium [1] are widely predicted to have major growth opportunities in the coming years in numerous imaging, safety, biomedical and environmental applications. In most of these areas, the design challenges are somewhat different from contemporary wireless communications systems in that data rates will be low, and power consumption and size of the sensor node are the key issues.

Truly “plug and forget” functionality, and the opportunity to embed sensor nodes into everyday objects or the surrounding environment, requires small volume solutions, the majority of which will be occupied by a large enough battery to prolong lifetime. These constraints place stringent requirements on the system for the following reasons:

- i. The communication frequency should be high enough in order to minimise the size of antenna and thus sensor node, although operating at higher frequencies incurs higher path loss, and higher DC power consumption due to higher losses for the inter-node radio transceiver.
- ii. Given the low RF power levels (due to DC power constraints), the transceiver antenna should have as high a gain as possible, yet given the fact that the network nodes are randomly deployed and can be moving with respect to one another, an omni-directional radiation pattern is required.
- iii. In addition to the constraint mentioned in (i) above, the total volume of the antenna should be minimised to maximise the size of the battery.
- iv. As large numbers of sensor nodes will be required in any network, all component costs, including the antenna should be minimised.

There has been research into this topic by organisations other than Speckled Computing Consortium, most notably Berkeley University and its Smart Dust project [2]. The goal of the Smart Dust project is to build a self-contained, millimetre-scale, sensing and communication platform for a distributed sensor

network. The device itself, called a 'mote', would be around the size of a grain of sand and contain sensors, computational ability, bi-directional wireless communications and a power supply, while being inexpensive enough to be deployed by the hundreds. The science and engineering goal of the Speckled Computing Consortium project is to build a complete, complex system into a tiny volume using the newest technologies (as opposed to futuristic technologies), which requires advances in integration, miniaturisation and energy management. When the project started many applications were foreseen for this technology such as:

- Weather/seismological monitoring on Mars
- Internet spacecraft monitoring
- Land / space communication networks
- Chemical / biological sensors
- Weapons stockpile monitoring
- Defence related sensor networks
- Inventory control
- Product quality monitoring
- Smart office spaces
- Sports

The main difference from Smart Dust is that the Speckled Computing Consortium looks well beyond typical sensor networks applications. Smart Dust motes are used in static networks, whereas specks are intended for use as dense, decentralized networks in which the specks can be moved around, if required. The other main difference is that Smart Dust uses a centralised controller. A good analogy to describe Smart Dust would be a queen ant that directs the other ants. Whereas, Specknet intends to be completely decentralised i.e. the ants thinking for themselves; this gives a truly ubiquitous network. However, before the goal of a truly ubiquitous network is realised there are many hurdles to overcome. These are as follows:

- Synchronisation of the device is very important. If the Speck is meant to be autonomous, when will it know to send or receive information?
- Power consumption. If the device is very small it can only have a limited power supply and cannot remain 'on' at all times otherwise its lifetime will be extremely short. It is therefore important for the project to come up with the most energy efficient designs.

It was decided early in the project that there should be certain criteria which each sub-section of the Speck should meet. The most important criteria, from the RF front-end point of view, were;

- The Specks should be able to communicate 10cm apart
- Transmit-receive (Tx/Rx) while only consuming 400 μ W of power.

The initial work reported in this thesis focused on Ultra Wide-Band (UWB) due to the perceived power savings, and the fact that it was a 'new' technology. UWB is discussed from a radio architecture perspective but with the main focus being on antenna design and performance.

Discussed in the following chapters is the development of a low power radio architecture, which allowed for design of antennas at much higher frequencies than originally anticipated. Antennas were investigated and designed for the frequencies of 2.4 GHz and 5.8 GHz. Ultra-Wide Band (UWB) antennas were investigated and designed. They operated over the frequency range of 3.1 to 10.16 GHz. Chapter 2 presents the history and theory of antennas. Chapter 3 evaluates common transmission lines used to feed antennas. Chapter 4 gives the fundamental parameters used for evaluating antenna performance. Chapter 5 discusses the experimental procedure followed when designing and testing antennas, such as the simulation software, fabrication procedure and the test apparatus. The remaining chapters are concerned with the design, analysis and testing of antennas fabricated.

2. An introduction to antennas

The history of antennas originates back to 1873 when James Clerk Maxwell presented ‘*A Treatise on Electricity and Magnetism*’ [1]. This work drew from empirical and theoretical work that had already been carried out by scientists such as Gauss, Ampere, Faraday, and others. Maxwell took the theories of electricity and magnetism and unified them. The equations he derived are presented below in differential form.

$$\nabla \times \vec{E} = -\frac{\partial \vec{B}}{\partial t} - \vec{M} \quad (2.1)$$

$$\nabla \times \vec{H} = \frac{\partial \vec{D}}{\partial t} + \vec{J} \quad (2.2)$$

$$\nabla \cdot \vec{D} = \rho \quad (2.3)$$

$$\nabla \cdot \vec{B} = 0 \quad (2.4)$$

Where, \vec{E} is the electric field intensity (V/m).
 \vec{H} is the magnetic field intensity (A/m).
 \vec{D} is the electric flux density (C/m²).
 \vec{B} is the magnetic flux density (Wb/m²).
 \vec{M} is the (fictitious) magnetic current density (V/m²).
 \vec{J} is the electric current density (A/m²)
 ρ is the electric charge density (C/m³)

Maxwell’s equations allow the calculation of the radiated fields from a known charge or current distribution. They also give a description of the behaviour of the fields around a known current distribution or a known geometry. Maxwell’s equations can then be used to understand the fundamental principles of antennas.

2.1 What is an antenna?

The IEEE definition [2] of an antenna or aerial is:

‘a means for radiating or receiving radio waves’

Radio waves are also referred to as electromagnetic waves, or light waves, as they travel at the speed of light and can be represented by sine waves. The distance a wave travels to complete one cycle is known as the wavelength, λ , of a signal.

$$\lambda = \frac{c}{f}(\text{metres}) \quad (2.5)$$

Where c is the speed of light and f is the frequency (cycles per second).

In a vacuum or air the speed of light is approximately 3×10^8 m/s. When a radio wave passes through a non-conducting medium other than air this slows the wave down and results in a shorter wavelength. This property is of great importance when designing antennas and is analysed throughout this thesis.

An antenna can be viewed as a device which sends and receives electromagnetic waves. Essentially, an antenna acts as an energy converter for a transmission line into free space radiation. Antennas are bidirectional so this relationship works exactly the same from free space to a transmission line. Figure 2.1 shows an antenna as a transition device [3]. The arrows displayed in Figure 2.1 correspond to the electric field lines as the wave is transitioned into free space.

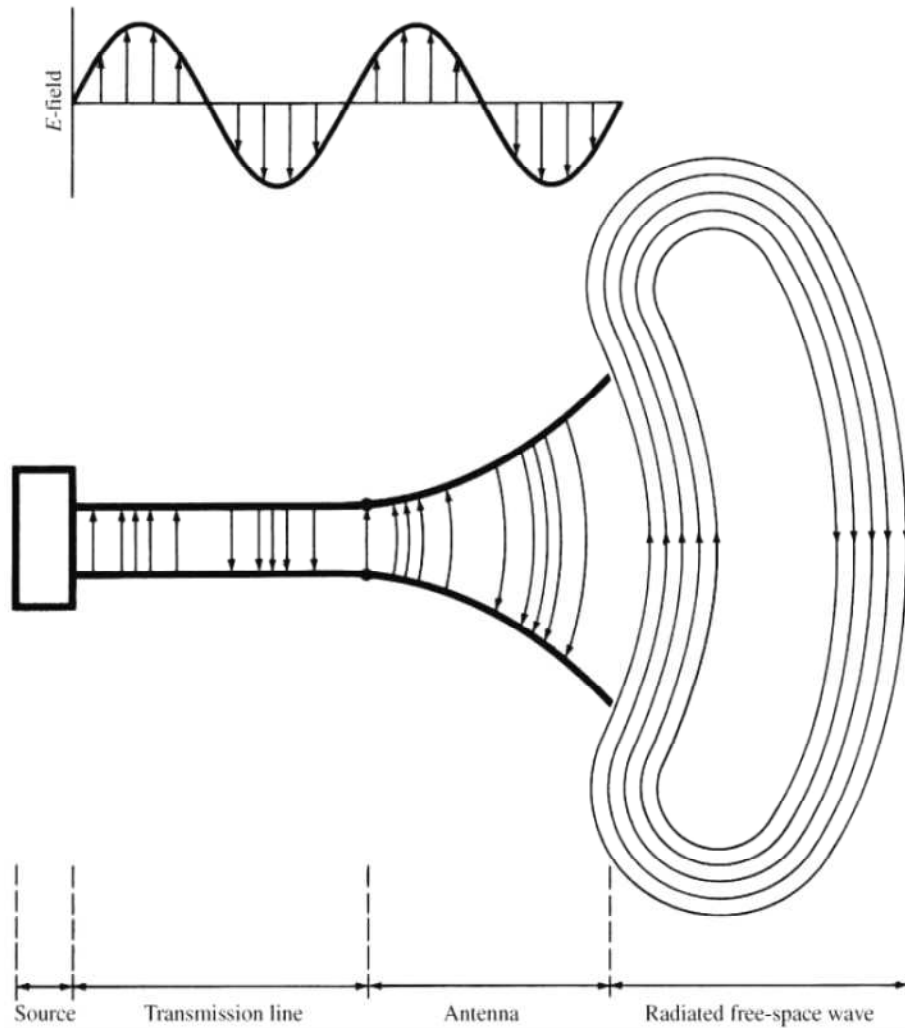


Figure 2.1 Antenna as a transition device

The transmitting antenna can be modelled as a Thevenin source, as shown in Figure 2.2. It consists of a voltage generator and series impedance, the transmission line being represented by a characteristic impedance Z_c , and the antenna is represented by load Z_A connected to the transmission line.

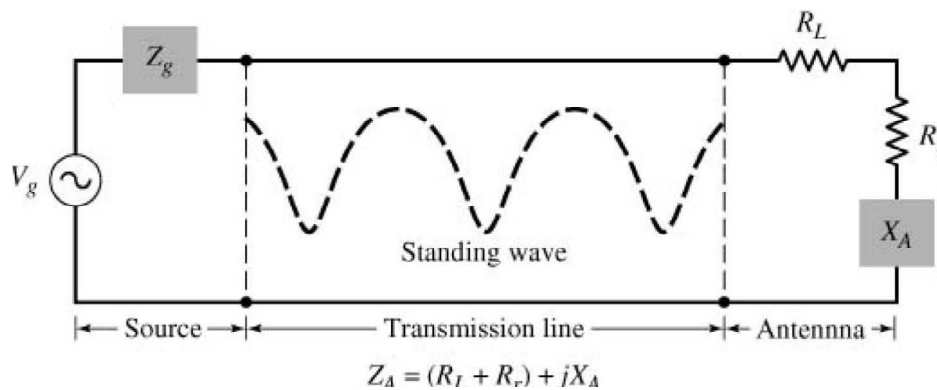


Figure 2.2 Transmission-line thevenin equivalent of antenna in transmitting mode

Antenna losses due to conductor, dielectric or heat are represented by the loss resistance, R_L . The radiation resistance, R_r , represents the real part of the radiation impedance of the antenna. The reactance, X_A , represents the imaginary part of the impedance associated with the radiation from the antenna.

2.2 Types of antennas

There are numerous types of antennas developed for many different applications; they can be classified into four distinct groups.

2.2.1 Wire antennas

Wire antennas are probably the most recognisable, as they are ubiquitous and typified by TV aerials, car aerials etc. Wire antennas can include dipoles, loops, helical, sleeve dipoles, Yagi-Uda arrays. Wire antennas generally have low gain and operate at lower frequencies (HF to UHF). They have the advantages of low cost, ease of fabrication and simple design.

2.2.2 Aperture antennas

Aperture antennas have a physical opening through which propagating electromagnetic waves flow. For example, a horn antenna opening acts as a “funnel” directing the waves into the waveguide. The aperture is usually several wavelengths long in one or more dimensions. The pattern has a narrow main beam which leads to high gain. For a fixed aperture size, the main beam pattern narrows down as frequency increases. These types of antennas are very useful in aerospace and spacecraft applications, because they can be easily flush-mounted on the skin of an aircraft or spacecraft. Examples of these antennas include parabolic reflector, horn antennas, lenses antennas and circular apertures.

2.2.3 Array Antennas

Array antennas are made up of a matrix of discrete sources which radiate individually. The pattern of the array is determined by the relative amplitude and phase of the excitation fields of each source and the geometric spacing of the sources. Typical elements in an array are dipoles, monopoles, slots in waveguides, open-ended antennas and microstrip radiators.

2.2.4 Printed Antennas

Printed antennas can encompass all of the antennas mentioned in sections 2.2.1 to 2.2.3, except they take a planar form. Printed antennas are made via photolithographic methods, with both the feeding structure and the antenna fabricated on a dielectric substrate. Printed antennas form the bulk of the structures discussed in this thesis.

2.3 Radiation Mechanism

All antennas, regardless of type, operate under the same basic principle that radiation is produced by an acceleration (or deceleration) of electrical charge. To illustrate the principle, a piece of conducting wire, as shown in Figure 2.3 [4], will be used.

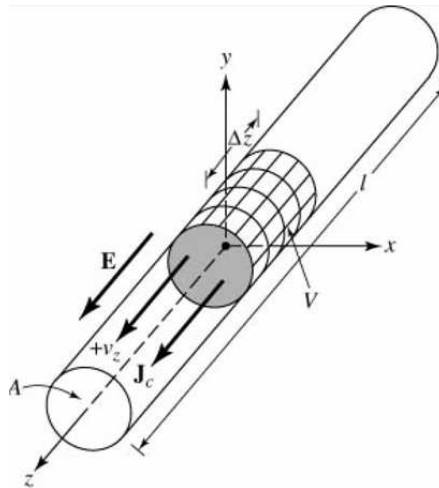


Figure 2.3. Charge uniformly distributed in a circular cross section cylinder wire

If the electric charge density, ρ , is uniform over the piece of wire, then by combining Maxwell's Equations, (2.2) and (2.3), it can be shown that:

$$J_z = \rho \cdot v_z \quad (2.5)$$

Where J_z is the component of current density, \vec{J}_c , in the z-direction and v_z is the velocity in which the charge, Q, is moving within the volume in the z-direction. If the wire is a perfect conductor then the current resides on the surface of the

conductor and current density becomes J_s (amperes/m). This is shown by Equation 2.6.

$$J_s = \rho_s \cdot v_z \quad (2.6)$$

ρ_s represents the surface charge density (coulombs/m²). If the wire is very thin, or zero radius, then Equation 2.6 reduces to:

$$I_z = \rho_l \cdot v_z \quad (2.7)$$

Where, ρ_l (coulombs/m) is the charge per unit length.

If the current varies with time then the derivative of Equation 2.7 can be written as:

$$\frac{dI_z}{dt} = \rho_l \frac{dv_z}{dt} \quad (2.8)$$

If the wire is of a length, L, then the Equation 2.8 can be written as:

$$L \frac{dI_z}{dt} = Q \frac{dv_z}{dt} \quad (2.9)$$

This equation is known as the basic equation of radiation and shows that time-changing current radiates and accelerated charge radiates. The radiation is perpendicular to the acceleration of charge, and the radiated power is proportional to the square of either the right or left hand side of Equation 2.9. For steady state harmonics the focus is on current and for transients or pulses the focus is on charge [5]. To create charge acceleration (or deceleration) the wire must be curved, bent, discontinuous or terminated. Periodic charge acceleration (or deceleration) or time varying current is also created when charge is oscillating in a time-harmonic motion. Therefore:

1. If a charge is not moving, current is not created and there is no radiation

2. If charge is moving in a uniform velocity:
 - a. There is no radiation if the wire is straight and infinite in extent
 - b. There is radiation if the wire is curved, bent, discontinuous, terminated, or truncated
3. If charge is oscillating in a time-motion, it radiates even if the wire is straight

2.4 The Dipole

To illustrate the principle of radiation from an antenna it is useful to look at one of the simplest and one of the most widely used antennas, the dipole. The dipole is realised by a short straight wire of finite length, which terminates at two points allowing charge to be collected. If an alternating current generator is connected to the centre of the wire dipole it can drive charge from one end to the other. This is illustrated in Figure 2.4 [6].

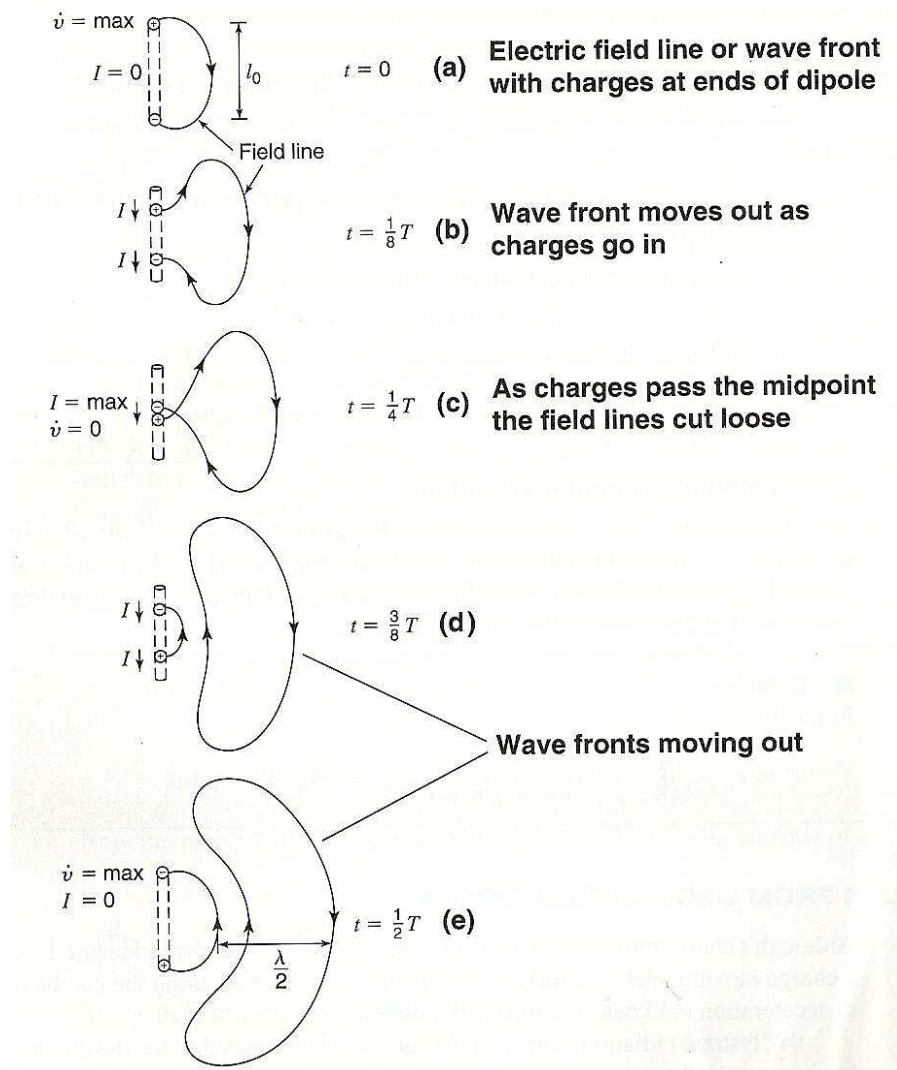


Figure 2.4. Oscillating electric dipole consisting of two electric charges in simple harmonic motion, showing propagation of an electric field and its detachment (radiation) from the dipole.

Arrows next to the dipole indicate current (I) direction

Shown in Figure 2.4(a) are two charges of equal magnitude and opposite polarity oscillating in a harmonic motion with a separation l (maximum separation l_0). For clarity there is only one electric field line shown. At $t=0$ the charges are at their maximum separation, l_0 , and have maximum acceleration, \dot{v} , as they reverse direction. At this instant, before they turn, the acceleration is zero, hence the current is zero.

Figure 2.4(b) shows the two charges moving towards each other $1/8^{\text{th}}$ of a period later with the wave front moving out. Figure 2.4(c) shows the charges at a $1/4$ of a period later where they pass through the midpoint. At this point, there is no net

charge (the current, I , is at a maximum) on the antenna and as a result the field line is forced to create its own loop. As time progresses to a $\frac{1}{2}$ period, the fields continue to move out, as shown in Figures 2.4(d) and 2.4(e). If the process is repeated and continued indefinitely then electric field patterns are created as shown in Figure 2.5 [7].

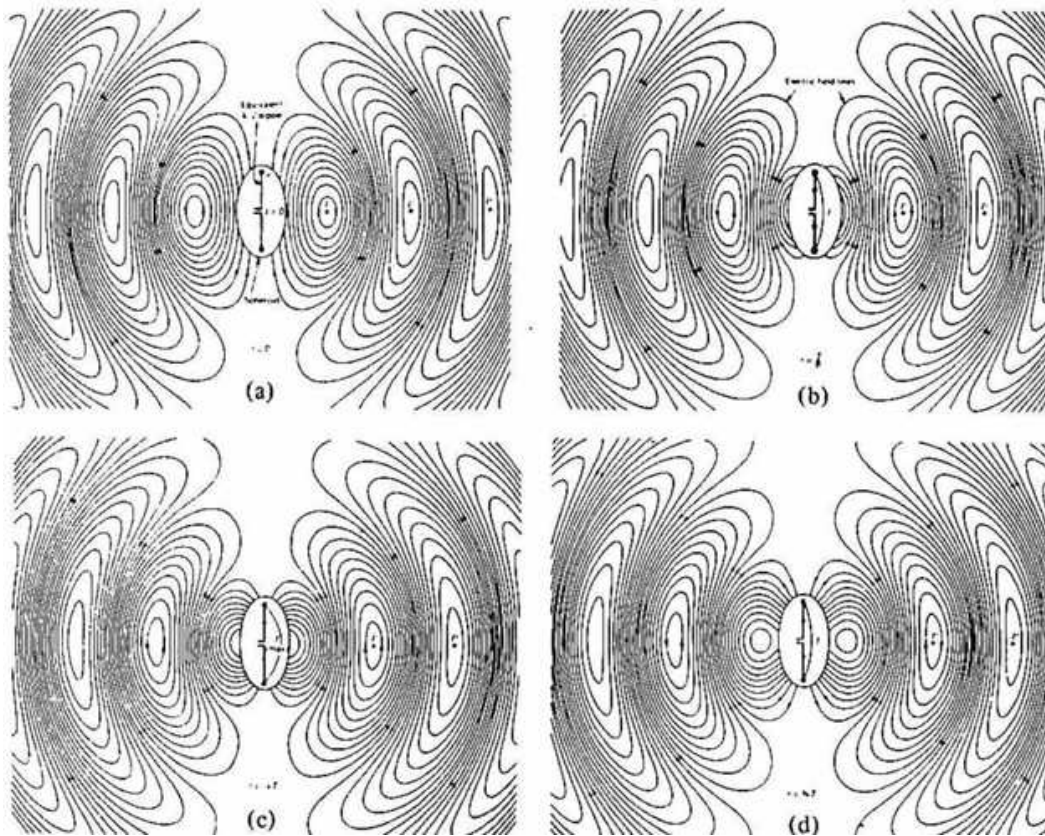


Figure 2.5. Electric field lines for a $\lambda/2$ antenna at (a) $t = 0$, (b) $t = T/8$, (c) $t = T/4$ and (d) $t = 3T/8$

2.5 Antenna Field Region

As an antenna radiates there are changes to the electromagnetic field structure as the radiation moves away from the antenna at a distance, R . These changes can be split into three distinct groups and are shown in Figure 2.5.

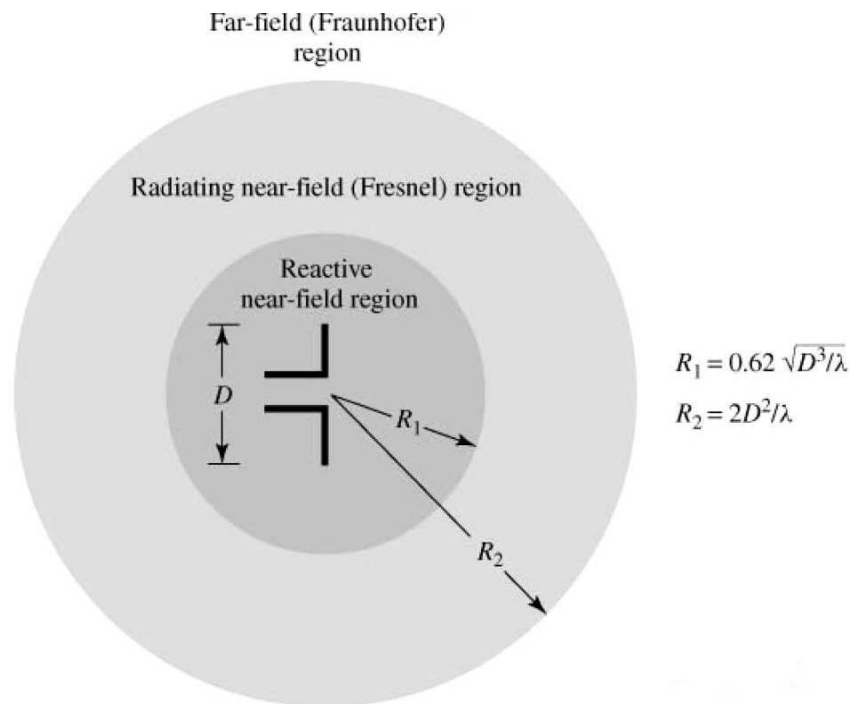


Figure 2.6. Field regions of an antenna

2.5.1 Reactive near-field region

The reactive near-field region, sometimes called the antenna region, is considered to be the volume of the field in the immediate vicinity of the antenna. For the majority of antennas this region exists at $R < 0.62\sqrt{D^3/\lambda}$ from the antenna, where R is radius and D is the maximum antenna dimension. Confined within this region is a high amount of non-propagating energy, or reactive power.

2.5.2 Radiating near-field or Fresnel region

The radiating near-field, or Fresnel region does not display spherical power flow and varies as a function of distance, R , from the antenna. Also, the longitudinal component of the electric field may be significant, for example, if using the dipole from Figure 2.5. The boundaries for this region are between

where $R \geq 0.62\sqrt{D^3/\lambda}$ and $R < 2D^2/\lambda$, and where D is the largest dimension. If the antenna is very small compared to wavelength this region may not exist.

2.5.3 Radiating far-field or Fraunhofer region

In the radiating far-field or Fraunhofer region the field components are transverse to the radial direction from the antenna and all the power flow is directed outwards in a radial fashion. In this region the shape of the field pattern is independent of the distance, R , from the antenna. The inner boundary is taken to be the distance $R = 2D^2/\lambda$, where D is the largest dimension of the antenna.

2.5.4 Characteristic impedance of EM waves

To help differentiate between near-field and far-field regions it is useful to analyse the characteristic impedance of plane waves. It can be shown [8], that the characteristic impedance of a plane wave for a lossless medium is given by:

$$Z_0 = \sqrt{\frac{\mu}{\epsilon}} (\Omega)$$

$$\mu = \mu_0 \mu_r \quad (2.10)$$

$$\epsilon = \epsilon_0 \epsilon_r$$

Where:

ϵ_0 = Permittivity of free space = 8.854×10^{-12} (F/m)

ϵ_r = Relative permittivity of the dielectric material

μ_0 = Permeability of free space = $4\pi \times 10^{-7}$ (H/m)

μ_r = Relative permeability of the magnetic material

For plane waves, this impedance is also known as the intrinsic impedance of the medium. In free space, where $Z_0 = 377\Omega$, the E-field and H-field are orthogonal to each other and orthogonal to the direction of propagation. If the wave is in the near-field, in a free space environment, $Z_0 \neq 377\Omega$ since the fields are not orthogonal to each other, or in the direction of propagation.

2.5.5 Velocity of Propagation

Another useful differentiation between the far-field and near-field regions, which gives an insight into the property of electromagnetic waves, is the velocity of propagation (m/s). The velocity of propagation of a plane wave, sometimes known as phase velocity, is the speed at which a wave moves through a medium and is given [9], for a lossless medium, by:

$$v_p = \frac{1}{\sqrt{\epsilon\mu}} = \frac{\omega}{k} (ms^{-1}) \quad (2.11)$$

Where:

ω = frequency (radians/s)

$\beta = \omega\sqrt{\mu\epsilon}$ = wavenumber (m^{-1})

For a plane wave travelling in free space, the velocity is equal to the speed of light, $c = 2.998 \times 10^8$ m/s. As with the wave impedance, for the wave to be planar (i.e. in the far-field) in free space then the phase velocity must equal the speed of light.

2.6 The fields of a short electric dipole

To help understand more complex geometries of antennas it is useful to consider the relatively simple case of a short dipole, shown in Figure 2.7[10]. This can be used as a starting point, which to analyse larger structures.

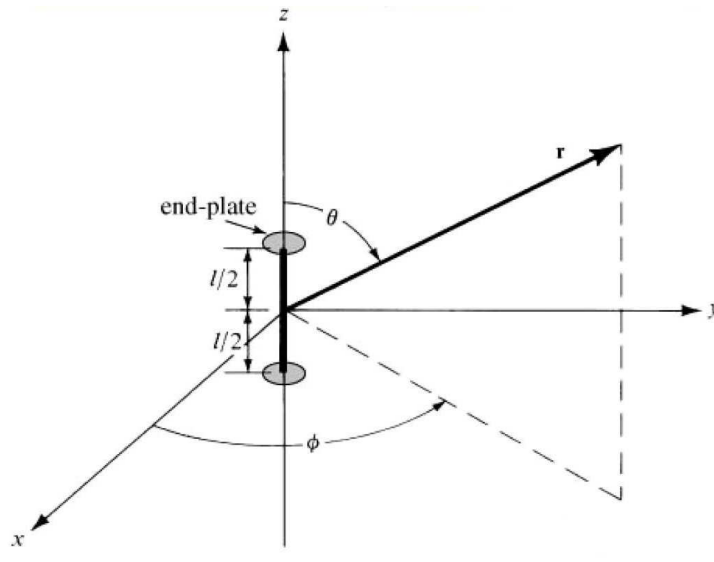


Figure 2.7. A short dipole antenna

The length (l) of the dipole is much shorter than the wavelength ($l \ll \lambda$). The two plates at the end provide capacitive loading. As a result of the short length, and the capacitive plates, there is a uniform current (I) along the entire length of the dipole. Radiation from the end plates is considered to be negligible. The dipole in Figure 2.7 can then be considered as a conductor of length, l , with a uniform current, I , and negative and positive point charges, q , at either end. The current and charge is related by:

$$I = \frac{\partial q}{\partial t} \quad (2.12)$$

To find the fields surrounding the short dipole the length, l , lies along the z-axis with the centre at the origin as shown by Figure 2.8 [11].

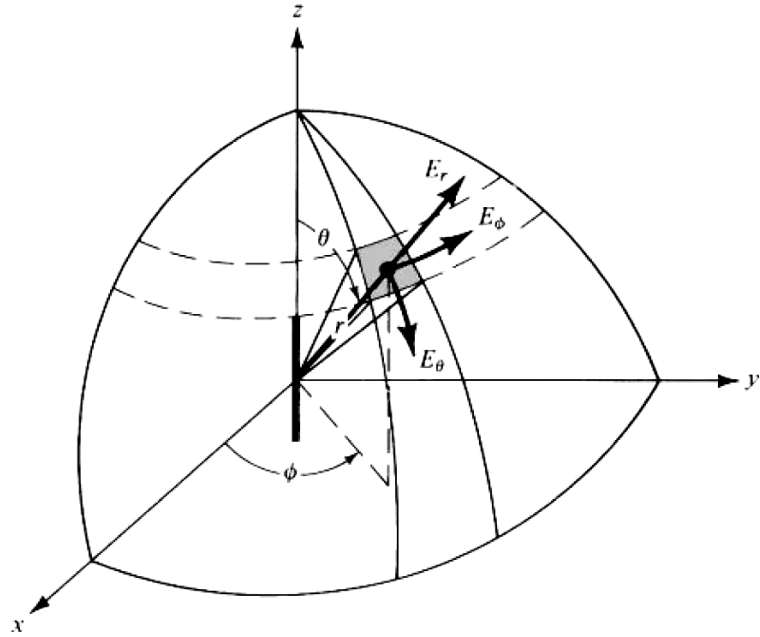


Figure 2.8. Electric field configuration

Using spherical coordinates, the electric field components (E_r , E_θ , E_ϕ) are orientated as shown in Figure 2.8. It is assumed that the dipole is in a vacuum. If the current is flowing in the short dipole shown in Figure 2.9 at some time, t , the effect of the current is observed at point P , some time later than t .

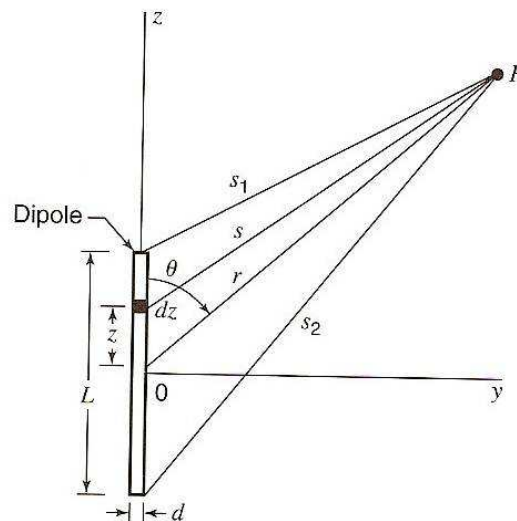


Figure 2.9. Geometry for a short dipole

As a result, instead of the current being expressed as [12]:

$$I = I_0 e^{j\omega t} \quad (2.13)$$

It should be expressed as:

$$[I] = I_0 e^{j\omega[t-(s/c)]} \quad (2.14)$$

Where, c is the velocity of light ($3 \times 10^8 \text{ ms}^{-1}$). Adding the r/c factor allows for the delay in point P sensing the effect of the current due to the velocity of light. This is known as the retardation effect and the value $[I]$ is known as the retarded current. This is important as it allows for investigation of the electric and magnetic fields at the dipole but also many wavelengths away.

To calculate the fields we have to use the retarded vector potential, \vec{A} . This is the magnetic vector potential and is useful for solving the EM field generated by a given harmonic electric current, \vec{J} . For the dipole in Figure 2.8, the retarded vector potential only has one component A_z . Its value is given as[13]:

$$A_z = \frac{\mu_0}{4\pi} \int_{-L/2}^{L/2} \frac{[I]}{s} dz \quad (2.15)$$

Where $[I]$ is the retarded current given by

$$[I] = I_0 e^{j\omega[t-(s/c)]} \quad (2.16)$$

Where, z = distance to a point on the conductor

I_0 = peak value in time of current (uniform along dipole)

μ_0 = permeability of free space = $4\pi \times 10^{-7} \text{ Hm}^{-1}$

To simplify the analysis further consider that point P is very far away from the dipole ($r \gg L$). Therefore, $s = r$ and the phase differences of the field contributions at different parts of the wire can be neglected. The integrand in Equation 2.15 is then regarded as constant and now becomes:

$$A_z = \frac{\mu_0 L I_0 e^{j\omega[t-(r/c)]}}{4\pi r} \quad (2.17)$$

The retarded scalar potential, V , of a charge distribution is:

$$V = \frac{1}{4\pi\epsilon_0} \int_V \frac{[\rho]}{s} d\tau \quad (2.18)$$

Where, $[\rho]$ is the retarded charge density given by:

$$[\rho] = \rho_0 e^{j\omega[t-(s/c)]} \quad (2.19)$$

and,

$d\tau$ = infinitesimal volume element

ϵ_0 = permittivity of free space = 8.85×10^{-12} F/m

The region of charge being considered is confined to the points at the ends of the dipole, as in Figure 2.8, so (2.18) reduces to:

$$V = \frac{1}{4\pi\epsilon_0} \left\{ \frac{[q]}{s_1} - \frac{[q]}{s_2} \right\} \quad (2.20)$$

Combining (2.12) and (2.16):

$$[q] = \int [I] dt = I_0 \int e^{j\omega[t-(s/c)]} dt = \frac{[I]}{j\omega} \quad (2.21)$$

Substituting (2.21) into (2.20) gives:

$$V = \frac{1}{4\pi\epsilon_0} \left\{ \frac{e^{j\omega[t-(s_1/c)]}}{s_1} - \frac{e^{j\omega[t-(s_2/c)]}}{s_2} \right\} \quad (2.22)$$

Referring to Figure 2.8, when $r \gg L$, the line connecting the ends of the dipole and the point P can be considered as parallel so that

$$s_1 = r - \frac{L}{2} \cos \theta \quad (2.23)$$

and

$$s_2 = r + \frac{L}{2} \cos \theta \quad (2.24)$$

Substituting (2.23) and (2.24) into (2.22) gives:

$$V = \frac{I_0 e^{j\omega(t-r/c)}}{4\pi\epsilon_0 j\omega} \left[\frac{e^{j\frac{\omega L \cos \theta}{2c}} \left(r + \frac{L}{2} \cos \theta \right) - e^{-j\frac{\omega L \cos \theta}{2c}} \left(r - \frac{L}{2} \cos \theta \right)}{r^2} \right] \quad (2.25)$$

The $L^2/4c\cos^2\theta$ term, which was present in the denominator has been omitted since $r \gg L$. Using de Moivre's theorem ($e^{jx} = \cos x + j\sin x$) Equation 2.25 becomes:

$$V = \frac{I_0 e^{j\omega(t-r/c)}}{4\pi\epsilon_0 j\omega r^2} \left[\begin{aligned} & \left(\cos \frac{\omega L \cos \theta}{2c} + j \sin \frac{\omega L \cos \theta}{2c} \right) \left(r + \frac{L}{2} \cos \theta \right) \\ & - \left(\cos \frac{\omega L \cos \theta}{2c} - j \sin \frac{\omega L \cos \theta}{2c} \right) \left(r - \frac{L}{2} \cos \theta \right) \end{aligned} \right] \quad (2.26)$$

Since the wavelength is much greater than the length of the dipole ($\lambda \gg L$) the following approximations can be made:

$$\cos \frac{\omega L \cos \theta}{2c} = \cos \frac{\pi L \cos \theta}{\lambda} \cong 1 \quad (2.27)$$

$$\sin \frac{\omega L \cos \theta}{2c} = \frac{\pi L \cos \theta}{2c} \quad (2.28)$$

Combining (2.27) and (2.28) into (2.26), the equation for the scalar potential reduces to:

$$V = \frac{I_0 L \cos \theta e^{j\omega(t-r/c)}}{4\pi\epsilon_0 c} \left(\frac{1}{r} + \frac{c}{j\omega r^2} \right) \quad (2.29)$$

The vector (\vec{A}) and scalar (V) potentials everywhere on a short dipole are represented by Equations 2.17 and 2.29 respectively. As a result, it is now possible to determine the electromagnetic fields with the help of Maxwell's equations.

Since the magnetic flux, \vec{B} , is solenoidal ($\text{div } \vec{B} = 0$) it can be represented as the curl of another vector due to the vector identity:

$$\nabla \cdot \nabla \times \vec{A} = 0 \quad (2.30)$$

Where, \vec{A} , is the vector potential. From the relationship between the magnetic flux density and the magnetic field intensity ($\vec{B} = \mu \vec{H}$) Equation 2.31 can be formed.

$$\vec{H} = \frac{1}{\mu} \nabla \times \vec{A} \quad (2.31)$$

Using Maxwell's curl equation:

$$\nabla \times \vec{E} = -j\omega\mu\vec{H} \quad (2.32)$$

and substituting (2.31) into it gives:

$$\nabla \times \vec{E} = -j\omega\nabla \times \vec{A} \quad (2.33)$$

This can also be written as:

$$\nabla \times [\vec{E} + j\omega\vec{A}] = 0 \quad (2.34)$$

The scalar potential (V) is the negative derivative of the vector potential (\vec{A}). Using the vector identity:

$$\nabla \times (-\nabla V) = 0 \quad (2.35)$$

We can now get an expression for the electric field:

$$\vec{E} = -j\omega\vec{A} - \nabla V \quad (2.36)$$

The next step is to obtain both \vec{E} and \vec{H} fields in polar coordinates. The vector potential expressed by polar coordinates is:

$$\vec{A} = \hat{a}_r A_r + \hat{a}_\theta A_\theta + \hat{a}_\phi A_\phi \quad (2.37)$$

The vector potential in this case only has a z -component. Therefore, $A_\phi = 0$ and A_r and A_θ are given by:

$$A_r = A_z \cos \theta \quad (2.38)$$

$$A_\theta = -A_z \sin \theta \quad (2.39)$$

Where A_z already been given by 2.17. In polar coordinates the gradient of V is given by:

$$\nabla V = \hat{a}_r \frac{\partial V}{\partial r} + \hat{a}_\theta \frac{1}{r} \frac{\partial V}{\partial \theta} + \hat{a}_\phi \frac{1}{r \sin \theta} \frac{\partial V}{\partial \phi} \quad (2.40)$$

As with (2.37) the E-field can be expressed as a sum of its polar coordinate components:

$$\vec{E} = \hat{a}_r E_r + \hat{a}_\theta E_\theta + \hat{a}_\phi E_\phi \quad (2.41)$$

From (2.36), (2.37) and (2.40) the three spherical coordinate components of the E-field are:

$$E_r = -j\omega A_r - \frac{\partial V}{\partial r} \quad (2.42)$$

$$E_\theta = -j\omega A_\theta - \frac{1}{r} \frac{\partial V}{\partial \theta} \quad (2.43)$$

$$E_\phi = -j\omega A_\phi - \frac{1}{r \sin \theta} \frac{\partial V}{\partial \phi} \quad (2.44)$$

Equation (2.44) reduces to zero, since $A_\phi = 0$ and V is independent of ϕ ($\partial V / \partial \phi = 0$). For E_r we substitute (2.38) into (2.42) and for E_θ we substitute (2.39) into (2.43). This is shown below:

$$E_r = -j\omega A_z \cos \theta - \frac{\partial V}{\partial r} \quad (2.45)$$

$$E_\theta = j\omega A_z \sin \theta - \frac{1}{r} \frac{\partial V}{\partial \theta} \quad (2.46)$$

If we re-introduce the previous results for A_z (2.17) and V (2.29) into (2.45) and (2.46) then the following results can be obtained:

$$E_r = \frac{I_0 L \cos \theta e^{j\omega[t-(r/c)]}}{2\pi\epsilon_0} \left(\frac{1}{cr^2} + \frac{1}{j\omega r^3} \right) \quad (2.47)$$

$$E_\theta = \frac{I_0 L \sin \theta e^{j\omega[t-(r/c)]}}{4\pi\epsilon_0} \left(\frac{j\omega}{c^2 r} + \frac{1}{cr^2} + \frac{1}{j\omega r^3} \right) \quad (2.48)$$

Equations (2.47) and (2.48) are known as the general expressions for the E-field of a short electric dipole.

The magnetic field may be calculated using Equation (2.31). The curl of \vec{A} in polar coordinates is:

$$\begin{aligned} \nabla \times \vec{A} = & \frac{\hat{a}_r}{r^2 \sin \theta} \left[\frac{\partial(r \sin \theta) A_\phi}{\partial \theta} - \frac{\partial(r A_\theta)}{\partial \phi} \right] + \frac{\hat{a}_\theta}{r \sin \theta} \left[\frac{\partial A_r}{\partial \phi} - \frac{\partial(r \sin \theta) A_\phi}{\partial r} \right] \\ & + \frac{\hat{a}_\phi}{r} \left[\frac{\partial(r A_\theta)}{\partial r} - \frac{\partial A_r}{\partial \theta} \right] \end{aligned} \quad (2.49)$$

Since $A_\phi = 0$ the first and fourth terms of (2.49) are zero. From (2.17), (2.38) and (2.39) it can be seen that A_r and A_θ are independent of ϕ . As a result the second and third terms of (2.49) reduce to zero. Only the last two terms in (2.49) contribute so that \vec{A} only has a ϕ component and consequentially by (2.31) so does the H-field. If we introduce (2.38) and (2.39) into (2.49), and reduce the terms to zero, then substitute the result into (2.31) the following results are obtained:

$$\vec{H} = H_\phi = \frac{I_0 L \sin \theta e^{j\omega(t-r/c)}}{4\pi} \left(\frac{j\omega}{cr} + \frac{1}{r^2} \right) \quad (2.50)$$

$$H_r = H_\theta = 0 \quad (2.51)$$

The results obtained show that a short electric dipole only has three components E_r , E_θ and H_ϕ . All the other components are equal to zero. Equations (2.47), (2.48) and (2.50) can be simplified further for the special case of existing in the far-field, when $r \gg \lambda$. The terms $1/r^2$ and $1/r^3$ for (2.47), (2.48) and (2.50) can be omitted. As a result, in the far-field $E_r \approx 0$, there are only two field components, E_θ and H_ϕ , which are given by:

$$E_\theta = \frac{I_0 L \sin \theta e^{j\omega[t-(r/c)]} j\omega}{4\pi\epsilon_0 c^2 r} = \frac{j60\pi I_0 e^{j\omega[t-(r/c)]} \sin \theta L}{r \lambda} \quad (2.52)$$

$$H_\phi = \frac{I_0 L \sin \theta e^{j\omega(t-r/c)} j\omega}{4\pi cr} = \frac{jI_0 e^{j\omega(t-r/c)} \sin \theta L}{r \lambda} \quad (2.53)$$

Using the ratio E_θ and H_ϕ as given by 2.52 and 2.53, the following relationship can be obtained:

$$\frac{E_\theta}{H_\phi} = \frac{1}{\epsilon_0 c} = \sqrt{\frac{\mu_0}{\epsilon_0}} = 376.7\Omega \approx 120\pi\Omega \quad (2.54)$$

This correlates with Equation (2.10) in Section 2.5.4 and is known as the intrinsic impedance of free space.

Equation (2.54) can be used to verify the statement in section 2.5 that an EM wave existing in the far-field has both the E and H components in phase. Shown in Figure 2.10 is a field pattern for E and H.

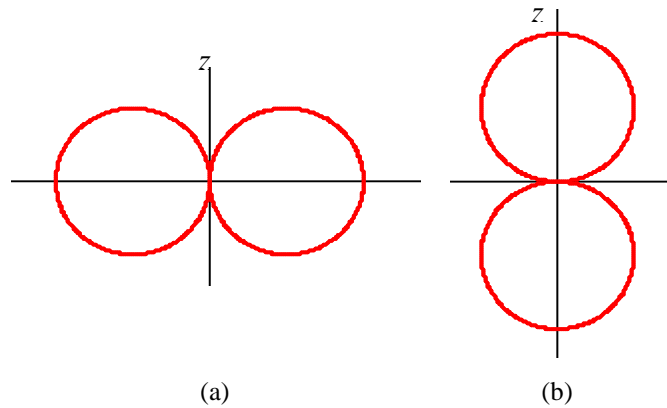


Figure 2.10. Near- and far-field patterns of E_θ and H_ϕ .

For the near-field equations given by (2.47), (2.48) and (2.58) and at a small distance, $r \ll \lambda$, from the dipole there are two electric field components, E_r and E_θ . Both of these field components are in time phase quadrature with the magnetic field. This verifies the statement in section 2.5.1. The E_θ and H_ϕ near-field patterns are the same as their far-field patterns and are proportional to $\sin\theta$. The near-field pattern for E_r is proportional to $\cos\theta$ and is indicated in Figure 2.11 by the ninety degree shift in the pattern compared to Figure 2.10.

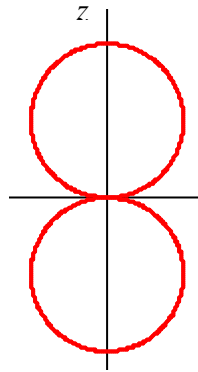


Figure 2.11. Near-field pattern for E_r component

2.7 The fields of a finite length dipole

The previous section explained the theory behind obtaining field plots for a short dipole. The theory obtained can now be used to obtain data on finite length dipoles, which will allow for a better understanding of some of the properties of the antennas investigated in this thesis.

The dipole under analysis in this section is presumed to have a diameter much smaller than the operating wavelength ($d \ll \lambda$). This allows the assumption that the current distribution along the dipole is sinusoidal given that it is fed at its centre by a balanced 2 wire transmission line. This approximation is considered suitable as there is no major discrepancy in the far-field patterns for the antennas investigated later in this thesis.

Examples of current distribution on a range of dipoles of a length up to 2λ are shown in Figure 2.12 [14].

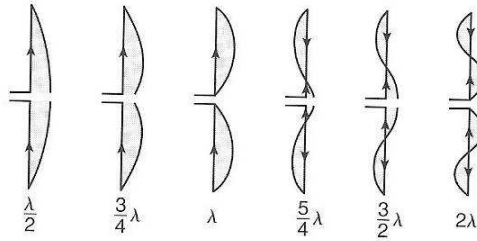


Figure 2.12 Approximate natural-current distribution for thin, linear, centre-fed antennas of various lengths.

A finite length dipole can be viewed as series of infinitesimal dipoles collinearly joined together. Hence, we can use the expressions for the far-field obtained in the previous section to establish new relationships for a dipole of finite length.

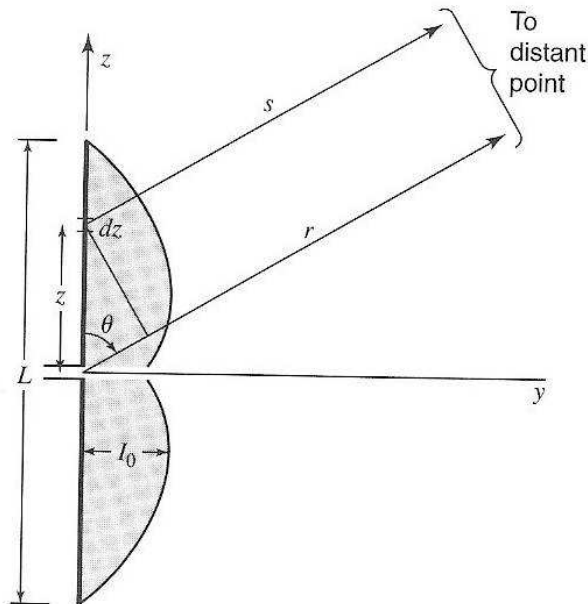


Figure 2.13. Finite dipole geometrical arrangement for a far-field approximation

For the dipole shown in Figure 2.13, which is centre-fed, thin, linear, and of a length, l , the retarded value of the current at any point, z , on the antenna referred to a point at a distance, s , can be given by [15]:

$$[I] = I_0 \sin \left[\frac{2\pi}{\lambda} \left(\frac{L}{2} \pm z \right) \right] e^{j\omega[t-r/c]} \quad (2.55)$$

In Equation 2.55 the factor inside the square brackets is known as the form factor for the current on the antenna. When $(L/2 + z)$ is used, $z < 0$, and $(L/2 - z)$ is used when $z > 0$. As the antenna can be regarded as a series of infinitesimal dipoles of length dz , the overall field of the antenna can be obtained by integrating the fields of all the dipoles that make up the larger dipole. From Equations 2.52 and 2.53, the far-fields dE_θ and dH_ϕ , at a distance s from the infinitesimal dipole of length, dz , can be given by:

$$dE_\theta = \frac{j60\pi[I]\sin\theta}{s\lambda} dz \quad (2.56)$$

$$dH_\phi = \frac{j[I]\sin\theta}{s\lambda} dz \quad (2.57)$$

As $E_\theta = ZH_\phi = 120\pi H_\phi$, it is only necessary to calculate H_ϕ . To find H_ϕ over the entire antenna, Equation 2.57 must be integrated over the length, L .

$$H_\phi = \int_{-L/2}^{L/2} dH_\phi \quad (2.58)$$

Substituting 2.55 into 2.57 and then substituting this result into 2.58 gives :

$$H_\phi = \frac{jI_0 \sin\theta e^{j\omega t}}{s\lambda} \left\{ \int_{-L/2}^0 \frac{1}{s} \sin\left[\frac{2\pi}{\lambda}\left(\frac{L}{2} + z\right)\right] e^{-j\frac{\omega s}{c}} dz + \int_0^{L/2} \frac{1}{s} \sin\left[\frac{2\pi}{\lambda}\left(\frac{L}{2} - z\right)\right] e^{-j\frac{\omega s}{c}} dz \right\} \quad (2.59)$$

For Equation (2.59), $1/s$ only affects the amplitude, and at large distances ($s \gg \lambda$) can be considered as a constant. As with the infinitesimal dipole at larger distances, $s = r$, which means that there is a negligible effect on the amplitude. Unlike the infinitesimal dipole the difference in phase must be considered. From Figure 2.12:

$$s = r - z \cos\theta \quad (2.60)$$

Substituting (2.60) into (2.59) gives:

$$H_{\phi} = \frac{jI_0 \sin \theta e^{j\omega(t-r/c)}}{2\lambda r} \left\{ \begin{aligned} & \int_{-L/2}^0 \sin \left[\frac{2\pi}{\lambda} \left(\frac{L}{2} + z \right) \right] e^{-j\frac{\omega \cos \theta}{c} z} dz \\ & + \int_0^{L/2} \sin \left[\frac{2\pi}{\lambda} \left(\frac{L}{2} - z \right) \right] e^{-j\frac{\omega \cos \theta}{c} z} dz \end{aligned} \right\} \quad (2.61)$$

As $\beta = \omega / c = 2\pi / \lambda$, and $\beta / 4\pi = L/2\lambda$, Equation 2.61 can be rewritten as:

$$H_{\phi} = \frac{j\beta I_0 \sin \theta e^{j\omega(t-r/c)}}{2\lambda r} \left\{ \begin{aligned} & \int_{-L/2}^0 e^{j\beta z \cos \theta} \sin \left[\beta \left(\frac{L}{2} + z \right) \right] dz \\ & + \int_0^{L/2} e^{j\beta z \cos \theta} \sin \left[\frac{2\pi}{\lambda} \left(\frac{L}{2} - z \right) \right] dz \end{aligned} \right\} \quad (2.62)$$

As the integrals take the form:

$$\int e^{ax} \sin(c + bx) dx = \frac{e^{ax}}{a^2 + b^2} [a \sin(c + bx) - b \cos(c + bx)] \quad (2.63)$$

For the first integral:

$$\begin{aligned} a &= j\beta \cos \theta \\ b &= \beta \\ c &= \beta L / 2 \end{aligned}$$

For the second integral, a and c are the same as the first integral, but $b = -\beta$.

Integrating and simplifying 2.62 yields:

$$H_{\phi} = \frac{j[I_0]}{2\pi r} \left[\frac{\cos((\beta L \cos \theta / 2) - \cos(\beta L / 2))}{\sin \theta} \right] \quad (2.64)$$

To obtain E_{θ} , H_{ϕ} is multiplied by $Z = 120\pi$, which gives:

$$E_{\theta} = \frac{j60[I_0]}{r} \left[\frac{\cos((\beta L \cos \theta / 2) - \cos(\beta L / 2))}{\sin \theta} \right] \quad (2.65)$$

Where, $[I_0] = I_0 e^{j\omega(t-r/c)}$.

Equations 2.64 and 2.65 give the far-field expressions of H_{ϕ} and E_{θ} respectively for a symmetrical, centre-fed, thin dipole of length, L. The expression in the brackets known as the pattern factor gives the far-field pattern. Shown in Figure 2.14 are polar plots for various lengths of antenna.

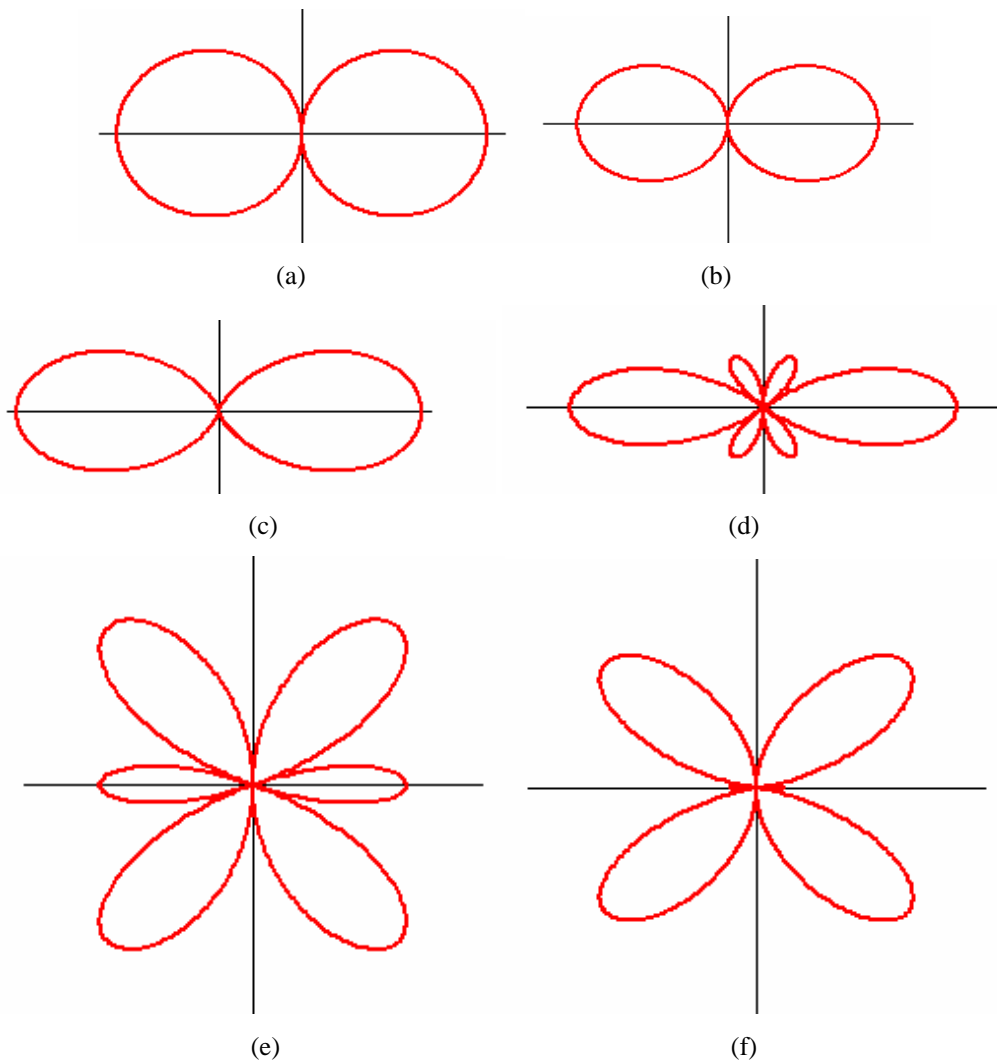


Figure 2.14. Polar plots for the radiation patterns of a dipole of length (a) 0.5λ (b) 0.75λ (c) 1λ (d) 1.25λ (e) 1.5λ (f) 1.75λ .

As the radiation mechanism and the radiated fields from thin linear dipoles have been investigated the next stage is to investigate the fundamental limitations of small antennas.

3. Fundamental limitations of small antennas

As outlined in chapter 1 the objectives of this project were to produce as a small an antenna as possible but with optimum performance. However, there are fundamental limits as to how small an antenna can be made i.e. its area. These limitations have been well researched and this chapter reviews the classical literature with respect to antenna size relative to wavelength, and its impact on overall performance.

3.1 Wheeler limit

The paper “*Fundamental limitations of small antennas*” published by Wheeler in 1947 [1] and was the first to address the problem. Wheeler defined an electrically small antenna as one whose maximum dimension is less than the radian-length, which is $1/2\pi$ wavelengths. This relationship can be expressed as:

$$ka < 1 \quad (3.1)$$

Where $k = \frac{2\pi}{\lambda}$ (radians/metre)

λ = free space wavelength (metres)

a = radius of sphere enclosing the maximum dimension of the antenna (metres)

The situation described by Wheeler is illustrated in Figure 3.1.

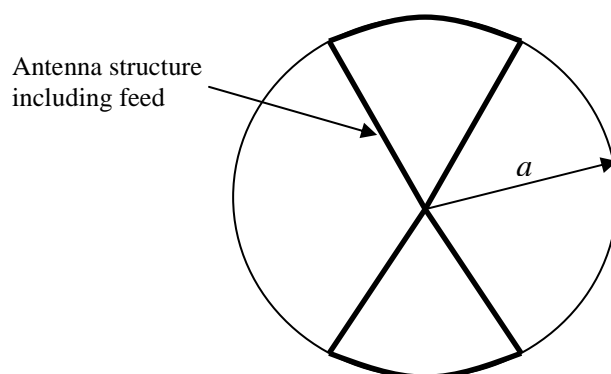


Figure 3.1 Sphere enclosing an electrically small radiating element

The electrically small antenna is considered to be in free space and enclosed by a sphere of radius a . The papers published by Wheeler [1], [2] derived the limits of a small dipole and a small loop (used as a magnetic dipole) from the limitations of a capacitor and an inductor, respectively. The capacitor and inductor were chosen to occupy, respectively, volumes equal to those of the dipole and the loop. For both these cases, Wheeler calculated a radiation power factor and hence the maximum power factor achievable by the antenna. The power factor is proportional to the antenna volume, V , and a shape factor. The nominal bandwidth is given as the power factor p multiplied by the resonant frequency (f_0) and is described by the following relationship.

$$V \propto p \propto \frac{\Delta f}{f_0} \quad (3.2)$$

Where
$$p = \frac{\text{antenna resistance}}{\text{antenna reactance}}$$

Further investigations of antenna size versus bandwidth capability were further investigated by L.J. Chu[3], and then by Roger Harrington. The following section investigates their work.

3.2 Chu-Harrington Limit

A different approach to that of Wheeler was taken by Chu [3]. Chu considered the field outside the sphere, as shown in Figure 3.1, is a result of an arbitrary current or source distribution inside the sphere. However, the field outside the sphere can be expressed as a complete set of orthogonal spherical vector waves propagating radially outward. Outside the spherical shell Chu assumed that the fields could be represented by a superposition of orthogonal spherical modes, each with their own wave impedance. Chu was able to construct a circuit, as depicted by Figure 3.2 (a) [4], with the same impedance and analyse the resonant behaviour of the antenna.

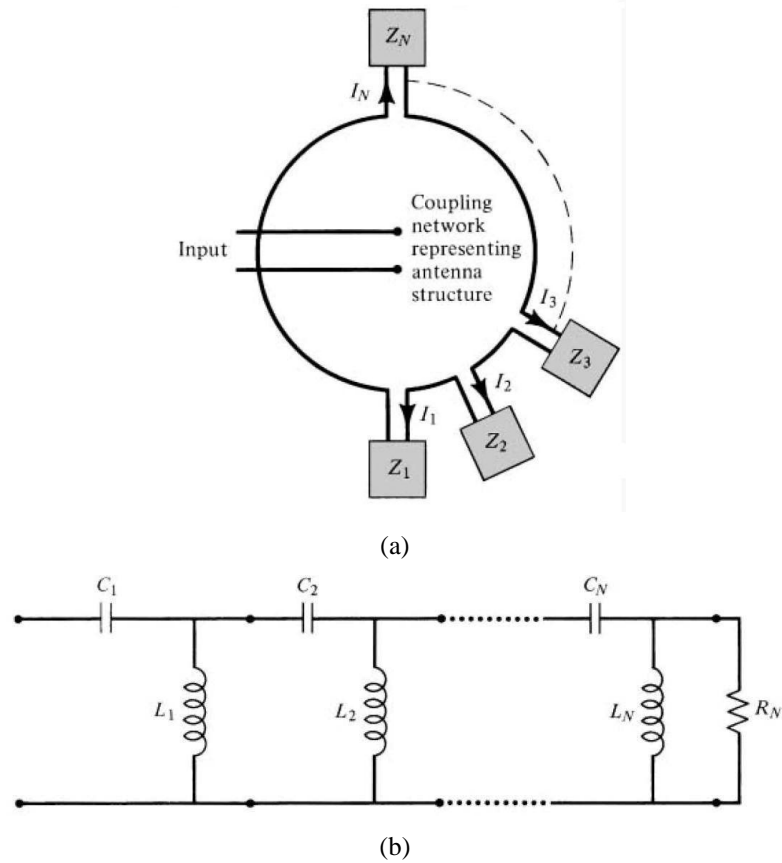


Figure 3.2. (a) Equivalent network of a vertically-polarised omni-directional antenna (b) Equivalent circuit for N spherical modes

As the spherical modes outside the sphere are orthogonal, the total energy (electric or magnetic) outside the sphere, and the complex power transmitted across the closed spherical surface are equal, respectively, to the sum of the energies and complex powers associated with each corresponding spherical mode. Therefore, there is no coupling, in energy or power, between any two modes outside the sphere. As a result, the antenna within in a specific volume can be reduced to an equivalent circuit problem.

The power radiated from the antenna can then be calculated from the propagating modes while all other modes contribute to the reactive power. When the sphere in Figure 3.1 becomes very small there exist no propagating modes. However, each mode still has a real part but it is very small. For a 100% efficient antenna the equivalent circuit is L – C ladder network, as shown in Figure 3.2 (b), which each individual L – C section representing a mode. The shunt resistance is used to

represent the normalised antenna radiation resistance. Using the circuit in Figure 3.2 (b) the input impedance can be found.

When the sphere in Figure 3.1 is very small the quality factor, Q , becomes very large, since the Q of each individual mode is a ratio of its stored energy to radiated energy. It has been reported by Hansen [5] and Mclean [6] that the higher order modes become evanescent when $ka < 1$. As a result, the quality factor for only the lowest order TM_{n0} mode i.e. corresponds to the fields of a point dipole is required. Chu's expression is therefore:

$$Q = \frac{1 + 2(ka)^2}{(ka)^3 [1 + (ka)^2]} \quad (3.3)$$

$$\text{If } ka \ll 1 \text{ then } Q \approx \frac{1}{(ka)^3}$$

If two modes are excited i.e. TE and TM, the values of Q are halved. The lowest achievable Q is related to the largest dimension linear dimension of an electrically small antenna, highlighted by equation 3.3. The Q is independent of the geometrical layout of the antenna structure within the sphere, shown in Figure 3.1. The geometrical layout only impacts on the type of mode being excited, such as TE, TM or TE and TM. Therefore equation 3.3 represents the fundamental limit on the electrical size of an antenna. Practically, this limit is only approached but is never exceeded or even equalled.

The Q is also related to the fractional bandwidth of the system by the following equation 3.4:

$$\text{Fractional bandwidth} = \text{FBW} = \frac{\Delta f}{f_0} = \frac{1}{Q} \quad (3.4)$$

where f_0 = centre frequency

Δf = bandwidth

Equation 3.4 is valid for $Q \gg 1$ as the equivalent resonant circuit with fixed values is a good approximation for use with an antenna.

3.3 Mclean Limit

In 1992, McLean [6] re-examined the fundamental limits of Q and proposed an alternate limit to antenna performance. McLean uses a definition of Q in terms of stored energy and radiated power, as shown by equation 3.5.

$$Q = \begin{cases} \frac{2\omega W_e}{P_{rad}} & W_e > W_m \\ \frac{2\omega W_m}{P_{rad}} & W_m > W_e \end{cases} \quad (3.5)$$

In equation 3.5, W_e is the time-average reactive, non-propagating, stored, electric energy. W_m is the time-average reactive, non-propagating, stored, magnetic energy. ω is the angular frequency and P_{rad} the radiated power. Equation 3.5 assumes that the antenna is resonated with an appropriate lossless circuit element, which results in a purely real input impedance at the design frequency. As a result, the definition of Q for an antenna is similar to the definition of Q for a practical circuit element, which stores energy but exhibits losses.

The time-average reactive electric energy for an electrically small dipole is given by the following equation 3.6 derived by Schantz [7]:

$$W_e = \frac{p_0^2 k^3}{24 \pi \epsilon_0} \left(\frac{1}{k^3 a} + \frac{1}{ka} \right) \quad (3.6)$$

The time average radiated power is given in the following equation 3.7 derived by Schantz [7]:

$$P_{rad} = \frac{p_0^2 k^3}{12 \pi \epsilon_0} \quad (3.7)$$

Substituting equations 3.6 and 3.7 into equation 3.5 yields McLean's expression for the Q of an electrically small dipole:

$$Q = \frac{2\omega W_e}{P_{rad}} = 2\omega \frac{p_0^2 k^3}{24\pi\epsilon_0} \left(\frac{1}{k^3 a} + \frac{1}{ka} \right) \frac{12\pi\epsilon_0}{p_0^2 \omega k^3} \quad (3.8)$$

$$= \frac{1}{k^3 a} + \frac{1}{ka}$$

3.4 Fundamental Limits of a 5.8 GHz antenna

To give some substance to the theory described in the previous sections, an example will be given for an antenna operating at 5.8 GHz. Using the following procedure it is possible to calculate the radius for the Wheeler sphere shown in Figure 3.1.

$$\lambda = \frac{c}{f} = \frac{2.998 \times 10^8}{5.8 \times 10^9} = 51.69 \text{ mm} \quad (3.9)$$

$$k = \frac{2\pi}{\lambda} = \frac{2\pi}{0.05169} = 121.475 \quad (3.10)$$

$$a < \frac{1}{k} = \frac{1}{121.475} = 8.232 \text{ mm} \quad (3.11)$$

The result of equation 3.11 shows that for an antenna to be electrically small at 5.8 GHz it must be occupy a spherical volume with a radius no greater than 8.232mm.

Using a small electrical dipole, of length equal to 0.1λ , it is possible to calculate values for the theoretical maximum gain [8], minimum Q (Eqn 3.8) and maximum bandwidth (Eqn 3.4) as follows:

$$G_{\max} = (ka)^2 + 2(ka) = 0.726 \text{ dBi} \quad (3.12)$$

$$Q_{\min} = \frac{1}{k^3 a} + \frac{1}{ka} = 35.5 \quad (3.13)$$

$$BW_{\max} = \frac{f_0}{Q} = 163.38 \text{ MHz} \quad (3.14)$$

Analysis of (3.12), (3.13) and (3.14) indicate that a small electrical dipole, of length 0.1λ , would give adequate performance at the operational frequency. However, these values would not be obtained, as the antenna in this case is assumed to be 100% efficient and factors such as substrate losses, matching errors etc would reduce the values in equation 3.12, 3.13 and 3.14. Figure 3.3 shows a plot derived from equation 3.8 over a range of values from zero to 8.232mm.

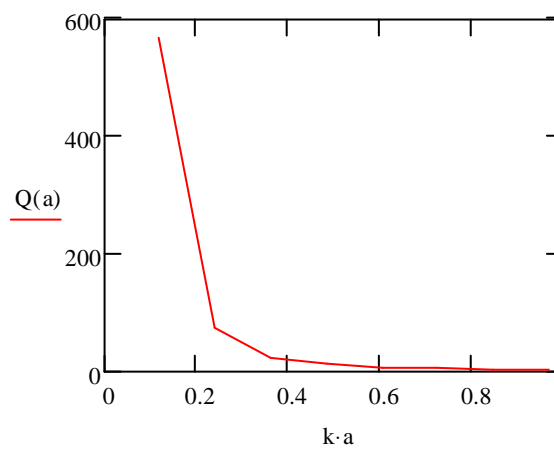


Figure 3.3 Fundamental limit of Q versus antenna size

Analysing the graph in Figure 3.3 shows that the bandwidth reduces exponentially as the size is reduced. To achieve higher bandwidth, the geometry of the antenna needs to be altered so that it efficiently utilises the space within the sphere of radius a . The antennas discussed in chapter 8 are elliptical dipoles and have a higher bandwidth at their resonant frequencies, which allow operation over a wide bandwidth.

The next chapter will investigate various transmission lines which are suitable for feeding antennas

4. Transmission lines

When designing antennas for specific applications, the method of exciting the antenna is as important as the antenna chosen. This chapter will analyse the different types of transmission lines used throughout this project. For each transmission line discussed, performance metrics will be presented.

4.1 Basic transmission line theory

Transmission line theory is extremely useful as a tool to bridge the gap between circuit theory and field analysis. Essentially, an abstract field analysis can be simplified to a circuit diagram where the transmission line is a distributed parameter network, and where voltages and currents can vary in magnitude and phase over its length. An example was shown in Figure 2.2 for the Thevenin equivalent of an antenna in transmitting mode. It is normal for a transmission line to be viewed schematically as a two-wire line, as transmission lines normally have at least two conductors to support transverse electromagnetic (TEM) propagation, or quasi-TEM propagation modes. Figure 4.1 shows a lumped-element equivalent of a two wire transmission line.

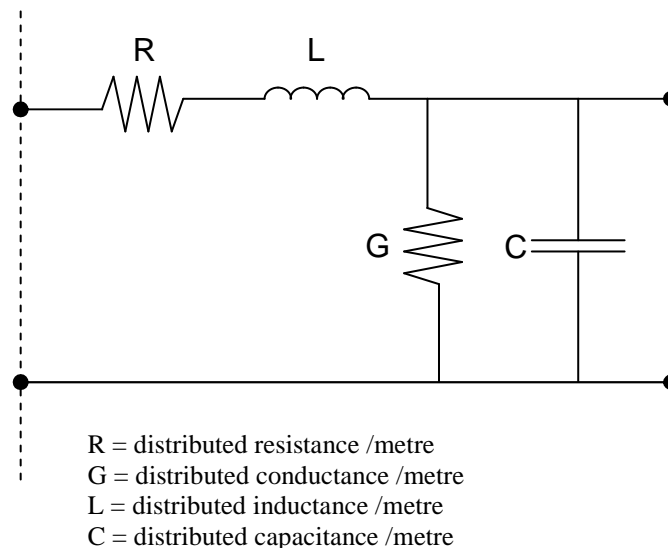


Figure 4.1. Model of a section of transmission line

Figure 4.1 illustrates that the series resistance models conductive losses while the conductance or shunt resistance models substrate losses. Using the model shown in Figure 4.1 [1] the characteristic impedance, Z_0 , of the line is given by:

$$Z_0 = \sqrt{\frac{R + j\omega L}{G + j\omega C}} \quad (4.1)$$

For an ideal lossless line, Equation 4.1 reduces to:

$$Z_0 = \sqrt{\frac{L}{C}} \quad (4.2)$$

4.2 Transmission Lines

When designing microwave circuits, there are many possible transmission lines that can be used to feed antennas, or to connect individual components together. This section briefly describes the orientation of the fields, derivation of the characteristic impedance and the effective wavelength.

4.2.1 Two-wire transmission line

Equation 4.2 is valid for a lossless two-wire transmission line as it can propagate TEM waves. Figure 4.4(a) shows the orientation of the EM fields in such a two-wire system. Quite often, the values of L and C are not known, but the physical dimensions (conductor diameter, spacing, dielectric properties, etc.) of the line are known. The following formula can be used to determine the characteristic impedance of a two-wire transmission line [2].

$$Z_0 = \frac{120\pi}{\sqrt{\epsilon_r}} \ln \frac{2D}{a} \quad (4.3)$$

Where,

ϵ_r is the relative dielectric constant of the material between the two conductors

D is the centre-to-centre separation of the two conductors

a is the diameter of the wires

4.2.2 Parallel plate waveguide

A parallel plate waveguide can be treated in the same way as a two wire transmission line, as it supports TEM propagation. Shown in Figure 4.2 is the geometrical layout of parallel plate waveguide. The characteristic impedance can be calculated simply by[3]:

$$Z_0 = \frac{\eta d}{W} \quad (4.4)$$

Where

$$\eta = \sqrt{\frac{\mu}{\epsilon}} \quad (4.5)$$

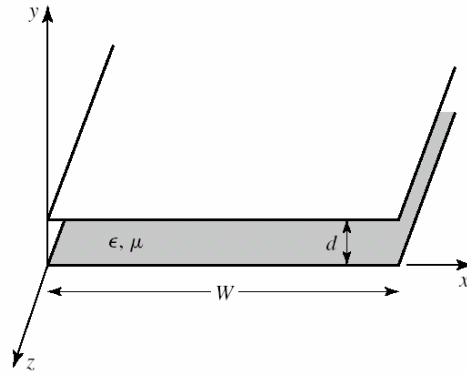


Figure 4.2 Parallel plate waveguide

4.2.3 Co-Axial line

Co-axial line consists of a round conducting wire surrounded by a dielectric spacer surrounded by a cylindrical conductor. Figure 4.3 shows the geometrical layout of co-axial line. The advantage of co-axial over the two previous transmission lines is that the electromagnetic field exists between the inner and outer conductors. This means (ideally), that it cannot interfere with, or suffer interference from external electromagnetic fields.

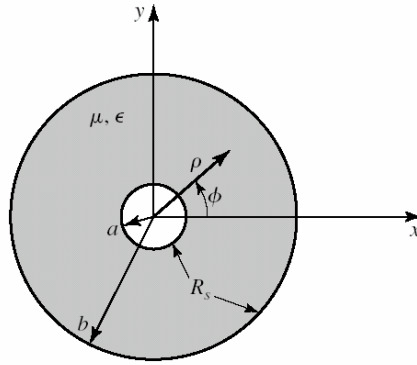


Figure 4.3 Co-axial transmission line

The characteristic impedance of co-axial line is defined as[4]:

$$Z_0 = \sqrt{\frac{\mu}{\epsilon}} \frac{\ln b/a}{2\pi} \quad (4.6)$$

Where, a = distance from centre to edge of inner conductor

b = distance from centre to outer conductor

4.2.4 Microstrip

When designing microwave integrated circuits (MIC) one of the most common transmission lines used is microstrip. This is because it can be easily fabricated using photolithographic processes, and can be easily integrated with other passive and active microwave devices. Microstrip propagates an almost TEM wave, sometimes called quasi-TEM. This allows for easy approximate analysis and can lead to wideband designs. Another advantage of microstrip is its connectivity to other transmission lines such as co-axial lines.

Microstrip is a two-conductor transmission line and can be considered to be an evolution from a two-wire line. This is shown in Figure 4.4 [5].

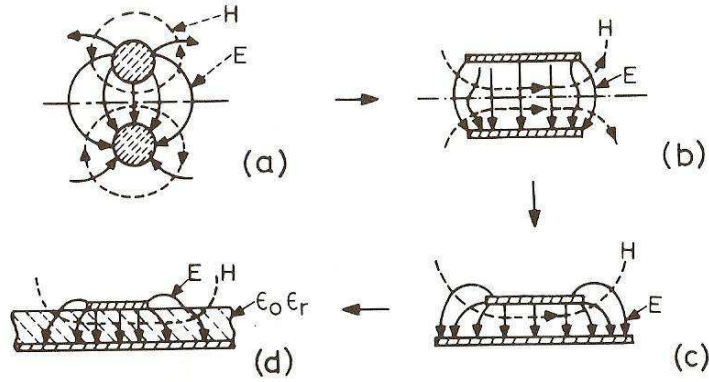


Figure 4.4 Conceptual evolution of a Microstrip line from a two-wire transmission line. (a) To a two wire transmission line. (b) To a parallel-plate waveguide. (c) To a microstrip line with no dielectric (d) To a microstrip line.

The characteristic impedance (Z_0) for microstrip is dependant on substrate height (h), line width (W) and substrate permittivity and is given by [6]:

$$Z_0 = \frac{60}{\sqrt{\epsilon_{re}}} \ln\left(\frac{8h}{W} + \frac{W}{4h}\right) \text{ for } W/h \leq 1 \quad (4.7)$$

$$Z_0 = \frac{120\pi}{\sqrt{\epsilon_{re}} [W/h + 1.393 + 0.667 \ln(W/h + 1.444)]} \text{ for } W/h \geq 1 \quad (4.8)$$

Where ϵ_{re} is the effective dielectric constant and is approximately given by:

$$\epsilon_{re} = \frac{\epsilon_r + 1}{2} + \frac{\epsilon_r - 1}{2} \frac{1}{\sqrt{1 + 12h/W}} \quad (4.9)$$

The effective dielectric constant, in this case, can be considered as an average value, which represents the fact that a portion of the field exists outside the dielectric. To calculate the effective wavelength (λ_g) of microstrip, the free space wavelength is divided by the square root of Equation 4.9, as shown below:

$$\lambda_g = \frac{\lambda_0}{\sqrt{\epsilon_{re}}} \quad (4.10)$$

4.2.5 Co-Planar Waveguide (CPW)

After microstrip, CPW transmission line is probably the most used line for designing microwave circuits. Particularly for mm-wave applications as it allows for easy fabrication of active devices due to the presence of the centre conductor and close proximity of the ground planes. A geometrical representation of CPW along with the orientation of the fields is shown in Figure 4.5.

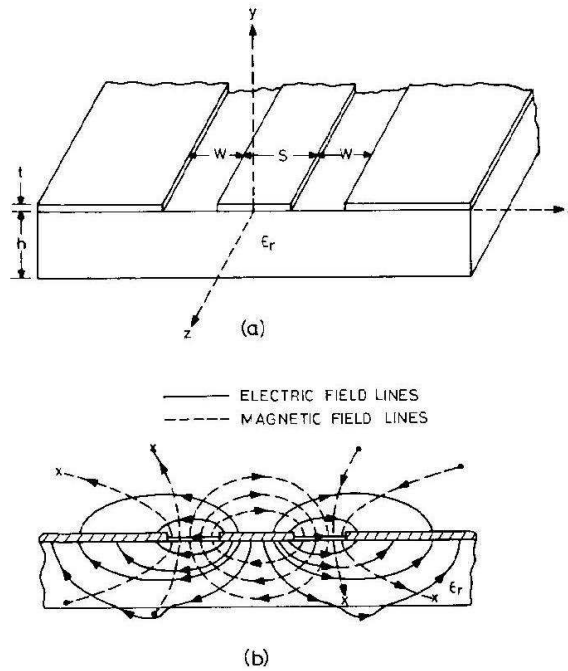


Figure 4.5 (a) Coplanar Waveguide (CPW) geometry
(b) Electric and magnetic field distributions on CPW

CPW is particularly useful for fabricating active circuitry, due to the presence of the centre conductor and the close proximity of the ground planes. Unlike microstrip, CPW has substantially less losses at frequencies approximately above 20 GHz. This is due to a large proportion (approximately half) of the field existing outside the dielectric. As a result, the dielectric loss is lower and the dispersion of the signal is considerably less.

Closed-form expressions for the characteristic impedance and effective dielectric constant of CPW are given below [7].

$$Z_0 = \frac{30\pi}{\sqrt{\epsilon_{re}}} \frac{K'(k)}{K(k)} \quad (4.11)$$

$$\text{Where, } k = \frac{S}{S + 2W}$$

The ratio K/K' can be defined as:

$$\frac{K(k)}{K'(k)} = \frac{1}{\pi} \ln \left[2 \frac{1 + \sqrt{k}}{1 - \sqrt{k}} \right] \text{ for } 0.707 \leq k \leq 1 \quad (4.12)$$

$$\frac{K(k)}{K'(k)} = \frac{\pi}{\ln \left[2 \frac{1 + \sqrt{k'}}{1 - \sqrt{k'}} \right]} \text{ for } 0 \leq k \leq 0.707 \quad (4.13)$$

The effective permittivity can be obtained using the following formula:

$$\epsilon_{re} = \frac{\epsilon_r + 1}{2} \left[\frac{\tanh\{1.785 \log(h/W) + 1.75\}}{+ \frac{kW}{h} \{0.04 - 0.7k + 0.01(1 - 0.1\epsilon_r)(0.25 + k)\}} \right] \quad (4.14)$$

This formula gives accuracy of 1.5 percent for $h/W \geq 1$. A good rule of thumb for effective permittivity is that value should be approximately the average of dielectric permittivity and air $((\epsilon_r + 1)/2)$, as the field approximately exists, half in the dielectric, and half in the air.

4.2.6 Slotline

Slotline was first introduced in 1968 by Cohn [8] as a transmission structure for microwave integrated circuits (MIC's). The basic slotline structure is shown in Figure 4.6.

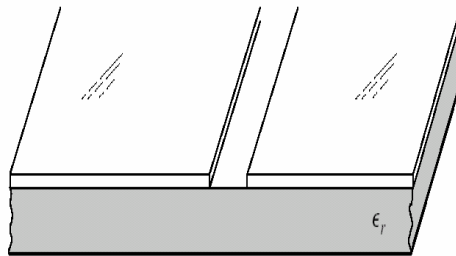


Figure 4.6 Slotline transmission line

Slotline consists of two parallel strips of metal separated by a narrow slot on top of a dielectric substrate. Normally, there is no metal on the underside. For MIC design, slotline is regarded as the third choice of transmission line and is only used when microstrip and CPW cannot meet the design requirements. Generally, it is only used in hybrid combinations with microstrip and CPW, an example of this is shown in chapter 9 when a CPW-to-slotline transition is used to give a balance feed to a dipole antenna.

In slotline, the wave propagates along the slot with the major electric field component situated across the slot. The mode of propagation is non-TEM and can be considered to be transverse electric (TE). Figure 4.7 shows the field distributions for slotline [9].

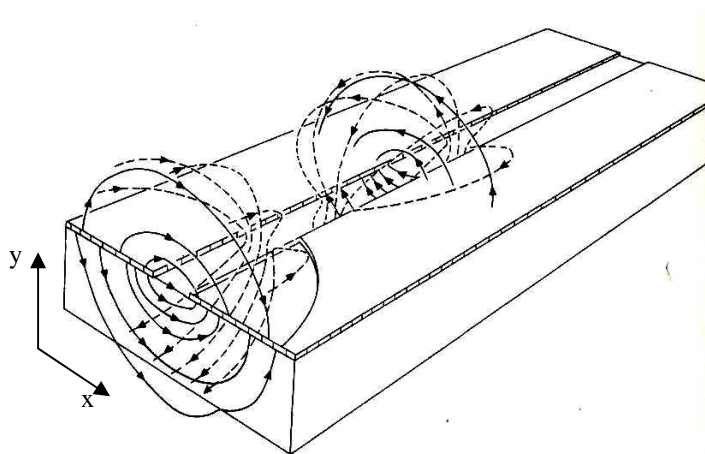


Figure 4.7. Field distribution of slotline. Solid line is E-field and dashed line is H-field.

As shown in Figure 4.7 a portion of the field exists outside the dielectric. For an infinitely thick dielectric the effective wavelength can be given by:

$$\epsilon_{re} = \frac{\epsilon_r + 1}{2} \quad (4.14)$$

$$\lambda_g = \frac{\lambda_0}{\sqrt{\epsilon_{re}}} \quad (4.15)$$

It has been shown [10] that these conditions hold for a finite thickness substrate (h) when using the following equation:

$$\left(\frac{h}{\lambda_0}\right)_c = 0.25/\sqrt{\epsilon_r - 1} \quad (4.16)$$

This relationship is used to derive the cut-off frequency for TE₁₀ surface wave mode and indicates the minimum height required for Equation 4.14 to hold. For the majority of cases, the value of effective permittivity will be much lower than the average of air and the dielectric constant. As an example, for an operating frequency of 5.8 GHz and a substrate with a relative permittivity of 12.9 the minimum height would have to be 3.75mm, which is well above the majority of general substrate heights at this frequency range. The effective wavelength can be calculated theoretically but they are complex, and unlike microstrip, as it is a function of free space wavelength due to the transverse electric mode that is present.

Calculating the slotline impedance is complex, for the same reasons as calculating the effective wavelength. The characteristic impedance cannot be defined uniquely due to the non-TEM propagation. A useful definition for the characteristic impedance (Z_0) is given by:

$$Z_0 = \frac{V^2}{2P} \quad (4.17)$$

Where V is the peak voltage across the slot and P is the average power.

Now that both a simple antenna and its possible transmission lines have been discussed the next step is to investigate the fundamental parameters used to characterise an antennas performance. These parameters are now discussed in the following section.

5. Antenna Analysis

To understand the challenges faced when designing antennas it is necessary to provide some background information on some of the key parameters and performance metrics. There are many antenna types with differing geometry but there are certain fundamental parameters can be used to describe all of them. Also discussed in this chapter is Ansoft's High Frequency Simulation Software (HFSS), which was used to design and simulate antennas investigated in this project.

5.1 Fundamental Antenna Parameters

The most fundamental antenna parameters are;

1. Impedance Bandwidth
2. S-parameters
3. Radiation pattern
4. Directivity
5. Efficiency
6. Gain
7. Polarisation

All of the parameters mentioned above are necessary to fully characterise an antenna, and to establish whether the antenna is optimised for its purpose.

5.1.1 Impedance Bandwidth

The term 'impedance bandwidth' is used to describe the bandwidth over which the antenna has acceptable losses due to mismatch. The impedance bandwidth can be measured by the characterisation of both the Voltage Standing Wave Ratio (VSWR) and Return Loss (RL) at the frequency band of interest. Both VSWR and RL are dependant on measuring the reflection coefficient (Γ). Γ is defined as the ratio of the amplitude of the reflected voltage wave (V_0^-) normalised to the amplitude of the incident voltage wave (V_0^+) at a load [1]. Γ can also be defined by using other field or circuit quantities and is defined by the following equation.

$$\Gamma = \frac{V_0^+}{V_0^-} \quad (5.1)$$

The VSWR is defined as the ratio between the voltage maximum and voltage minimum of the standing wave created by the mismatch at the load on a transmission line. The VSWR equation is shown in Equation 5.2.

$$VSWR = \frac{|Z_L|}{|Z_0|} = \frac{1+|\Gamma|}{1-|\Gamma|} \quad (5.2)$$

The return loss (*RL*) is the magnitude of the ratio of the reflected wave to that of the incident wave, and is defined in dB as:

$$RL = -20\text{Log}|\Gamma| \quad (5.3)$$

The scattering parameter S_{11} is equivalent to Γ . It is common for S_{11} to be defined in dB as:

$$S_{11} = 20\text{Log}|\Gamma| \quad (5.4)$$

The maximum acceptable mismatch for an antenna is normally 10% of the incident signal. For the reflection coefficient, this equates to $\Gamma = 0.3162$. For VSWR the impedance bandwidth lies between $1 < VSWR < 2$, and for Return Loss its value must be greater than 10dB or $S_{11} < -10$ dB. A description of S-parameters follows is given in the following section.

5.1.2 S-Parameters

When designing antennas as part of a network, or on their own, it is advantageous to create a model which allows the designer insight into the performance of the system/antenna. It is common to extract useful data via a Vector Network Analyser (VNA). The data is normally presented in the form of S-parameters. At low frequencies, simple circuit models normally suffice but at high frequencies a

distributed model is needed to account for a variety of possible physical effects, such as:

- Skin depth ($\delta = \sqrt{2 / \omega \mu \sigma}$)
- Energy propagation
- Radiation
- Reflections / Transmission
- Fringing fields (coupling)
- Energy splitting / combining

Also S-parameters enable broadband characterisation unlike impedance and admittance parameters, which need open or short-circuit terminations to characterise and are not conducive to broadband characterisation.

The S-parameters allow for a complete description of a N-port network as seen at its N-ports in Figure 5.1.

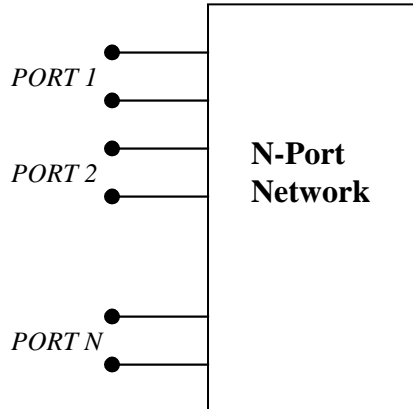


Figure 5.1 An N-Port network

The S-Parameters are defined by measuring the voltage travelling waves between the N-ports. To explain this concept it is best to look at a two port network, as shown by Figure 5.2.

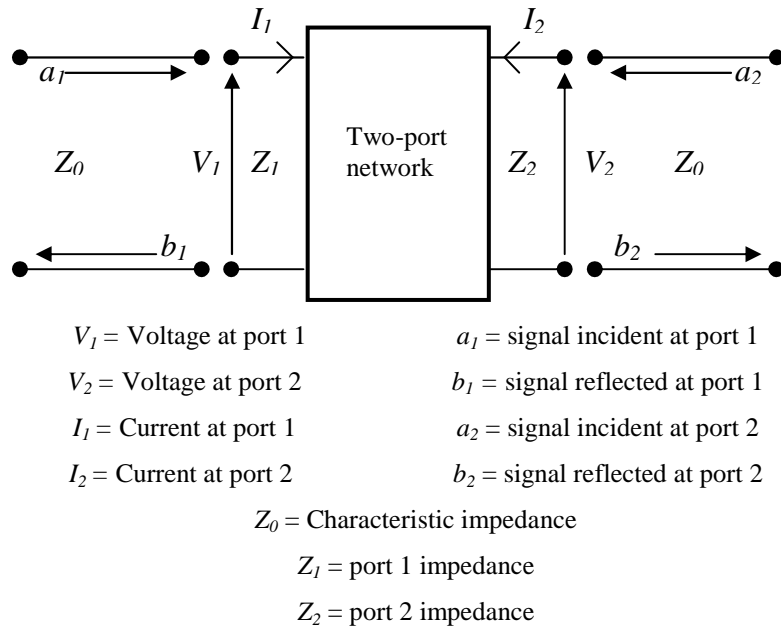


Figure 5.2 Two port network definition

It is also important to define the incident and reflected signals, which take the form:

$$a_x = \frac{|V_x^+|}{\sqrt{Z_0}} (\sqrt{\text{watts}}) \quad (5.5)$$

$$b_x = \frac{|V_x^-|}{\sqrt{Z_0}} (\sqrt{\text{watts}}) \quad (5.6)$$

Combing equations 5.5 and 5.6 we get four possible results.

- The input reflection coefficient, when port 2 is matched, $S_{11} = \frac{b_1}{a_1} \Big|_{a_2=0}$
- The reverse transmission gain, when port 1 is matched, $S_{12} = \frac{b_1}{a_2} \Big|_{a_1=0}$
- The output reflection coefficient, when port 1 is matched, $S_{22} = \frac{b_2}{a_2} \Big|_{a_1=0}$
- The forward transmission gain, when port 2 is matched, $S_{21} = \frac{b_2}{a_1} \Big|_{a_2=0}$

Typically, when using S-parameters to characterise antennas the reflection coefficients and forward transmission gain are most frequently used. Ideally reflection coefficients should tend towards zero ($S_{11}=S_{22}=0$) as this means that there is no power being reflected back due to a good match to the characteristic impedance of the feeding structures, usually 50Ω . The forward transmission gain should ideally tend towards one, but this is generally not the case for low gain antennas where the path loss can be 20dB or greater.

It is normal to express the S-parameters in terms of decibels as follows:

$$S_{ij} (dB) = 20 \log S_{ij} \quad (5.7)$$

5.1.3 Radiation Pattern

An antenna radiation pattern is defined in the IEEE Standard Definitions of Terms for Antennas [2] as:

“A mathematical function or a graphical representation of the radiation properties of the antenna as a function of space coordinates. In most cases, the radiation pattern is determined in the far-field region and is represented as a function of the directional coordinates. Radiation properties include power flux density, radiation intensity, field strength, directivity, phase or polarisation.”

Primarily, when measuring the radiation pattern, the property of most interest is the energy radiated relative to the antennas position. This is usually measured using spherical coordinates as shown in Figure 5.3 [3].

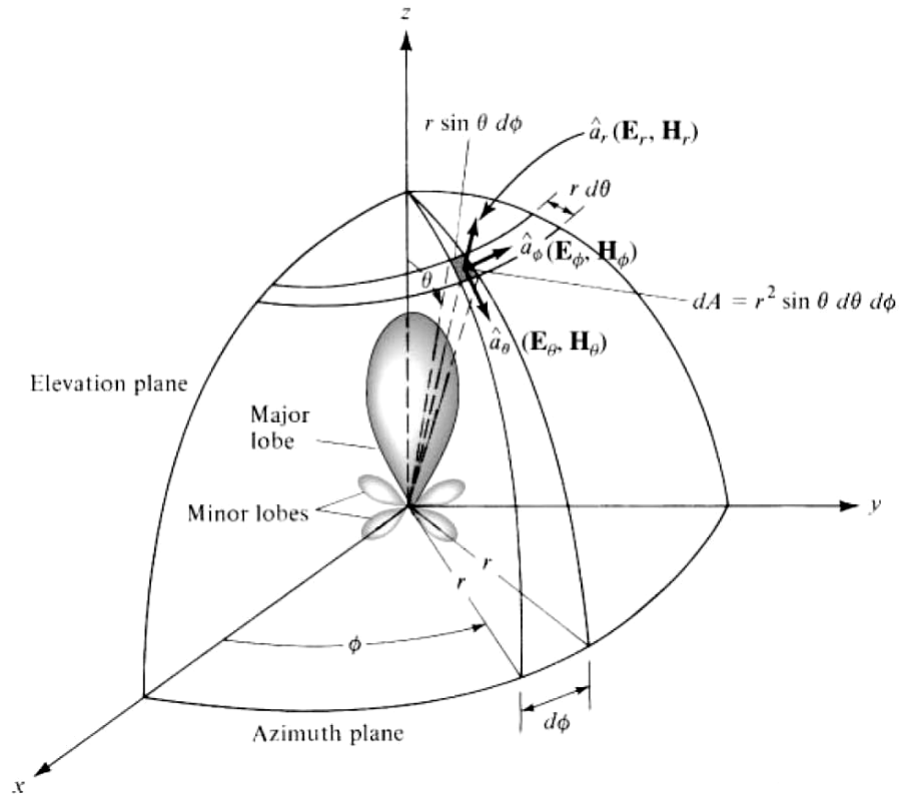


Figure 5.3 Coordinate system for antenna analysis.

The antenna under test is placed at the origin and is rotated through $\phi = 0^\circ - 360^\circ$ and $\theta = 0^\circ - 180^\circ$ while the power is measured in the far-field. As shown in Figure 5.3 the x-z plane is considered the elevation plane. This is normally aligned with the electric field vector and is called the E-plane. The x-y plane is normally aligned with the magnetic field vector and is termed the H-plane.

5.1.4 Directivity (D)

Antenna directivity in the IEEE Standard Definitions of Terms for Antennas [4] as:

“The ratio of the radiation intensity in a given direction from the antenna to the radiation intensity averaged over all directions. The average radiation intensity is equal to the total power radiated by the antenna divided by 4π . If the direction is not specified, the direction of the maximum radiation intensity is implied.”

Essentially, this means that the directivity of an antenna is the ratio of the radiation intensity in a given direction over that of a isotropic source. This can be written as:

$$D = \frac{U}{U_0} = \frac{4\pi U}{P_{rad}} \quad (5.8)$$

Where, U = radiation intensity (W/unit solid angle)

U_0 = radiation intensity of an isotropic source (W/unit solid angle)

P_{rad} = total radiated power (W)

If the antenna was to radiate in all directions (isotropic radiator) then its directivity would be unity. As an isotropic radiator cannot be realised practically, the most comparable antenna is a short dipole, which has a directivity of 1.5. Any other antenna will have a higher directivity than 1.5, which means their patterns are more focused in a particular direction.

5.1.5 Antenna Efficiency (η)

Like other microwave components, antennas can suffer from losses. The total antenna efficiency takes into account the losses at the input terminals, and within the structure of the antenna itself.

The mismatch or reflection efficiency (η_r) is directly related to the return loss (Γ) and can be defined as:

$$\eta_r = (1 - |\Gamma|^2) \quad (5.9)$$

The radiation efficiency (η) is a measure of how much power is lost in the antenna due to conductor and dielectric losses. These losses reduce the radiation in any given direction and can be expressed as:

$$\eta = \frac{P_{rad}}{P_{in}} \quad (5.10)$$

Another way of describing antenna efficiency is to view it as an effective aperture [5]. Shown in Figure 5.4 is a diagram of an antenna collecting a plane wave.

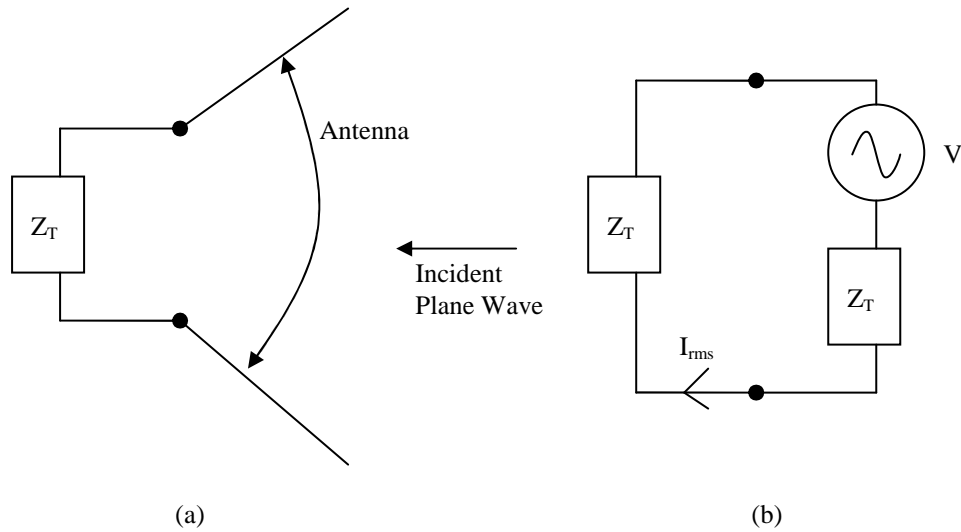


Figure 5.4. Schematic diagram of antenna terminated in impedance Z_T with plane wave incident on antenna (a) and equivalent circuit (b)

Figure 5.4(a) shows an incident plane wave being received by an antenna. The antenna collects the power, P (W/m^2) from the wave and delivers it to the load, Z_T . Using the equivalent circuit in Figure 5.2 (b), where the antenna has been replaced by a Thevenin generator having a voltage, V , and antenna impedance, Z_A , the rms current produced by the plane wave can be written as:

$$I_{rms} = \frac{V_{rms}}{(Z_T + Z_A)} \quad (5.11)$$

Where, $Z_T = R_T + jX_T$

and $Z_A = R_A + jX_A$

The antenna resistance, R_A is divided into two parts, the radiation resistance R_r and the loss resistance R_l .

$$R_A = R_r + R_l \quad (5.12)$$

The real power delivered to the load is then defined as:

$$W = I_{rms}^2 R_T \text{ (Watts)} \quad (5.13)$$

The ratio between the power (W) at the load, and the power density (P) of the incident wave, is known as the effective aperture, A_e , and can be described as:

$$A_e = W/P \text{ (m}^2\text{)} \quad (5.14)$$

As shown, the effective aperture takes into account any mismatch losses and radiation losses, and can be thought of as the ‘capture area’ of the antenna. If there are no losses due to mismatch or the antenna, then it can be seen, for a given frequency, that if the antenna size is reduced, its efficiency is reduced. The limit on the size reduction of antennas, and the consequent impact on efficiency will be discussed in chapter 9.

5.1.6 Antenna Gain

Antenna gain, G, is the product of efficiency and directivity, and is defined in the IEEE Standard Definitions of Terms for Antennas [6] as:

“The ratio of the intensity, in a given direction, to the radiation intensity that would be obtained if the power accepted by the antenna were radiated isotropically. The radiation intensity corresponding to the isotropically radiated power is equal to the power accepted by the antenna divided by 4π ”

This can be expressed as:

$$G = \frac{4\pi U(\theta, \phi)}{P_{in}} \quad (5.15)$$

Unless specified, it is assumed that the antenna is receiving a signal in the direction of maximum gain. It is also common for the gain to be expressed in decibels and referenced to an isotropic source ($G = 1$), as shown in Equation 5.16.

$$G \text{ (dBi)} = 10 \text{ Log } (G/1) \quad (5.16)$$

5.1.7 Polarisation

The polarisation of an antenna refers to the orientation of the electric field vector of the radiated wave and is defined in the IEEE Standard Definitions of Terms for Antennas [7] as:

“The property of an electromagnetic wave describing the time-varying direction and relative magnitude of the electric-field vector; specifically, the figure traced as a function of time by the extremity of the vector at a fixed location in space, and the sense in which it is traced, as observed along the direction of propagation”

Polarisation is the curve traced by the tip of the electric field vector viewed in the direction of propagation. Figure 5.5 shows a typical trace as a function of time [8].

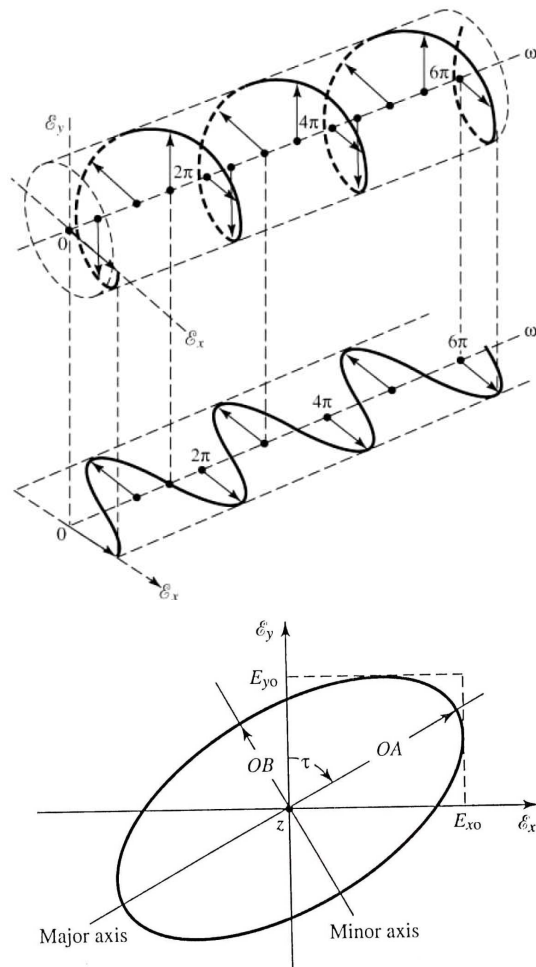


Figure 5.5. Rotation of a plane electromagnetic wave and its polarisation ellipse at $z = 0$ as a function of time.

The polarisation of the wave may be linear, circular, or elliptical. The instantaneous electric field of a plane wave, travelling in the negative z direction, may be written as:

$$E(z, t) = E_x(z, t)\hat{x} + E_y(z, t)\hat{y} \quad (5.17)$$

The instantaneous components are related to their complex counterparts by:

$$E_x(z, t) = E_x \cos(\omega t + \beta z + \theta_x) \quad (5.18)$$

and

$$E_y(z, t) = E_y \cos(\omega t + \beta z + \theta_y) \quad (5.19)$$

Where E_x and E_y are the maximum magnitudes and θ_x and θ_y are the phase angles of the x and y components respectively, ω is the angular frequency, and β is the propagation constant.

For the wave to be linearly polarised, the phase difference between the two components must be:

$$\begin{aligned} \Delta\theta &= \theta_y - \theta_x = n\pi, \\ \text{Where, } n &= 0, 1, 2, \end{aligned} \quad (5.20)$$

For the wave to be circularly polarised, the magnitudes of the two components must be equal i.e. $E_x = E_y$, and the phase difference $\Delta\theta$ is an odd multiple of $\pi/2$. This is illustrated by Equation 5.21.

$$\Delta\theta = \theta_y - \theta_x \quad (5.21)$$

If $E_x \neq E_y$ or $\Delta\theta$ does not satisfy (5.20) and (5.21), then the resulting polarisation is elliptical, as shown in Figure 5.3. The performance of a circularly-polarised antenna is characterised by its axial ratio (AR). The AR is defined as the ratio of the major axis to the minor axis and is described below.

$$AR = \frac{\text{major axis}}{\text{minor axis}} = \frac{OA}{OB} \quad (5.22)$$

For circular polarisation $OA = OB$ (i.e. $AR = 1$), whereas for linear polarisation $AR \rightarrow \infty$. Typically, it is only possible to generate AR over a limited frequency range. The 3dB bandwidth is used to define $AR = 1 = 0\text{dB}$ at the operating frequency.

Now that the fundamental parameters used to characterise an antennas performance have been discussed the next stage is to investigate the simulation software used, the fabrication process and the test apparatus used. This is discussed in the next chapter.

6. Antenna design, fabrication and experimental analysis

The object of this chapter is to give an insight into the process involved in designing, fabricating and experimentally verifying an antenna. The software used to design antennas is discussed, along with the fabrication process and the tools used to characterise the performance of antennas.

6.1 High Frequency Simulation Software (HFSS)

HFSS was used as an evaluation and design tool for the majority of the work carried out in this thesis. Many papers have been published in the past, [1] and more recently [2], verifying its accuracy. HFSS utilizes a 3D full-wave Finite Element Method to compute the electrical behaviour of high-frequency and high-speed components [3]. Models can be created with different materials, boundaries and geometries. The basic mesh element used is a tetrahedron, which allows the user to mesh any arbitrary 3D geometry, such as complex curves and shapes. The mesh can be defined automatically by the solver, but quite often this does not give satisfactory results and the user has to define mesh operations, such as, seeding the mesh, maximum aspect ratio and curve surface approximations. The next section discusses the process once a model has been subdivided into elements.

6.1.1 Theoretical basis of HFSS

Once a mesh is created, basis functions are defined for each tetrahedra. The basis functions, W_n , define the conditions between the nodal locations in the overall mesh of tetrahedral based on the problem inputs. The basis functions are then multiplied by the field Equation, 6.1, derived from Maxwell's equations.

$$\nabla \times \left(\frac{1}{\mu_r} \times \vec{E} \right) - k_0^2 \epsilon_r \vec{E} = 0 \quad (6.1)$$

The result is then integrated over the volume of the tetrahedron as shown by Equation 6.2.

$$\int_V \left[W_n \cdot \nabla \times \left(\frac{1}{\mu_r} \times \vec{E} \right) - k_0^2 \epsilon_r \vec{E} \right] dV = 0 \quad (6.2)$$

This is then rewritten using the Green's and divergence theorems and is then set equal to the excitation/boundary terms, as shown in Equation 6.3.

$$\int_V \left[(\nabla \times W_n) \cdot \left(\frac{1}{\mu_r} \times \vec{E} \right) - k_0^2 \epsilon_r \vec{E} \right] dV = \int_S \text{boundary term} \quad (6.3)$$

The electric-field vector is then written as a summation of unknowns; X_m , multiplied by the same basis functions used in generating the initial series of equations, and is shown by Equation 6.4.

$$\vec{E} = \sum_{m=1}^N X_m W_m \quad (6.4)$$

The resulting equations allow the solution of the unknowns, X_m , to find the electric-fields. The general form of the expression is shown by Equation 6.5.

$$\sum_{m=1}^N X_m \cdot \left(\int_V \left[(\nabla \times W_n) \cdot \left(\frac{1}{\mu_r} \times W_m \right) - k_0^2 \epsilon_r W_n W_m \right] dV \right) = \int_S (\text{boundary terms}) dS \quad (6.5)$$

Once the values have been calculated using the solver, a second adaptive pass occurs and HFSS compares the S-parameters to the previous mesh-based solution. This process is repeated and the difference between the two solutions calculated. This process is continued until the solution has converged to an acceptable difference, usually 2% or less, this being defined by the user. Shown in Figure 6.1 is a structure subdivided into elements after several passes.

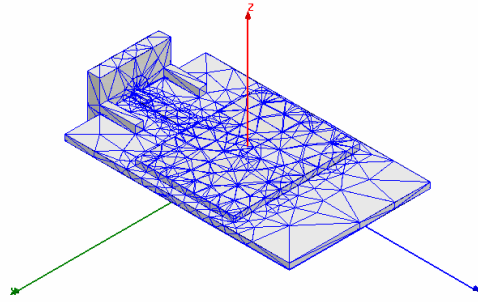


Figure 6.1. 3D structure sub divided into elements

HFSS was mainly used in this thesis for evaluating S-parameters, radiation characteristics and field distributions for both antennas and passive components. Importing and exporting models for analysis and design was also carried out. The operation of HFSS is best illustrated by using a practical example of a 6.8 GHz proximity coupled patch antenna, which was developed in the course of this project.

6.1.2 Simulating structures in HFSS

Models in HFSS are created relatively easily, by the user or imported in a DXF, GDSII etc. file format. An example of a 5.8 GHz proximity-coupled patch user-defined model is shown in Figure 6.2.

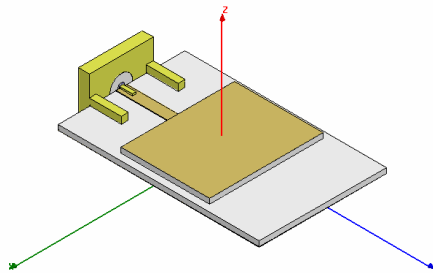


Figure 6.2. 5.8 GHz proximity coupled patch antenna

HFSS has an extensive library of materials but it is also possible to create new materials not contained within the library. Creating your own material can be useful for investigating the effects of changing certain material parameters, such as permittivity, conductivity, etc.

With the model created, the boundary conditions need to be specified. Generally, these can be split into excitations or surface approximations. There are many types of excitations possible in HFSS, but the main ones used for the models throughout the thesis are either wave ports or lumped ports. Ports are a unique type of boundary condition that allows energy to flow into and out of a structure.

- Wave ports – These ports can be placed internally or externally, and support multiple modes of transmission. They also support reference plane de-embedding and arbitrary mode re-normalisation. They are well suited for exciting most transmission lines, though setting them up can be complex.
- Lumped ports – These ports are recommended only for surfaces internal to the geometric model. There is only a single mode excited at the port (TEM) and there is no de-embedding. They are simpler to set up and are ideal for exciting transmission lines such as microstrip.

Figure 6.3 shows an example of a wave-port being used to excite a co-axial mode. The orientation of the field at the port can clearly be seen to be in a co-axial mode.

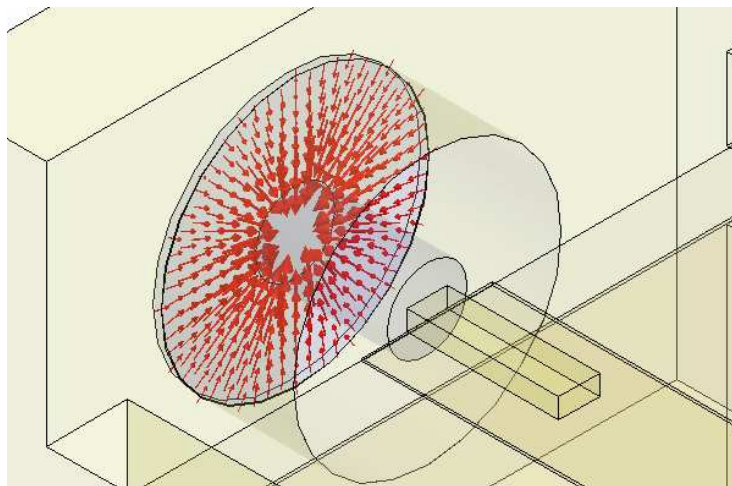


Figure 6.3. Wave port excitation on a SMA connector

With the model created and a excitation specified, the next stage is to select the surface approximation for the radiation boundary. There are two main options:

- Radiation Boundary – The radiation boundary (also known as the Absorbing Boundary Condition, ABC) allows waves to radiate infinitely far into space. The boundary is normally assigned to an airbox, which is placed at least one quarter of a wavelength, at the lowest frequency of interest, away from any radiating object. A drawback to this boundary is that if there is any energy incident at an angle greater than 30 degrees it will be reflected. This means for curved surfaces, the boundary should follow the shape. For example, a wire dipole should have a cylindrical boundary around it.
- Perfectly Matched Layer (PML) – Like the radiation boundary, the PML allows waves to radiate infinitely far into space. The PML is not strictly a boundary condition but a fictitious, complex, anisotropic material that fully absorbs the electromagnetic fields impinging upon the PML boundary. The main advantages of the PML is that there is no angle of incidence problem and the boundary can be placed a minimum of one tenth of a wavelength, at the lowest frequency of interest, away from any radiating object.

Figure 6.4 shows the 5.8 GHz proximity coupled patch antenna enclosed in an airbox with and without the boundary.

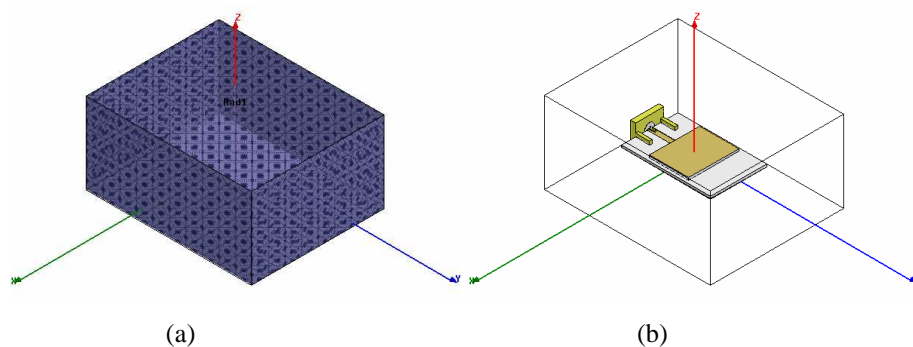


Figure 6.4 HFSS model (a) with and (b) without radiation boundary

The second last stage of the simulation process is to select a frequency at which to solve the model, called the adaptive frequency. The adaptive frequency should be set 'in band' at the expected solution frequency, especially for highly resonant structures. The reason behind this is that the meshing is a function of the adaptive

frequency i.e. higher frequency, larger mesh. It is a common misconception that setting the adaptive frequency higher will give greater accuracy. If the adaptive frequency is set higher than the operating frequency the resonance may be missed. If a wideband structure is being analysed, then the frequency should be set at the highest frequency of expected operation. After selecting the adaptive frequency, the final stage is to choose the frequency sweep. When specifying the frequency sweep there are three options.

- Discrete – This sweep offers the highest accuracy as it performs a full solution at every frequency specified in the sweep. This sweep is best when only a few frequency points are necessary to accurately represent the results in a frequency range.
- Interpolative - Estimates a solution for an entire frequency range. This sweep is best when the frequency range is wide and the frequency response is smooth e.g. a filter.
- Fast - Generates a unique full-field solution for each division within a frequency range. This sweep is best for models that will abruptly resonate or change operation in the frequency band. A fast sweep will obtain an accurate representation of the behaviour near the resonance.

Generally, either the discrete or fast sweep is used throughout this thesis.

As the model is simulated, it is important to observe the convergence of the solution. For higher accuracy it is normal to specify at least three concurrent convergent passes within the specified accuracy, normally 2% or less. This is shown in Figure 6.5.

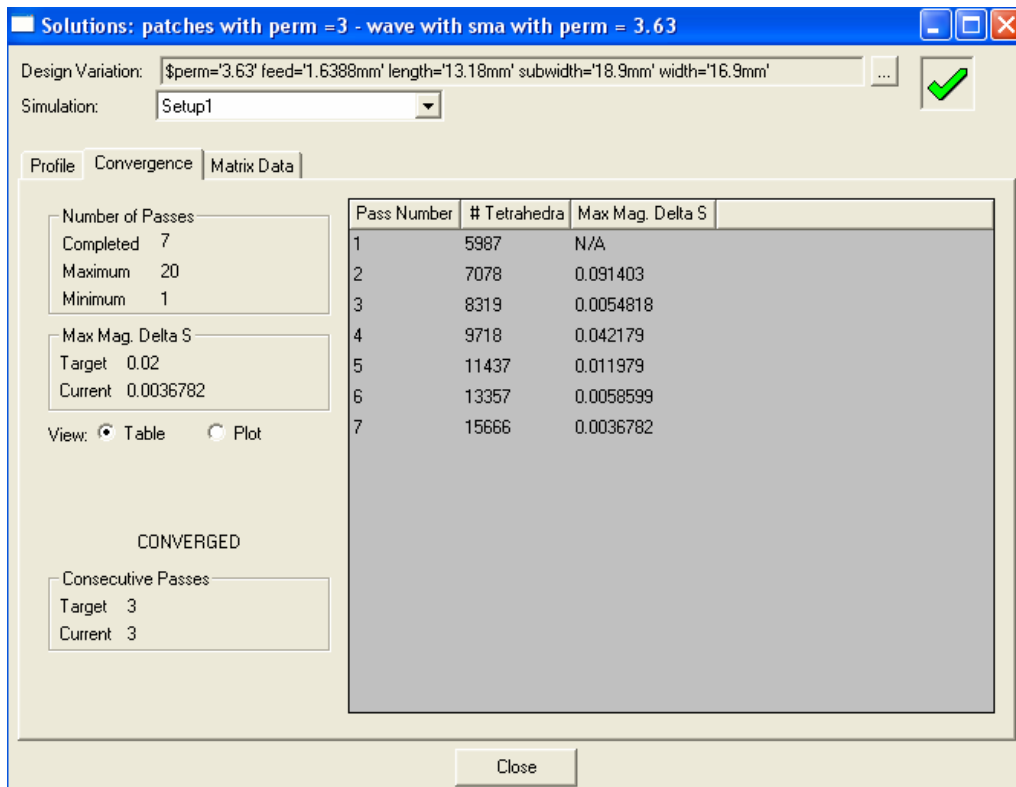


Figure 6.5 Solution data for seven passes

From inspection of Figure 6.5 it shows there were seven adaptive passes and the final three passes converged within a minimum of 2% accuracy, with the final pass having a 0.36782 % error compared to the previous pass. It is important to note that if consecutive converged passes had been set to one, then the simulation would have stopped at adaptive pass three, which would probably have resulted in a less accurate solution. Setting the minimum number of converged passes greater than one ensures that convergence occurs correctly and the solution is not an aberration.

The entire process, including the sweep, took 3 minutes 15 seconds, using 15666 tetrahedra for the 5.8 GHz proximity-coupled patch antenna [4]. The simulation was allowed to run until the desired three consecutive passes occurred. Once the designer is satisfied with the simulated results it is time to fabricate the device.

6.3 Fabrication Processes

The fabrication of the antennas, investigated in this thesis, was carried out using two technologies. The first is the standard PCB processing method, which involves:

- Print mask
- Board with mask in place is exposed to light and developed
- Board is placed in a proprietary etch, which removes the copper that is not protected by the exposed and developed resist

The resolution of the PCB process is limited, as the smallest gap that can be obtained is between 250 μm and 300 μm .

The second process for fabrication of antennas in this thesis utilises the technology available at the James Watt Nano-Fabrication Centre (JWNC). The material used for the substrate is gallium arsenide (GaAs), a semiconductor used to make devices such as Monolithic Microwave Integrated Circuits (MMIC's), infrared light-emitting diodes, laser diodes and solar cells. The antennas designed in chapter nine were constructed using the following process:

- Submit design to beam writer
- Spin resist on wafer
- Pattern transferred to resist using electron beam lithography
- Metal deposited via metal evaporation, which leaves a 1.2 μm Gold (Au) on top of a 50nm Nickel Chromium (NiCr) layer
- Wafer is then treated by a solvent, which removes resist plus any metal not attached to the substrate

The second process has a minimum feature size of 10nm.

6.4 Testing facilities

Throughout this thesis several testing apparatus were used. These include various Vector Network Analysers (VNA), some with on-wafer probing capability, as well as Spectrum Analysers and Communications Analysers. As there were many different models of VNAs used, the models are specified in the relevant sections.

Antenna radiation patterns have been obtained for various antennas by using either near- field or far-field systems. Towards the end of this project, Glasgow University purchased a spherical near-field antenna measurement system. This is now described.

6.4.1 Near-field anechoic chamber

The Near-field anechoic chamber at Glasgow University is a NSI-700S-90 spherical near-field measurement system (manufactured and installed by Near-field Systems Inc (NSI)). This means that it can give near-complete 3D characterisation of the antenna. The chamber works on the principle of measuring the electromagnetic field distribution near the antenna and using Huygens principle to compute the far-field response [5].

The chamber has a selection of Open Ended Waveguide Probes (OEWG) with high frequency limit of 20 GHz, which are used for accurate measurement of highly directional antennas. There is also a wideband (500MHz to 18 GHz) Dual Polarised Log-Periodic antenna (DPLA), which can be used for any antenna but is better suited to low-gain omni-directional antennas. The dual-polarisation also allows for measurement of circular polarisation and cross-polarisation levels. Figure 6.6 shows a simple diagram layout of the chamber with the measurement coordinates.

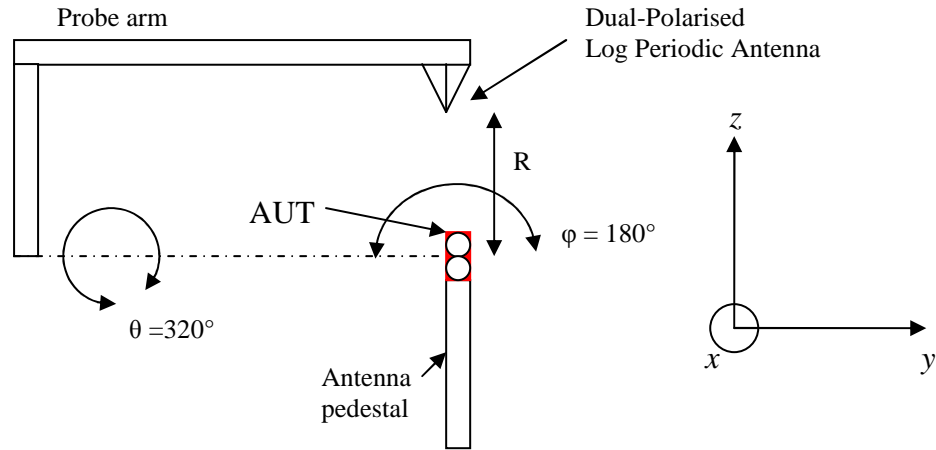


Figure 6.6. Layout of chamber. $R = \text{probe to centre of AUT} = 111.5 \text{ cm}$

The probe is a Theta over Phi (θ/ϕ) measurement system. This means that the azimuth is scanned by rotation of theta, and elevation is scanned by rotation of phi. The probe arm rotates $\theta \pm 160^\circ$ while the AUT rotates $\phi \pm 90^\circ$.

As highlighted design tools such as HFSS can greatly assist a design engineer to create antennas with the expected response. Combining this with accurate test equipment, it is possible to fully characterise and develop antennas for specific applications. The next chapter investigates a 5.8 GHz patch antenna, which is designed, modelled and tested using the processes outlined in this chapter.

7. A proximity-coupled 5.8 GHz patch antenna

To help illustrate the process of designing and testing an antenna, a 5.8 GHz patch antenna was chosen as an example, as it is a relatively simple structure to design. The final design of antenna that is achieved in this chapter is used as the basis of another antenna described and characterised in chapter nine.

7.1 Background theory

In this thesis so far, the antennas discussed have been based on conventional dipoles, which are based on a current element. That is to say, the excitation of radiation has been based on current travelling along the elements. The patch antenna is based on a voltage element of which the patch represents an aperture which collects or transmits the electromagnetic energy. The patch antenna may take many shapes as illustrated by Figure 7.1.

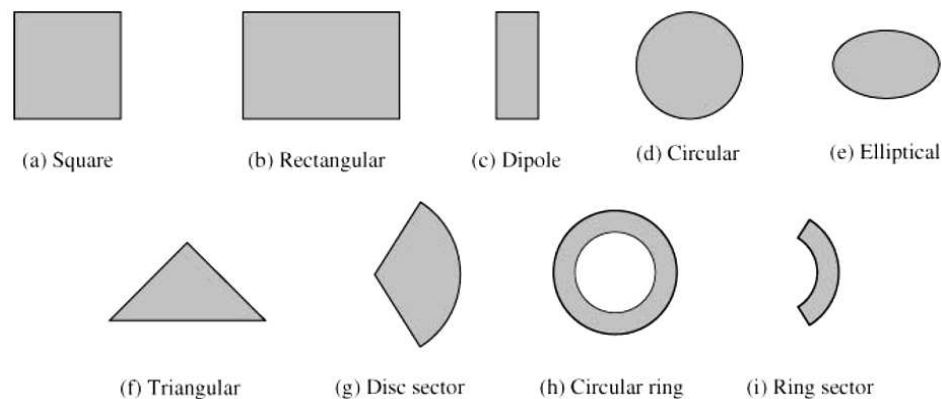


Figure 7.1. Representative shapes of microstrip patch antennas

The research conducted in this thesis focused on rectangular elements, as there was a large amount of information available on the design techniques. There was also the added advantage of quicker simulation times, as there were no rounded edges, which in turn, reduced mesh size.

The patch is made of metal, usually etched using a photolithographic process, and mounted on a dielectric substrate of thickness (h) much smaller than the free space wave length ($h \ll \lambda_0$, usually $0.003 \lambda_0 \leq h \leq 0.05 \lambda_0$) with a ground plane underneath. An example of this shown in Figure 7.2 [1].

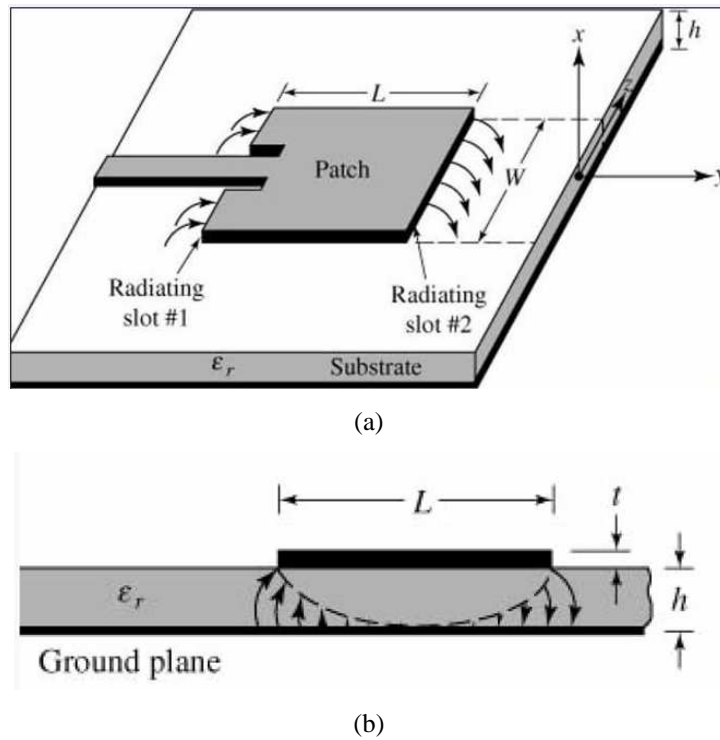


Figure 7.2. (a) Microstrip antenna (b) side view

The patch acts as a $\lambda_g/2$ parallel-plate microstrip transmission line, where λ_g is the wavelength in the dielectric medium. Radiation occurs from the fringing fields between the patch and the ground plane, shown by radiating slot #1 and #2 in Figure 7.2. Maximising radiation is a trade-off between desirable element size and good antenna performance. Size reduction can be achieved by increasing the dielectric constant (ϵ_r) and reducing the substrate height (h) but this affects the general performance of the antenna by binding the fields tightly into the substrate, which increases losses and decreases bandwidth. Alternately, the patch antenna can have excellent performance with increased substrate heights and low dielectric constant. This has the effect of having the fields bound much more loosely to the substrate, resulting in much greater antenna efficiency and bandwidth, but unfortunately the radiating element becomes much larger in size.

Another of the patch antennas advantages is the multitude of ways available to feed the antenna. Excitation can be achieved by microstrip, CPW, coaxial probe, aperture coupling and proximity coupling.

7.2 Design of Patch antenna - The transmission line model

There are many methods of analysis used with patch antennas. One of the most popular is the transmission line model, which is based on equivalent magnetic current distribution around the patch edges. The patch is viewed as a transmission line resonator with no transverse field variations i.e. the field only varies along the length, and the radiation occurs from the fringing fields, which are viewed as open circuits at the ends of the transmission line. The patch is then represented as two slots spaced by the length of the patch. The transmission line model cannot be used for all shapes of patch and is not the most accurate, but it is very quick and easy to use, especially when used in conjunction with a finite element solver such as HFSS.

The fundamental mode of a patch antenna is the TM_{01} mode. The subscript depicts the orientation i.e. along the y-axis of the two radiating slots, or voltage maximums, as shown in Figure 7.2. To excite the TM_{01} mode, the length, L , should be slightly less than $\lambda_g/2$, where λ_g is defined by:

$$\lambda_g = \frac{\lambda_0}{\sqrt{\epsilon_{re}}} \quad (7.1)$$

Where, ϵ_{re} is the effective dielectric constant in the medium. This value accounts for the fact that not all the fringing fields are bound inside the substrate. The effective dielectric constant is less than the dielectric constant and is given by [2]:

$$\epsilon_{re} = \frac{\epsilon_r + 1}{2} + \frac{\epsilon_r - 1}{2} \left[1 + 12 \frac{h}{W} \right]^{-1/2} \quad (7.2)$$

Where, W is the width of the patch.

Equation 7.2 omits the fact that the effective dielectric constant is frequency dependant. As frequency increases, the fields occupy more of the substrate and the value of effective dielectric constant moves towards the value of dielectric

constant of the substrate. For the purposes of investigating patch antenna design in this thesis Equation 7.2 is considered adequate.

The electrical length of the patch is greater than the physical dimensions due to the fringing fields. This illustrated by Figure 7.3 [3].

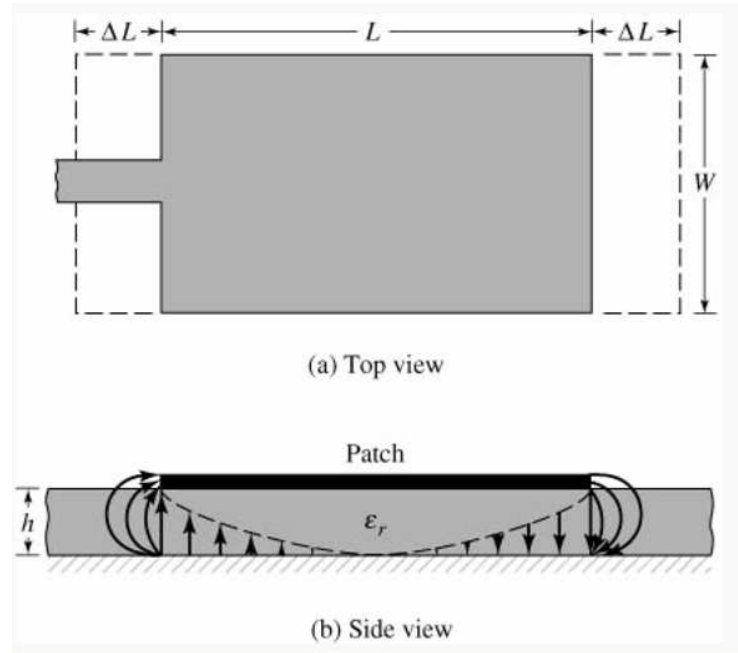


Figure 7.3. Physical and effective lengths of rectangular microstrip patch

The fringing fields are accounted for by the distance ΔL , which is a function of the effective dielectric constant. The electrical length of the patch is given by:

$$L_e = L + 2\Delta L \quad (7.3)$$

The extension in length may be calculated by:

$$\Delta L = \frac{h}{\sqrt{\epsilon_{re}}} \quad (7.4)$$

It is already known that the effective length of the patch is equal to $\lambda_g/2$, so for a given frequency, f_0 , the effective length can be calculated by:

$$L_e = L + 2\Delta L = \frac{\lambda_0}{2\sqrt{\epsilon_{re}}} = \frac{c}{2f_0\sqrt{\epsilon_{re}}} \quad (7.5)$$

Where, c = velocity of light in free space = 3×10^8 m/s. To obtain the resonant frequency for any TM_{mn} mode the following expression can be used [4]:

$$f_0 = \frac{c}{2\sqrt{\epsilon_r}} \left[\left(\frac{m}{L} \right)^2 + \left(\frac{n}{W} \right)^2 \right]^{1/2} \quad (7.6)$$

To calculate the effective dielectric constant using Equation 7.6, W must be known. W is taken as being equal to a half-wavelength corresponding to the average of the two dielectric mediums i.e. substrate and air.

$$W = \frac{c}{2f_0\sqrt{\frac{\epsilon_r + 1}{2}}} \quad (7.7)$$

The value obtained for W by using Equation 7.7 can be increased or decreased. If it is increased then both bandwidth and directivity are increased due to the larger aperture area. If W is further increased then higher order modes will be excited. Decreasing W has the opposite effect on bandwidth and directivity but is sometimes advantageous, particularly when trying to excite circular polarisation.

The design procedure for obtaining physical dimensions of the patch antenna is as follows:

- Specify operating frequency (f_0) and substrate (ϵ_r)
- Calculate width (W)
- Calculate effective permittivity (ϵ_{re})
- Calculate physical length (L)

The radiation patterns for the fundamental TM_{01} mode are given by Kumar [5] and are based on the combination of two radiating slots of width W_e and length

ΔL . The normalised radiation patterns in the E-plane (E_ϕ in $\phi = 0^\circ$ plane) and the H-plane (E_ϕ in $\phi = 90^\circ$ plane) are given by:

$$E_\theta = \frac{\sin\left(\frac{k_0 \Delta L \sin \theta}{2}\right)}{\frac{k_0 \Delta L \sin \theta}{2}} \cos\left(\frac{k_0 (L + \Delta L) \sin \theta}{2}\right) \quad (7.8)$$

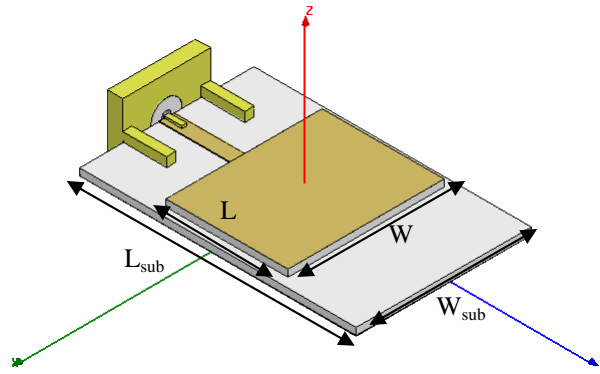
$$E_\phi = \frac{\sin\left(\frac{k_0 W_e \sin \theta}{2}\right)}{\frac{k_0 W_e \sin \theta}{2}} \cos \theta \quad (7.9)$$

Where θ is the angle measured from the broadside of the patch and $k_0 = 2\pi/\lambda$. For thin substrates ($h \ll \lambda$) equation 7.8 reduces to:

$$E_\theta = \cos\left(\frac{k_0 (L + \Delta L) \sin \theta}{2}\right) \quad (7.10)$$

7.3 Simulated Results

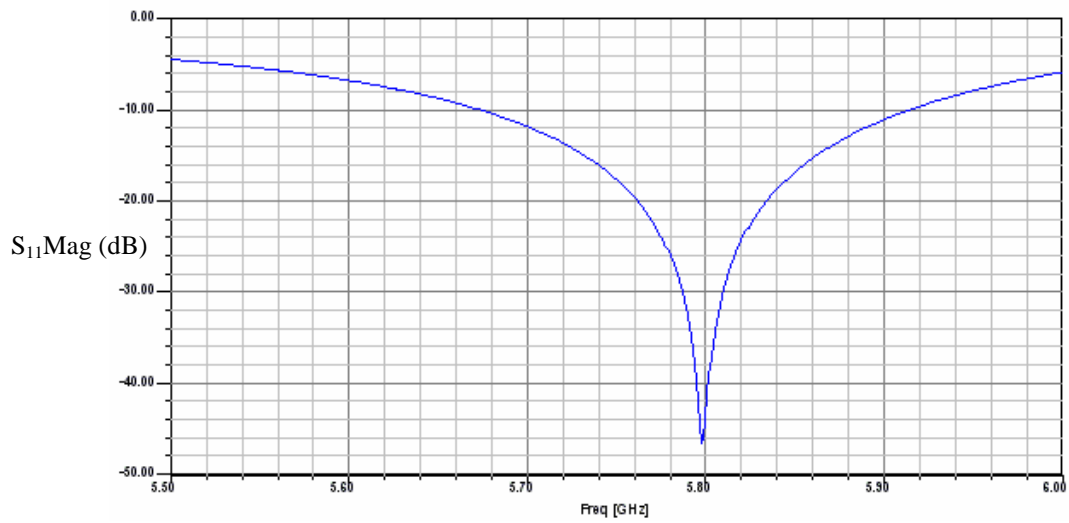
Using the design equations given in section 7.1, a 5.8 GHz patch antenna was created in HFSS. Usually, the first design is not fully optimised and it is normal to adjust the model to further refine the dimensions. The final dimensions are shown in Figure 7.4. The patch is constructed on Rogers 4350 high frequency laminate board of thickness 0.762mm, relative permittivity of 3.48, and a metallization layer of 35 μ m of copper.



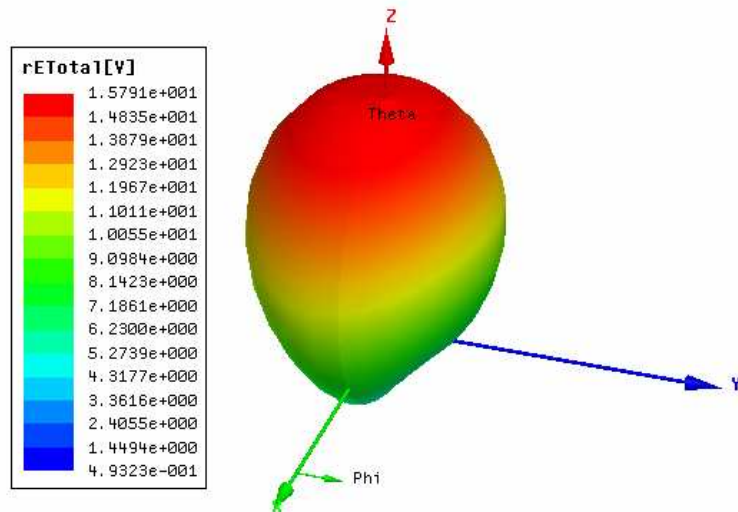
L	W	L _{sub}	W _{sub}
13.225 mm	16.9 mm	40 mm	19 mm

Figure 7.4. HFSS model of 5.8 GHz patch antenna with final dimensions

The simulated results for S_{11} and the 3D E-field are shown in Figure 7.5.



(a)



(b)

Figure 7.5 Simulated results for (a) S_{11} and (b) 3D E-field

7.4 Testing antenna and redesign

Once the antenna has been fabricated two main investigations are carried out, S-parameters and radiation pattern measurement. The S-parameters were measured using an Agilent Vector Network Analyser (VNA). Figure 7.6 shows simulated and experimental results for the 5.8 GHz patch antenna.

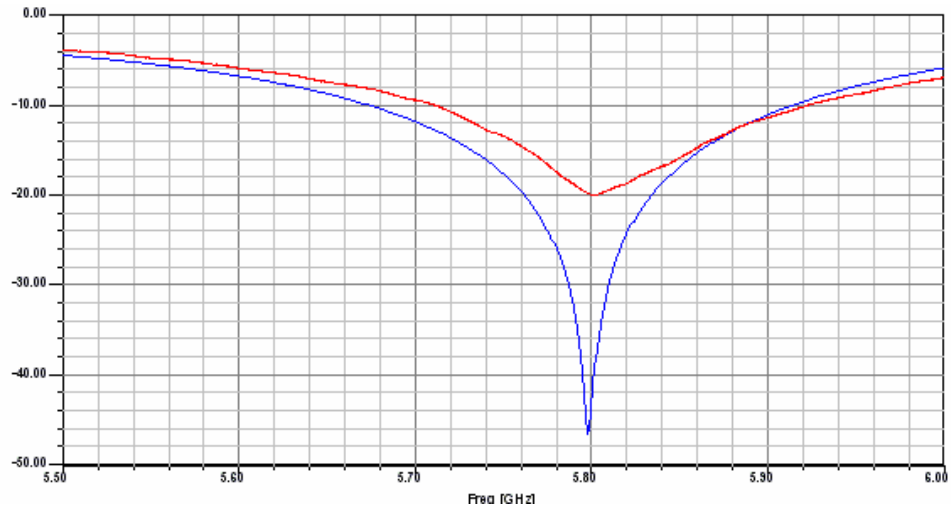


Figure 7.6. Simulated (blue) and experimental (red) results for S_{11}

Inspection of Figure 7.6 shows that both the simulated and experimental results are in agreement about the frequency of operation. However, there is quite a large discrepancy between the values of magnitude for S_{11} . When designing antennas, the performance of the experimental results can differ from the simulated results. This can usually be attributed to factors, such as design equation error, improper use of simulation tools, fabrication and test equipment error and interference from feed cables. If the frequency of design is greater than a few GHz then these errors become pronounced. As the simulation in the previous section did not take account of the test-cables, a model was created with a 10cm SMA cable attached to it. This is shown in Figure 7.7.

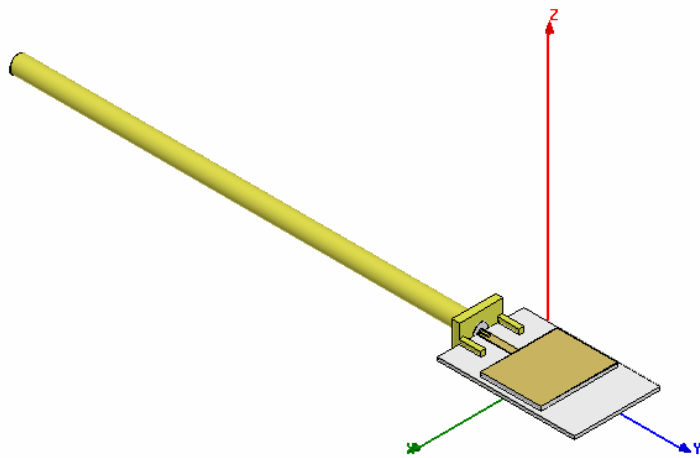


Figure 7.7. 5.8 GHz patch antenna with 10 cm SMA cable

Using HFSS it is possible to view the fields to allow for a full understanding of the operation of the antenna and cable. Figure 7.8 shows the surface current present on the cable and antenna.

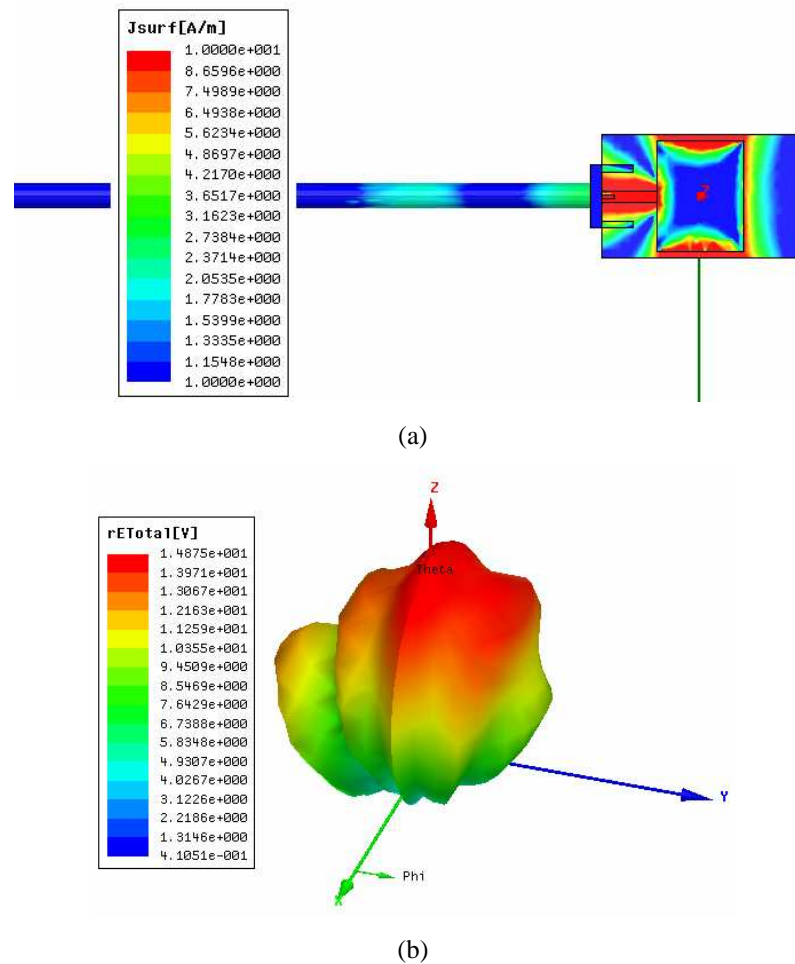


Figure 7.8. Surface current on 5.8 GHz patch antenna with 10 cm SMA cable

Inspection of the surface current revealed an interaction with the test cable. Analysis of the 3D E-field, shown in Figure 7.8 (b), reveals the impact that the test cable has on the radiation pattern. However, the simulated and experimental results for S_{11} are in much better agreement and are shown in Figure 7.9. This verifies the impact of the test-cable.

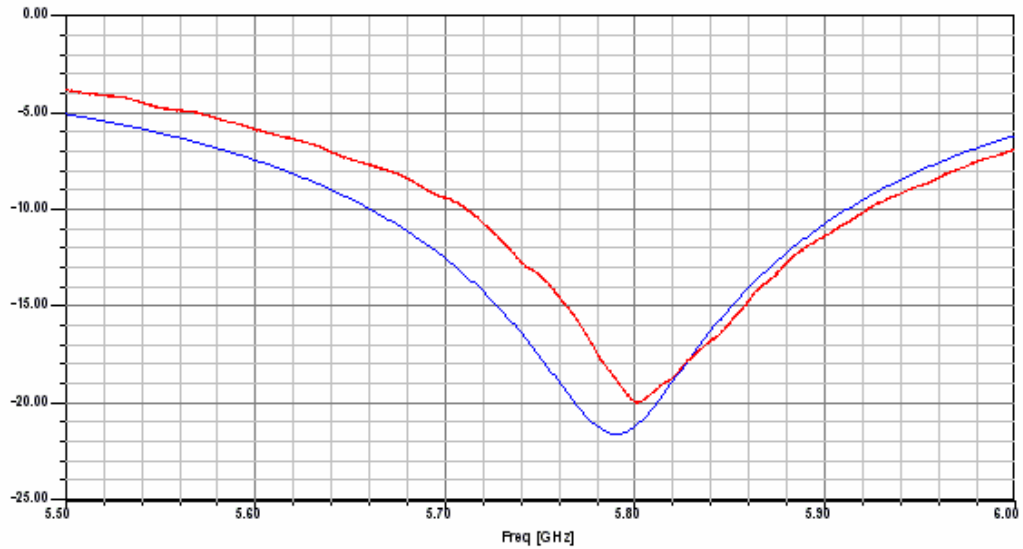
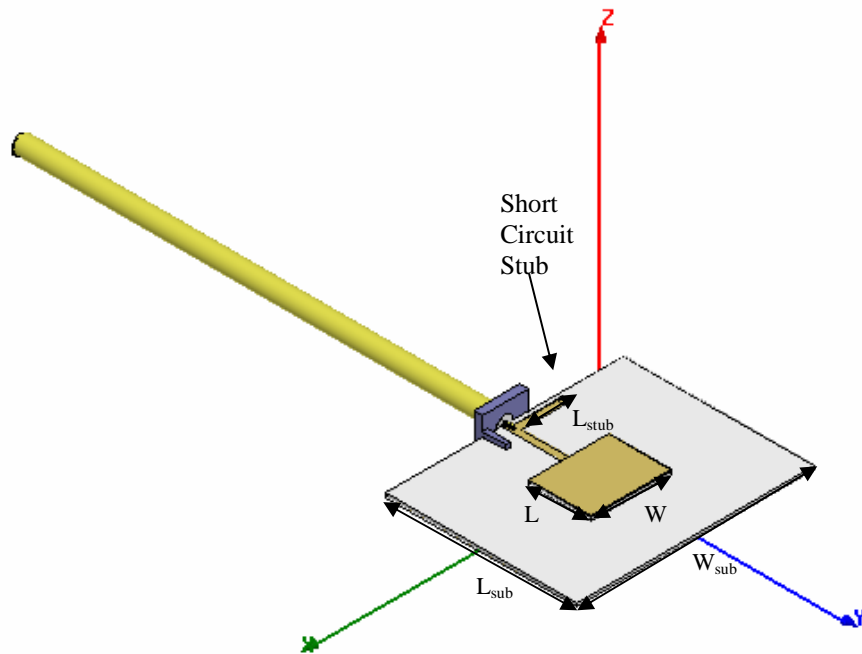


Figure 7.9. Simulated (blue) and experimental (red) results for S_{11}

To try to improve the performance of the antenna, a short-circuit-matching stub was inserted into the design to improve the matching. The stub acts as a form of conjugate matching [6], which results in a maximum power transfer to and from the antenna. The HFSS model is shown in Figure 7.10.



L	W	L_{sub}	W_{sub}	L_{stub}
13.18 mm	16.9 mm	40 mm	50 mm	8.5 mm → 9.5mm

Figure 7.10 Geometrical layout of 5.8 GHz patch antenna with short circuit stub

To investigate the impact of the stub a HFSS, parametric analysis was carried out. This involved varying the length to obtain the best match. Figure 7.11 shows the effect of varying the stub length.

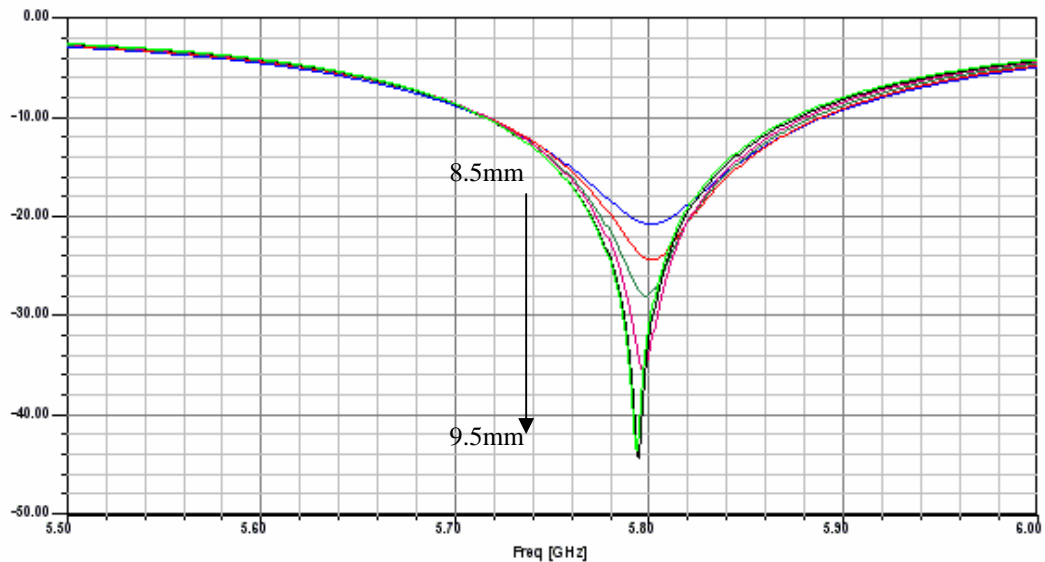


Figure 7.11. Effect of varying short circuit stub length on S_{11} .

The length is varied from 8.5mm to 9.5mm.

The manufacturing process for the short circuit stub involved drilling a via through the substrate. As this was done by hand, it was difficult to get the via positioned exactly 9.5mm along the short circuit stub. The experimental result for S_{11} , shown in Figure 7.12, suggests it was closer to 8.5mm.

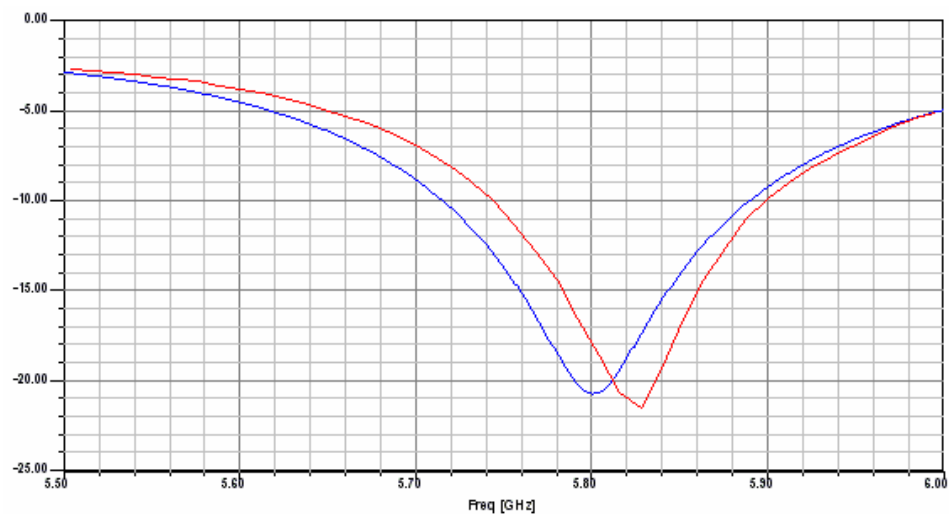


Figure 7.12. Simulated (blue), $L=8.5\text{mm}$, and experimental (red) results for S_{11}

The agreement between simulated and experimental results for S_{11} is good. The impact of the stub on reducing the leakage current present on the cable is shown in Figure 7.13.

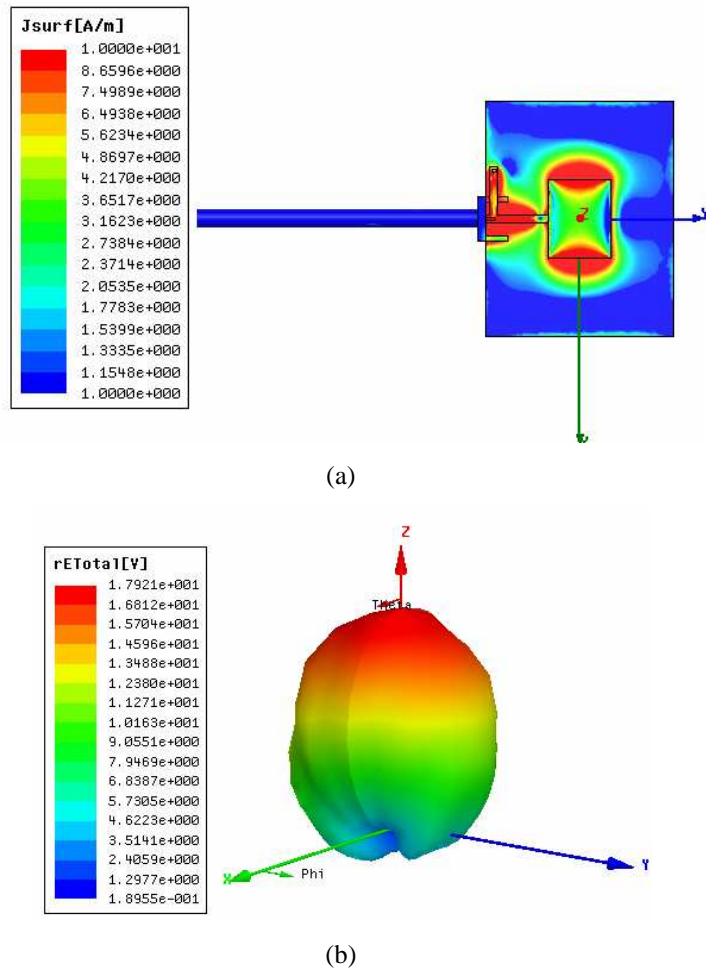
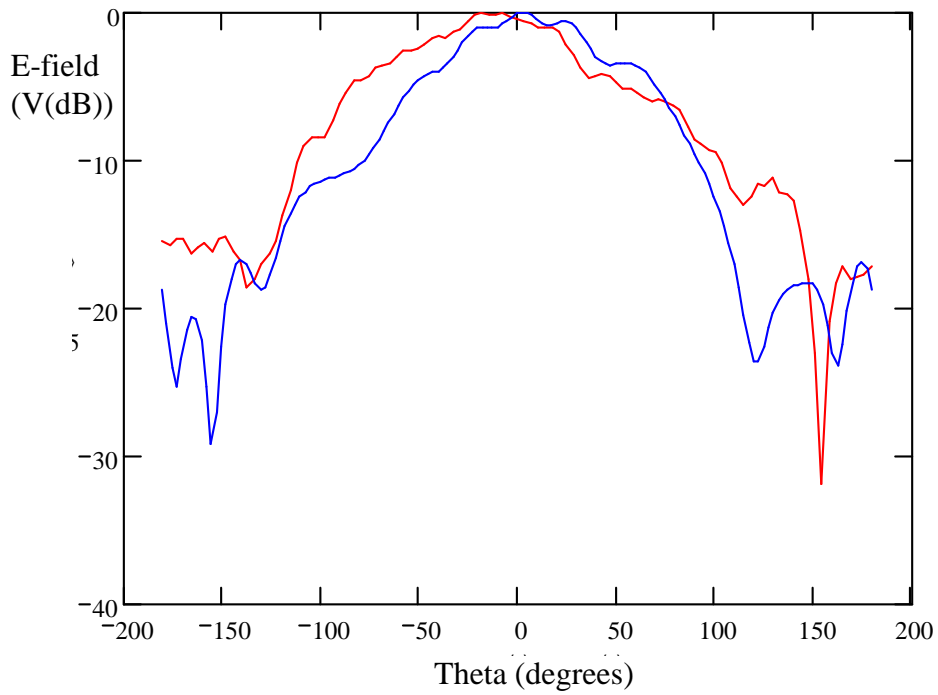
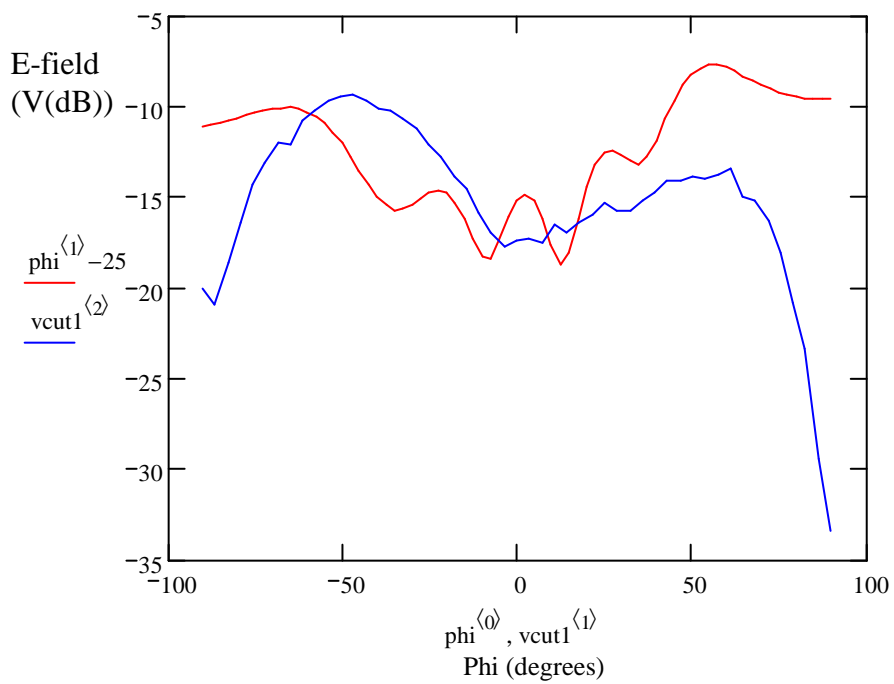


Figure 7.13. Simulated results for 5.8 GHz antenna with short circuit stub ($L=8.5\text{mm}$)
 (a) Surface current (b) 3D E-field pattern

Inspection of the results for Figure 7.13, when compared to Figure 7.8, shows a marked improvement in terms of radiation pattern consistency and reduction of leakage current. However, an analysis of the radiation pattern appears to show some surface current present. The experimental results obtained in the anechoic chamber for the radiation pattern are shown in Figure 7.14.



(a)



(b)

Figure 7.14. Experimental radiation plots (a) horizontal cuts; red = principle cut; blue = simulated
(b) vertical cuts; red = principle cut; blue = simulated

The plots obtained are from the near-field data. The data obtained for the far-field, which is obtained via a Fourier transform, was extremely noisy. As the apparatus had been commissioned just before the end of the research discussed in

this thesis, and a full familiarity was not obtained, the exact cause of the distortion is unknown.

Inspection of the plots displayed in Figure 7.14 (a) show excellent agreement between the simulated and experimental values for the principal cut. The plots in Figure 7.14 (b) are not in such close agreement as those shown in Figure 7.14 (a) but still show a drop in signal level at $\phi = 0^\circ$. Although the near-field data is used to analyse the fields generated by the antenna, the plots in Figure 7.14 demonstrate that the near-field data, from the anechoic chamber, can be used to extract useful data.

HFSS, combined with an awareness of the limitations of the manufacturing process, the test equipment and interaction with surrounding bodies such as cables, can accurately model 3D electromagnetic structures. Armed with this knowledge of the difficulties associated with the simulation, antennas can be modelled. The following chapters will now present the work carried out into the research of various antenna structures for wireless sensor networks.

8. Ultra-Wide Band (UWB) Antennas

The overall aim of this chapter is to discuss Ultra-wideband architectures, the key requirements for the Speckled Computing Consortium with respect to UWB, and the UWB antennas designed, manufactured and tested during this project.

UWB antennas can be split into two classes, large and directional, and small and omni-directional. An example of each is discussed. Typical performance indicators such as return loss, radiation patterns and impulse response will also be discussed.

8.1 UWB Architecture

UWB is defined as any radio technology that occupies greater than 500 MHz of bandwidth, or greater than 25% of the operating centre frequency. In contrast, most narrowband systems occupy a bandwidth of less than 10% of their operating frequency. UWB radio is the term used to describe a technology that is also known as "carrier-free", or "impulse radio". The basic concept of UWB radio is to transmit and receive an extremely short duration burst of radio frequency (RF) energy – typically a few tenths of picoseconds to a few nanoseconds in duration. The advantage of this approach, compared to conventional narrowband systems, is that the signal is transmitted over a very large frequency range (i.e. very short pulse) and a signal with a very low spectral density can be received. The difference of this technology over conventional narrowband systems is illustrated in Figure 8.1.

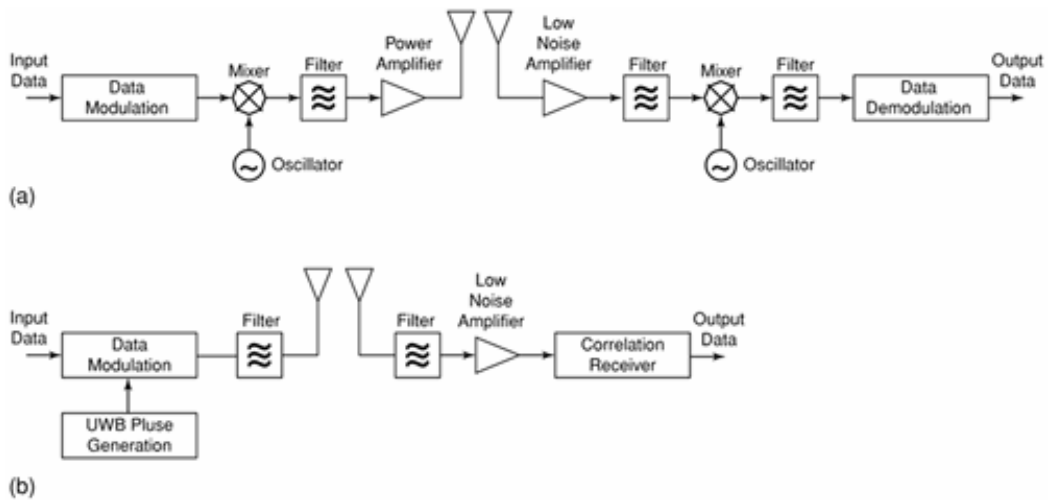


Figure 8.1 Comparison of (a) Narrowband and (b) UWB architectures.

UWB removes the complex up-converting and down-converting stages of narrowband radio, as shown by Figure 8.1. In effect, it simplifies the architecture, which should result in lower power consumption. Other advantages of the UWB approach are its potential to offer secure communications, resistance to multi-path and high data rates [1]. A modulation scheme that can be used for UWB is pulse position modulation (PPM) [2]. PPM is achieved by varying the position of a pulse in time and/or its polarity. The following section looks at some important requirements and some key performance indicators of UWB antennas.

8.2 Key requirements for UWB antennas

The key requirements that should be considered are as follows:

1. All of the parameters described in Chapter 4 i.e. pattern, gain efficiency etc. must be considered when designing any type of antenna that is part of a RF-front end. However, UWB antennas have additional design challenges. For example, as the name suggests, the antenna must operate over a large bandwidth when compared to narrowband antennas. The bandwidth is specified by both the Federal Communications Commission (FCC) and the Office of Communications (OFCOM) as 3.1 to 10.6 GHz; hence the antenna must achieve an impedance bandwidth of 7.5 GHz.

2. Another important requirement is group delay. Group delay is defined as the rate of change of the total phase shift, θ , with respect to the angular frequency, ω , as shown in Equation 8.1.

$$\text{Group delay} = \frac{d(\theta)}{d(\omega)} \quad (8.1)$$

If the phase is linear throughout the bandwidth then the group delay is constant throughout the bandwidth. Group delay can then be used as an indicator to show how well a pulse will be transmitted with consideration of distortion and dispersion. Normally, group delay is not considered in narrowband antenna design because linear phase is normally quite easy to achieve over a narrow band. Generally, if the group delay is in the tens of nano-seconds range, or less the performance is acceptable [3] [4].

3. The radiation pattern is an extremely important requirement for UWB antennas. For wireless sensor network applications, it is desirable to have an omni-directional pattern so orientation of the transmitter/receiver is not as important. As the antenna operates over a large bandwidth, its pattern at the low frequency cut-off (3.1 GHz) is different to that of the pattern at the higher frequency end (10.6 GHz), although good design can minimise this effect.

4. There are several other key requirements that are desirable for UWB antennas and are summarised below:

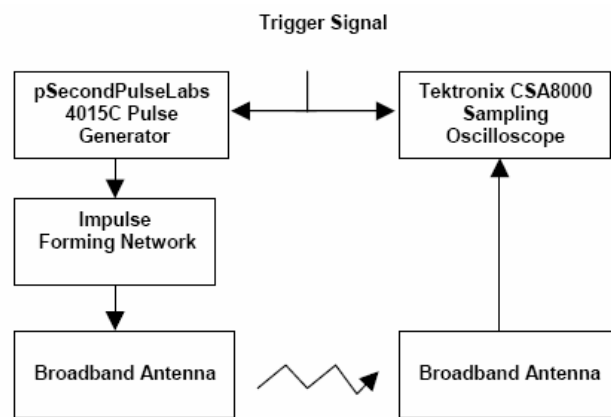
- Compactness – Size is critical in terms of cost, as well as achieving the ultimate aim of 5mm^3 for this project.
- Planar – Ease of integration into monolithic circuits.
- Good VSWR (<2) – This is required across the whole band of operation so as to maintain good matching and efficient operation.
- Constant Gain – This is desirable across the whole band of operation because the signal is transmitted instantaneously across the whole (or a large part) of the frequency band (3.1 – 10.6 GHz).

8.3 Initial designs of UWB Antennas

The theory and design of UWB antennas is not as well established as narrowband antennas. However, many designs that have been validated by experimentation and the results published [5]. Their performance has been evaluated for pulse transmission and reception, as well as return loss, group delay and radiation pattern. Two types of antenna, the Vivaldi [6] and a coplanar waveguide (CPW)-fed monopole [7] were evaluated using a test-system developed at Glasgow in the first year of the project and were published [8]. This evaluation was carried out as follows.

8.3.1 UWB test system

The test system was used for investigating modulation formats, channel characteristics, as well as the performance of the antennas in sending and receiving pulses. The test system developed used bench equipment and readily available materials. It consisted of a Tektronix CSA8000 sampling oscilloscope, a Pulse Labs 4015C pulse generator with a 4015 pulse head, an impulse-forming network (IFN 5208) and two broadband antennas for sending and receiving pulses. The basic block diagram of the test system is given in Figure 8.2.



(a)

Figure 8.2 Basic block diagram of the test system.

Shown in Figure 8.3 is the signal before it is propagated through the antennas under test, which are in a back-to-back configuration.

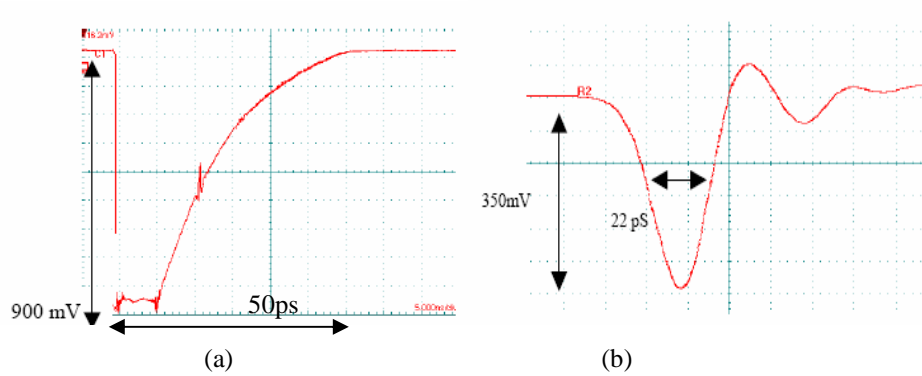


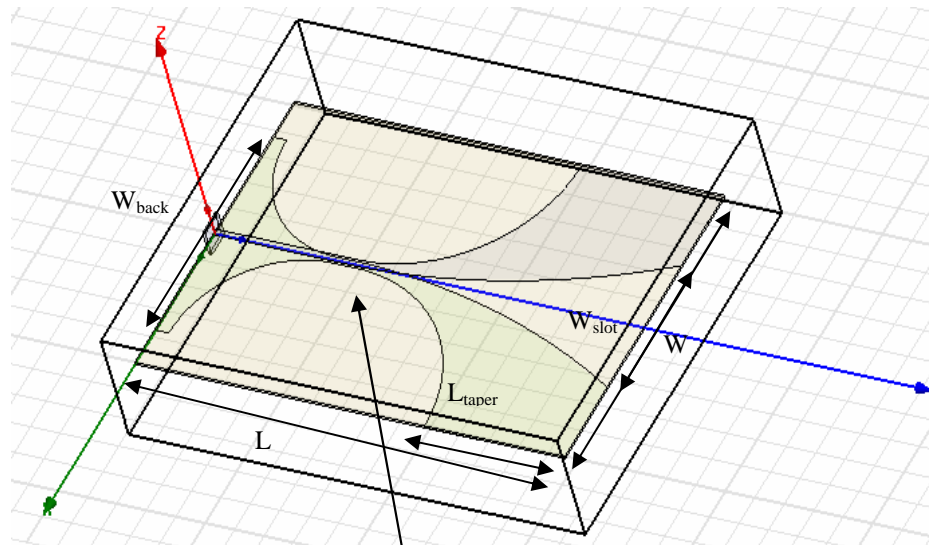
Figure 8.3 (a) Output waveform from 4015C pulser with 10x attenuation (b) Output waveform after the impulse forming network stage.

Return Loss measurements of the various UWB antennas were measured using a HP8510 Vector Network Analyser (VNA).

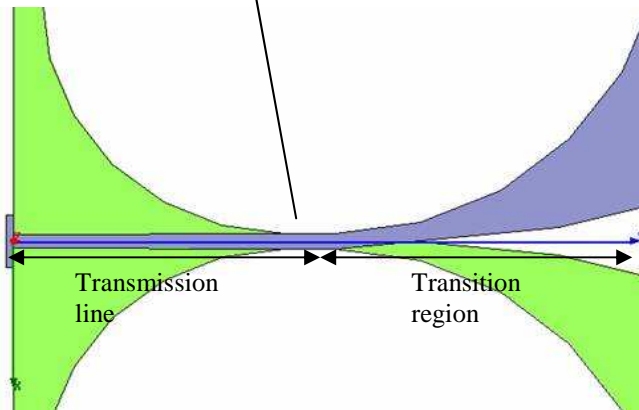
8.3.2 The Vivaldi Antenna

The Vivaldi antenna was first described and characterised in 1979 by Gibson [6]. It is a wideband antenna that has been used extensively in radar applications as part of arrays and ground penetrating applications [9]. More recently, the Vivaldi antenna has been identified as being suitable for UWB communications [10]. With increasing interest in UWB as a viable radio architecture, the Vivaldi antenna has attracted interest due to its theoretically infinite bandwidth. It is a directional antenna with an end-fire characteristic.

The Vivaldi antenna designed in this project was constructed on a copper-clad duroid substrate with a permittivity (ϵ_r) of 3.48 and a substrate thickness of 1.524 mm. The antenna was designed and verified by simulation using HFSS. A schematic diagram of the antenna is shown in Figure 8.4.



(a)



(b)

L	W	W_{back}	L_{taper}	W_{slot}
292.1mm	203.2 mm	150 mm	96.32 mm	93.75 mm

Figure 8.4. (a) Schematic of Vivaldi antenna designed in this project schematic. Length = 292.1mm, Width = 203.2 mm. (b) Magnified view of transition

As the radiating element of the Vivaldi antenna is a balanced structure, it was important to create a balun to provide a match between the 50Ω co-axial input and the antenna. The balun consists of a 50Ω microstrip to parallel plate transmission line, which tapers into a slotline configuration, which then feeds the radiating element. Figure 3.4 from chapter 3 shows the manipulation of the fields in the balun.

To help illustrate the Vivaldi antenna as a transition device between a guided wave and free space, HFSS was used to plot the electric field over the antenna. This is shown in Figure 8.5.

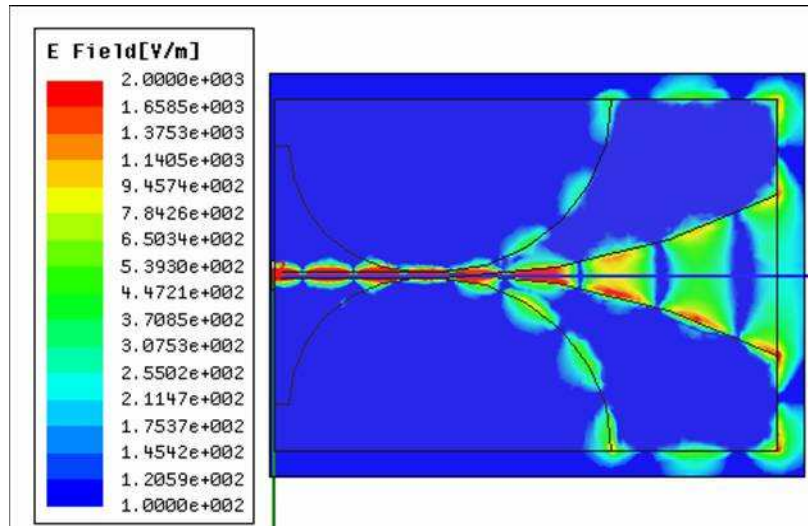


Figure 8.5. Plan view of Vivaldi Antenna showing the magnitude of the E-field (V/m)

A comparison of the simulated and experimental reflection coefficients, S_{11} , is shown in Figure 8.6.

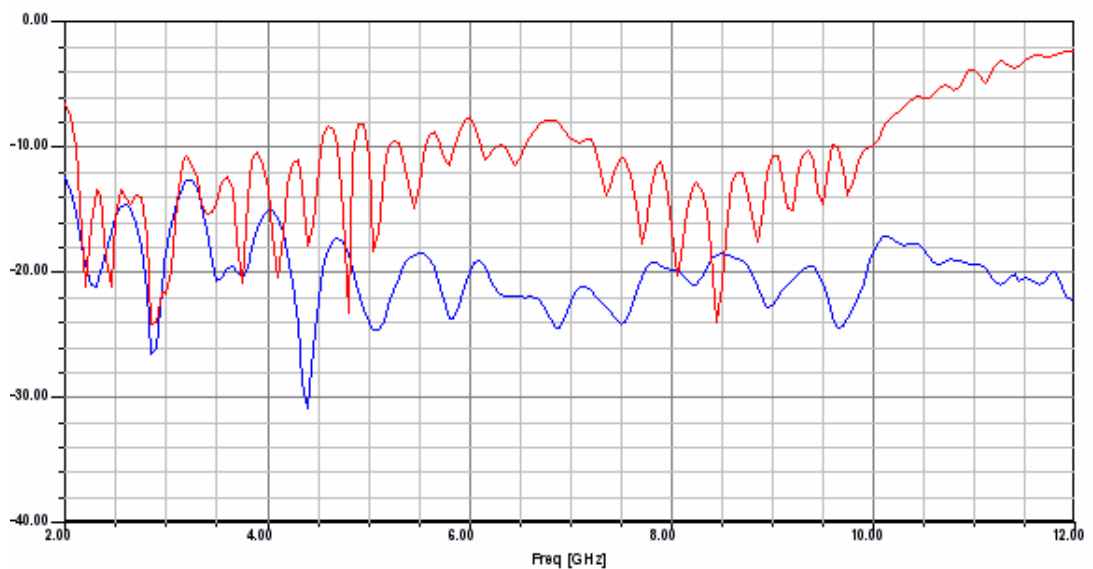


Figure 8.6. Simulated (blue) and experimental (red) S_{11} for Vivaldi antenna

Figure 8.6 shows there is relatively poor correlation between the simulated and experimental results. The reasons for this are considered to be as follows. From a simulation point of view, the antenna was electrically very large. This caused problems in trying to get an accurate mesh to model the antenna properly. From an experimental perspective there were problems in manufacturing the antenna. To achieve the correct substrate height, 1.542mm, two separate substrates of 0.762 mm were used. As a result, there was misalignment between the top and bottom elements due to gluing the substrates together. The height of 1.524mm was necessary to smooth the transition from microstrip to parallel plate. For substrate height of 1.524mm and line width of 1.9mm the characteristic impedance was 50Ω for both the microstrip and parallel plate.

To determine the radiation properties of the Vivaldi antennas two identical antennas were separated by 20cm and the transmission response measured, as shown in Figure 8.7.

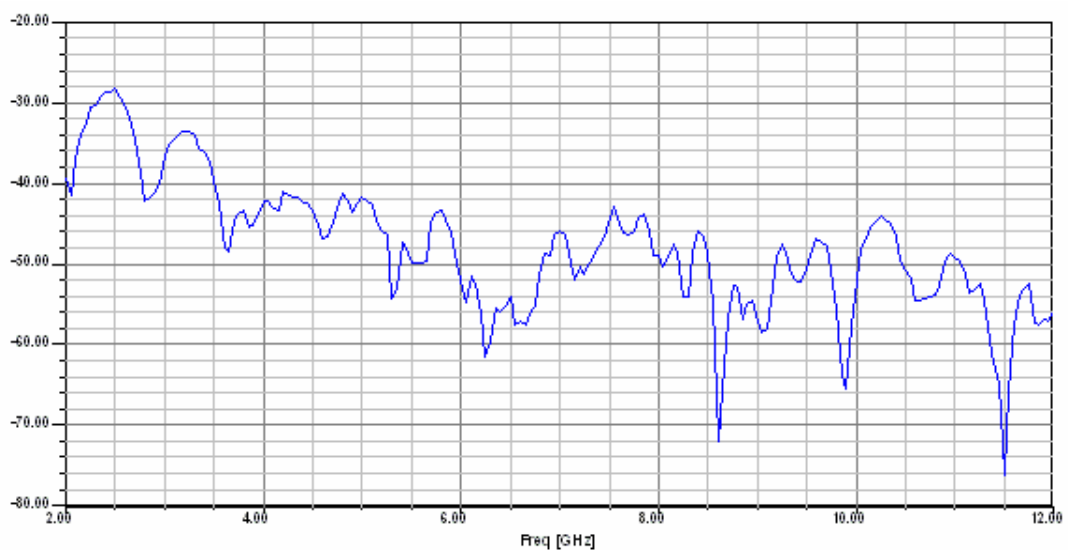


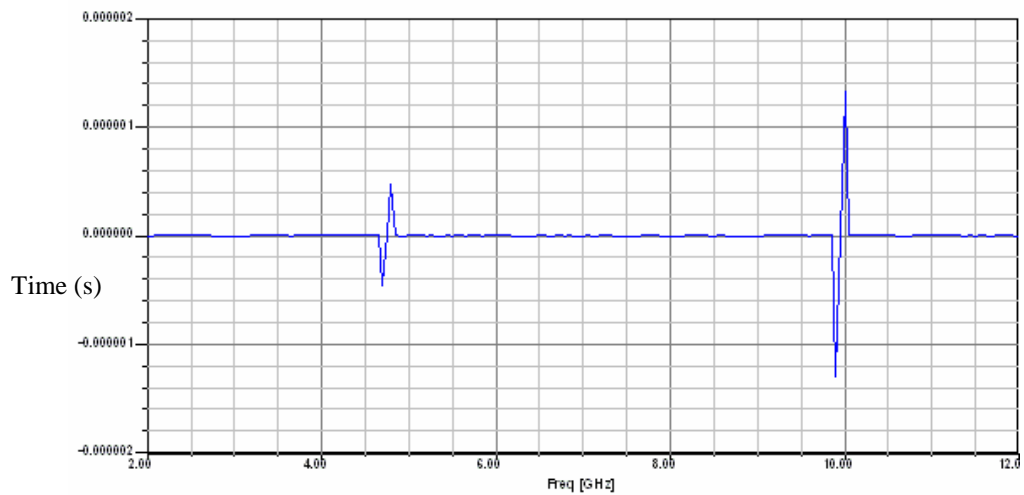
Figure 8.7. Transmission response (S_{21}) for Vivaldi.

Distance between antennas =20 cm.

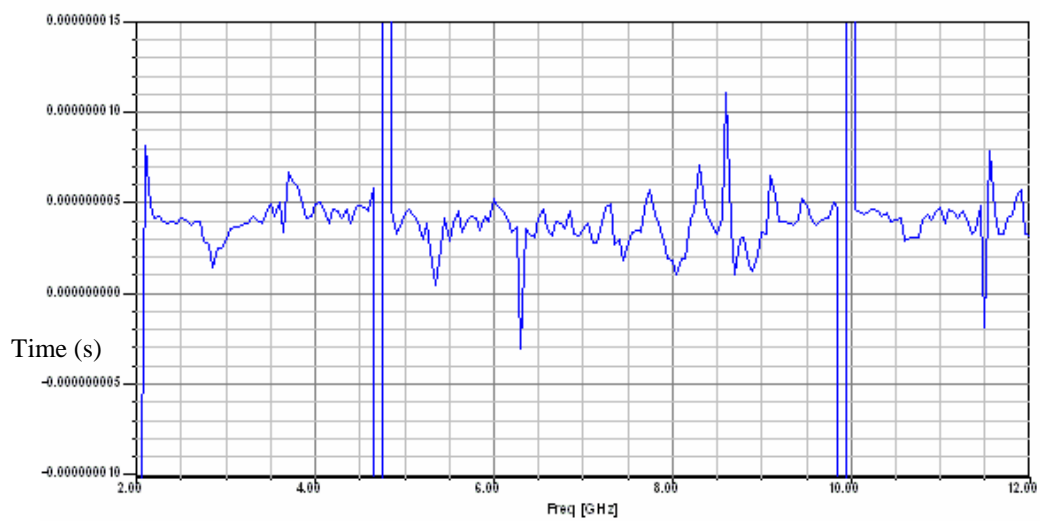
The results for the transmission response are disappointing as there is quite a high loss for such a short distance, especially since the gain of the antenna should be around 10 dBi. However, the transmission is not linear and shows a high

transmission loss; this may be due to the Vivaldi operating in the reactive near-field boundary, which occurs at 31.4 cm.

As stated in section 8.2, it is desirable to have a constant group delay, as this can indicate the performance of the antenna for sending and receiving pulses. As shown in Figure 8.6, there are a high number of modes present over the operational bandwidth of the antenna. As a result, a phase shift is expected; therefore linear phase cannot be attained over the frequency bandwidth. Figure 8.8 shows the experimental results for group delay obtained from the transmission response.



(a)

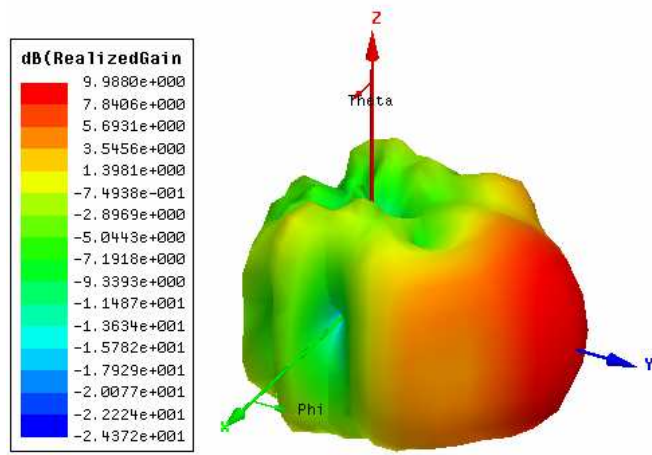


(b)

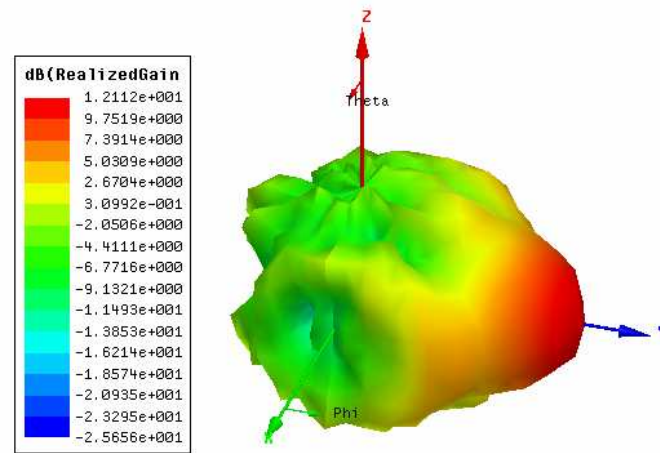
Figure 8.8. (a) Experimental group delay for Vivaldi antenna (b) magnified view for group delay
Distance between antennas = 20 cm.

Apart from the two sharp spikes at 4.8 and 10 GHz, the group delay response is linear with a maximum variation of 10 ns. The spikes are a result of some non-linearity in the system as yet undetected. Acceptable group delay performance is if the variation is in the tens of nano-seconds or less, range.

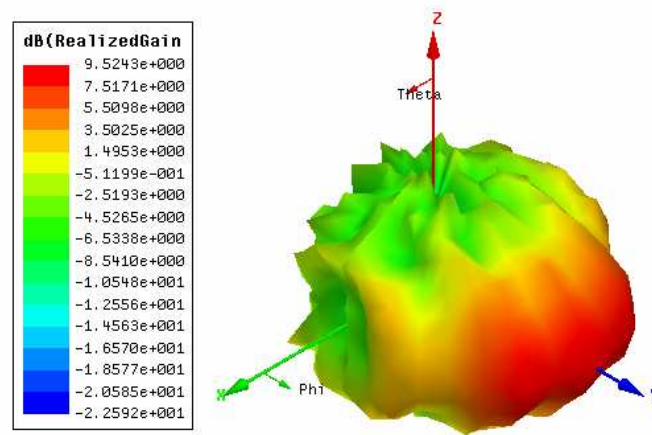
As mentioned at the start of this section, the Vivaldi is an end-fire antenna, which as the name suggests, radiates the main beam out from the end of the antenna. Analysing the radiation pattern over the frequency bandwidth shows the Vivaldi maintains a highly directive pattern. For point-to-point communication, this can be desirable, but for a wireless sensor network application where the orientation of the transmitter is not known, it is desirable to have an omni-directional radiation pattern. The simulated radiation patterns for 3, 6 and 9 GHz are shown in Figure 8.9. The x,y,z coordinates correspond with those in Figure 8.4 (a).



(a)



(b)



(c)

Figure 8.9. Simulated Vivaldi antenna 3D radiation (Gain (dB)) patterns for (a) 3 GHz (b) 6 GHz and (c) 9 GHz

The waveform in the previous Figure 8.3 (b) was used as the input to the transmit antenna and the pulse received is shown in Figure 8.10.

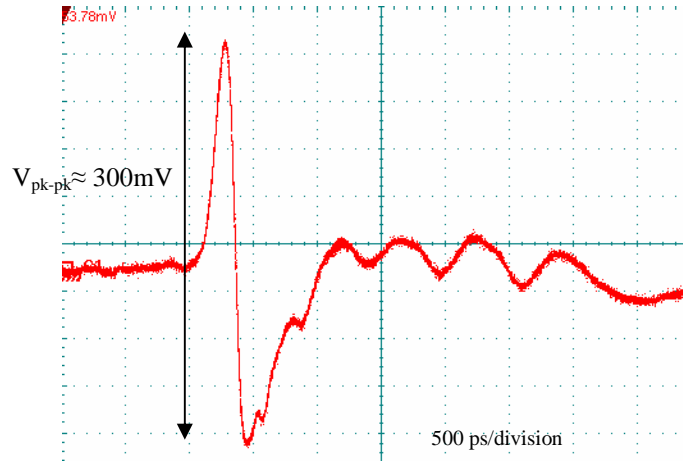


Figure 8.10. Received pulse for Vivaldi antenna.

The overall results obtained for the Vivaldi were considered to be favourable towards the use of UWB. While it did not have an omni-directional radiation pattern, nor small size (30cm x 18cm), the results for pulse transmission were good as it transmitted a pulse with low dispersion. Possible reasons behind the low pulse dispersion were:

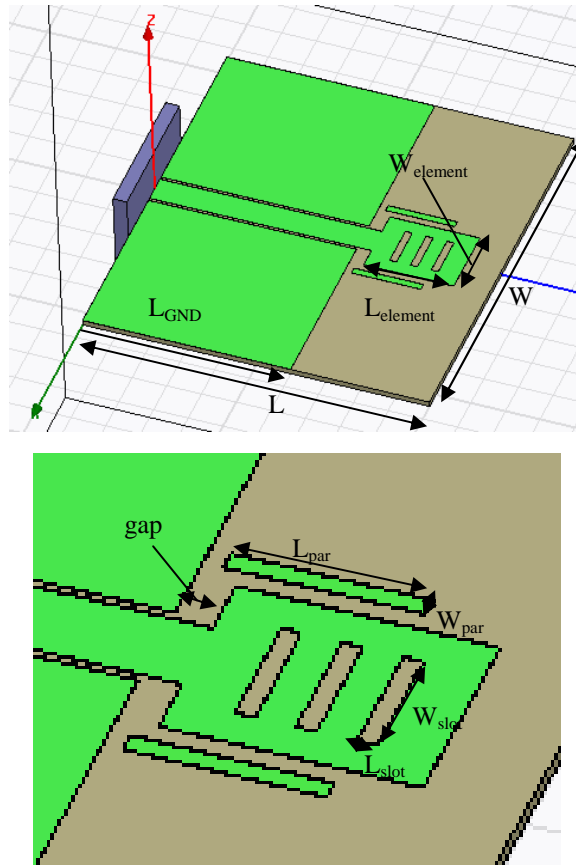
- good group delay
- constant radiation pattern over the operational band in the direction of transmission i.e. highly directive
- Acceptable impedance bandwidth over operational bandwidth

The Vivaldi meets many of the performance metrics stated in section 8.2 except compactness and an omni-directional radiation pattern. To compare the Vivaldi performance another UWB antenna was investigated that was small and omni-directional. This is discussed in the following section.

8.2.2 The CPW-fed Monopole Antenna

There have been many papers published on the use of planar monopoles for UWB applications [11]. The CPW-fed wideband monopole antenna presented by

Chung [7] is novel because of its compact size (50 x 50 mm) and apparent good performance. As a result, this antenna was chosen for analysis and results for S_{11} , group delay and radiation pattern were obtained. A schematic of the CPW-fed monopole antenna that was studied is shown in Figure 8.11.



L	W	W_{element}	L_{element}	L_{GND}
50 mm	50 mm	10 mm	13 mm	30 mm
gap	L_{par}	W_{par}	L_{slot}	W_{slot}
2 mm	10 mm	1 mm	1 mm	6 mm

Figure 8.11. The CPW-fed monopole.

The antenna was fabricated on a duroid substrate with a permittivity of 3.48. The radiating element is a rectangle with three slots cut into it and two strips placed on either side of the rectangle. The strips act as parasitic coupling elements, which provide improved matching over the operational bandwidth as a whole. This is achieved by the strips acting as complex RLC loads between the antenna feed and ground. The slots improve bandwidth by creating a larger current path at the

higher frequency end of the band, allowing higher order modes to resonate ‘in band’, hence improving the bandwidth.

The monopole is fed by CPW, which allows for potential ease of integration into any active circuitry. The antenna designed by Chung [7] was simulated using HFSS but did not yield similar results to those published. A possible reason behind this discrepancy was the characteristic impedance of the feed line, which was found to be 62Ω . This was corrected by altering the gap in the feed lines from $400\mu\text{m}$ to $260\mu\text{m}$. The simulation and experimental results for S_{11} are shown in Figure 8.12.

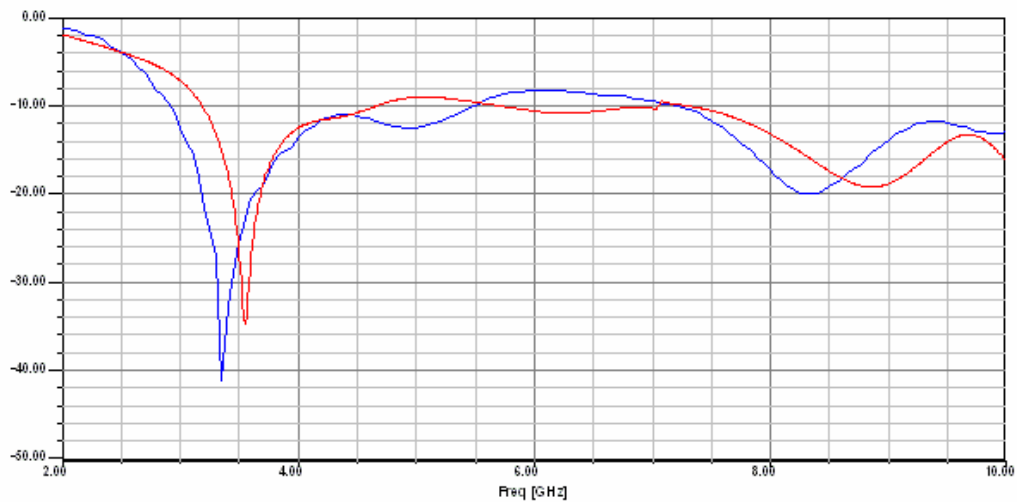


Figure 8.12. (a) Simulated (red) and (b) experimental (blue) S_{11} results for CPW-fed monopole

The results for simulated and experimental S_{11} were in better agreement than those of the Vivaldi antenna in Section 8.3.2. The reason behind this increase in accuracy is that the CPW-fed monopole is much smaller electrically, and, as a result, it is easier to apply a finer mesh when using HFSS, hence there is an increase in accuracy. The CPW monopole was much easier to fabricate as it only required one layer of metallization to be defined and, as result, led to good correlation between simulated and experimental results.

Even though there is good agreement between simulated and experimental results, the matching between 4.5 GHz and 6.25 GHz is not good enough to meet the

impedance bandwidth requirements. This is confirmed by the results for the transmission response, shown in Figure 8.13.

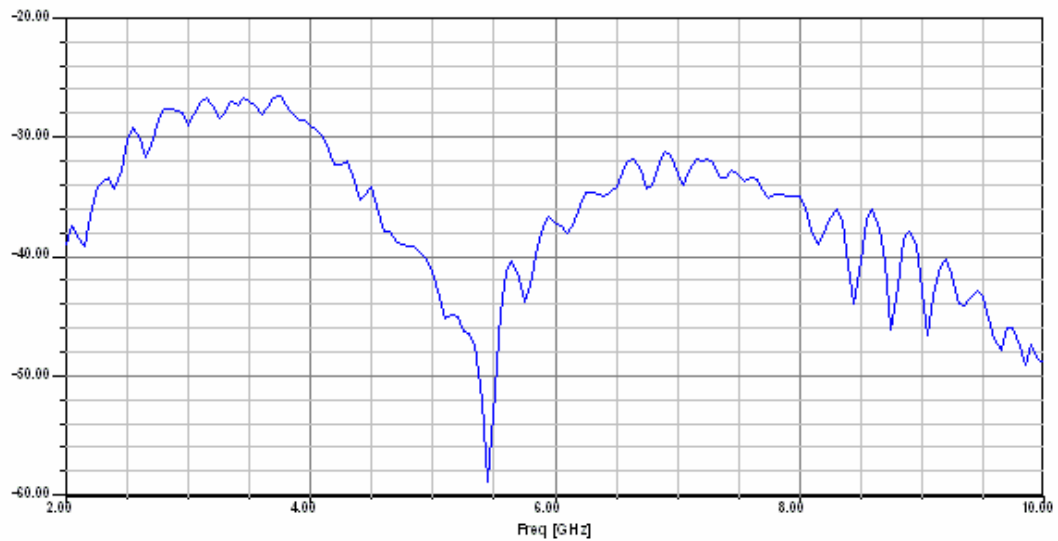


Figure 8.13. Transmission response (S_{21}) for CPW-monopole.
Distance between antennas =20 cm.

The CPW-monopole is basically a narrowband antenna modified for UWB operation. Analysis of the transmission response shows that the region between 5 and 6 GHz has a very large insertion loss. For good pulse transmission, it is desirable to have a linear transmission response otherwise pulse distortion will occur i.e. partial loss of the signal portion between 5 and 6 GHz.

Analysis of the group delay, shown in Figure 8.14, reveals that the group delay of the CPW monopoles group delay is comparable to that of the Vivaldi antenna. There are two large spikes in the operational band, one as expected between 5 and 6 GHz and the another occurring at 8.5 GHz, which is unexpected. Apart from these spikes, the maximum variation is 2 ns, which is a slightly improved performance over the Vivaldi.

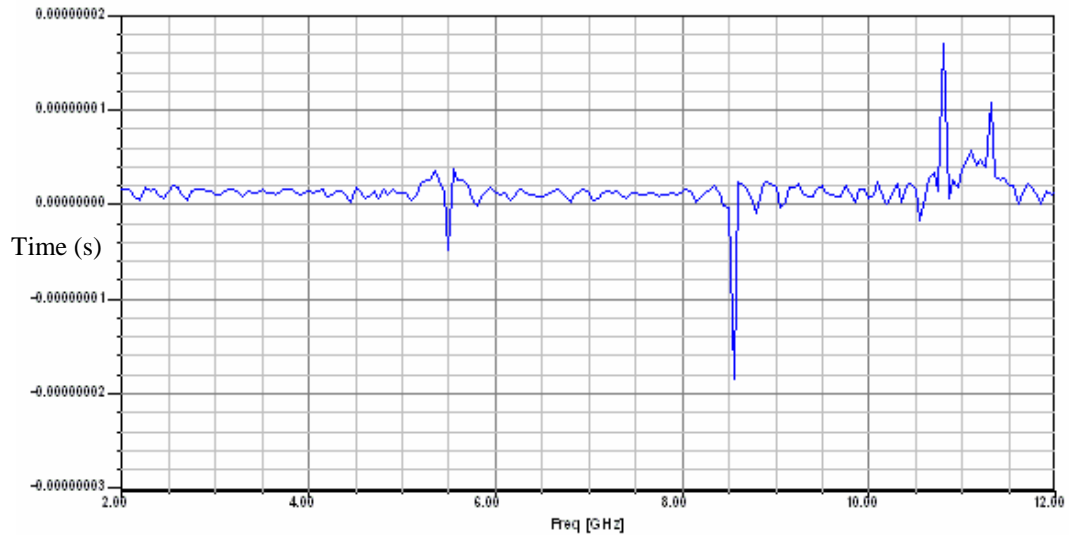


Figure 8.14. Experimental (blue) results for Group delay Vs frequency

The HFSS simulated radiation patterns for the CPW-fed monopole, shown in Figure 8.5, are the more omni-directional of the two antennas investigated in this section; Unlike the Vivaldi, the CPW-fed monopole yields a true omni-directional ‘doughnut’ pattern at the low end of the operational bandwidth. The change in the radiation pattern as the frequency is increased is due to the antenna becoming electrically larger ($> \lambda/2$). At 10 GHz the radiation pattern has equivalence with a 1.5λ monopole.

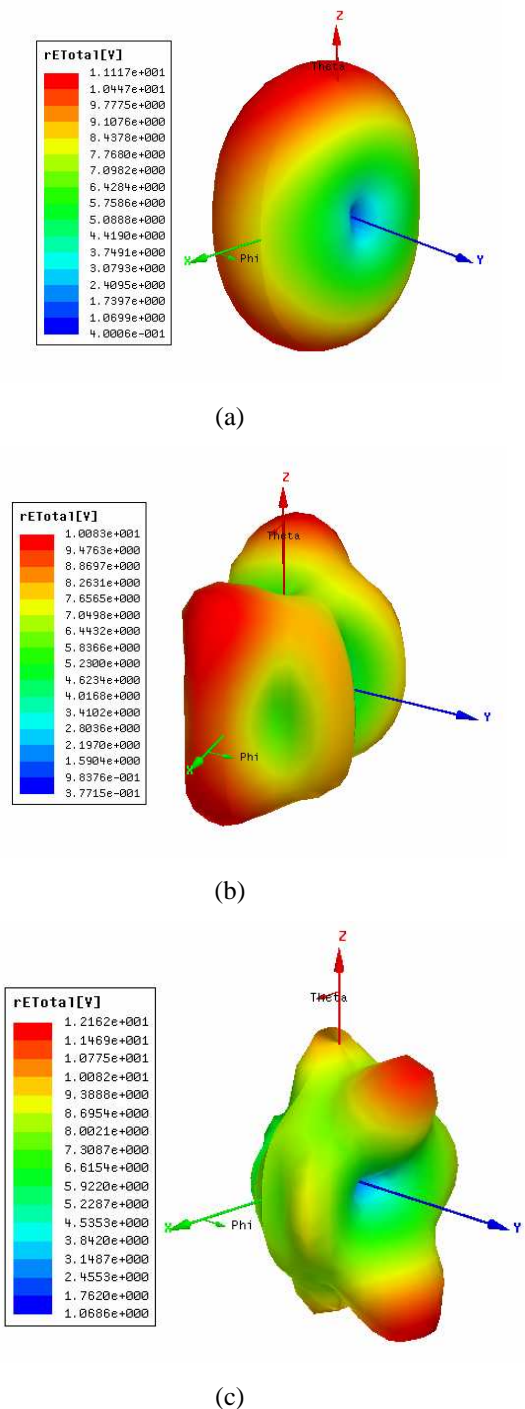


Figure 8.15. Simulated radiation patterns for (a) 3 GHz (b) 6 GHz and (c) 9 GHz

The CPW-fed monopole had worse performance in terms of pulse distortion. Inspection of the received pulse, shown in Figure 8.16, shows the effects of ‘ringing’. The reasons behind this are considered to be as follows:

- Large insertion loss in the middle of the band

- Non-uniform radiation pattern over the operational bandwidth resulting in variation of gain, which results in only certain portions of the signal being received

In an ideal situation, a UWB antenna would have a flat response with no sharp peaks over the impedance bandwidth, and an omni-directional pattern over the bandwidth. This would mean that the power being radiated from the antenna would be equal over the bandwidth, hence no distortion would occur. While the Vivaldi antenna described in Section 8.3.2 does not have an ideal flat response it still has a better pulse response due to its ability to send and receive the signal over the required bandwidth (i.e. a wider impedance bandwidth) and a constant radiation pattern in the direction of propagation.

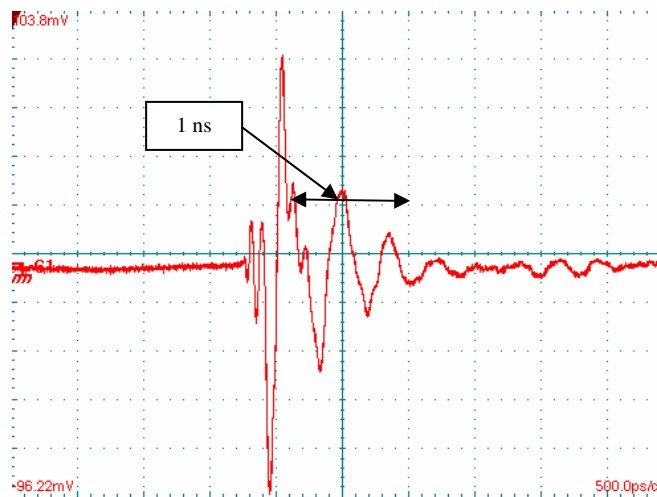


Figure 8.16. Pulse received by CPW-fed monopole

8.4 Initial UWB Evaluation

While there are many potential positives with UWB, such as reduced RF architecture complexity, there are a few drawbacks, particularly from the wireless-sensor networks perspective. These drawbacks include:

- **Antenna size:** due to the large bandwidth required (>500 MHz) the size of the antenna will not achieve the target size of 5mm^3 , even if moved to a much higher frequency.

- **Modulation:** there are problems trying to implement a PPM strategy with ubiquitous wireless sensor networks due to synchronisation issues. Implementing an OFDM modulation strategy, more typical in a contemporary UWB system, also introduces challenges, due to the requirement for a heterodyne system with local oscillators and mixers, which may consume significant amounts of power, thereby offsetting the perceived advantages of UWB.
- **Reduction of complexity:** initially it was thought that UWB would remove some of the extra stages from the radio architecture required for conventional systems. This was found not to be the case. To recover the pulse, there was a requirement for multiple amplifier stages and, as a result, UWB would have consumed more power than some conventional radio architectures.

The two antennas discussed in this chapter didn't fully meet the performance criteria outlined in section 8.2. Table 8.1 shows a comparison.

Antenna	Impedance Bandwidth	Groupdelay	Radiation Pattern		Compact	Planar	Pulse Transmission
			CG	Omni			
Vivaldi	No	Ok	Yes	No	No	Yes	Excellent
CPW-monopole	No	Good	No	Yes	Yes	Yes	Poor

Table 8.1 Antenna performance table. CG = Constant Gain

As a result, the drawbacks highlighted in this section, and the fact that UWB is still an emerging technology, it was felt that it would be more productive to investigate a more conventional narrowband antenna and use a narrowband system. However, there may still be an opportunity in the future for integrating some form of UWB into the Speckled Computing Consortium Specks.

9. A UWB channel modelling experiment

An important aspect of the Speckled Computing Consortium research is the opportunity to undertake interdisciplinary research. One such example was a UWB channel modelling experiment led by the Strathclyde University signal processing group. As the expertise of Strathclyde lay with signal processing and not antenna design, the onus fell on Glasgow to design a suitable antenna. The design criteria for the antenna was that it operated from 3.16 to 10.6 GHz, be omni-directional, have relatively standard gain and a good phase response over the band. As none of the antennas investigated in chapter 8 fully met the criteria, there was a need for a different type of antenna. The antenna chosen was the UWB dipole. The test system and design of the antennas will now be considered.

9.1 UWB test system

A channel can be modelled physically by calculating the various processes which modify the transmitted signal. For example, in wireless communications, the channel can be modelled by calculating reflection from every object in the environment. The channel modelling experiment carried out at Strathclyde University was to determine the impact on sending and receiving a UWB pulse of the antennas discussed in this chapter.

Figure 9.1 shows the block diagram of the test system, although this will be covered in greater detail in Section 9.6. For the transmission results discussed in this chapter, the antennas were placed 20 cm apart from each other, and both antennas elements were aligned so they were in boresight i.e. the direction of transmission was perpendicular to the antenna elements. All the antennas are operating outside the far-field boundary specified by $2D^2/\lambda$ except the antenna section 9.2.4 due to a large transmission line feed. Section 9.2.4 compares the field of a half-wavelength dipole to that of the antenna under investigation. The field plot is then used to evaluate whether or not the feed should be included in the maximum linear dimension, D , for the far-field boundary calculation.

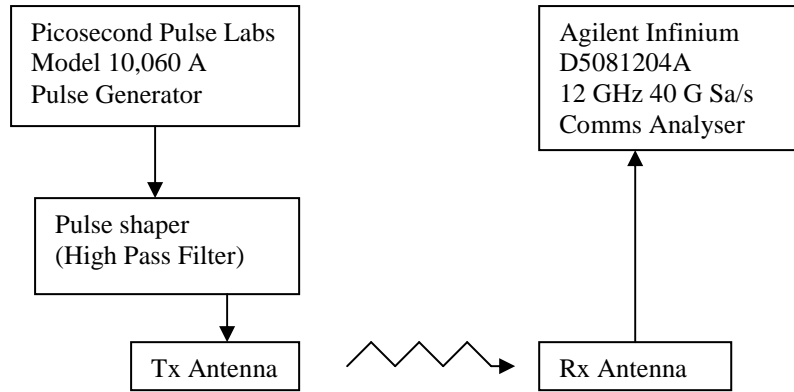


Figure 9.1 Block diagram for Strathclyde UWB test system

Also used in the experiments was an Agilent technologies N5230A 10 MHz – 20 GHz PNA series network analyser. This was used to obtain transmission and reflection coefficients for the antennas.

9.2 UWB dipole

In 2002, Schanz published a paper on a UWB planar elliptical dipole [1]. Since then, there have been many published papers on this class of antenna. The main consideration, apart from the shape, when designing UWB dipoles is the feed configuration into the antenna element. There are three potential feeding points for this antenna illustrated in Figure 9.2.

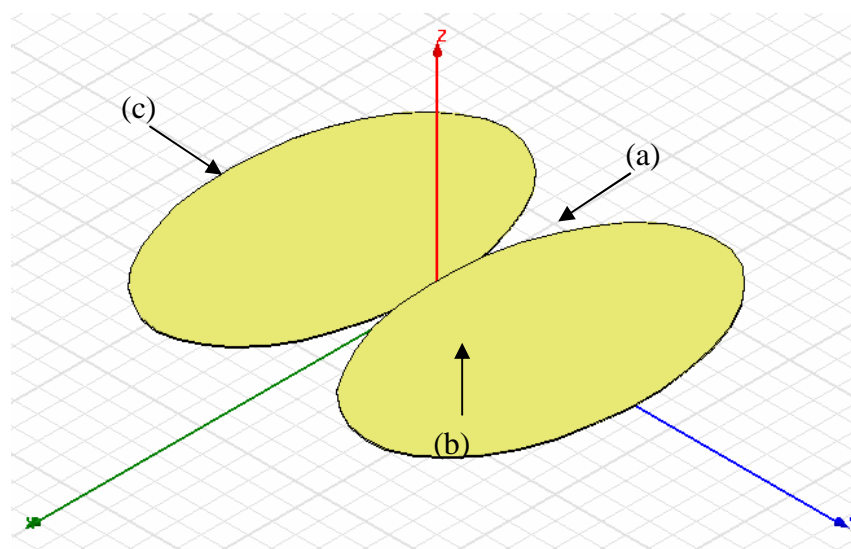


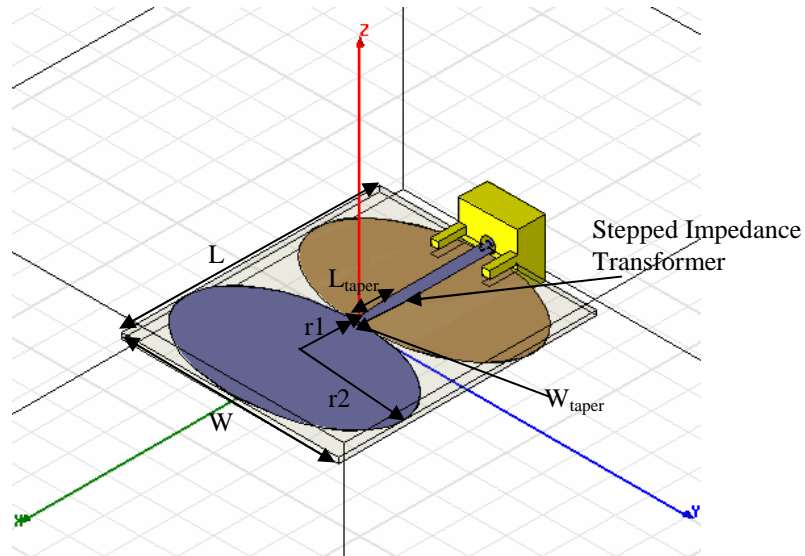
Figure 9.2. Elliptical dipole element with suggested feeding points (a) centre (b) bottom and (c) edge.

If the antenna is fed from position (a), typically using some form of slotline configuration, this results in the antenna having a very directional end-fire radiation pattern similar to the Vivaldi antenna. Feeding this way creates a travelling wave structure, as opposed to a standing wave resulting in end-fire operation.

In the paper that Schanz presented [1], the antenna is fed from the underside (b). If this feeding method is used, then the feed cable from the test system is in the main electric-field beam. To avoid this, an edge-fed configuration (c) was chosen for this work and is discussed further in the following section.

9.2.1 Microstrip Edge-fed UWB dipole

The first approach to designing the UWB dipole was to use a microstrip feed into the centre of the antenna from the edge. The correct microstrip mode could then be propagated using one of the elements as a ground plane. The arrangement was convenient as it orientated the antenna in such a manner that the feeding cables were outside of the main pattern. This also meant that the antenna was in the correct position for the test system. Included in the design was a stepped impedance transformer, which was placed just before the antenna terminals. This is shown in Figure 9.3.



L	W	r1	r2	L_{taper}	W_{taper}
35.25 mm	29.75 mm	8.75 mm	14.875 mm	5.25 mm	1 mm

Figure 9.3. Microstrip edge-fed UWB dipole with taper. The brown element is the ‘GND’ for the microstrip feed.

The impedance at the terminal of the antenna increased with frequency, typically from 73Ω to 80Ω over the operational band, so the addition of the transformer improved matching in the higher frequency ranges. The optimum length and the width of the taper were found using HFSS parametric analysis and found to be 5.3mm and 1.2mm, respectively. The final values were then implemented into the manufactured design. The simulated and experimental results for S_{11} are shown in Figure 9.4.

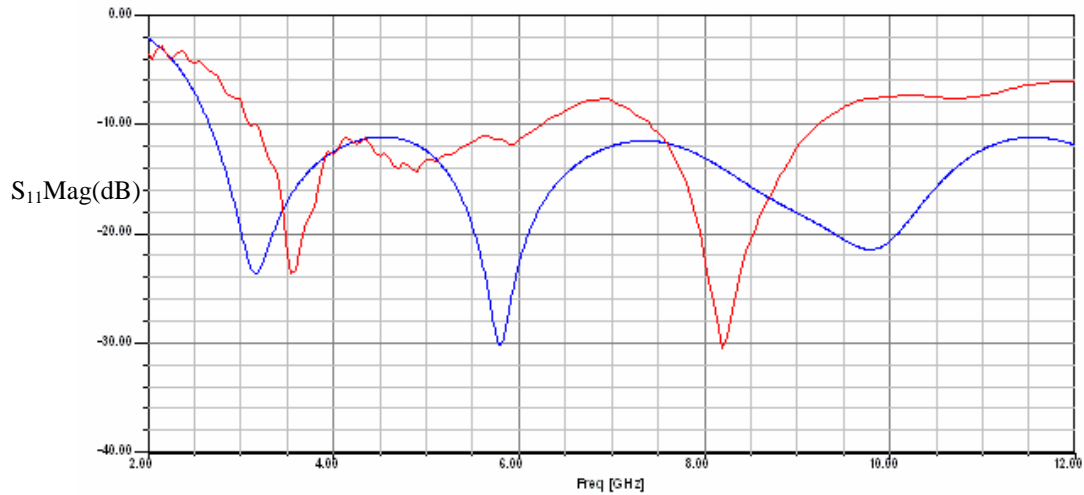


Figure 9.4. Simulated (blue) and experimental (red) results for S_{11} Vs. Frequency

The discrepancy in the results was traced to the impact of the cables used to connect the network analyser to the antenna. Although the cable was positioned out of the far-field radiation pattern it was almost certainly being excited by the reactive near-field. This is shown later in section 9.2.2.1. At the position indicated by Figure 9.1 (c) there was an area of high electric field, particularly at the lower end of the band. The electric field excites the leakage current along the length of cable, which means that the feed cable becomes part of the antenna and, as a result, increases the amount of modes present. The distortion on the plot in the frequency range from 2 to 6 GHz seen on the experimental S_{11} results is evidence of this effect. The effect is also seen in experimental results for phase, shown in Figure 9.5.

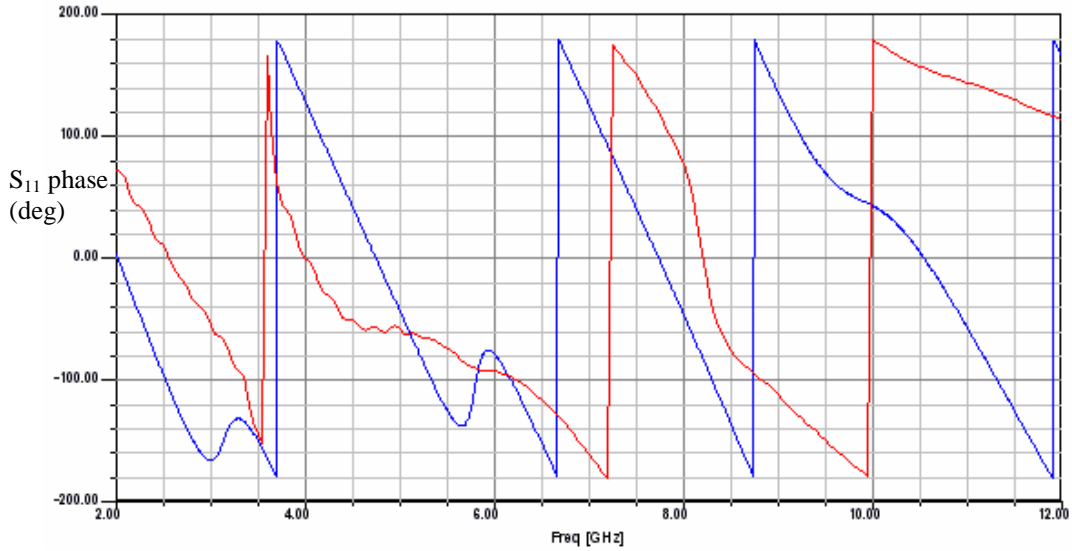


Figure 9.5. Microstrip-fed UWB dipole S_{11} phase results (i) simulated (blue) (ii) experimental (red)

The leakage current also appears to have a detrimental effect on the transmission response, as shown by Figure 9.6. Due to the orientation of the antennas, bore-sighted at 20 cm, the value of S_{21} would be expected to be approximately -25 dB at the lower end of the frequency band. A possible explanation to the discrepancy in the behaviour was attributed to the test cables.

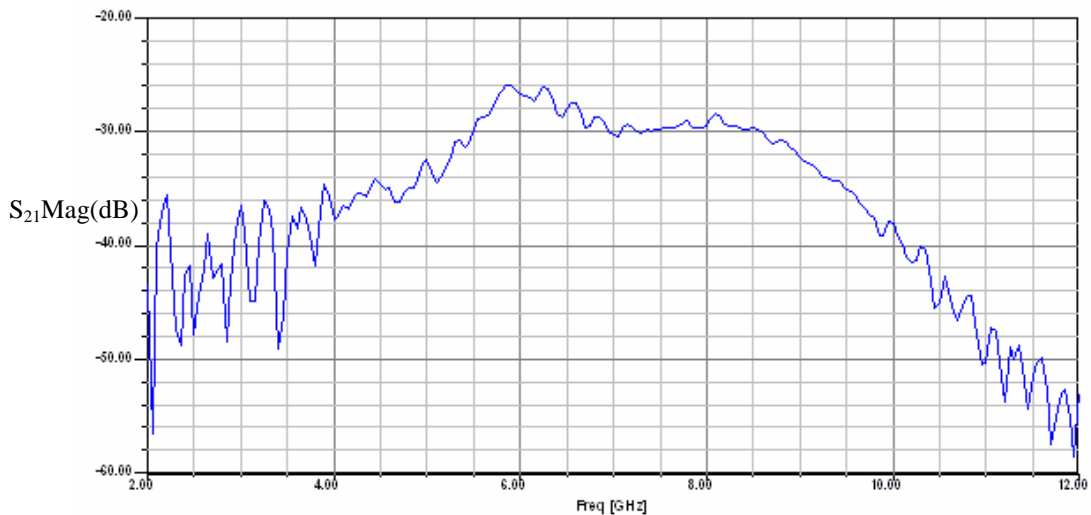


Figure 9.6. Transmission response (S_{21}) for Microstrip-fed UWB dipole.
Distance between antennas =20 cm.

Analysis of the group delay, shown in Figure 9.7, correlates with the results in Figure 9.6. Between 4 and 10.16 GHz, the group delay has a maximum variation

of 1.5 ns, compared to the spike of 15 ns at 2 GHz. This result for group delay is better than both the UWB antennas previously discussed in chapter 6.

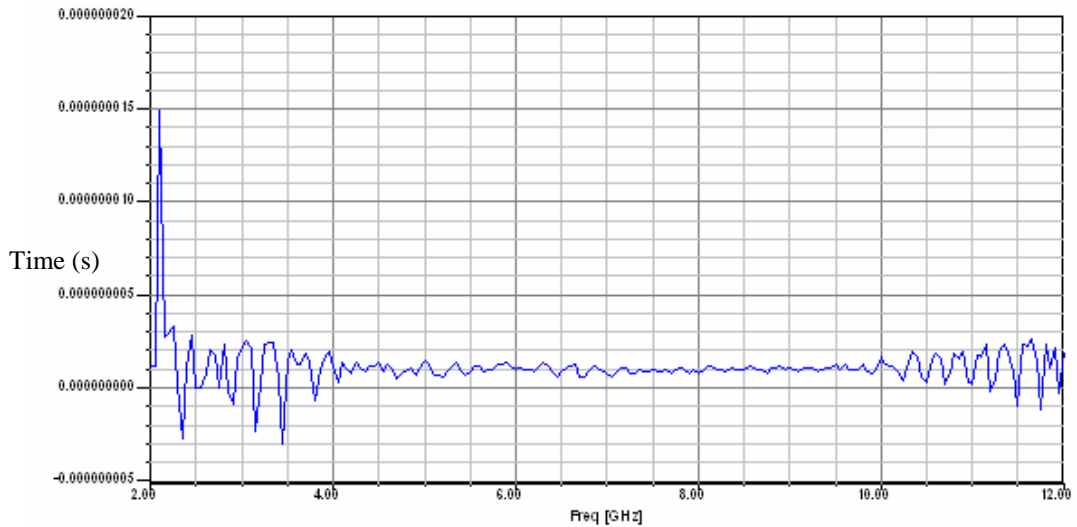


Figure 9.7. Experimental group delay for microstrip edge-fed UWB dipole.
Distance between antennas = 20 cm.

Analysis of both Figures 9.6 and 9.7 indicate that a pulse transmitted via an edge-fed UWB dipole is possible. Some distortion will be present, due to the non-linearity of the phase over frequency, at the lower end of the band. The results for pulse transmission are presented and discussed in section 9.3.

9.2.1.1 Radiation pattern results

Results were obtained using the near-field anechoic chamber outlined in Chapter 5. The orientation of the antenna with respect to the coordinate system is shown in Figure 9.8.

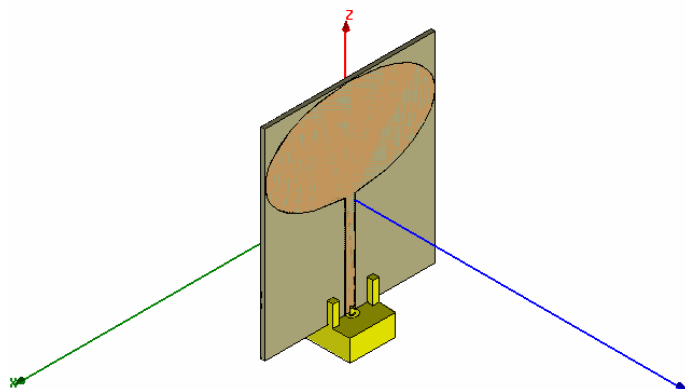
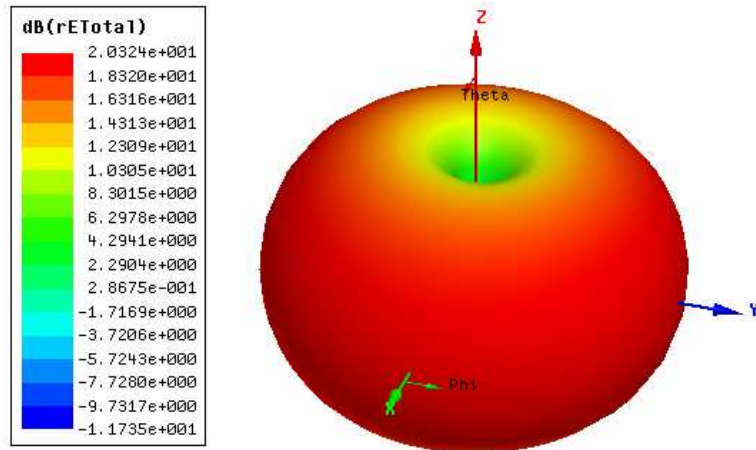
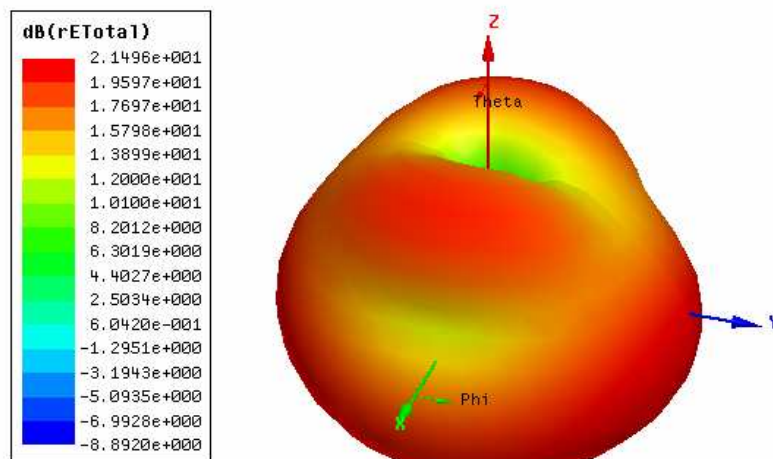


Figure 9.8. Orientation of antenna with respect to coordinate system used for measurements

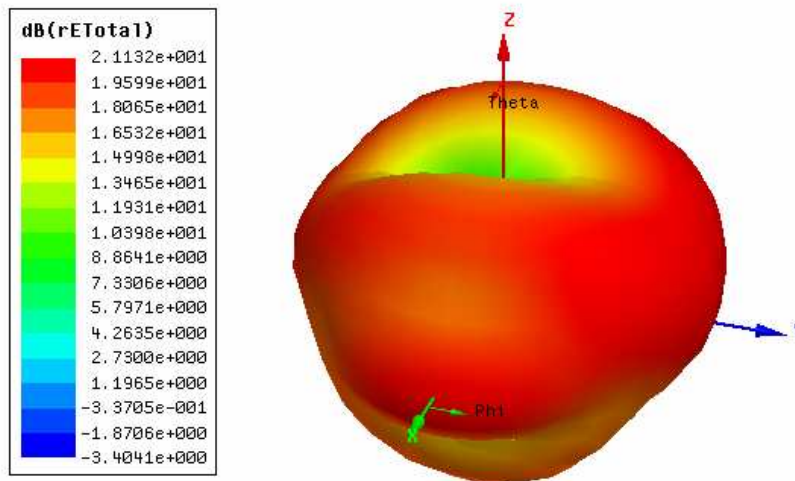
The results for the simulated 3D radiation patterns for electric field in decibels are shown in Figure 9.9. Analyses of the patterns indicate that the antenna is acting as a half-wave dipole at 3 GHz through to a 1.5 wavelength dipole at 9 GHz, as predicted by the theory in Chapter 2, section 2.7.



(a)



(b)

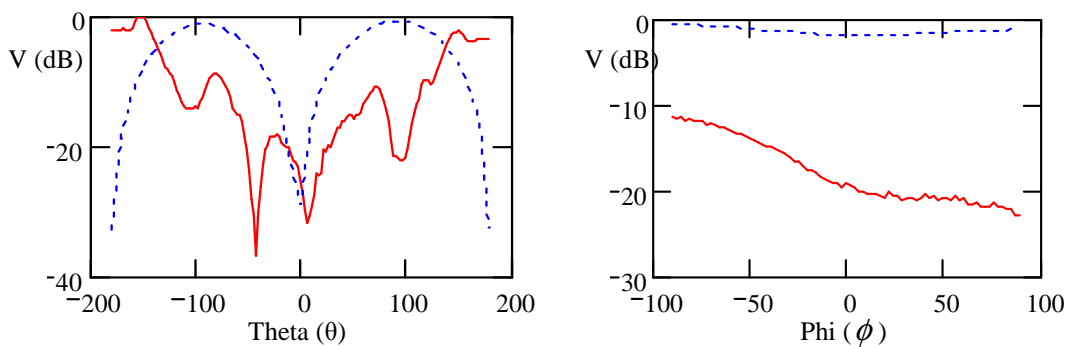


(c)

Figure 9.9. Microstrip edge-fed UWB dipole simulated 3D E-field radiation patterns for (a) 3 GHz (b) 6 GHz and (c) 9 GHz

The radiation plot at 3 GHz, shown in Figure 9.9 (a), highlights the discrepancy in the transmission results from Figure 9.6, as we would expect a higher gain as there is maximum gain in z-axis direction.

The simulated and experimental results for the radiation patterns at 3, 6 and 9 GHz are shown in Figure 9.10 in the form of horizontal and vertical cuts.



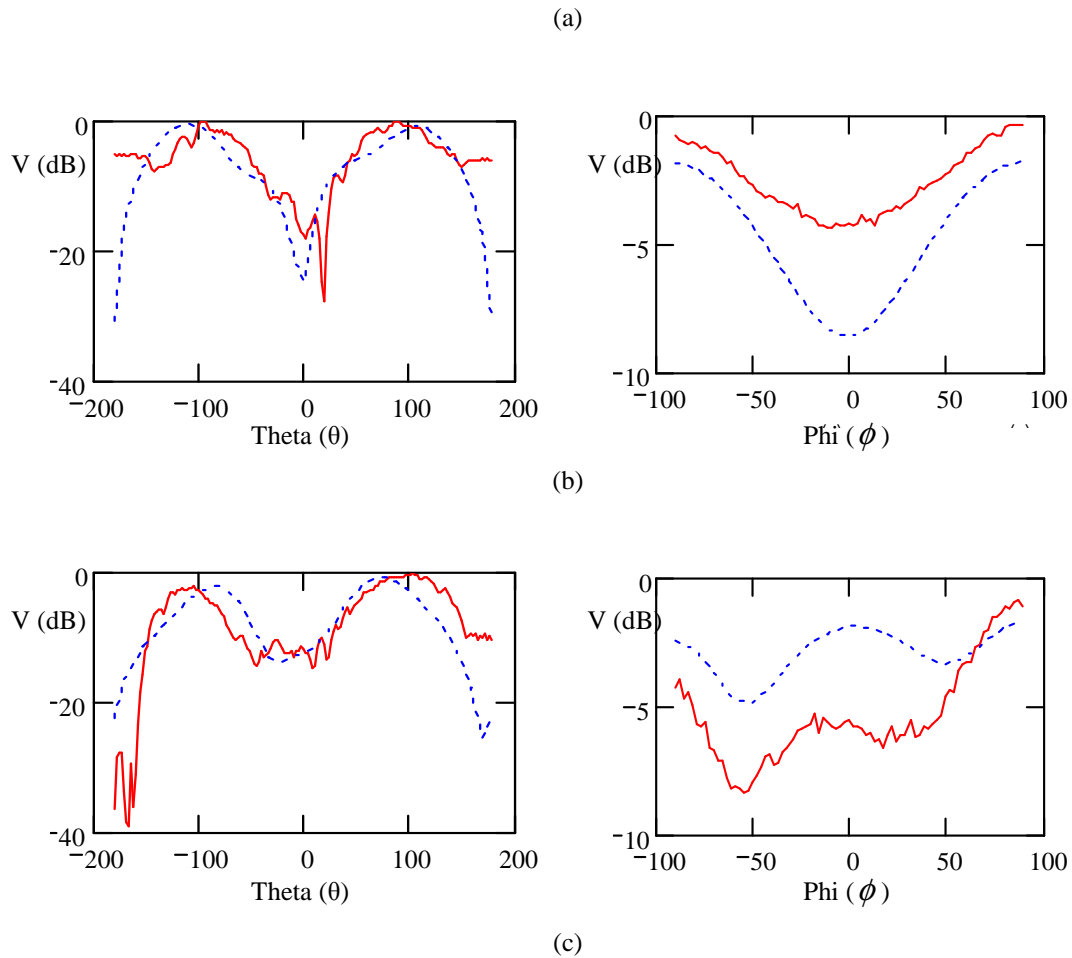


Figure 9.10 Microstrip-fed UWB dipole simulated (blue) and experimental (red) horizontal and vertical cuts for (a) 3GHz (b) 6 GHz and (c) 9 GHz

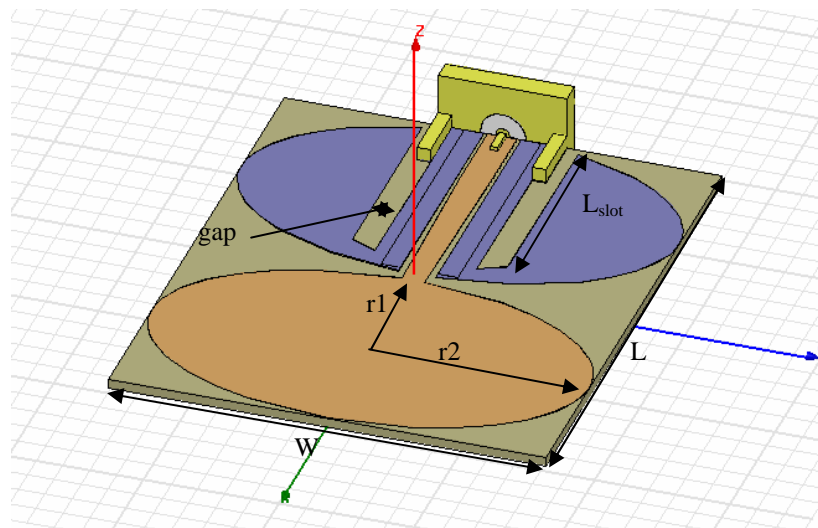
Inspection of the results in Figure 9.10 (a) shows poor agreement between simulated and experimental results. This explains the poor transmission response in Figure 9.6 at the start of the operational band as the field at boresight ($\theta = 90^\circ$, $\phi = 90^\circ$) is -20dB less than the simulated value. The multiple nulls present on the theta cut is a direct result of leakage current present on the feed cable. Figure 9.10 (b) and (c) are in closer agreement with the simulated results though the response is uneven, with the possibility that leakage current is distorting the experimentally obtained results.

If the simulated results had been validated by the experimental results, then the microstrip-fed dipole would be an excellent candidate for a UWB system. Section 9.6 will assess the performance of this antenna in a system, with respect

to the other antennas investigated in this chapter using pulse transmission. The next section investigates the reasons behind leakage current excitation.

9.2.2 UWB dipole with slots

To try and eliminate the effects of the measurement cable, the feeding arrangement was converted to a CPW feed, and slots were inserted either side of the feed. This antenna design was based on the previously published antenna by Kwon [2], though the shape of the antenna element is different. A schematic of the layout is shown in Figure 9.11.



L	W	r1	r2	gap	L _{slot}
38.802 mm	32.3 mm	9.5 mm	16.15 mm	2 mm	17 mm

Figure 9.11. CPW-fed dipole with slots

9.2.2.1 Effect of slots on antenna

As described in Section 9.2.1, there is a leakage current excited down the co-axial feed cable. This can be separated into two types of current that are excited along the outer surface of the co-axial cable. These currents are depicted in Figure 9.12. The first type is directly at the co-axial-to-CPW interface. The current that flows back down the cable between the centre conductor and inner surface (signified by the dash-dot-dot line) is considered a component of the reflection co-efficient.

The current that flows in the $-y$ direction on the outside (dash-dash line) is a component of the leakage current.

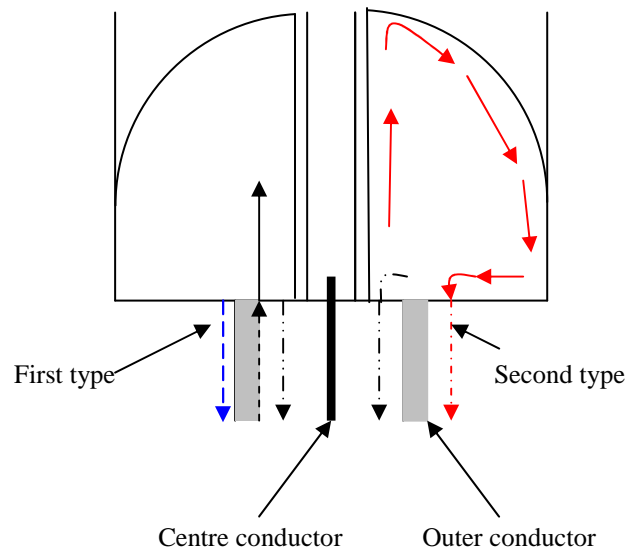


Figure 9.12. Current flow around the antenna at the cpw to co-axial interface.

The majority of the current is fed along the CPW trace to the centre of the antenna and results in the second type of leakage current (dash-dot line). The current travels around the edges of the dipole and, as a result, back down the feed cable. The purpose of the slots on either side of the feed are meant to stop the second type of leakage current flowing down the outside of the co-axial feed cable. A model was created in HFSS to establish the effect of the slots in reducing the leakage current, and is shown in Figure 9.13. The results of this analysis show that the slots reduce the leakage current but not completely. The remaining leakage current can be attributed to the first type of leakage current shown in Figure 9.12.

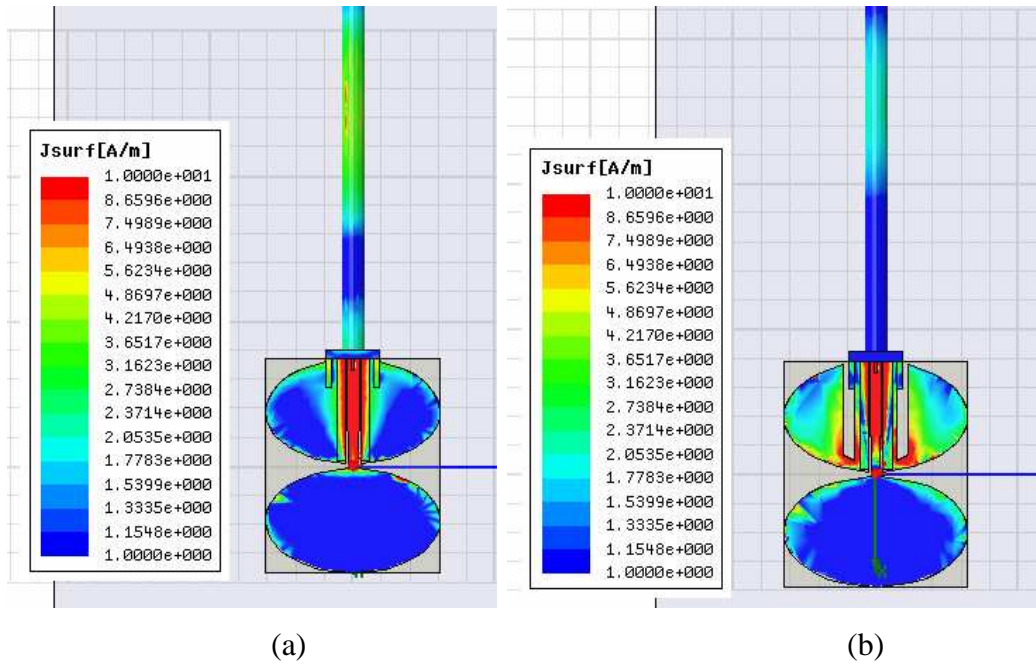


Figure 9.13. Comparison of CPW-fed dipole antenna (a) with and (b) without slots

To obtain a better understanding of the radiation mechanism due to the leakage current a sheet was placed away from the antenna. This allowed the electric field lines to be viewed, and the result is shown in Figure 9.14.

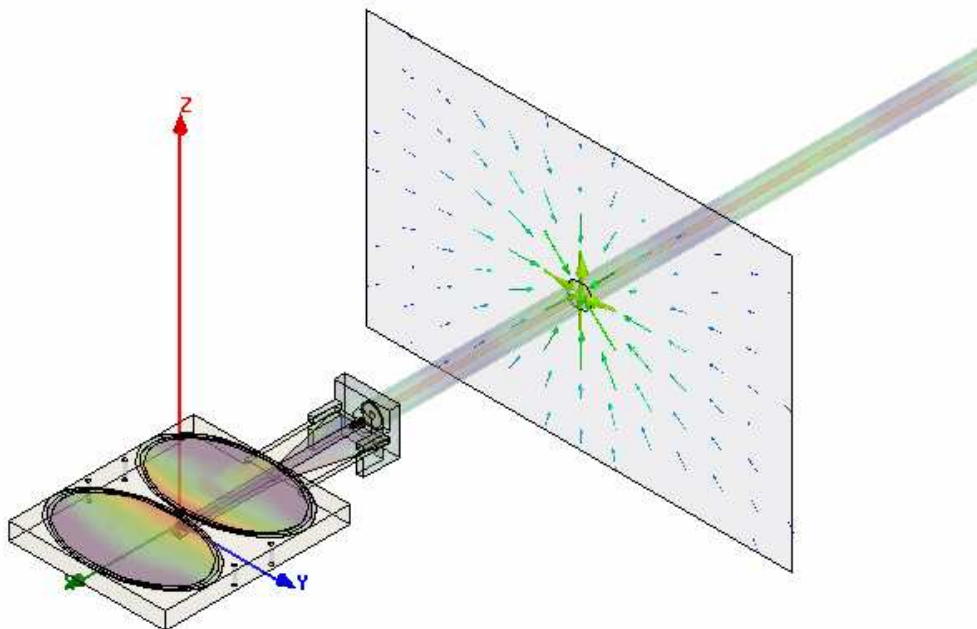


Figure 9.14 Analysis of leakage current using E-field vector plot

The excitation of the leakage current can be explained as follows. A positive charge accumulates on the end of the feed cable with antenna attached to it, while the other end of the feed cable has a negative charge accumulation. As a result current is driven back along the cable. This is a realisation of the theory explained in sections 2.3 and 2.4.

Using HFSS parametric analysis, a study was carried out on the effect of the slot dimensions. Initially, the experiment was to find the optimum length for the best match whilst reducing the leakage current. A parametric sweep was carried out where the length of the slot was varied from 6 mm to 17 mm. The results are shown in Figure 9.15.

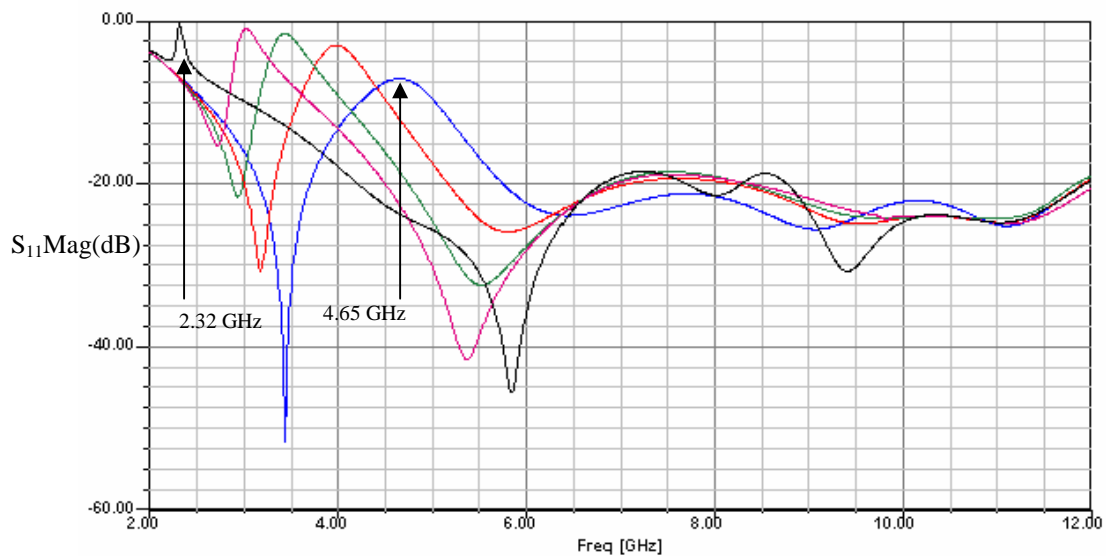
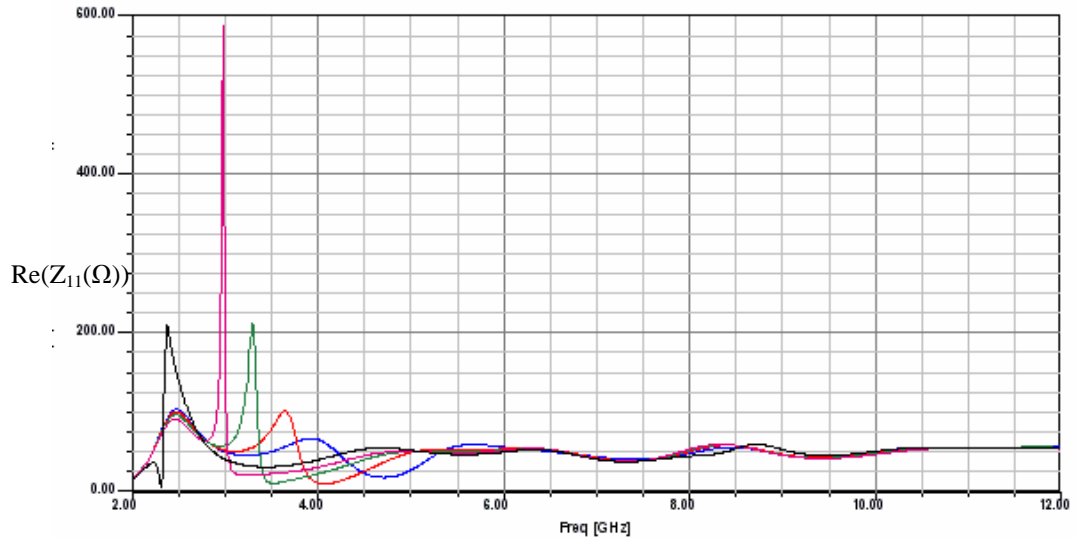


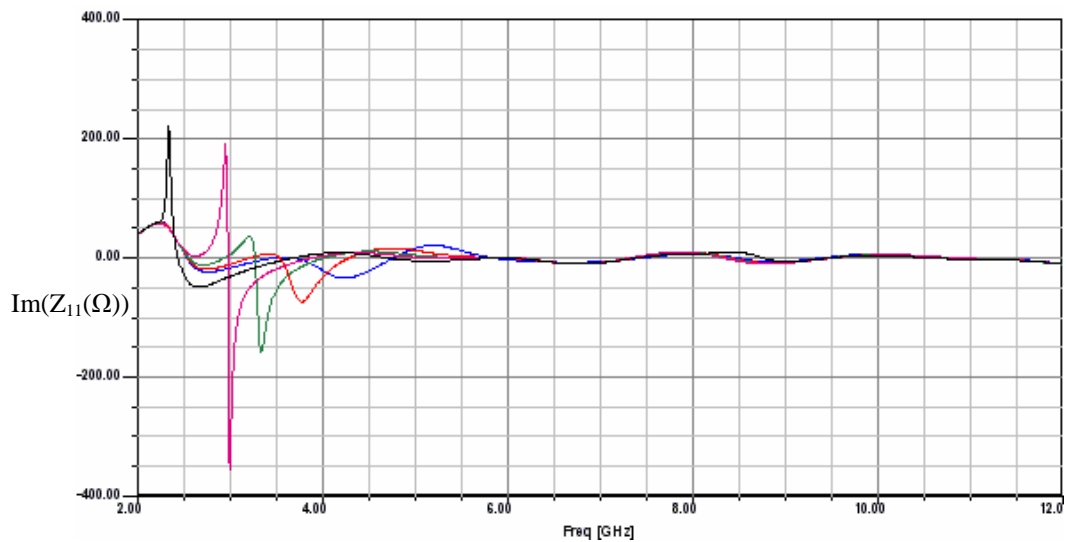
Figure 9.15. Simulated S_{11} results for the increasing slot length; blue = 6mm, red = 8mm, green = 10mm, magenta = 12mm, black = 17mm

It is important to note the shift of the reflection coefficient (S_{11}) peak from 4.65 GHz to 2.32 GHz as the slot length is increased. The presence of this peak indicates an impedance mismatch for a section of the band, sometimes known as a ‘stop band’ effect. This effect is caused by the two slots resonating as quarter-wavelength notch filters as reported by I. Yoon [3] and H. Yoon [4]. The slots act as narrowband resonant structures, which act as wave traps, capturing particular frequency components and reflecting them away. At the frequency of resonance a destructive interference occurs, rendering the antenna non-responsive at that frequency. This is validated by inspecting the impedance at the resonant

frequency, which is very high. Simulated values of impedance for different lengths of slots are shown in Figure 9.16.



(a)



(b)

Figure 9.16. (a) Real and (b) Imaginary input impedance versus frequency for increasing slot length; blue = 6mm, red = 8mm, green = 10mm, magenta = 12mm, black = 17mm

Using HFSS it was possible to view the surface current in terms of a vector plot and magnitude. This identified a non-propagating mode present at the specific frequency of the stop band. Figure 9.17 shows the difference between 2.32 GHz and 3 GHz.

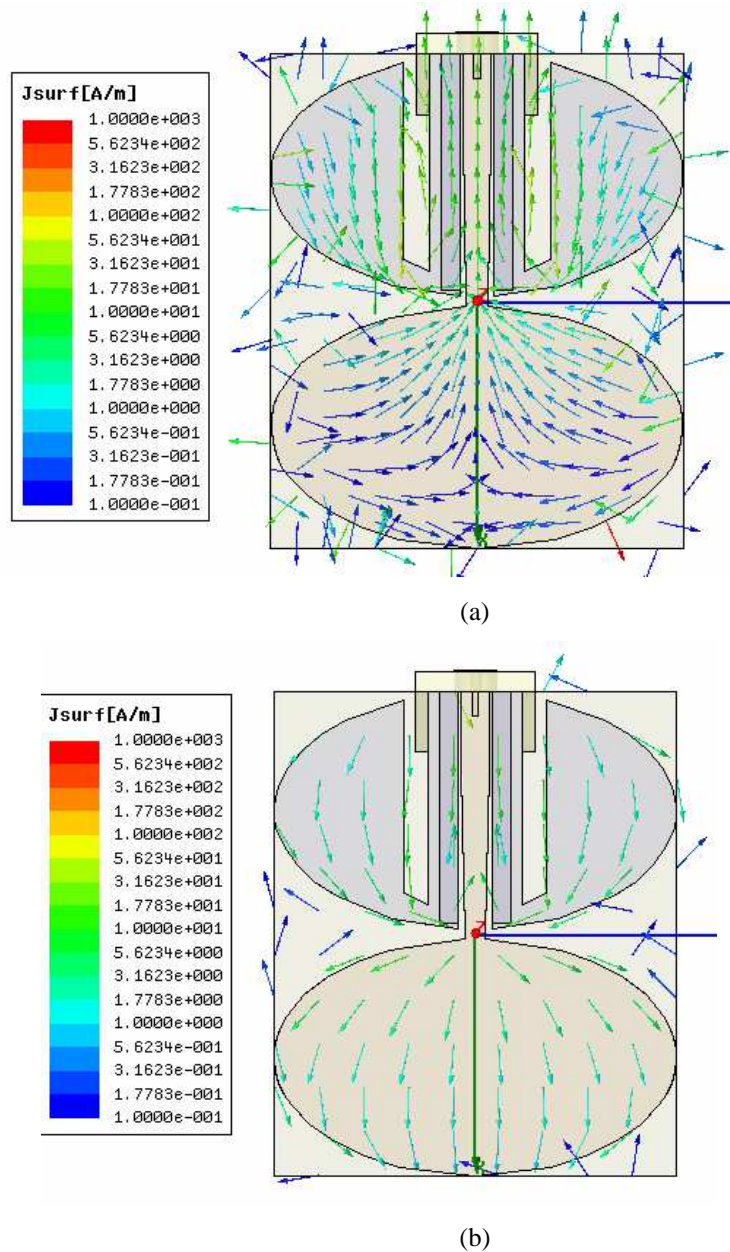


Figure 9.17. (a) Vector surface current plots (a) 2.32 GHz and (b) 3 GHz
The slot = 17 mm for both plots.

Comparing the two plots, the effects of slot at resonance can be clearly seen. Analysing Figure 9.17 (a), the magnitude of the current is much larger around the slots and the flow of the current is exactly 180 degrees out of phase along the length of both sides of the slots. This is the characteristic that causes the antennas impedance to be much larger than 50Ω . This happens because the net flow of current across the dipole has been reduced, as shown by Figure 9.16. For the antenna to radiate in its fundamental mode, the current needs to flow in a uniform direction across the dipole, as shown by Figure 9.17 (b).

9.2.2.2 S-parameter results for UWB dipole with slots

A CPW-fed UWB dipole with slots with a slot length of 17mm was manufactured, and then tested using a vector network analyser. The simulated and experimental results of the return loss for the UWB dipole with slots are shown in Figure 9.18.

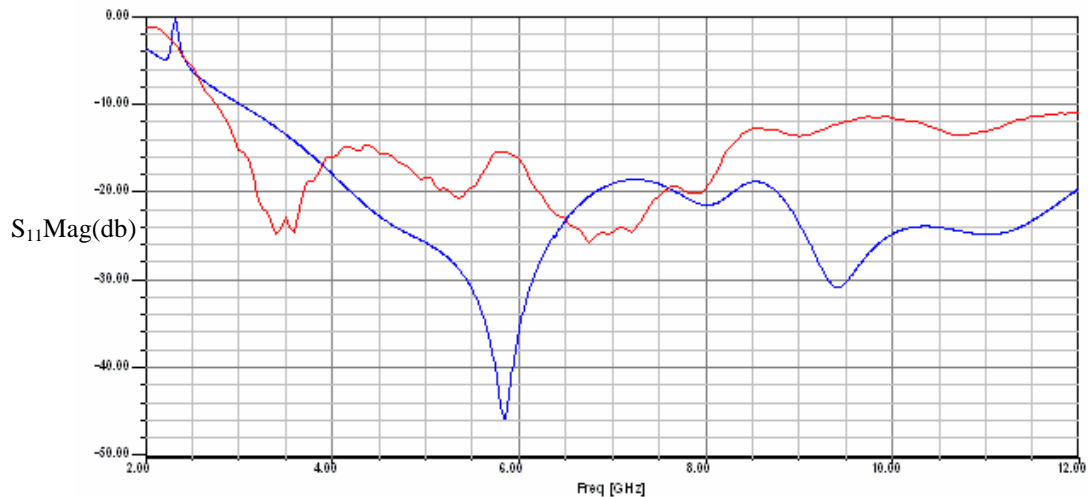


Figure 9.18. Simulated (blue) and experimental (red) results for S_{11} .

Inspection of the results shows that there is still evidence of leakage current affecting the results, as shown by the multiple nulls up to 7 GHz. The stop band also appears to be present in both the theoretical and experimental results at 2.3 GHz, however correlation between experimental and simulated data is poor. Whether this can wholly be attributed to the leakage current is unclear. Apart from these drawbacks, the antenna still has an acceptable bandwidth for pulse transmission.

Analysis of the simulated and experimental results for phase, highlights the effect of leakage current present on the test cables. The results are shown in Figure 9.19.

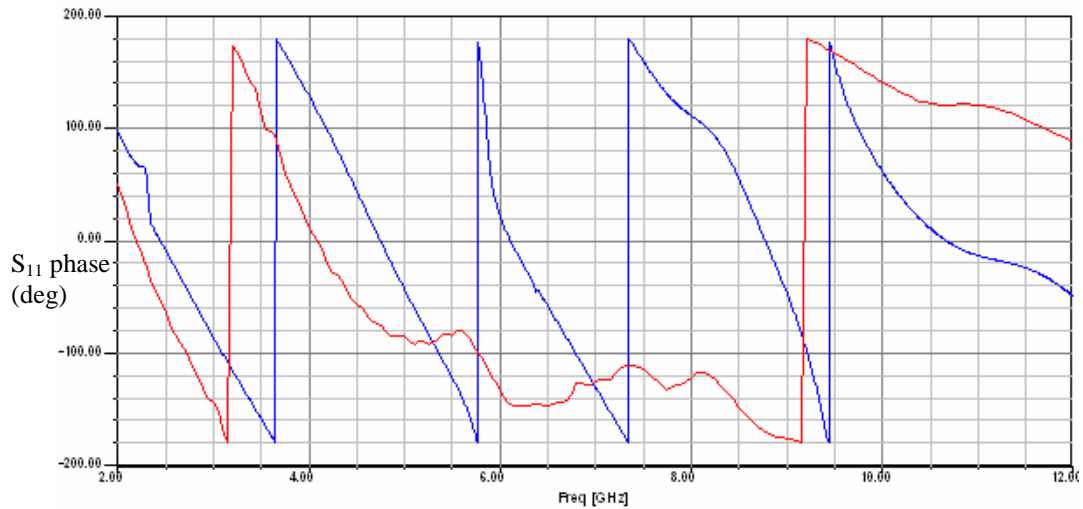


Figure 9.19. UWB dipole with slots S_{11} phase results (i) simulated (blue) (ii) experimental (red)

The correlation between experimental and simulated phase response is poor and can be attributed directly to leakage current. However, the transmission response and group delay both exhibit good characteristics for pulse transmission. They are shown in Figures 9.20 and 9.21 respectively.

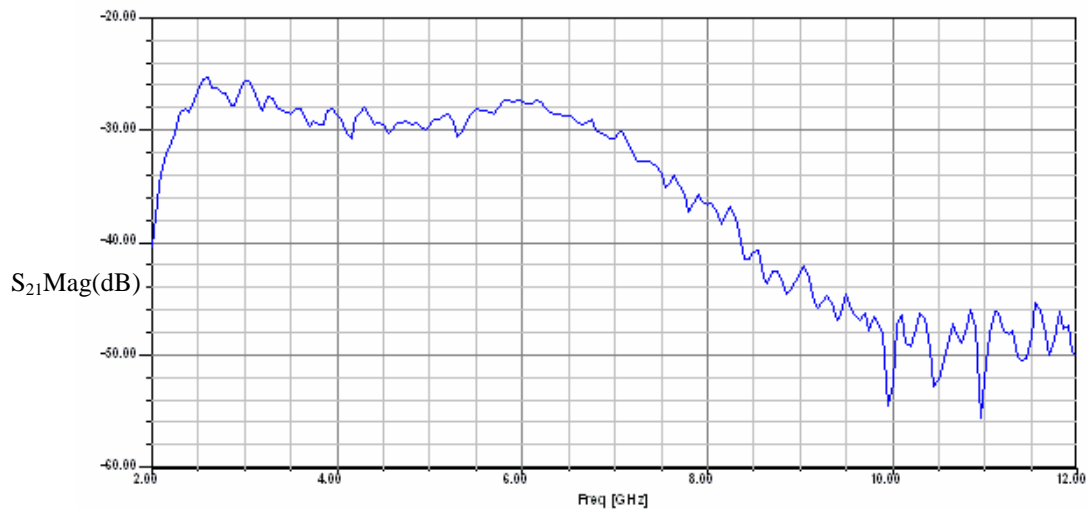


Figure 9.20. Transmission response (S_{21}) for CPW-fed UWB dipole with slots.

Distance between antennas =20 cm.

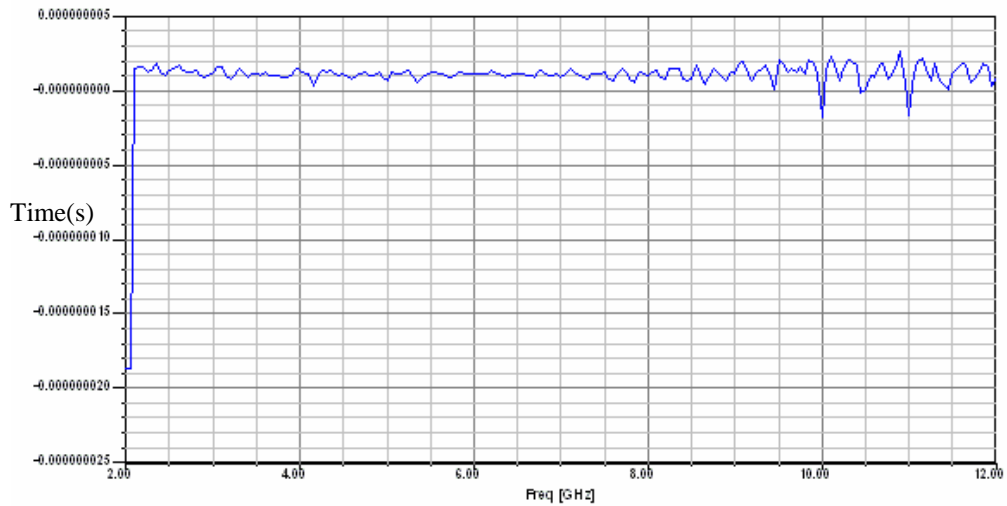


Figure 9.21. Experimental group delay for UWB dipole with slots.
Distance between antennas = 20 cm.

The UWB dipole with slots exhibits the best transmission response and group delay results of all the UWB dipoles reviewed in this thesis. The group delay has a good response since there are no sudden variations in the transmission response and has a maximum variation of 2ns over the operational bandwidth. Good transmission response is a result of the radiation patterns of the antenna, which are discussed in the next section.

9.2.2.3 Radiation pattern results for UWB dipole with slots

Results were obtained using the anechoic chamber outlined in Chapter 5. The orientation of the antenna with respect to the coordinate system is shown in Figure 9.22.

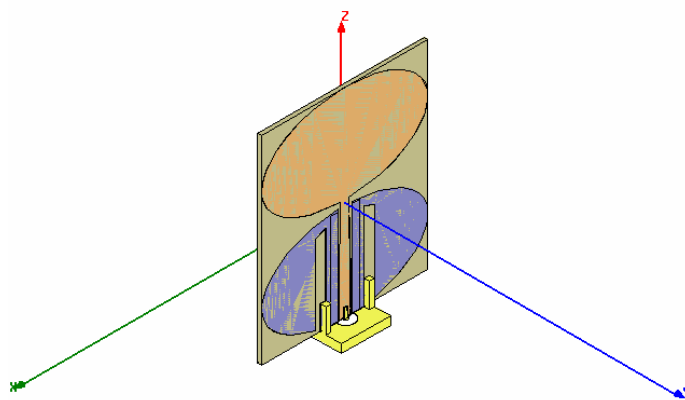
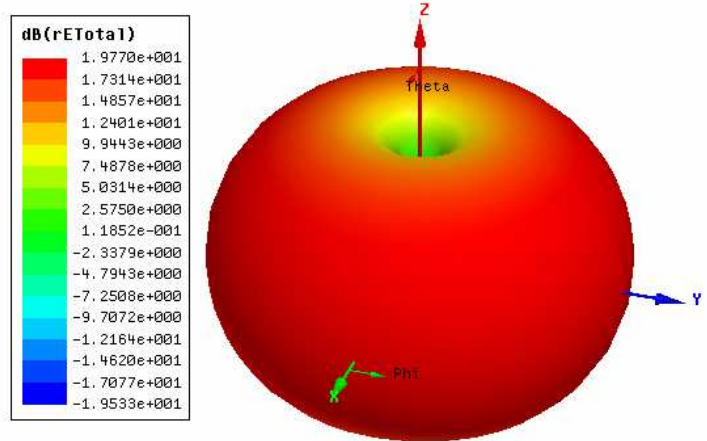
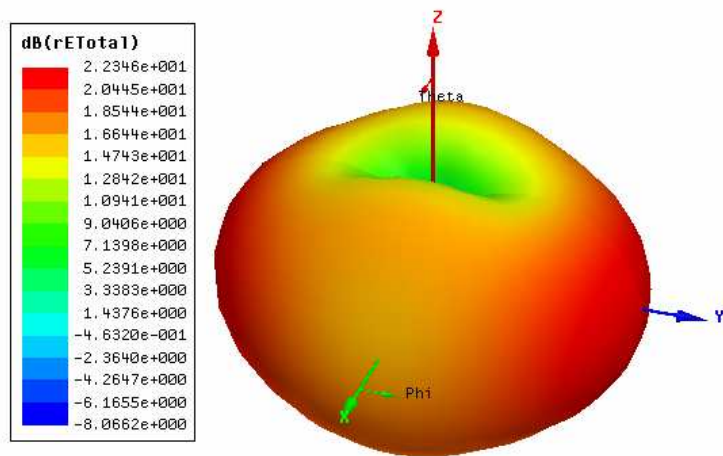


Figure 9.22. Orientation of antenna with respect to coordinate system used for measurements

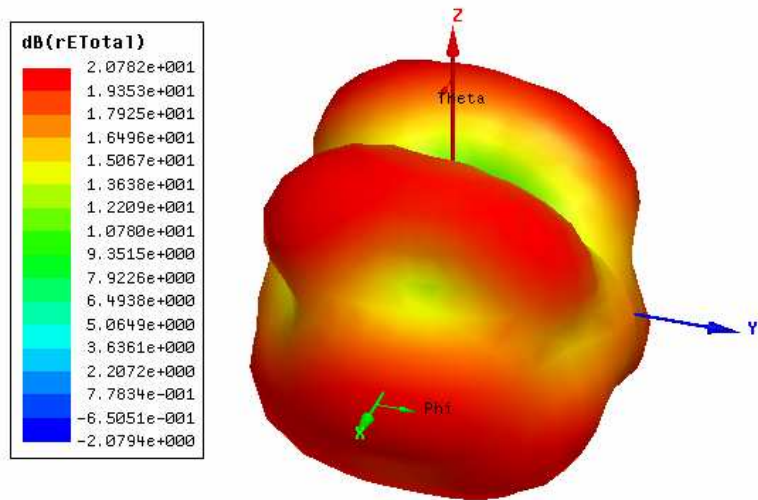
The results for the simulated 3D radiation patterns for electric field in decibels are shown in Figure 9.9. Analyses of the simulated patterns indicate that the antenna is acting as a half-wave dipole at 3 GHz through to a 1.5 wavelength dipole at 9 GHz, which confirms the theory in chapter 2.



(a)



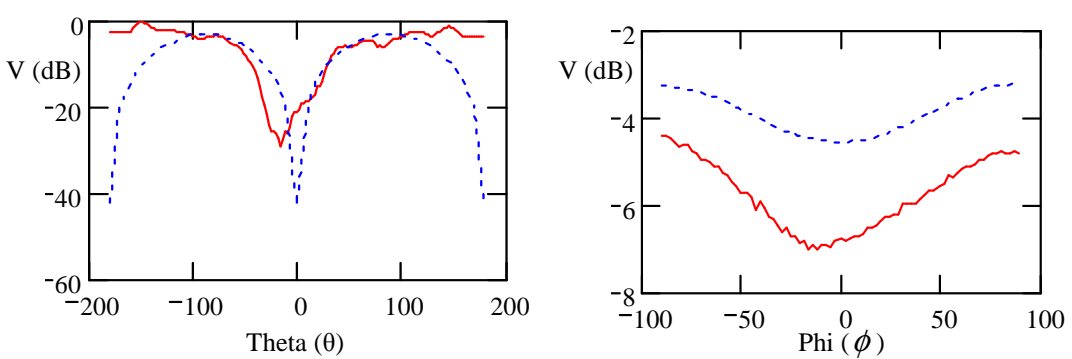
(b)



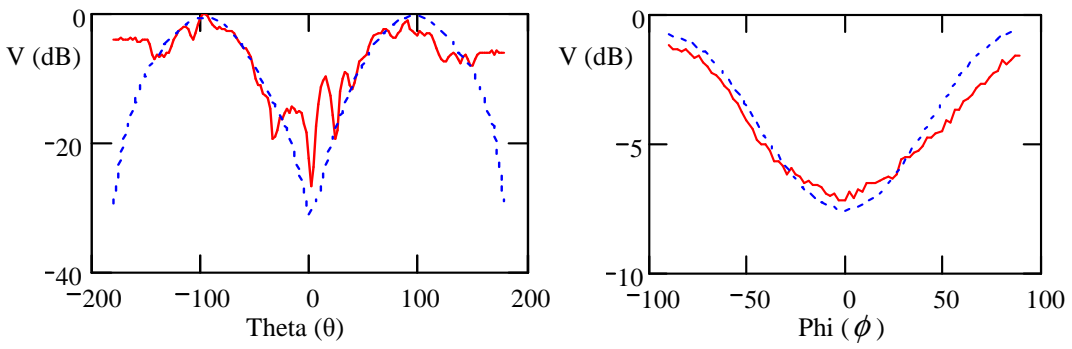
(c)

Figure 9.23. Simulated 3D E-field radiation patterns for (a) 3 GHz (b) 6 GHz and (c) 9 GHz

The simulated and experimental results for the radiation patterns at 3, 6 and 9 GHz are shown in Figure 9.24 in the form of horizontal and vertical cuts.



(a)



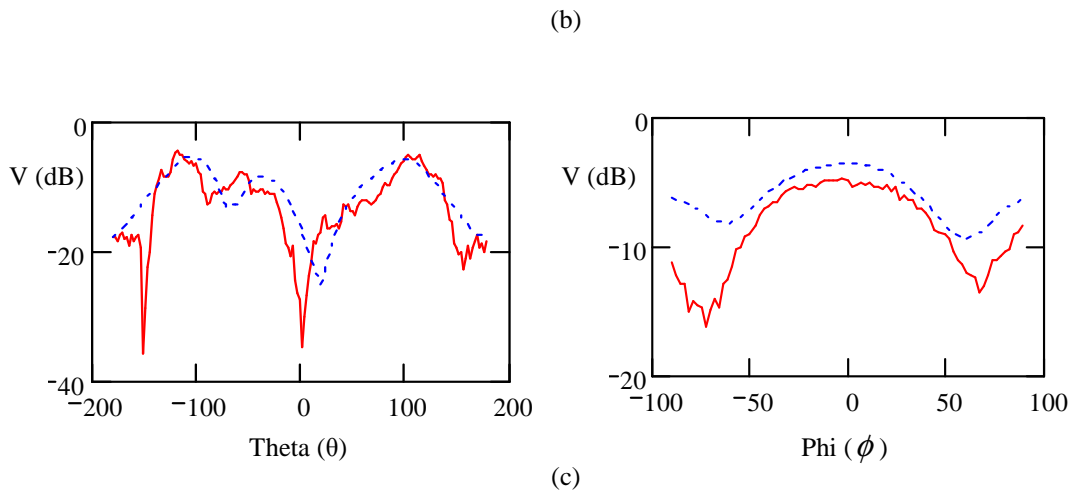


Figure 9.24 CPW-fed UWB dipole with slots simulated (blue) and experimental (red) horizontal and vertical cuts for (a) 3GHz (b) 6 GHz and (c) 9 GHz

Inspection of the results in Figure 9.24 shows good agreement between simulated and experimental results, especially when compared to microstrip-fed UWB dipole in the previous section. There is still some distortion present particularly on the theta cuts. The results also correlate with the good transmission response shown in Figure 9.20. It appears that the slots are effective in reducing leakage current, and as a result improving the radiation pattern characteristics. The antenna in the next section attempts to further improve on these results.

9.2.3 A hybrid feed for a edge-fed UWB dipole antenna

The evaluation of the UWB dipole described in the previous section showed that the impact of leakage current due to the nature of the feed was still having too much impact on the performance of the antenna. To try and reduce the effect of the leakage current, the feed into the antenna had to be balanced. To date, the only edge-fed dipole with a proper balanced feed appears to be the catfish dipole of Hans Schantz [5]. A drawback to this design is that there appears to be an extremely complex matching stub with no description on how it was constructed; however, one point made clear was that to achieve the best feed into the antenna there had to be a microstrip-to-parallel plate transition i.e. unbalanced to balanced.

The hybrid-feed dipole that was investigated contains much of the same geometry as the previous two dipoles (CPW with slots and microstrip-fed). The elliptical elements are both on the same side of the substrate and are initially fed by two

vias, which act as a two wire transmission line and are connected to the parallel plate, which in turn, is tapered into a microstrip line. Figure 9.25 shows the geometrical layout for the antenna.

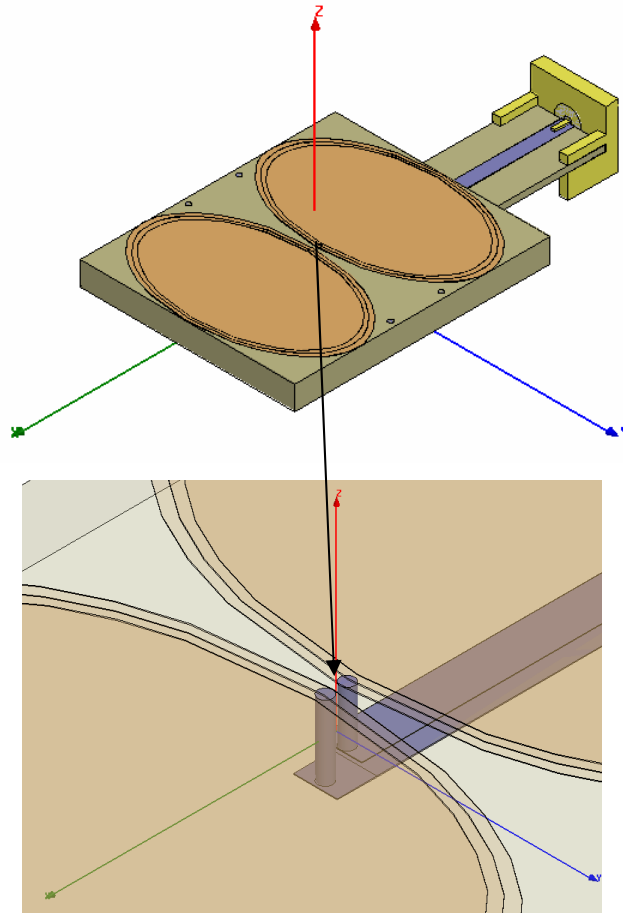
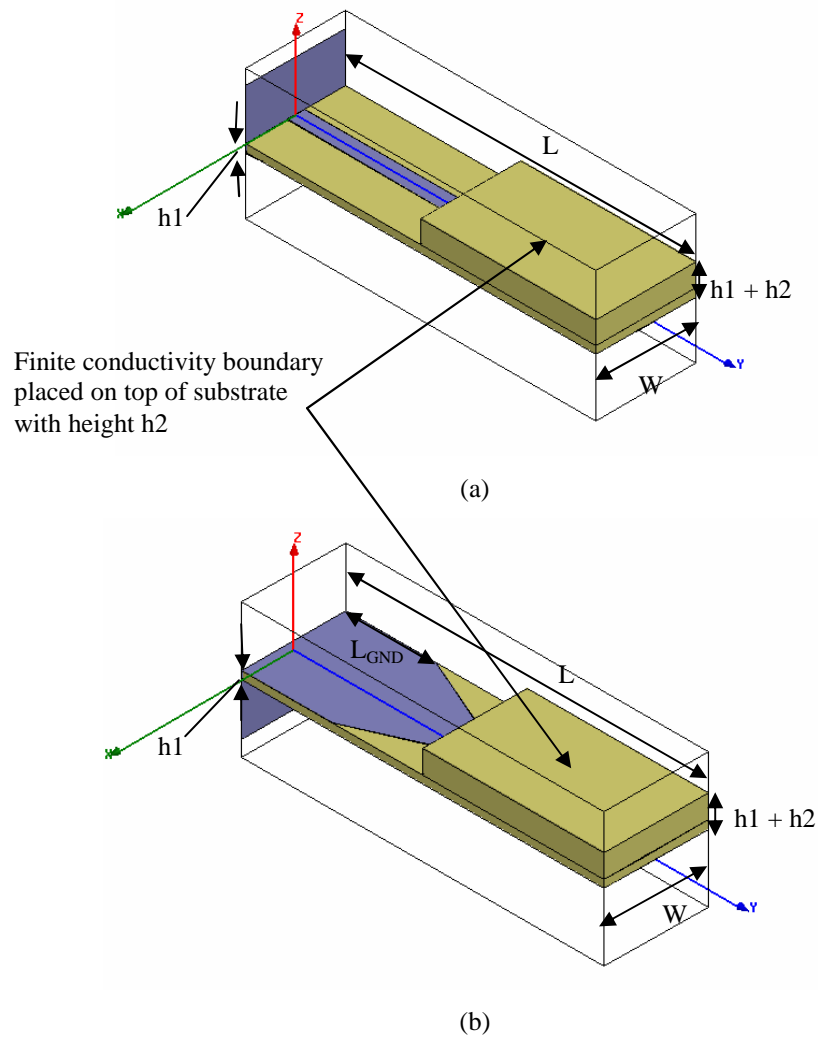


Figure 9.25. Hybrid-fed UWB dipole with enlarged view of the two feeding vias 250 μm apart

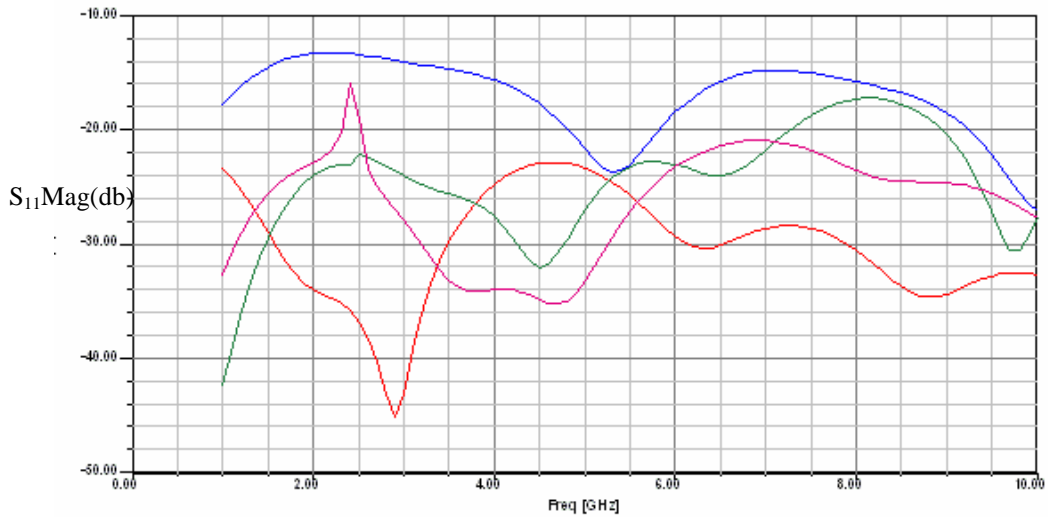
As shown in Figure 9.25 the portion of the substrate, with elliptical elements on it, is thicker than the feed into it. This was to minimise the effect of the radiating elements on the characteristic impedance of the parallel plate and also reduce any interaction between the feed and the radiating elements. A model was created in HFSS to deduce how close the radiating elements could be placed to the parallel-plate transmission line. The model was varied in two main ways. One had the variation of the substrate height, the parameter h_2 , on the same side as the ground for the microstrip. The other had the exact opposite, with the increase on the substrate height, parameter h_2 , on the same side as the signal line. For both cases, the topside of the varying substrate had a finite conductivity boundary place on them. This is shown in Figure 9.26.



L	W	h1	h2	L_{GND}
32.025 mm	9.5 mm	0.762 mm	2.286 mm	7.9375 mm

Figure 9.26. HFSS model for parallel plate interaction with metal (a) GND clear (b) signal clear

Both models were parametrically analysed with the substrate height increased in increments of 0.762mm, which was the standard substrate height for the Rogers 4350 board. If there was a separation of one board, then there was substantial coupling into the metal creating a stripline mode. Through parametric analysis, it was found for both models that an acceptable amount of coupling was achieved by using a three substrate thickness of $h_2 = 2.286$ mm. Results for return and insertion loss for both models are shown in Figure 9.27 and 9.28 respectively.



(a)

Figure 9.27. S_{11} and S_{22} for sub thickness = 2.286 mm; Blue (S_{11}) and Red (S_{22}) belong to signal clear (Figure 9.26 (b)); Green (S_{11}) and Magenta (S_{22}) belong to GND clear (Figure 9.26 (a)).

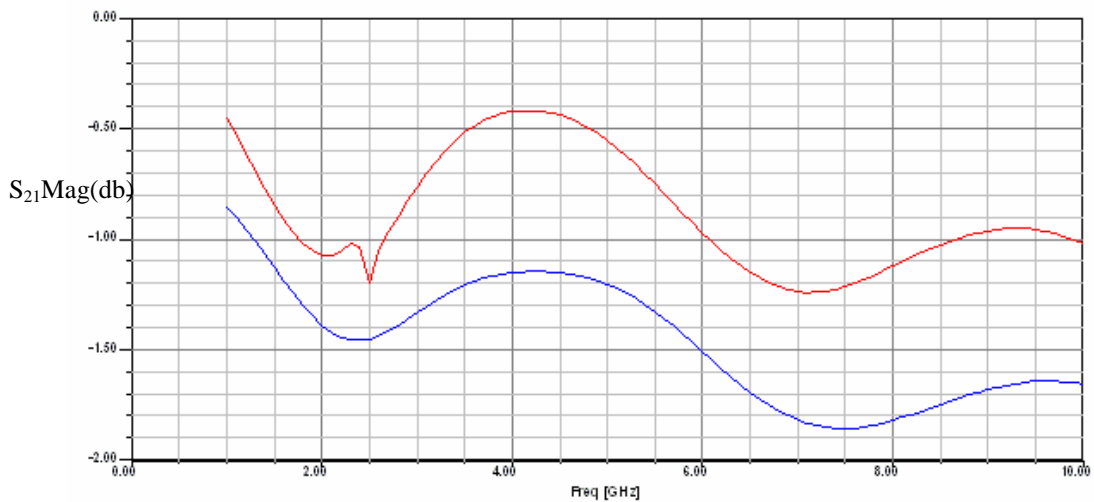
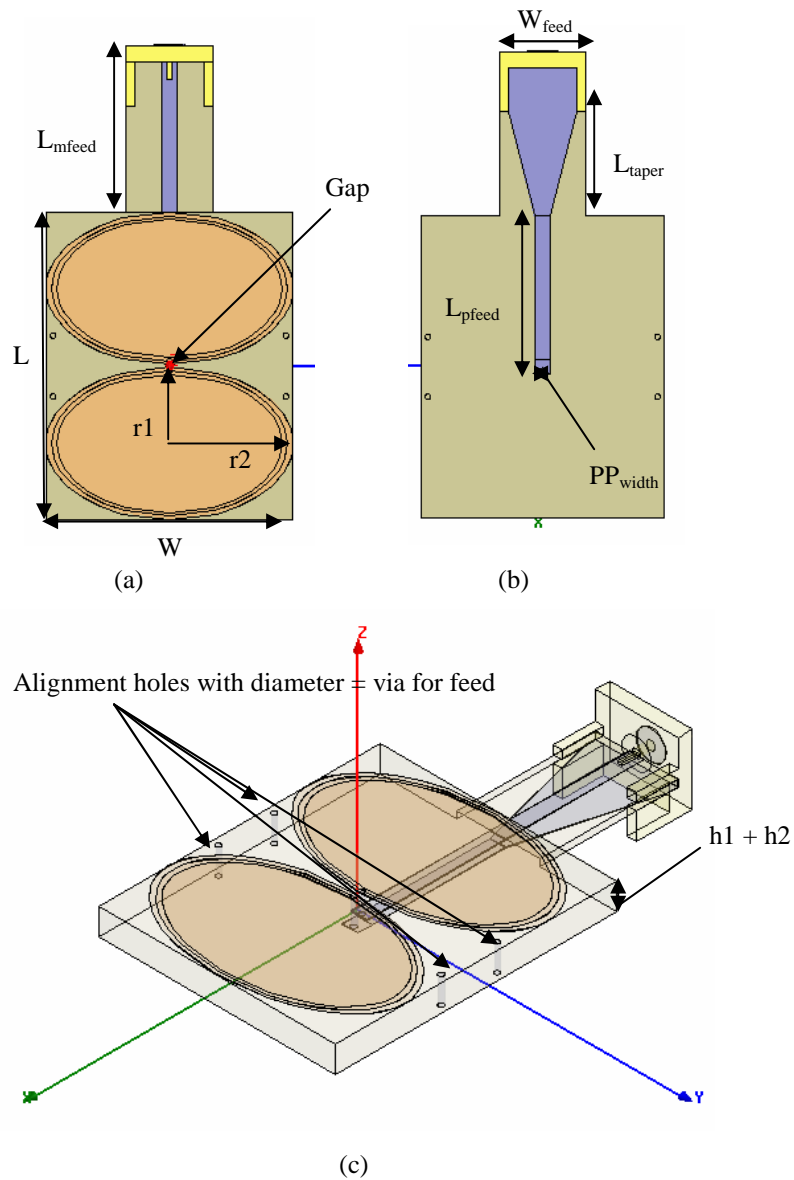


Figure 9.28 Insertion Loss for sub thickness = 2.286 mm – GND clear (blue), Signal clear (red).

Throughout the analysis of the two models, it was apparent that having the microstrip ground on the side that was opposite to side of the antenna elements would give a significantly better performance. A possible explanation to this behaviour was that as the ground was clear, it gave a better balance in terms of field manipulation to the signal, and less dispersion occurred when it entered into the thicker substrate.

With the substrate height and feeding arrangement optimised, the full model was created. The most critical part of the design was the gap between the two

radiating elements, which determined the input impedance for the antenna. This gap was optimised by placing a lumped port between the two wire transmission lines. This determined the optimum gap between the two elements and indicated what the impedance of the parallel plate feeding into the two wire feed should be. After this was determined, the full model was analysed with feed coming from the SMA connector. The antenna was optimised further by running parametric analysis on the tapering between the microstrip and the parallel plate. Figure 9.29 shows different views of the antenna with the various optimum dimensions outlined.



L	W	r1	r2	h1	h2
32.3 mm	27.2 mm	8 mm	13.6 mm	0.762 mm	2.286 mm
L_{pfeed}	W_{feed}	L_{taper}	PP_{width}	Via_diameter	gap
17 mm	9.5 mm	14.85 mm	2.15 mm	0.6 mm	0.25 mm

Figure 9.29. Balanced feed UWB dipole (a) top view (b) underside view (c) 3D see-through view

To try and establish the effect of the balanced feed in reducing leakage current a model was created in HFSS with the balanced feed UWB dipole attached to a feeding co-axial cable. This was then compared to CPW fed dipole with slots and is shown in Figure 9.30.

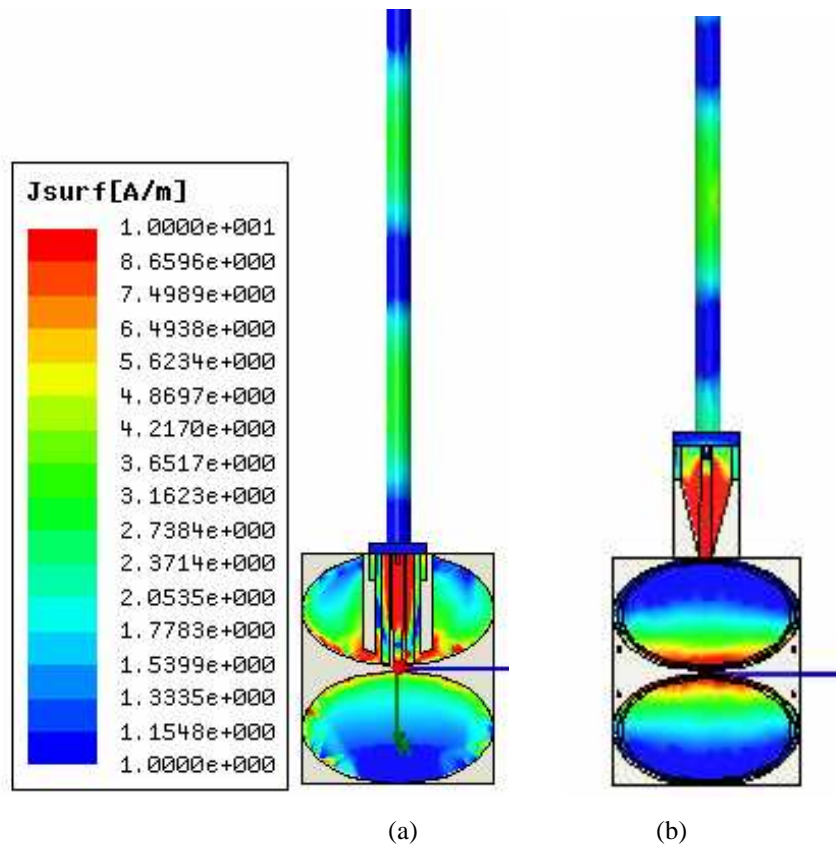


Figure 9.30 Comparison of leakage current at 3 GHz on UWB dipole antennas
 (a) CPW feed with slots (b) balanced feed

At first glance, the results appear disappointing, as it was hoped that the balanced feed would completely eradicate the leakage current. In fact it is better to suggest that both antennas are successful in suppressing the leakage current, though not fully. Analysing both HFSS models there is a peak surface current in excess of 700 A/m for both models, with most of the surface current residing internally in the co-axial cable, and in-and-around both antennas. For both the models in Figure 9.30, the maximum surface current residing on the outside of the co-axial cable is approximately 3.5 A/m.

As some current will exist on the surface of the co-axial cable, it is important to choose the right cable and/or some form of choking of the current to stop it flowing down the cable. If leakage current does happen then there can be distortion to the radiation pattern, which is usually seen as multiple lobes on the far-field radiation pattern. An example of this is shown in Figure 9.31.

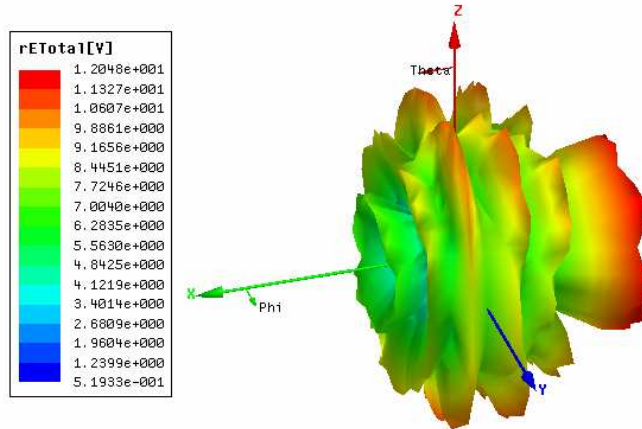


Figure 9.31 Far-field pattern for hybrid feed UWB dipole connected to co-axial cable

There are many ways to ensure that any leakage current on the exterior of the co-axial cable is reduced or eliminated, including:

- Use of RF chokes, such as ferrites or steel wool wrapped around the co-axial cable before it connects to the antenna to help produce lossy loading, which resistively dissipates leakage current
- Selection of cable is important as well. Certain types of SMA cable are better than others at dealing with leakage current as they have an extra braid layer to provide better shielding. This extra shielding on the cable has an added bonus as it reduces leakage current via lossy loading.

The easiest way of detecting whether or not there is leakage current present on the cable is to simply touch it. If there is a significant change in the return loss then that means that the cable is ‘hot’.

9.2.3.1 S-Parameter results for hybrid feed UWB dipole

S-parameter results, obtained using an Agilent N5230A VNA are shown in Figure 9.32.

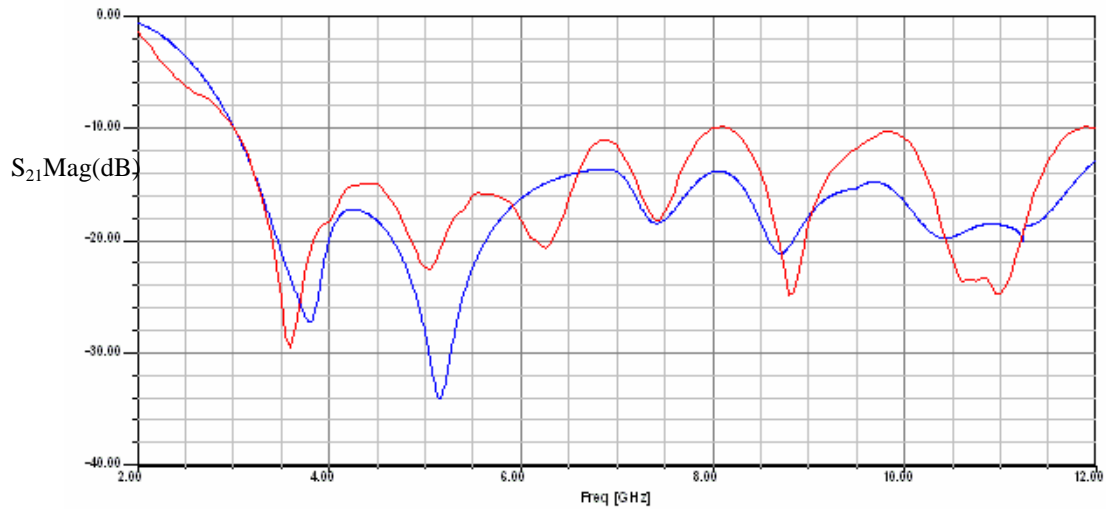


Figure 9.32. S_{11} for simulated (blue) and practical (red)

At first inspection, the correlation between simulated and practical results is good, considering that the analysis is over a large frequency range. The nulls match at various frequencies, which give confidence that the HFSS model gives an accurate description of the antenna. The discrepancies that do exist can be attributed to manufacturing errors since the antenna was engineered by hand. The vias were particularly hard to drill, and there was no guarantee that the boards were perfectly aligned.

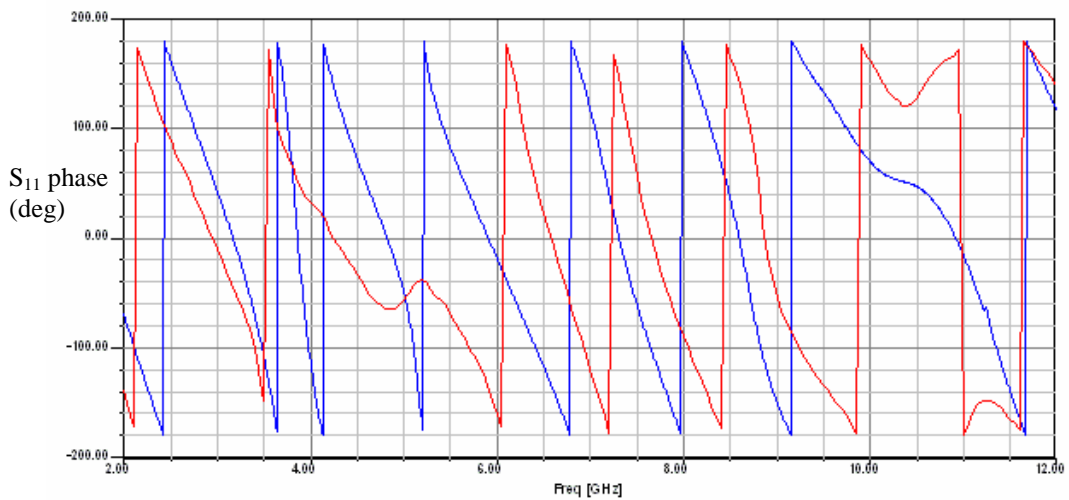


Figure 9.33 Simulated (blue) and experimental (red) results for phase

Analysis of phase shows poor correlation between simulated and experimental results, but there is a marked improvement on the two previous antennas investigated in terms of linearity.

The results for transmission response and group delay are shown in Figures 9.34 and 9.35 respectively.

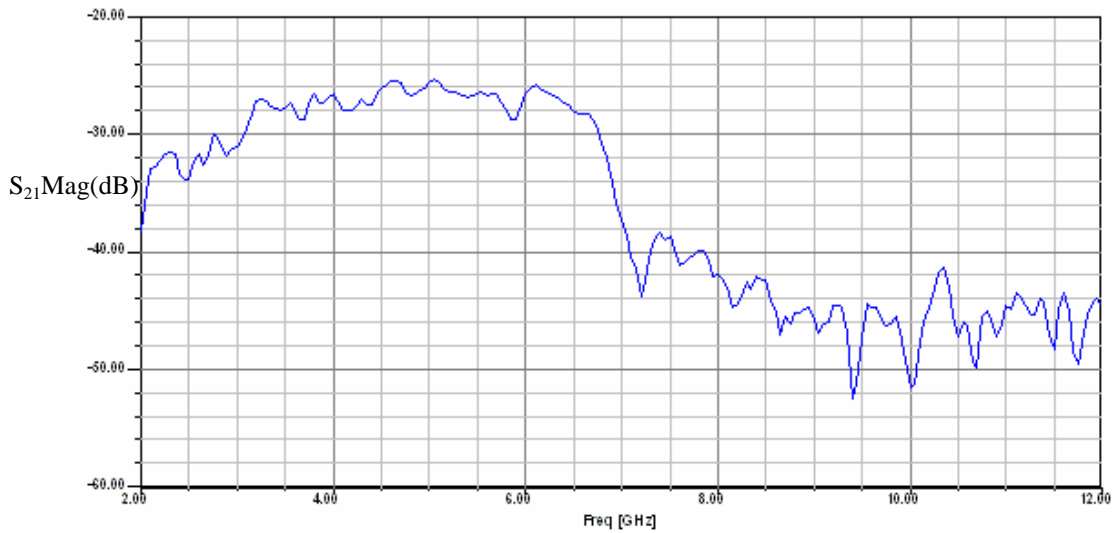


Figure 9.34. Transmission response (S_{21}) for hybrid fed UWB dipole.
Distance between antennas = 20 cm.

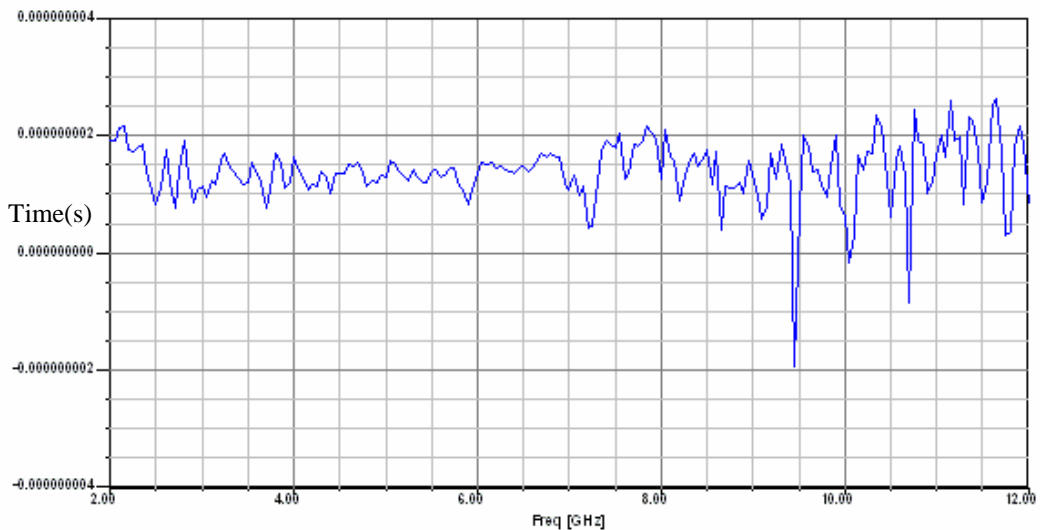


Figure 9.35. Experimental group delay for hybrid fed UWB dipole.
Distance between antennas = 20 cm.

Analyses of the group delay correlates with the transmission response in respect that it degrades after 7 GHz though still has a maximum variation of 2ns comparable to the CPW-fed UWB dipole with slots. The transmission response

for the hybrid fed UWB dipole is excellent, though not quite as linear a response as the CPW fed dipole with slots. The next section investigating the radiation patterns will attempt to address this.

9.2.3.2 Radiation pattern results for hybrid fed UWB dipole

Results were obtained using the anechoic chamber outlined in Chapter 5. The orientation of the antenna with respect to the coordinate system is shown in Figure 9.36.

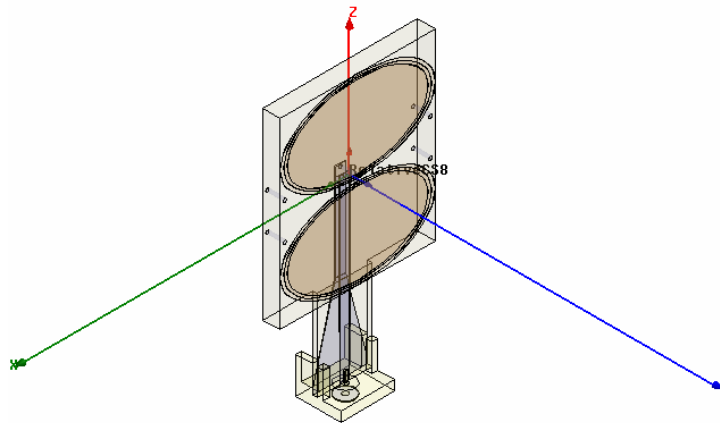
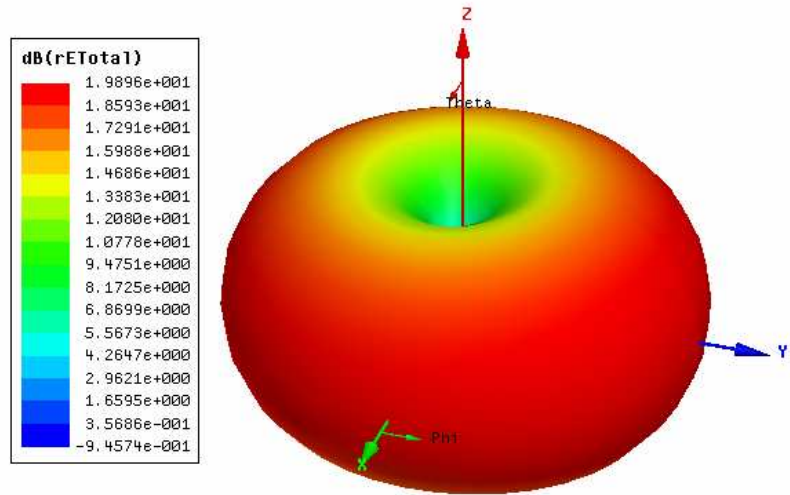
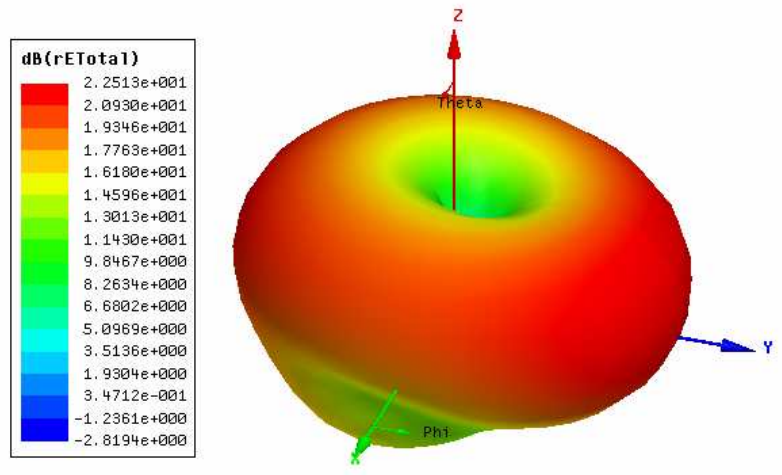


Figure 9.36. Orientation of antenna with respect to coordinate system used for measurements

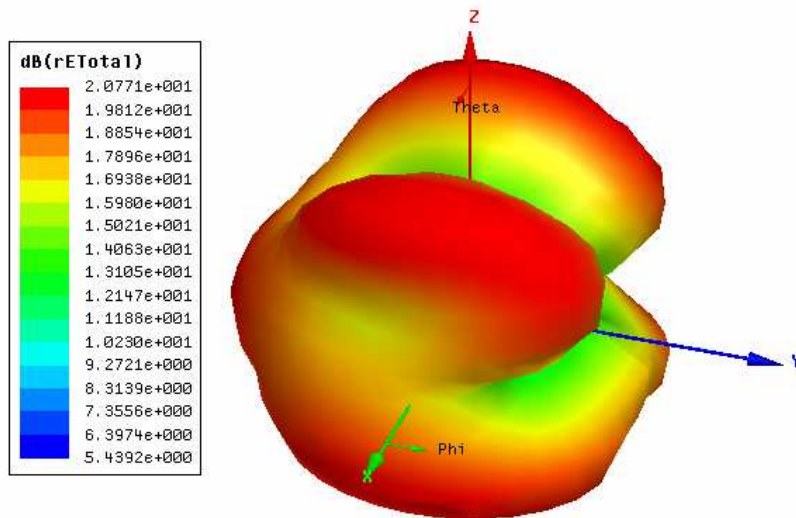
The results for the simulated 3D radiation patterns for electric field in decibels are shown in Figure 9.37. Analyses of the radiation patterns indicate that the antenna is acting as a half-wave dipole at 3 GHz, which confirms the theory in chapter 2.. There appears to be some distortion of the patterns shown by Figure 9.37 (b) and (c), which can be possibly attributed to interaction with the feed due to surface waves. Surface waves will be discussed further in Chapter 9.



(a)



(b)



(c)

Figure 9.37. Simulated 3D E-field radiation patterns for hybrid fed UWB dipole at

(a) 3 GHz (b) 6 GHz and (c) 9 GHz

The simulated and experimental results for the radiation patterns at 3, 6 and 9 GHz are shown in Figure 9.38 in the form of horizontal and vertical cuts.

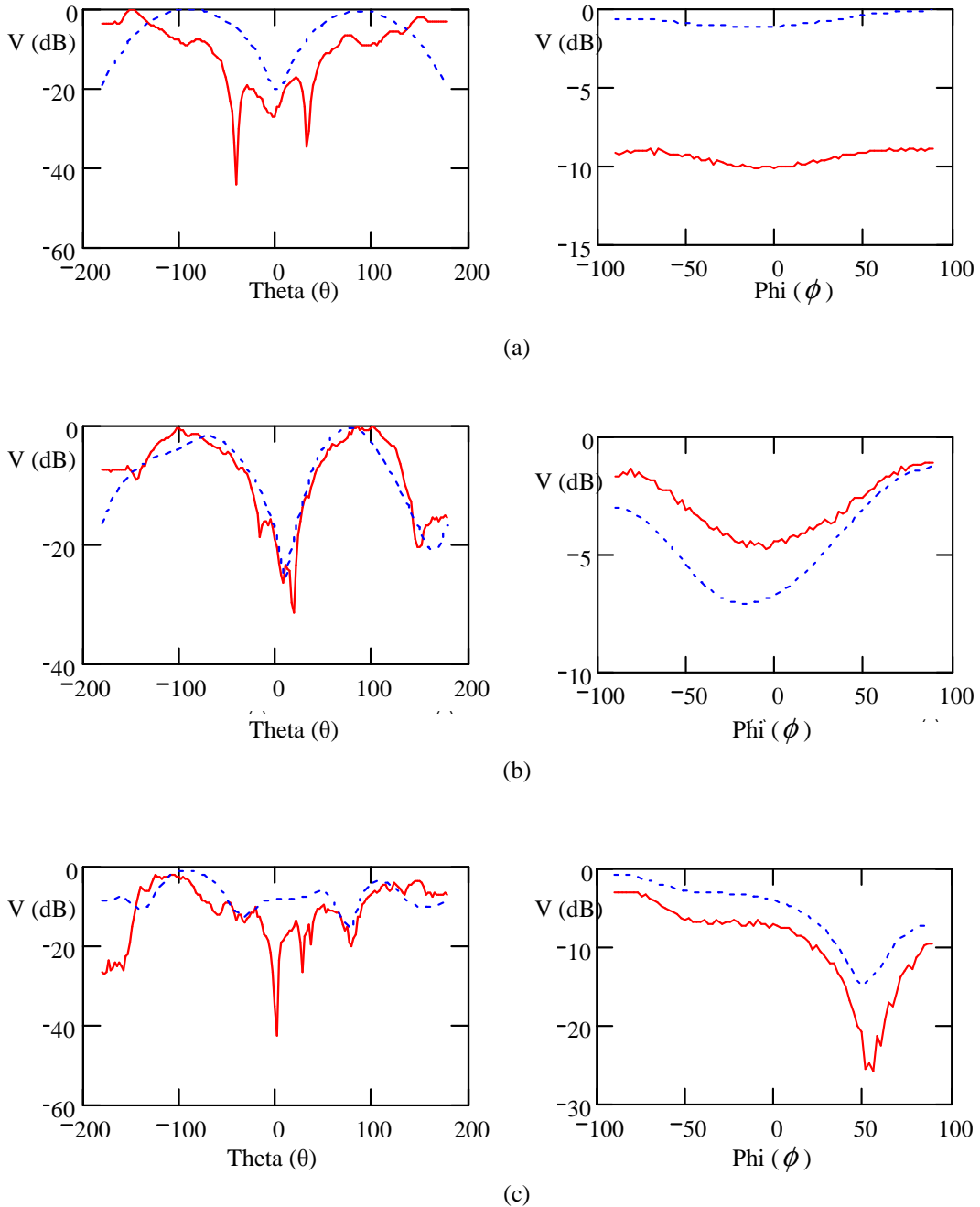


Figure 9.38 Hybrid feed UWB dipole simulated (blue) and experimental (red) horizontal and vertical cuts for (a) 3GHz (b) 6 GHz and (c) 9 GHz

Inspection of the results shown in Figure 9.38 is quite disappointing as the correlation between simulated and experimental results is poor. Figure 9.38 (a)

appears to show evidence of leakage current as there are multiple nulls present and the signal level at boresight is 10dB less than the simulated value. This poor result is reciprocated by the value transmission response, shown in Figure 9.34, at 3 GHz. The phi cut for Figure 9.38 (c) possibly explains the sudden drop in the transmission response at around 7GHz with a large null very close to boresight. The final antenna analysed in this chapter attempts to completely eradicate the leakage current present on the cable and is discussed in the next section

9.2.4 A tapered feed UWB dipole

As a result of both the CPW-fed UWB dipole with slots and the hybrid-fed UWB dipole producing leakage current, it was imperative that an antenna should be designed that did not allow leakage current. To achieve this goal, a transition was designed that was based on the microstrip-to-parallel-plate tapered line balun first introduced by Duncan and Minerva [6]. This balun offers good broadband performance over an octave of bandwidth. Figure 9.39 shows the geometrical layout of the balun.

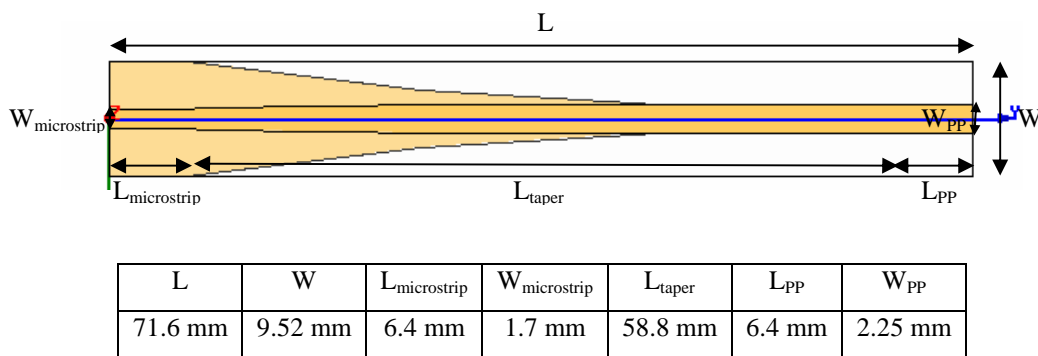


Figure 9.39. Layout of microstrip to parallel-plate tapered line balun. Overall dimensions - length = 71.6mm, width = 9.52mm.

The balun in figure 9.39 operates as follows. The signal is inputted into the balun from a unbalanced source such as a co-axial cable. Co-axial is unbalanced as it has a current, at any given instant, at any location along the line, which flows on the centre conductor, and return currents flow on the inside of the surface of the ground sheath. This configuration is known as an “unbalanced line”. The same principle applies for microstrip line, which is unbalanced. The balun transforms

the signal to the parallel plate waveguide, which consists of a pair of symmetrical conductors. At any given instant, at any location along the parallel plate waveguide transmission line, equal and opposite currents flow. This configuration is known as “balanced”.

The balun was simulated and designed using Rogers 4350 board (permittivity = 3.48). Using HFSS it was possible to manipulate the tapering using three point arcs on both the top and bottom sections. This allowed for the optimum transition between the microstrip and the parallel-plate waveguide. The length of the taper should be approximately at least half a wavelength at the low end of the operational band. This allows for proper manipulation of the fields from a microstrip mode (unbalanced) to parallel-plate (balanced) mode. To verify this, Figure 9.39 shows the surface current plot on both the top and bottom sections.

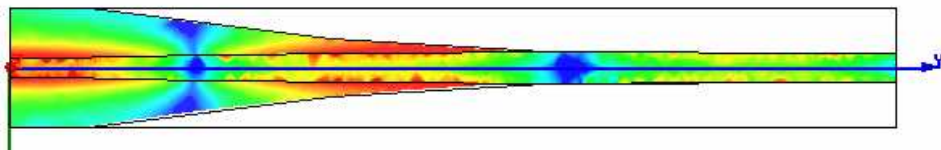
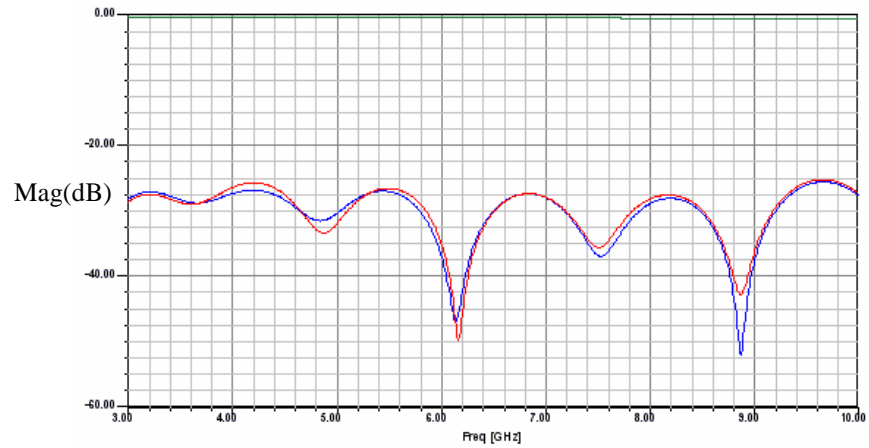
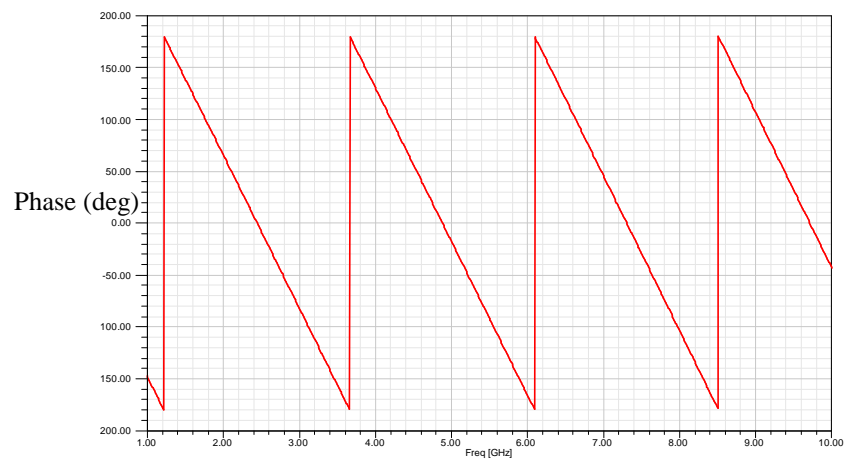


Figure 9.40. Surface current plot for balun at 3 GHz

A quick inspection of Figure 9.40 verifies that length of the transition is greater than a half wavelength at lower end of the operational band (3 GHz). Simulated results for S-parameters after optimisation are shown in Figure 9.40.



(a)

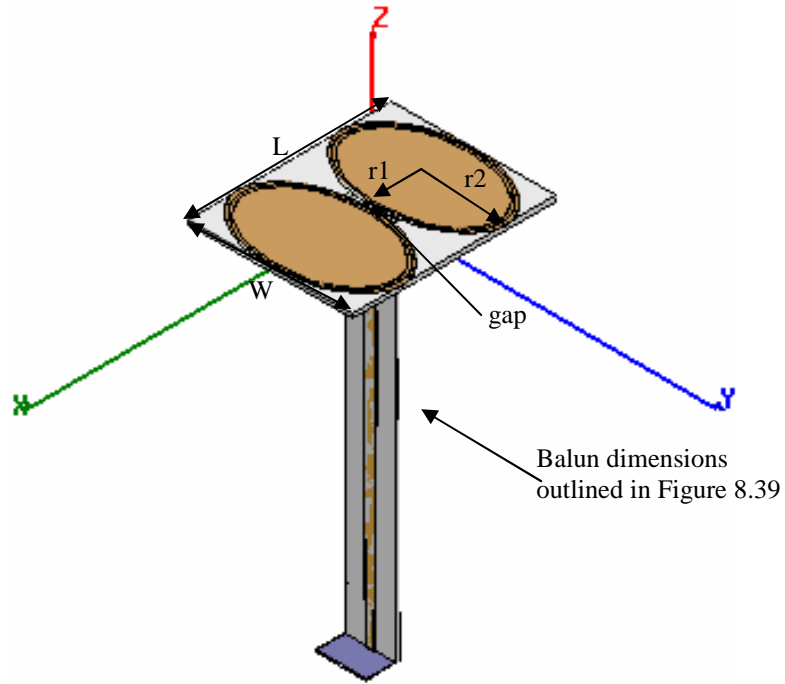


(b)

Figure 9.41 Simulated S-parameter results for balun. (a) S_{21} = Green; S_{11} = Blue; S_{22} = Red
(b) S_{21} phase

As shown by the results in Figure 9.41 the balun offers an excellent transition over the frequency band of interest. The insertion loss at 10 GHz is just 0.55 dB.

The next stage was to integrate the balun with the elliptical antenna elements. Due to the nature of the transition, the only way to integrate this was from the underside, into the centre of the antenna. This is shown in Figure 9.42.



L	W	r1	r2	gap
38.35 mm	30.875 mm	9.5 mm	17.1 mm	0.45 mm

Figure 9.42 Geometrical layout of tapered feed UWB antenna.

To verify that there would be no leakage current present on the feed cable a model was created in HFSS with a 20 cm coaxial cable attached to the antenna and is shown in Figure 9.43.

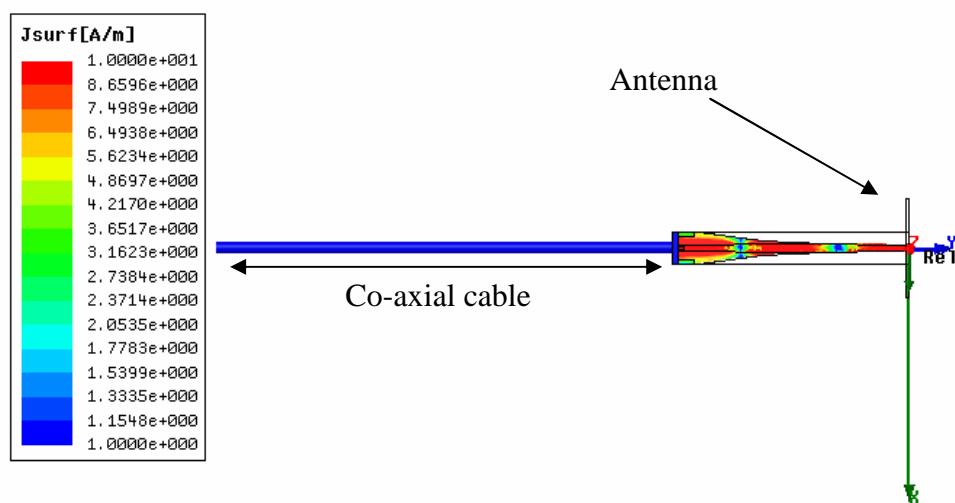
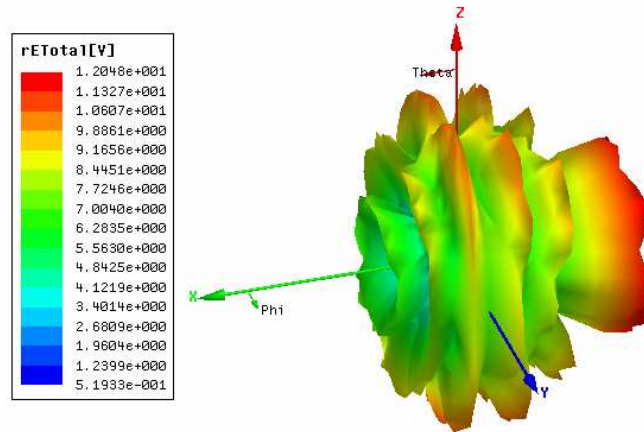
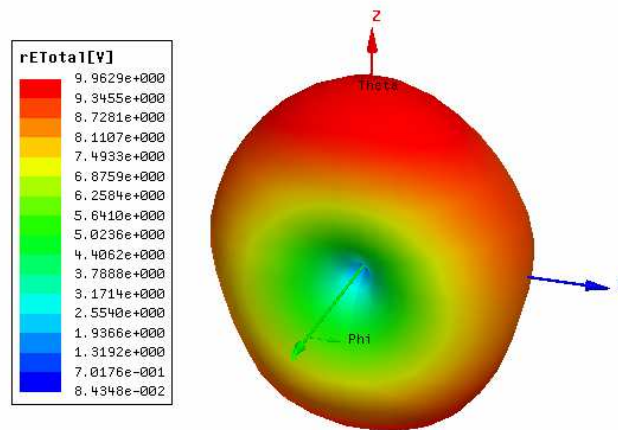


Figure 9.43 Analysis of surface current on tapered feed antenna connected to co-axial cable.

The first thing to note about Figure 9.42 is that the scale is exactly the same as was used for the two previous UWB dipoles analysed in Figures 9.13 and 9.30. With respect to the other UWB dipoles analysed, the tapered feed completely eradicates the problem of leakage current. Another verification of this is the simulated 3D E-field plot at 3 GHz, when compared to the similar plot in Figure 9.31. A comparison is shown in Figure 9.44.



(a)



(b)

Figure 9.44. Comparison of 3D e-field patterns connected to a co-axial cable for (a) Hybrid feed UWB dipole and (b) Tapered feed UWB dipole

As a result of the removal of leakage current on the feed cable the other modes present on the cable are removed. This in turn results in the radiation pattern expected at 3 GHz, that of a half-wavelength dipole.

9.2.4.1 S-parameter results for tapered feed UWB dipole

All practical results obtained in this section were obtained using a Agilent N5230A VNA. The results for the simulated and experimental S_{11} are shown in Figure 9.45.

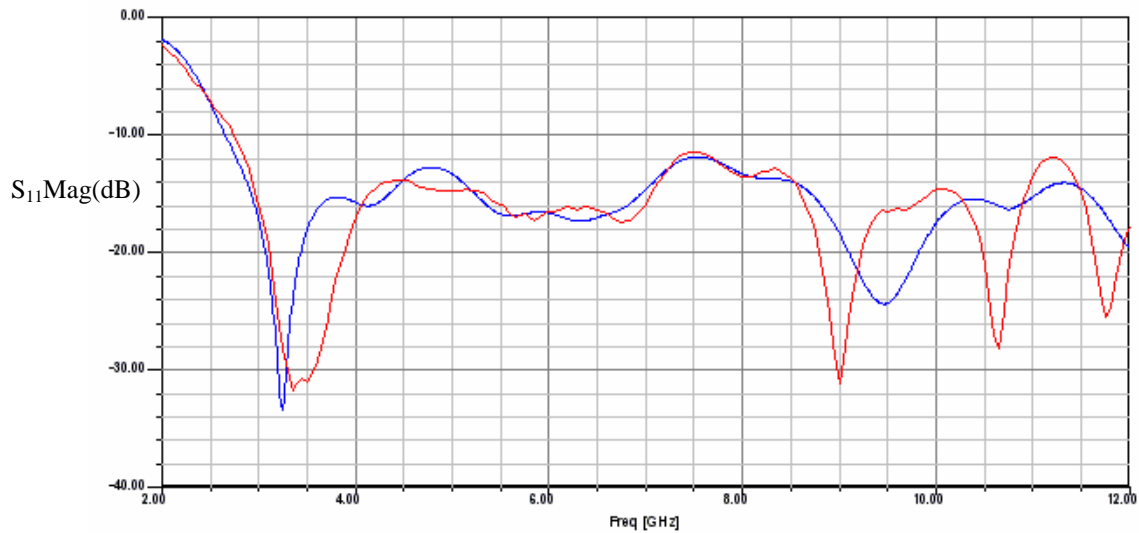


Figure 9.45. Tapered-feed UWB dipole S_{11} results for simulated (blue) and experimental (red)

The correlation between simulated and experimental results for S_{11} is good. There is relatively good agreement over the frequency range and the nulls almost match up, apart from the higher frequency end. The antenna also has the required impedance bandwidth to operate over the UWB spectrum.

An explanation into the slight discrepancy between the experimental and simulated results can be attributed to the manufacturing process. Insertion of the balun into the underside of the dipole elements was extremely tricky and the yield of antennas was very low. This was mainly due to the fabrication process, which involved a metal file being used to remove substrate around the parallel-plate end so that the feed could be inserted into the elliptical elements. A hammer and screwdriver were also used to create a hole for inserting the feed. Once the feed was inserted, the parallel-plate was soldered to the antenna elements. Additional mechanical support was provided by using a cyanoacrylate adhesive.

As mentioned at the start of the chapter the tapered feed UWB dipole is operating in the near-field specified by the boundary limit of $2D^2/\lambda$, which is due to its

maximum linear dimension of 72.362 mm and means that the theoretical far-field boundary exists at 35.5 cm. To investigate whether or not the balun should be included in determining the maximum linear dimension a HFSS simulation was setup to compare the electric field of the tapered feed UWB dipole to that of a half-wavelength dipole at the top end of the operational band, 10.16 GHz. The results are shown in Figure 9.46.

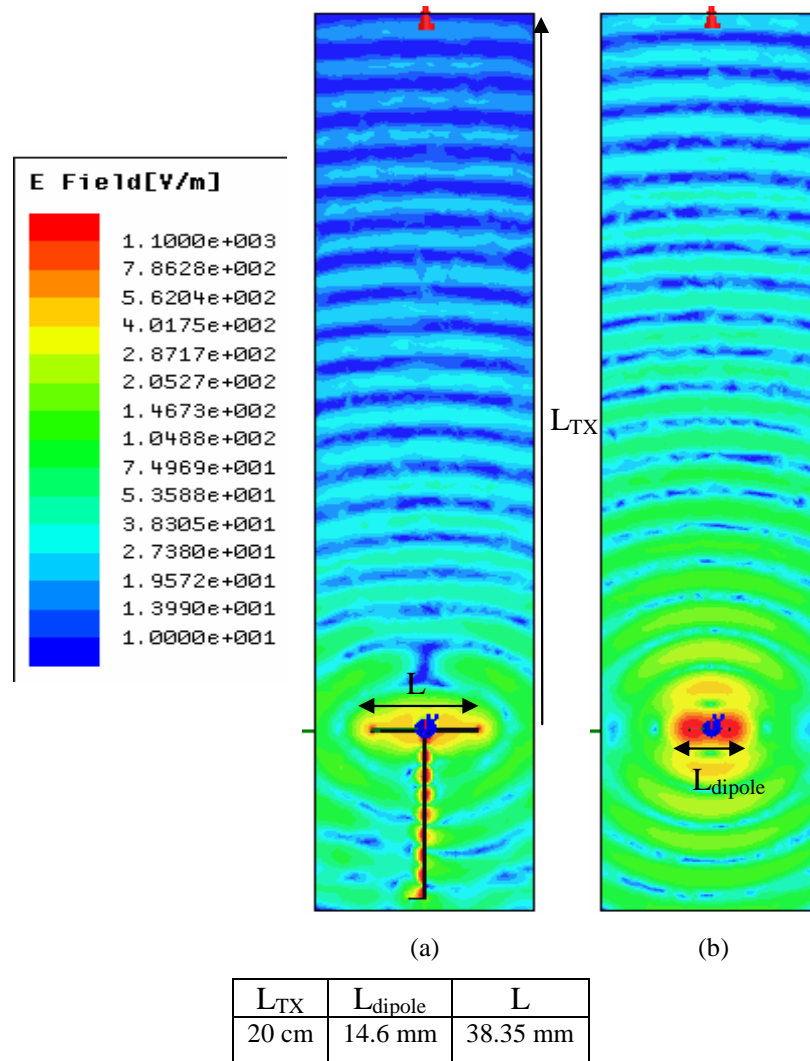


Figure 9.46. E-field at 10.16 GHz for (a) Tapered feed UWB dipole
(b) half-wavelength dipole

Analysis of figure shows that the field being transmitted in the bore sight direction L_{TX} quickly falls into an approximation of a plane wave at about 10 cm. This value is also the theoretical value of the boundary limit, specified by $2D^2 / \lambda$,

for a maximum linear dimension of 38.35mm, which equals L for the tapered feed UWB dipole.

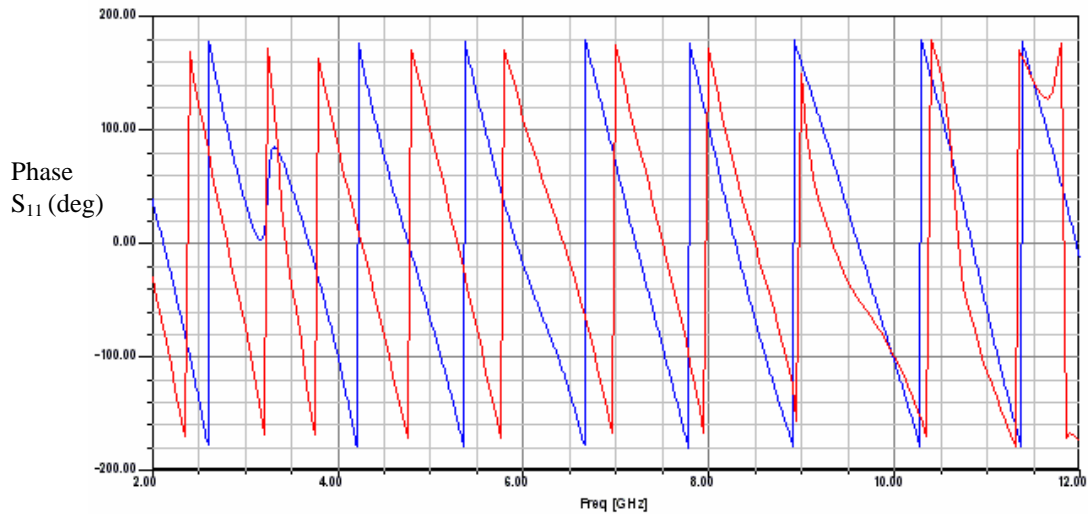


Figure 9.47. Simulated (blue) and experimental (red) results for phase

Analysis of the phase in Figure 9.46 shows good correlation between experimental and simulated results, especially when compared to the results obtained from the previous three antennas analysed in this section. At the lower end of the operational band, the experimental results were out of phase when compared to the simulated result. However the experimental phase has greater linearity over the entire band when compared to the simulated results. The reasons for this are as yet unclear.

Analysis of the transmission response, shown in Figure 9.47, shows excellent performance up to 9 GHz, where the response drops away quite suddenly to a very low level. If transmission response did not drop to -60 dB between 9 and 10 GHz then the tapered feed UWB dipole would be outperforming all the antennas previously discussed in this section.

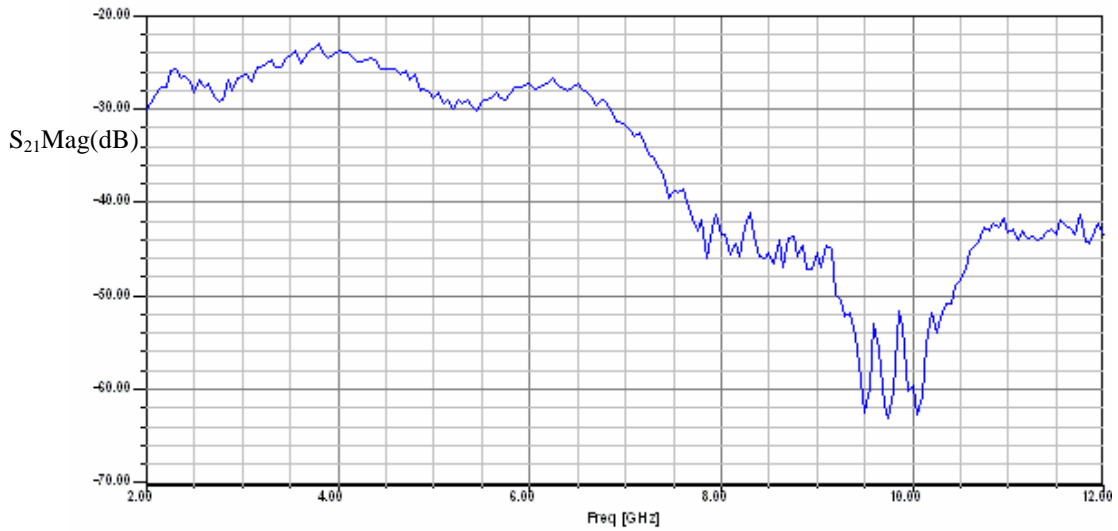


Figure 9.48. Transmission response (S_{21}) for tapered feed UWB dipole.

Distance between antennas = 20 cm.

Analysis of the group delay, shown in Figure 9.49, reveals a large spike located between 9 and 10 GHz. At this late stage in the project it is hard to ascertain what is causing this large degradation in performance for both the transmission and group delay responses. However, apart from the spike, the tapered feed UWB dipole has good performance with a maximum variation of 10 ns.

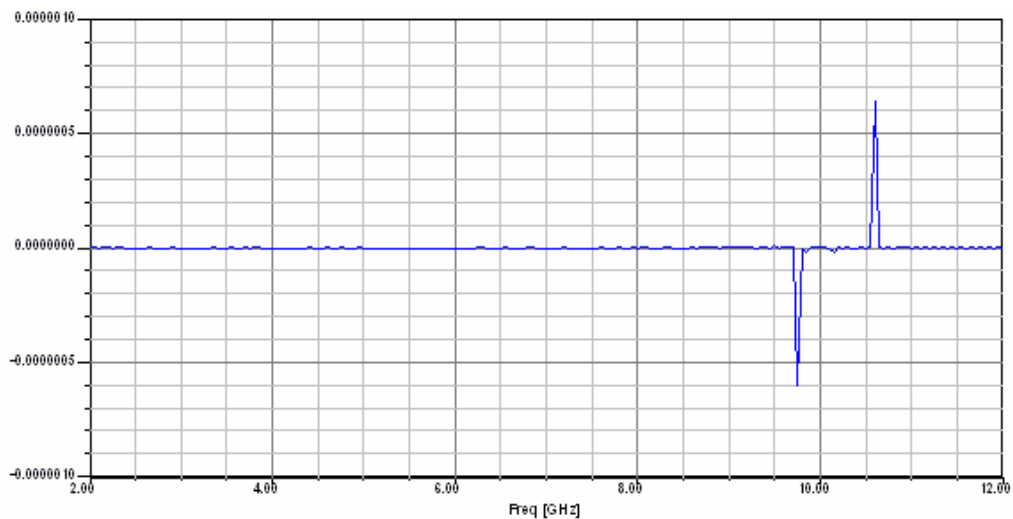


Figure 9.49. Experimental group delay for tapered feed UWB dipole.

Distance between antennas = 20 cm.

9.2.4.2 Radiation pattern results for tapered feed UWB dipole

Results were obtained using the anechoic chamber outlined in Chapter 5. The orientation of the antenna with respect to the coordinate system is shown in Figure 9.49.

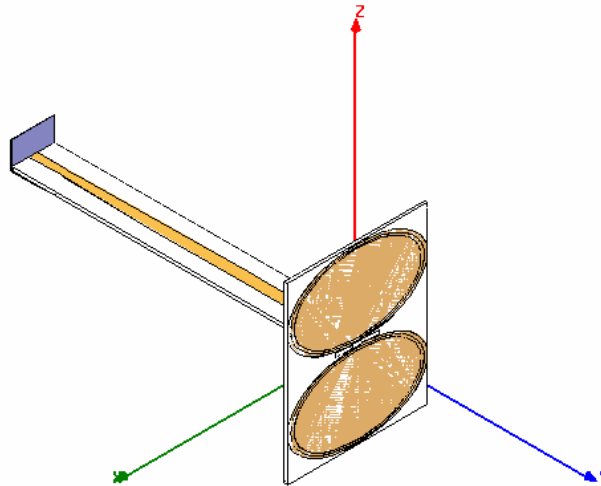
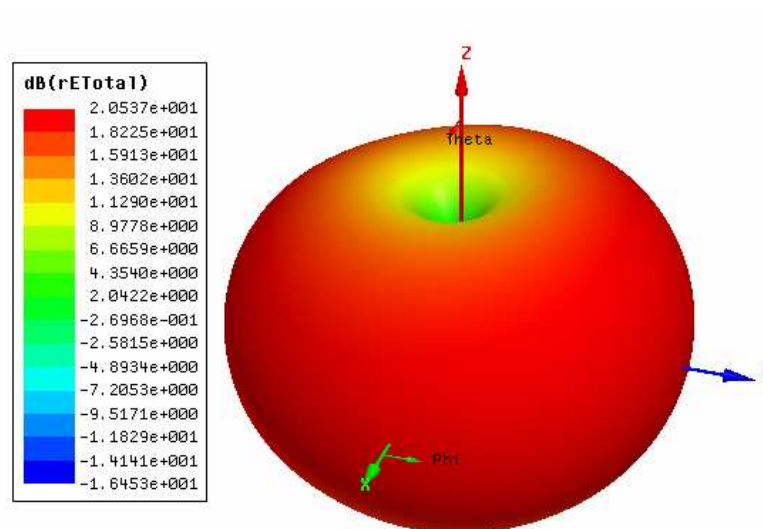


Figure 9.50. Orientation of antenna with respect to coordinate system used for measurements

The results for the simulated 3D radiation patterns for electric field in decibels are shown in Figure 9.50. Analyses of the simulated patterns indicate that the antenna is acting above a half-wave dipole at 3 GHz, hence the slightly misshapen pattern. This is due to the fundamental frequency being slightly lower, around 2 GHz. The other radiation patterns at 6 and 9 GHz conform to the expected shape, which confirms the theory in chapter 2.



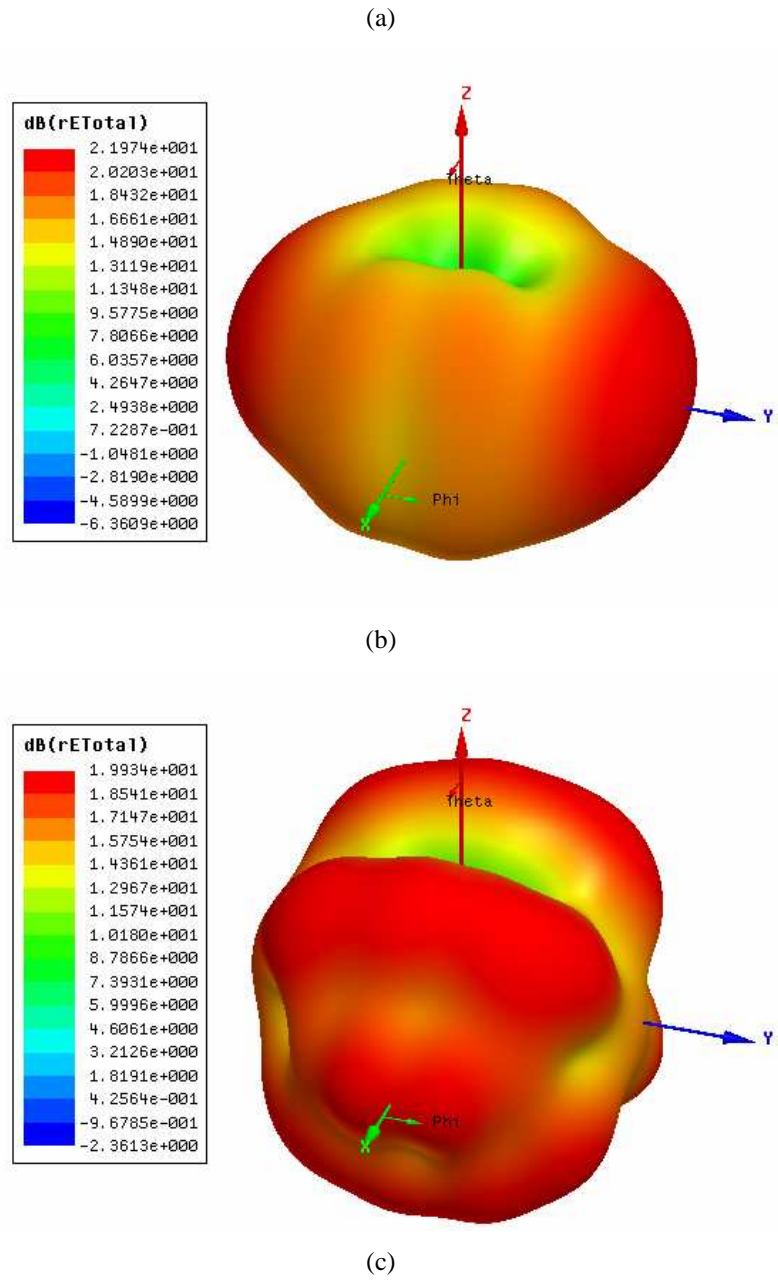


Figure 9.51. Simulated 3D E-field radiation patterns for tapered feed UWB dipole at (a) 3 GHz (b) 6 GHz and (c) 9 GHz

The simulated and experimental results for the radiation patterns at 3, 6 and 9 GHz are shown in Figure 9.51 in the form of horizontal and vertical cuts.

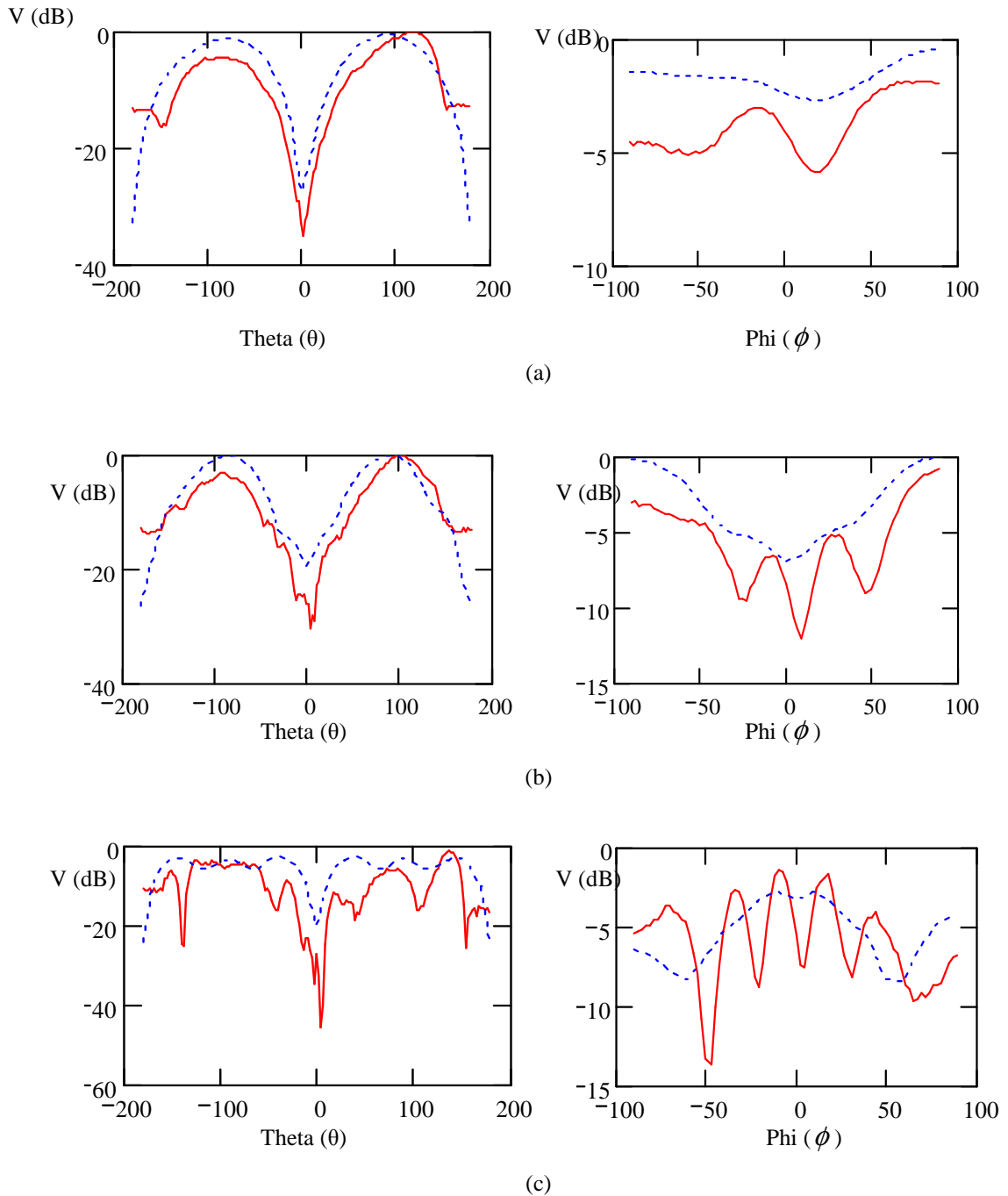


Figure 9.52 Tapered feed UWB dipole simulated (blue) and experimental (red) horizontal and vertical cuts for (a) 3GHz (b) 6 GHz and (c) 9 GHz

Inspection of the results shown in Figure 9.51 show relatively good agreement between simulated and experimental for the theta cuts. The results for Figure 9.51 (b) and (c) are quite surprising as they are not indicative of leakage current as the main beam is normal to the feed cable, and as result is normally observed via the horizontal cut. A possible explanation is that due to the fabrication of the antenna there is an excitation of another mode due to mismatch at the higher frequency end of the operational band. Inspection of the S_{11} response in Figure 9.45 shows three sharp resonances that are not visible on the simulated response.

This unexpected radiation pattern response may also explain the dip in transmission response, shown in Figure 9.47, which occurs after 7 GHz. The next section evaluates the UWB pulse transmission performance of the various antennas described in this chapter.

9.3 Comparison of UWB dipoles for pulse transmission

Once the characterisation of the UWB dipoles was completed the next step was to evaluate their performance within a UWB test system. The test system used was the previously shown Figure 9.1.

In UWB engineering the Gaussian family of time domain signals are commonly used. A Gaussian signal has the mathematical form:

$$v(t) = Ae^{-\frac{(t-B)^2}{2\tau^2}} \quad (9.1)$$

Where,

A = amplitude of signal

B = centre position of peak

τ = half-width of pulse

Using Mathcad [7] an example of a zero order Gaussian pulse is shown in Figure 9.52.

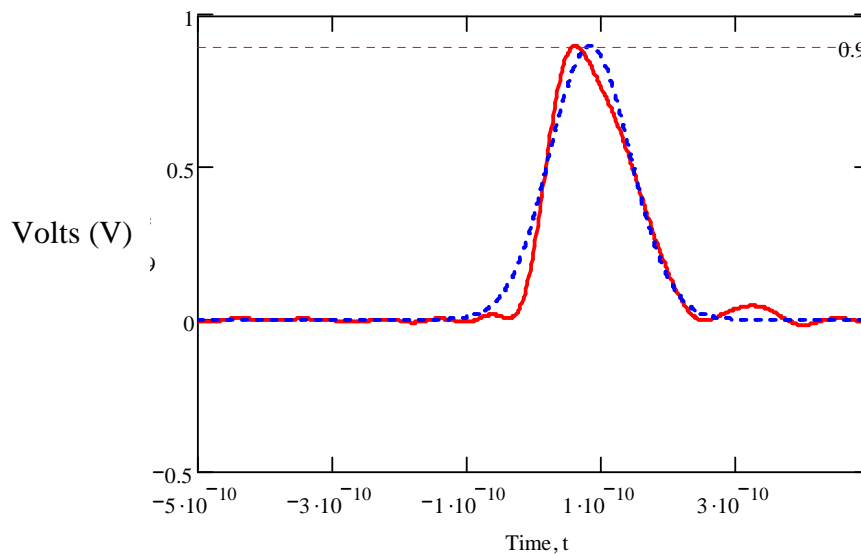


Figure 9.53. Comparison of theoretical (blue) and experimental (red) results for a 100 ps pulse

The other waveform displayed in Figure 9.52 was the signal received from the pulser obtained via the communications analyser. The pulser was set to transmit a 100 ps pulse with a voltage of 1V. As shown in Figure 9.51 the signal received has a voltage of 0.9V. The difference can be attributed to loss in the cable.

A 100 ps pulse has bandwidth of 10 GHz and the antennas were designed to operate above 3 GHz. This meant any signal portion below 3 GHz would theoretically not be received and would potentially result in major dispersion. To avoid this, a high pass filter was inserted into the system. The high pass filter allowed all frequencies above 3 GHz to be transmitted and shaped the pulse into a ‘monocycle’, which is the first derivative of a Gaussian signal. This is shown in Figure 9.53.

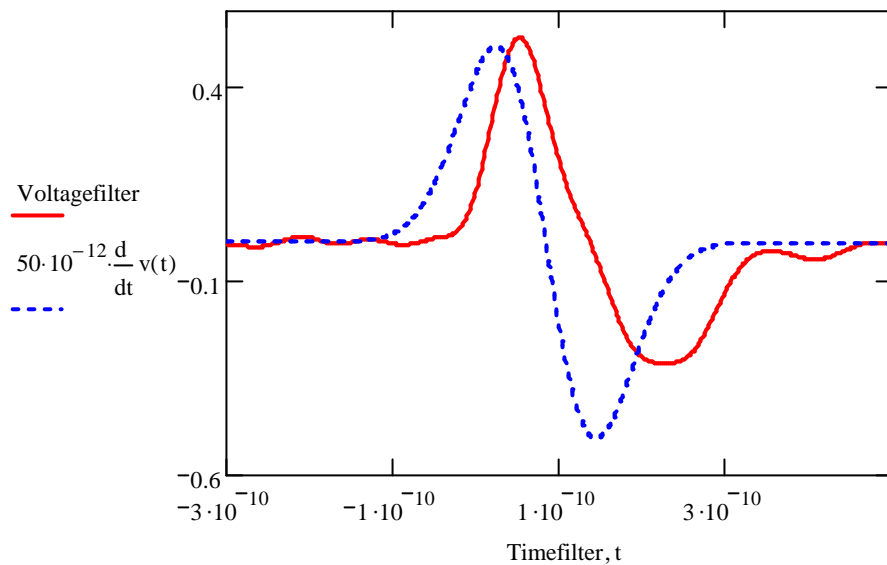


Figure 9.54. 1st derivative of Gaussian function experimental (red) and theoretical (blue) results

The theoretical result has to be multiplied by a value of 50×10^{-12} otherwise it does not fit within the scale. The reason behind this is because the slope of the original function is so steep. In reality only an approximation to the derivative could be obtained. It is noted that there is some distortion and signal loss, due to the system, on the pulse already.

Before investigating pulse transmission it was important to anticipate what would happen to the waveform during transmission. The expected result was that of a 2nd derivative of the Gaussian function as the antennas are acting as high pass filters, which differentiate the signal. The theoretical waveform is shown in Figure 9.54.

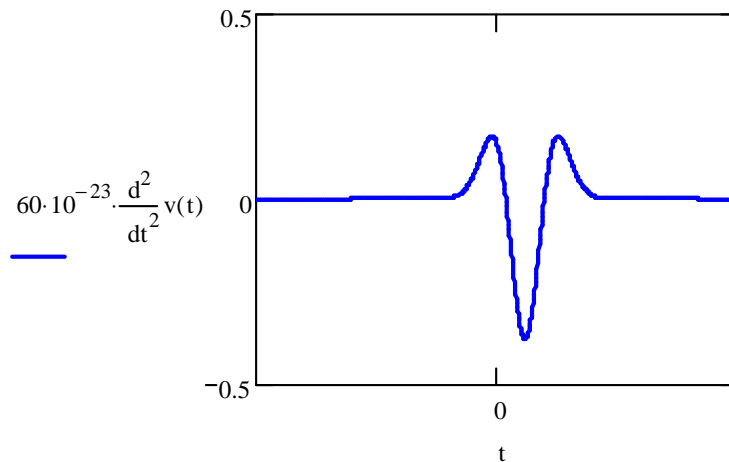


Figure 9.55. 2nd derivative of Gaussian function

The pulse was transmitted line of sight over a distance of 20 cm. The elliptical elements were facing each other and perpendicular to the direction of propagation. The voltage on the Pulser was set to 10V, which was the maximum. The results for pulse transmission are shown in the following sections.

9.3.1 Pulse transmission via microstrip fed UWB dipoles

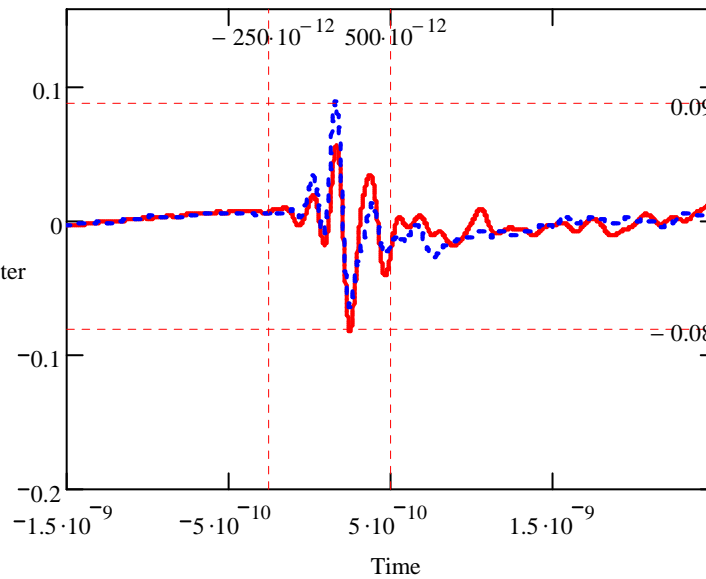


Figure 9.56. Pulse received using microstrip-fed UWB dipole with filter (red) and without filter (blue)

The results for pulse received, with and without a filter, for the microstrip-fed UWB dipole is shown in Figure 9.55. The microstrip-fed UWB dipole yields poor results for pulse transmission. The 2nd order Gaussian is distinguishable but the amplitude of the signal received is poor. The surprising aspect is that the filter appears to add distortion to the pulse as it is designed as a high pass filter for 3 GHz and beyond. One possible explanation is that inserting the filter into the network has an adverse impact on the matching for the antenna used in the system. A slight drop in the received signal voltage is expected as extra insertion loss is added as a result of the filter in the system.

The peak to peak voltage received is approximately 0.155 V. Using the following formula it is possible to calculate the loss (in dB) due to the channel plus antennas.

$$Loss(dB) = 20 \log \frac{V_1}{V_2} \quad (9.2)$$

If $V_1 = 15.5$ mV and $V_2 = 10$ V it represents an overall loss of -35.4 dB, comparable with the transmission losses measured in Figure 9.6.

To the authors knowledge there is currently no method used to quantify received pulse quality with respect to distortion. The following method is proposed to give a quick insight into the quality. Ideally the pulse should arrive with no distortion, which means a completely flat response after the pulse. In the case of Figure 9.54 the response should be flat after 500ps i.e. a zero voltage level. A relationship between the peak-to-peak voltage of the pulse and the distortion after it is defined as:

$$\text{Distortion Factor (DF)} = \frac{\text{Max distortion (} V_{pk} \text{) after pulse}}{\text{Pulse voltage (} V_{pk} \text{)}} \quad (9.3)$$

Equation 9.3 implies that distortion factor will be zero if there is no distortion after the pulse. It is also useful to quantify the amount of noise relative to the amplitude of the received pulse. Values for distortion factor were calculated for the pulses in Figure 9.53.

With filter:

$$DF = \frac{0.03}{0.14} = 0.21$$

Without filter:

$$DF = \frac{0.033}{0.155} = 0.16$$

Analysing the results for distortion factor it is clear that the microstrip-fed UWB dipole performs better without the filter.

9.3.2 Pulse transmission via CPW-fed UWB dipole with slots

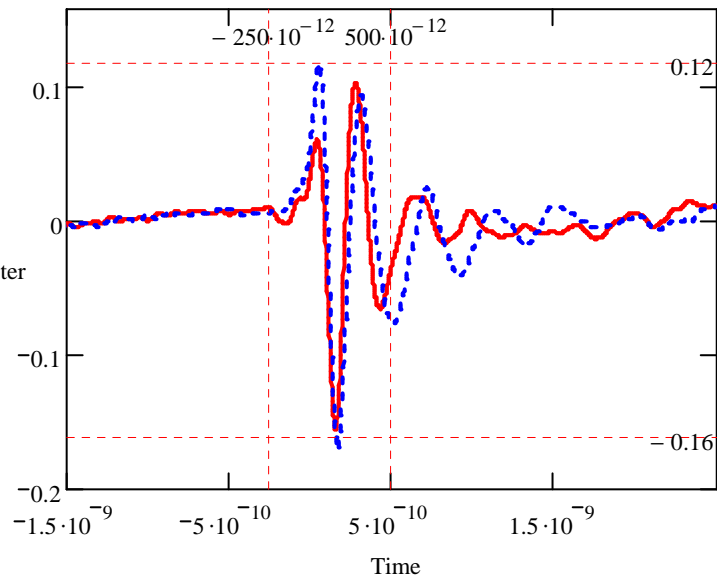


Figure 9.57. Pulse received using CPW-fed UWB dipole with slots with filter (red) and without filter (blue)

The results for pulse received, with and without a filter, for the CPW-fed UWB dipole with slots are shown in Figure 9.56. Compared to the microstrip-fed UWB dipole of the previous section the signal received by using the CPW-fed UWB dipole, has a larger peak-to-peak voltage both with and without the filter. The overall channel loss is -31 dB (using a peak-to-peak voltage of 0.28 V), in general agreement with the transmission response shown in Figure 9.20. For this antenna it appears that incorporating the filter is advantageous as it reduces dispersion.

Using Equation 9.3 distortion factor values were calculated with the filter:

$$DF = \frac{0.04}{0.265} = 0.15$$

Without the filter:

$$DF = \frac{0.055}{0.29} = 0.18$$

Analysing these value they correspond to Figure 9.55 that the pulse with the filter has less distortion. Also the pulse received using the filter plus the CPW-fed UWB dipole performs better than the pulse received by microstrip-fed UWB dipole.

9.3.3 Pulse transmission via hybrid feed UWB dipole

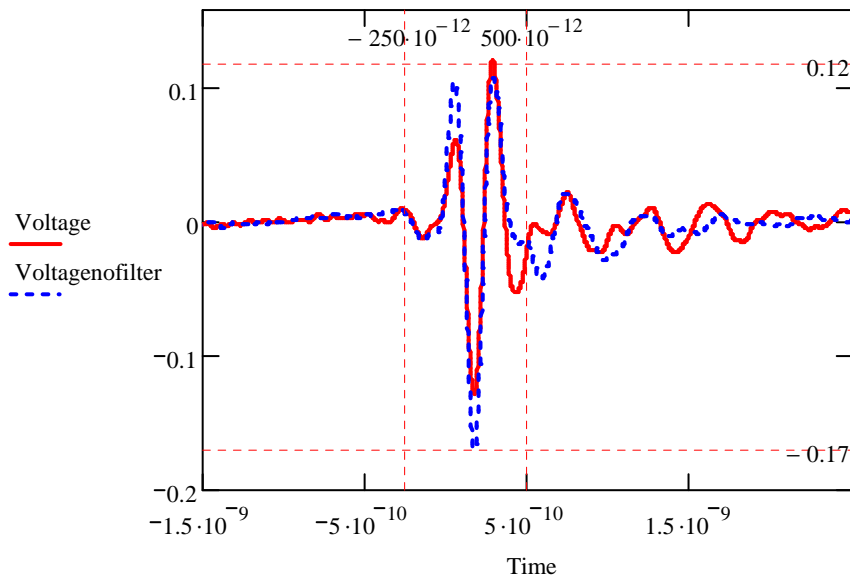


Figure 9.58. Pulse received using hybrid feed UWB dipole with filter (red) and without filter (blue)

The results for pulse received, with and without a filter, for the hybrid feed UWB dipole are shown in Figure 9.57. Analysis of the pulse received using the hybrid-fed UWB dipoles shows a slightly narrower pulse received than the previous two antennas in 9.3.1 and 9.3.2. A narrower pulse indicates that less dispersion is occurring due to the antennas. The overall channel loss is -30.7 dB using a peak-to-peak voltage of 0.29 V. This value corresponds with the transmission response in Figure 9.34. For this antenna the dispersion is slightly less without the filter, reasons for this are discussed in section 9.3.4.

Using Equation 9.3 distortion factor values were calculated with the filter:

$$DF = \frac{0.04}{0.25} = 0.16$$

Without the filter:

$$DF = \frac{0.04}{0.28} = 0.14$$

These values suggest that the pulse without the filter has slightly less distortion. While there is not much difference between the distortion factor values, inspection of Figure 9.57 shows the distortion on the pulse without the filter tends to zero after 1.5 ns, while the pulse with the filter still has distortion present.

9.3.4 Pulse transmission via tapered feed UWB dipole

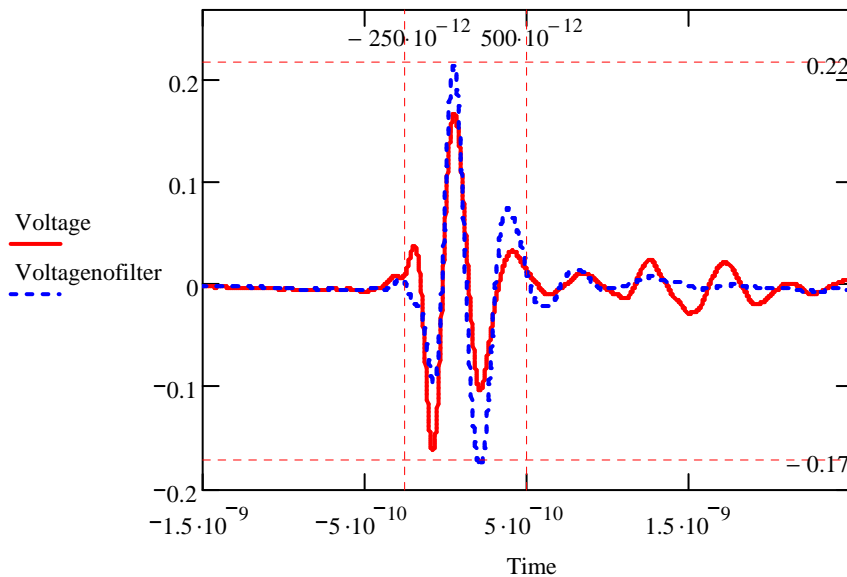


Figure 9.59. Pulse received using tapered-feed UWB dipole with filter (red) and without filter (blue)

The results for pulse received, with and without a filter, for the tapered feed UWB dipole are shown in Figure 9.58. As expected, the pulse received for the tapered-feed UWB dipole has the best response both with and without the filter. The pulse is short and without the filter there is hardly any distortion. Another possible explanation for the distortion can now be given. The filter that is used in the test system is effectively a short circuit stub fabricated in microstrip and is not shielded. The distortion could represent a portion of the signal being radiated via the stub at frequencies at the higher end of the operational bandwidth.

Using the a peak-to-peak voltage of 0.39 V the loss due to the channel is -28.1 dB, which is in agreement with Figure 9.46. Using Equation 9.3 distortion factor values were calculated with the filter:

$$DF = \frac{0.055}{0.33} = 0.166$$

Without the filter:

$$DF = \frac{0.032}{0.395} = 0.081$$

The difference between the distortion factor values highlights the impact of the filter in adding distortion.

9.4 Evaluation of UWB dipoles

This section compares appropriate performance metrics of the various antennas discussed in this chapter. As all antennas have similar simulated radiation patterns and group delay results these parameters are omitted from table 9.1.

Antenna	Microstrip-fed UWB dipole with slots	CPW-fed UWB dipole with slots	Hybrid-fed UWB dipole	Tapered feed UWB dipole
Operates over bandwidth (3.16-10.16 GHz)	No	Yes	Yes	Yes
Leakage Current	Yes	Yes	Yes	No
Size	Small	Small	Medium	Large
DF with filter	0.21	0.15	0.16	0.166
DF without filter	0.16	0.18	0.14	0.081
Signal Loss (dB)	-35.4	-31	-30.7	-28.1

Table 9.1. Performance comparison of UWB dipoles

It is clear from table 9.1 and all the previous work in this chapter that the tapered feed UWB dipole has the best characteristics for operation in a UWB channel modelling experiment. The only drawback is the size and ease of integration into a integrated circuit due to the complex feeding arrangement. If the feeding arrangement for Hybrid-fed UWB dipole was extended then it would likely give a similar performance to that of the tapered feed UWB dipole. It would also have the advantage of having the null of the far-field radiation pattern positioned so that the feed cable sits in the null for the majority of operational bandwidth. Though from pulse transmission experiment, which is only line of sight, it appears this does not matter.

This chapter concludes the research carried out on suitable UWB antennas for wireless sensor network applications. The following chapter investigates narrowband transceiver architectures and suitable antennas.

10. Narrowband Antenna Design

This chapter discusses the design work carried out in direct relation to the Speckled Computing Consortiums objective of designing a 5mm³ ‘Speck’. Antennas discussed in this chapter are designed at the 2.4 GHz and 5.8 GHz ISM bands. To give an understanding of frequencies chosen the next section discusses the radio architectures investigated during this project.

10.1 Narrowband Radio Architectures

As discussed in chapter 1, for the autonomous wireless sensors of the Speckled Computing Consortium strict requirements are placed on the RF-front end. Perhaps the most challenging is low power consumption (less than 400uW). As the power requirements for conventional narrowband systems far exceeded the power budget for the RF front-end a lower power system was investigated. The design chosen removed the power consuming mixers, and simplified the topology. The architecture chosen was based on incoherent diode detection, and is discussed in the next section.

In combination with a super regenerative detector receiver, a further reduction in the power consumption was obtained. This architecture is outlined in section 10.1.1.

10.1.1 Diode rectifier

One way to reduce power consumption is to use a simple modulation scheme such as On-Off Keying (OOK), as this facilitates the design of very simple circuits with small numbers of active devices. Figure 10.1 shows the layout of a diode rectifier circuit which comprises of a directly modulated oscillator and antenna on the transmit (TX) side. The receive (RX) side comprises of an antenna, a low noise amplifier and an envelope detector. It was found that it was necessary to insert an amplifier at the Rx side to get a usable signal level.

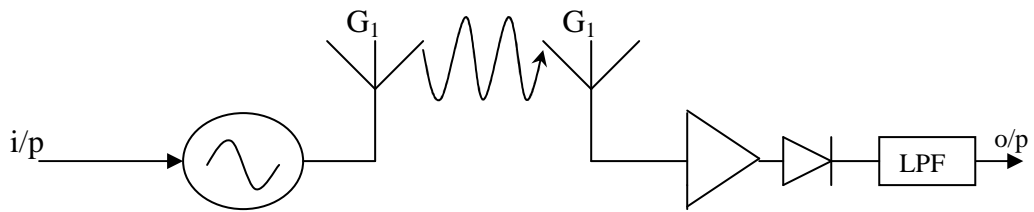


Figure 10.1. Diode rectifier circuit.

This architecture proved very sensitive, with signals as low as -45 dBm being detected. However, after further research, a radio architecture with even greater sensitivity was uncovered, the Super Regenerative Receiver (SRR).

10.1.2 Super Regenerative Receiver (SRR)

Savings in power can be made if a super heterodyne receiver is replaced with a passive envelope detector, or a super-regenerative detector. Super-regenerative detectors were invented in 1922 by Armstrong [1], and uses the high gain that an oscillator generates when it is repeatedly pulled in and out of oscillation by a quenching signal used to ‘regenerate’ the incoming OOK signal. This regenerated signal is then applied to an envelope detector to produce the base-band data. Figure 10.2 shows a block diagram of the SRR.

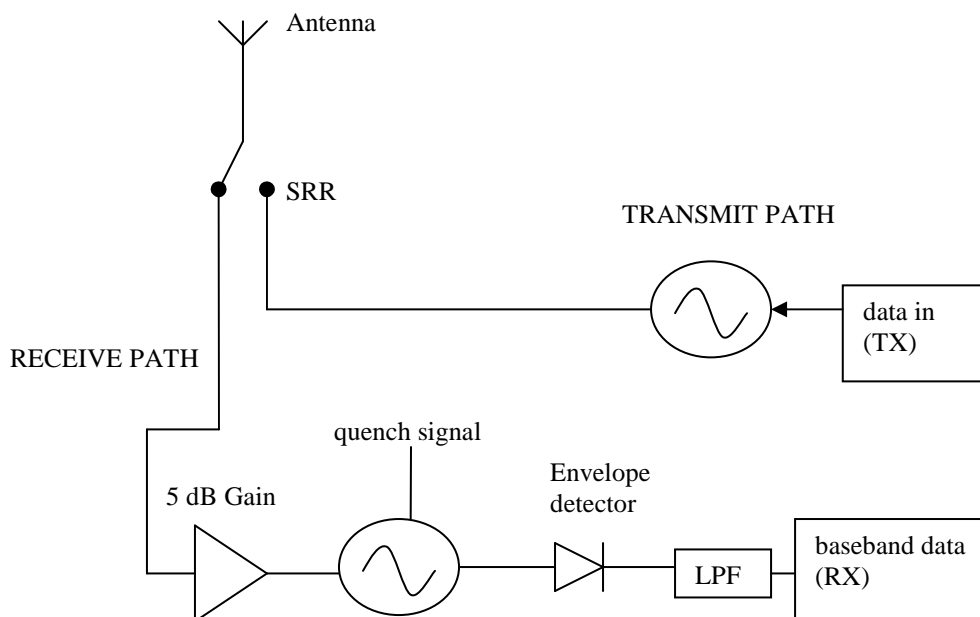


Figure 10.2. Block diagram of complete narrowband transceiver

The receiver consists of a low noise, low gain (5dB) amplifier, a super-regenerative oscillator, and passive envelope detector, which includes a second-order low-pass filter. The amplifier isolates the super-regenerative oscillator signal from the antenna and hence prevents transmission during reception. The amplified OOK signal is applied to the gate of the oscillator along with the quenching signal but this time through the biasing circuit. The regenerated signal is then detected and processed at baseband.

The super-regenerative architecture ensures large output voltages for small input powers but also introduces noise to the signal. These noise levels are acceptable however, as the SRR enables work to be carried out within the stringent power budget of $400 \mu\text{w}$. Shown in Figure 10.3 is a comparison of the output voltage for both diode rectifier circuit and the SRR as a function of input signal power, published by I. Mcgregor [2].

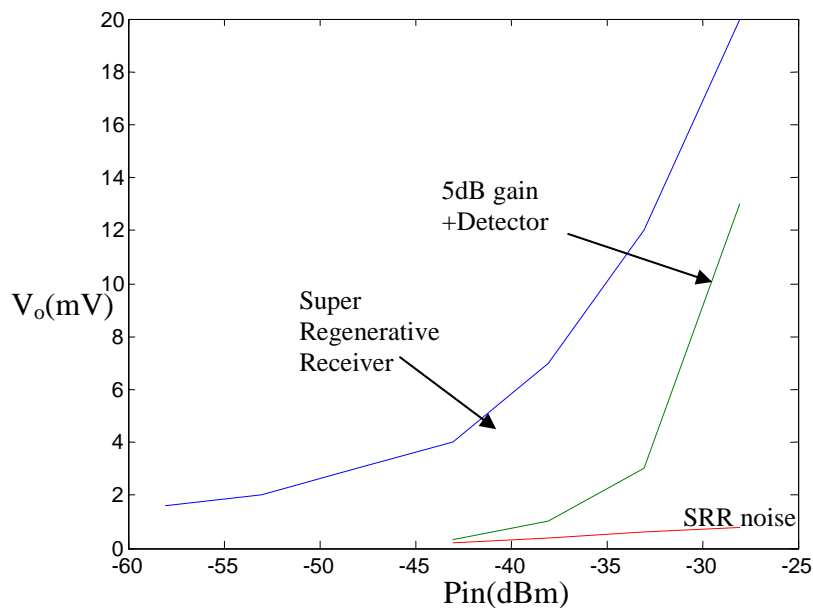


Figure 10.3. Output voltage vs. Input power for diode rectifier and SRR

10.1.3 Comparison of SRR link budgets at varying frequencies

This section illustrates the impact of the frequency on the power-link budget. The two architectures that are covered in this section are the diode rectifier and the

SRR. Three antennas (rectaxial, folded dipole and pseudo patch) are used in this comparison at representative frequencies of operation

The power-link budget is calculated by using collected data from simulated and experimental results. The Friis equation is given for power and power in dBm by Equations 10.1 and 10.2. A block diagram showing the parameters used to calculate the free space loss is shown in Figure 10.4.

$$P_r = \left(\frac{\lambda}{4\pi R} \right)^2 G_1 G_2 P_t \quad (10.1)$$

$$P_{r(dBm)} = 10 \text{Log} \left(\frac{P_r}{1 \times 10^{-3}} \right) \quad (10.2)$$

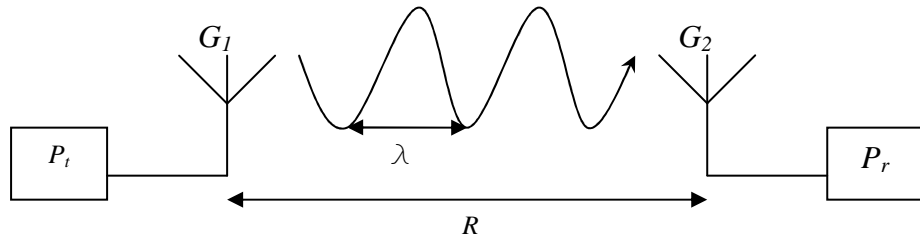


Figure 10.4 Basic block diagram illustrating Friis equation.

The Friis transmission equation is defined by Balanis [3]. It relates the power delivered to the receiver (P_r) to the input power of the transmitting antenna (P_t) between two antennas separated by a distance, R , greater than $2D^2 / \lambda$ where D is the maximum linear dimension of the antenna. The term $(\lambda/4\pi R)^2$ is known as the free-space loss factor and accounts for the spherical spreading of energy by the antenna. For example, at 2.45 GHz, $\lambda=0.1224$ m and if both antennas are considered to be isotropic radiators (i.e. gain of 1), with a separation of $R = 0.1$ m, and input power of 0 dBm (1mW), then the output power will be -40 dBm (0.1 μ W). This means that there is a -20 dB loss in the channel. It is important to remember that this only occurs if the antennas are pointing directly at each other and there is no polarisation mismatch.

To calculate the power link budget known values of gain, and output powers are combined with the Friis equation to create a table including all the losses and gains. The target power consumption for the system is to be less than $400 \mu\text{W}$ (-4 dBm). Shown in tables 10.1, 10.2 and 10.3 are approximate link budgets for a 10 cm distance between transceivers at 2.45 GHz and 5.8 GHz. The values for antenna gain in table 10.1 are measured, while those in tables 10.2 and 10.3 are simulated values. It is assumed that the characteristic impedance of the system is 50Ω . The antennas given in tables 10.2 and 10.3 are discussed in Sections 10.2 and 10.3 respectively.

Frequency = 2.45 GHz; R = 0.1 m; Antenna Type: Rectaxial				
Oscillator	Antenna(Tx)	Channel Loss	Antenna(Rx)	Amplifier
-10.85dBm	2.2dBi	-20 dB	2.2dBi	5 dB
Received Power		Output Voltage (rms)		
-21.45 dBm		20 mV		

Table 10.1 Power link budget for 2.45 GHz

Frequency = 5.8 GHz; R = 0.1 m; Antenna Type: Folded dipole over ground				
Oscillator	Antenna(Tx)	Channel Loss	Antenna(Rx)	Amplifier
-10.85dBm	-8.6 dBi	-34 dB	-8.6 dBi	5 dB
Received Power		Output Voltage		
-57.05 dBm		0.315 mV		

Table 10.2 Power link budget for 5.8 GHz

Frequency = 5.8 GHz; R = 0.1 m; Antenna Type: Pseudo patch antenna				
Oscillator	Antenna(Tx)	Channel Loss	Antenna(Rx)	Amplifier
-10.85dBm	-3.2 dBi	-34 dB	-3.2 dBi	5 dB
Received Power		Output Voltage		
-39.45 dBm		1.121 mV		

Table 10.3 Power link budget for 5.8 GHz

All three tables are representative of both the diode rectifier method and the SRR. While they are speculative they still illustrate the power levels involved. The important point illustrated by Figure 10.3 is that the SRR is much more sensitive and can detect signals down to -60 dBm.

10.2 The Rectaxial antenna

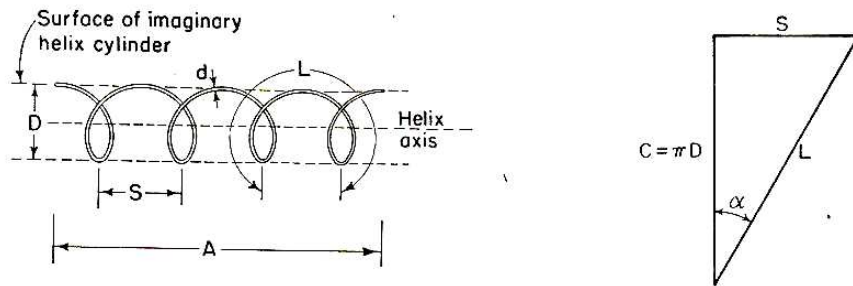
With the development of the SRR outlined in the previous section the narrowband transceiver could now be operated at a relatively low frequency (2.45 GHz or 5.8 GHz). The rectaxial antenna was the first antenna designed in this project that offered an electrically small size with good performance. At the time the SRR was being developed, the focus was on the 2.4 GHz ISM band. When the SRR became fully operational there was an attempt to move up to the next ISM licence exempt band at 5.8 GHz. Unfortunately, the rectaxial antenna did not scale with frequency. The reasons behind this are discussed in a later section of this chapter.

10.2.1 Background theory

The rectaxial antenna is a derivation of the helical antenna first developed by Krauss in 1947 [4]. The helical antenna consists of a piece of conducting wire wound into a helix and in most cases is placed either perpendicular or asymmetrically relative to a ground plane. The helical antenna operates in two fundamental modes the ‘axial’ mode and the ‘normal’ mode.

The ‘axial’ mode occurs when the dimensions are at, or greater than, the operating wavelength. For 2.45 GHz operation, this corresponds to 12.24 cm. The space between the coils and the diameter of the coils determine the antenna's wavelength. The antenna can be classed as ‘endfire’ and increasing the number of coils increases the directivity. Another benefit of this mode is that it can generate circular polarisation (CP) by simply using the direction of the winding to generate left hand CP (anti-clockwise) or right hand CP (clockwise). As this class of antenna size is comparable to its wavelength, (for CP operation the diameter should approximately be one wavelength), there is no further discussion of the ‘axial’ mode as it is not relevant to the required geometries of the target application.

In the 'normal' mode the helix dimensions are very small compared to wavelength. Figure 10.5 shows a helix and the relevant parameters as described by Krauss [5].



Where, D = diameter of helix (centre to centre)

C = circumference of helix = πD

S = spacing between turns (centre to centre)

α = pitch angle = $\arctan S / \pi D$

L = Length of 1 turn

n = number of turns

A = axial length = nS

d = diameter of helix conductor

Figure 10.5. (a) Helix and associated dimensions (b) Relation between circumference, spacing, turn length, and pitch angle of a helix.

The normal radiation mode occurs when the helix is very short i.e. $nL \ll \lambda$. In this case, the current can be considered to be of uniform magnitude and phase along the entire helix. Using the helix described by Krauss [6] as shown in Figure 10.6 (a) the maximum radiation in this case is normal to the helix axis and there is zero field in the direction of the z -axis.

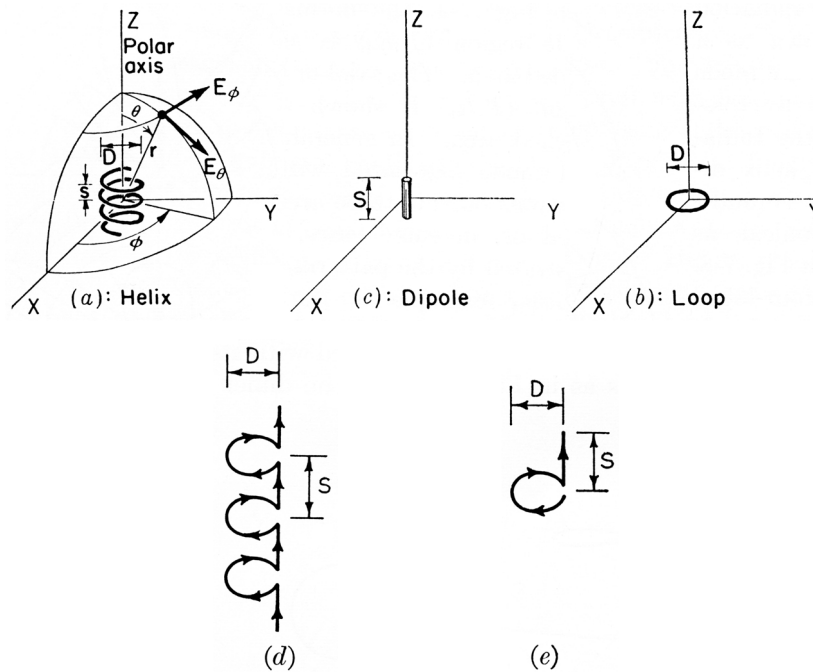


Figure 10.6. Dimensions and coordinates for (a) helix (b) loop and (c) dipole.
 (d) Helix as a succession of loops and dipoles (e) Helix for normal mode calculations

When the pitch angle is zero, the helix can be considered to be a loop, as shown by Figure 10.6 (b). When the pitch angle is ninety degrees, the helix straightens out and becomes straight wire, as shown by Figure 10.6 (c). These two cases are the limits of the helix and can be used to calculate the radiation patterns. Essentially a helical antenna operating in the normal mode can be analysed as a series of small loops and short dipoles connected in series. For the helix to be analysed using this approximation it has to satisfy the criteria of $D \approx 0.1\lambda$ and $S \approx 0.05\lambda$.

As the current magnitude and phase are uniform over the helix, the far-field patterns are independent of the number of turns. As a result, the far-field patterns can be calculated by using the field patterns of a small loop antenna and an infinitesimal dipole. The far-field of a small loop only has a E_ϕ component. Its value is given by [7].

$$E_\phi = \frac{120\pi^2 [I] \sin \theta}{r} \frac{A}{\lambda^2} \quad (10.3)$$

Where the area of the loop $A = \pi D^2/4$.

In contrast the far-field of a short dipole only has a E_θ component. Its value is given as:

$$E_\theta = j \frac{60\pi[I] \sin \theta S}{r \lambda} \quad (10.4)$$

Where, S has been substituted for L, as the length of the dipole.

Analysing both Equations 10.3 and 10.4 it is evident that both fields are in phase quadrature due to the presence of the j operator.

The main advantages of operating in this mode are the small dimensions relative to wavelength, near omni-directionality and ease of design. The next section, which is taken from published work arising from this thesis, [8] illustrates these principles.

10.2.2 A 2.45 GHz rectaxial antenna

The antenna design is based on the helical configuration [9] [10] [11]. As it is not a true helix, and consists of rectangular loops printed on the top and bottom of a duroid board and interconnected by a thru-board via, shown schematically in Figure 10.7, the antenna is described as ‘rectaxial’.

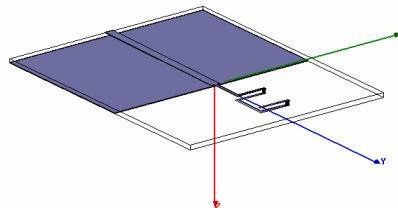


Figure 10.7. Schematic of rectaxial antenna.

The antenna can support many modes of propagation but the one considered is the ‘normal mode’ which is propagated when the perimeter is very much less than the operating wavelength. In this mode the antenna exhibits dipole-like radiation. A

good starting point for the optimisation was empirically found by setting the perimeter of the helical turn to be one tenth of a wavelength. Using Equation 10.3 and Figure 10.4, the spacing between turns was found as follows:

$$\text{Spacing between turns } (S_\lambda) = \text{Perimeter } (P_\lambda)^2/2 \quad (10.5)$$

Where $P=2X+2h$

X = diameter of Rectaxial element (mm)

h = substrate height (mm)

The values calculated fall within the limits described by Krauss [9] for the normal mode of operation.

Prior to optimisation in HFSS, consideration was made of the fabrication tolerances in the practical realisation of the antenna. A duroid board of permittivity 3.48, thickness 0.762 mm and loss tangent 0.002 was used in the antenna realisation. This board is coated on both sides with 35 μm thick copper. Using the available pattern transfer techniques, track sizes with tolerance $\pm 100 \mu\text{m}$ were achievable. This was incorporated into HFSS as a parametric limitation. An additional constraint was the minimum via-hole diameter of 600 μm .

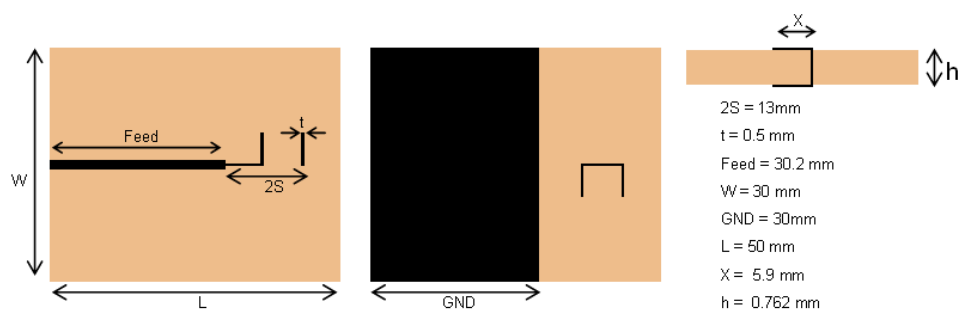


Figure 10.8. Diagram of rectaxial antenna with dimensions.

Using the starting conditions and constraints mentioned above, parametric analysis and optimisation in HFSS was used to find the dimensions to simultaneously maximise factors such as antenna gain, return loss and minimum volume. The final antenna dimensions are shown in Figure 10.8.

The optimisation resulted in the spacing between turns giving a slightly larger value than calculated using Equation (10.5), because the spacing strongly influences the return loss (RL). If the spacing between turns is too small then higher reflections occur. A target value for return loss of -20 dB in simulation was set to ensure a good match and minimise power loss for the smallest possible antenna area.

The optimised antenna was fabricated and an SMA end-launcher connector added. A 9 GHz Anritsu Scorpion Vector Network Analyser was used to determine the centre frequency and return loss of the antenna. As shown in Figure 10.9, excellent agreement in the 2.45 GHz operating frequency between measurement and simulation is obtained. The slight degradation in return loss can be accounted for by the vias between the top and bottom traces on the duroid, which were soldered and trimmed by hand.

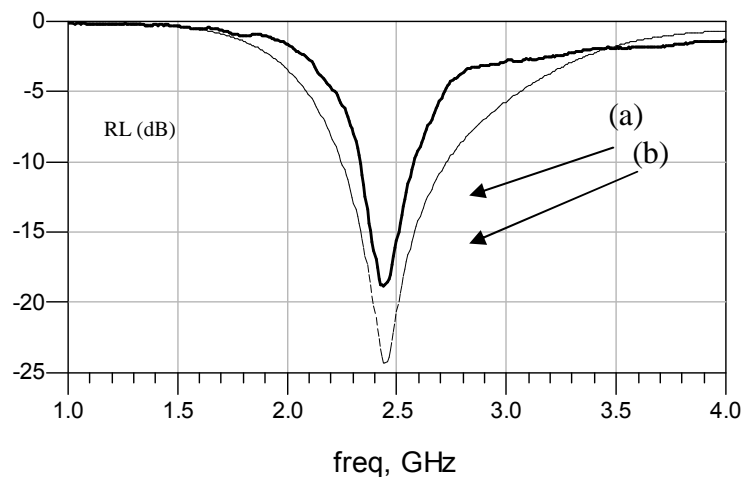


Figure 10.9 Return Loss (RL) results for both simulation (a) and measured (b) results.

The radiation patterns were measured using an anechoic chamber with a far field setup. The rectaxial antenna was placed upon a pedestal and connected to the receiver via a SMA Cable. The antenna was then rotated in both the vertical and horizontal to obtain cuts for the azimuth and elevation respectively. The results were then compared with the simulation plots via normalisation of the values obtained. The normalised radiation plots are shown in Figure 10.10. The results show good agreement between simulation and measurement. Using the received

power level from a dipole as a reference, an average gain of 2.2 dBi was obtained with a peak gain of 2.69 dBi along the boresight.

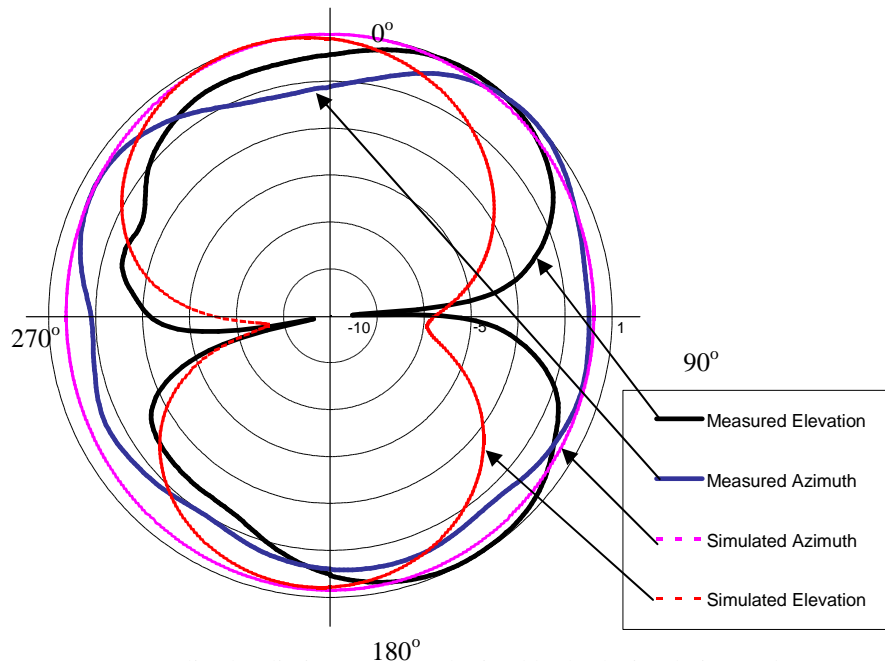


Figure 10.10. Normalised radiation patterns obtained by both simulation and measurement.

10.2.3 Design of 5.8 GHz rectaxial antenna

After the previous antenna had been designed and fabricated and appeared to operate well, it was decided to investigate its performance at a higher frequency. 5.8 GHz was chosen as it is a licence exempt band [12]. Using the design equations outlined in the previous section a model was created using HFSS that resonated at 5.8 GHz. A schematic of the model is shown below in Figure 10.11.

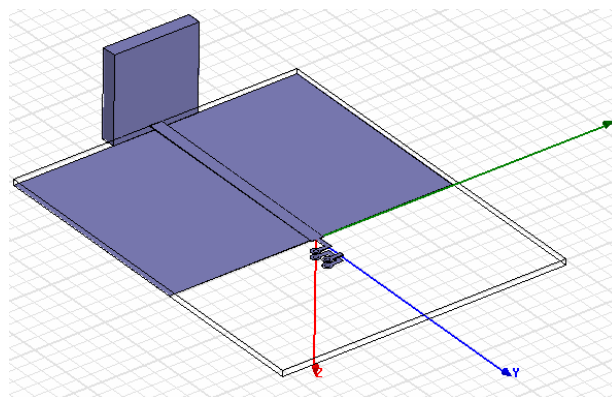


Figure 10.11. Schematic of 5.8 GHz rectaxial antenna

All the dimensions were the same as shown in Figure 10.8 except that $2S = 4.4$ mm and $x = 2.65$ mm. The simulated results for return loss are shown in Figure 10.12.

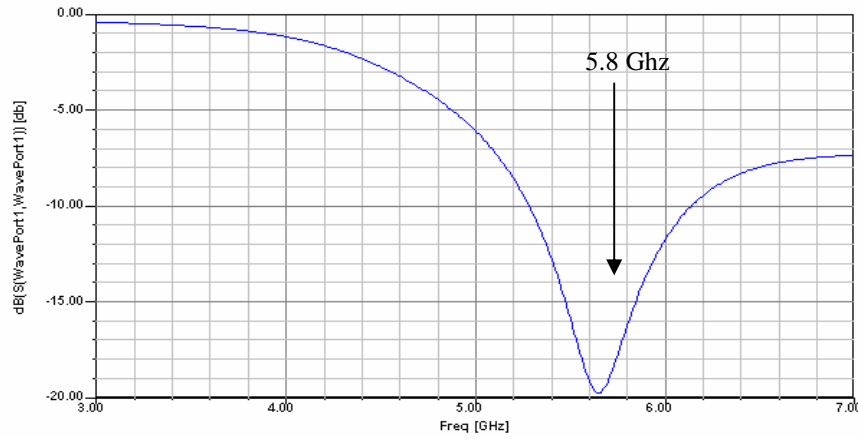


Figure 10.12. Return loss for 5.8 GHz rectaxial antenna.

On first inspection, the return loss appears to be good but under closer inspection there is a tapering off at the higher frequency which does not return to 0 dB. This indicates excitation of other modes other than the ‘normal’ mode. The 3D E-field radiation patterns for 2.45 GHz and 5.8 GHz are shown in Figure 10.13.

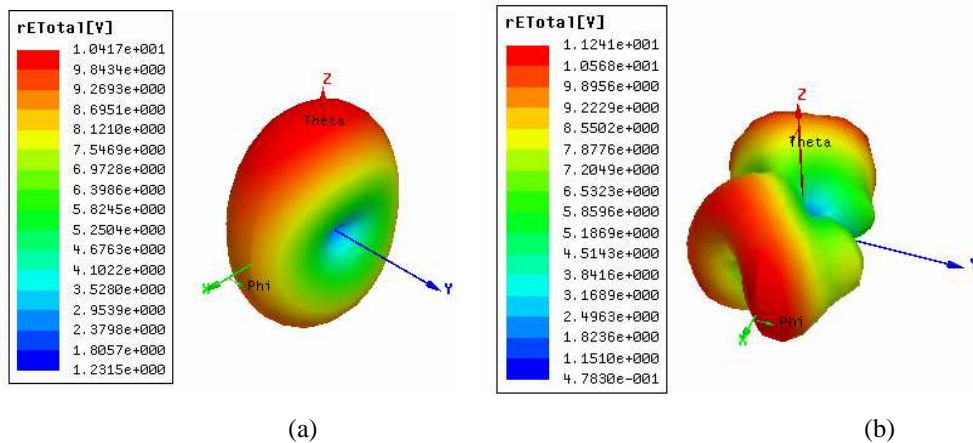


Figure 10.13. (a) E-field for 2.45 GHz rectaxial antenna.

(b) E-field for 5.8 GHz rectaxial antenna.

As can be seen from Figure 10.13 (b) the rectaxial antenna is not operating in the normal mode. To explain this behaviour it is necessary to analyse the fields over

the antenna. Figure 10.14 shows a comparison of the 2.45 GHz and 5.8 GHz rectaxial antennas.

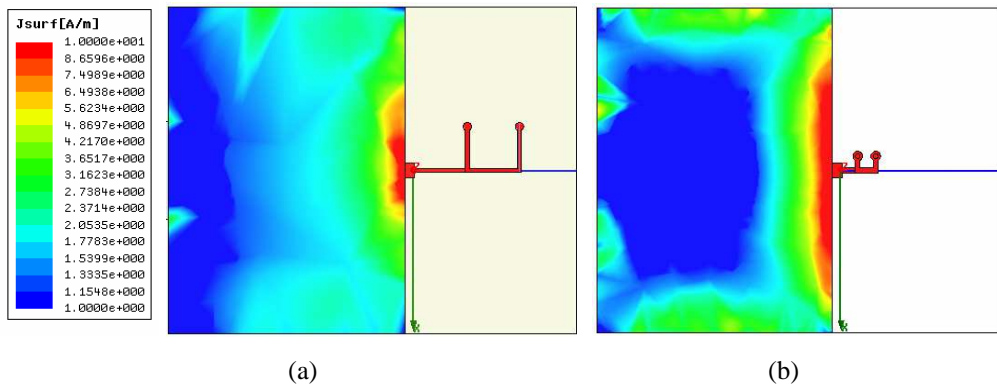


Figure 10.14. Comparison of surface currents on the ground planes.
 (a) 2.45 GHz rectaxial antenna (b) 5.8 GHz rectaxial antenna

Analysing the surface current over the two antennas, Figure 10.14, it is noted that there is more surface current present over the ground plane of the 5.8 GHz antenna. The main reason is that at the higher frequency there is more energy contained in the substrate as a result of surface waves. Section 10.2.4 gives a brief insight into surface wave propagation.

10.2.4 Surface waves in a grounded dielectric

Surface waves are excited when a plane wave is totally reflected at a dielectric interface. At microwave frequencies they are generally considered to be in the dielectric and not on the surface. Surface waves are commonly excited when using planar transmission lines especially at higher frequencies and when using higher permittivity dielectrics. Figure 10.15 shows a simplified situation of a grounded dielectric slab [13].

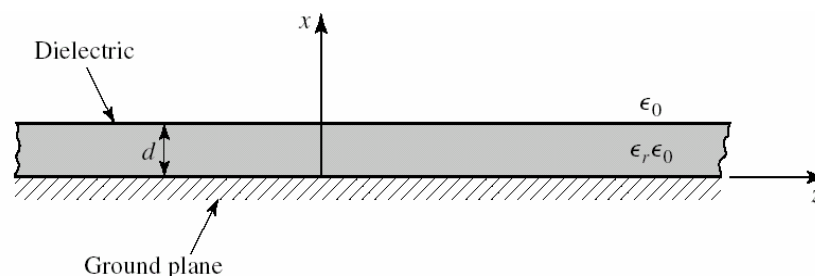


Figure 10.15. Geometry of a grounded dielectric slab

The dielectric slab has a thickness d and a dielectric constant of ϵ_r . For any dielectric slab of nonzero thickness and a permittivity greater than unity, there is one mode that can always propagate within the substrate. The mode is transverse magnetic and is known as the TM_0 mode. This mode has a zero cut-off frequency and propagation is assumed to be in the z direction and has a $e^{-j\beta z}$ propagation factor. We are not concerned with the higher order TM modes or any of the TE modes as they all occur at much higher frequencies. The cut-off frequencies for both TM and TE modes are given by Pozar[14]. The TM modes are given by:

$$f_c = \frac{nc}{2d\sqrt{\epsilon_r - 1}}, \quad n = 0,1,2,\dots \quad (10.6)$$

For the TE modes:

$$f_c = \frac{(2n-1)c}{4d\sqrt{\epsilon_r - 1}}, \quad n = 1,2,3,\dots \quad (10.7)$$

As the frequency increases with a constant substrate height the substrate becomes electrically larger allowing more energy to be propagated as surface wave mode within the substrate. The next section applies this knowledge to the problems associated with the 5.8 GHz rectaxial antenna.

10.2.5 Field analysis of 5.8 GHz Rectaxial antenna

Surface waves are launched via any type of discontinuity from planar transmission lines. In the case of the rectaxial antenna, the surface wave is launched at the interface between the feed and the antenna. To verify this, HFSS was used plot the electric field vector at the interface. This is shown in Figure 10.16.



Figure 10.16 E-field vector plot of substrate

Figure 10.16 shows the TM_0 propagating in both the positive and negative x directions. Establishing that surface waves are being propagated now allows for a speculative explanation into the distortion of the radiation pattern.

The radiation pattern can be broken down into two main components, radiation due to surface waves, and radiation due to the rectaxial element. To help understand the flow of the fields across the ground plane, vector plots for surface current are shown in Figure 10.17.

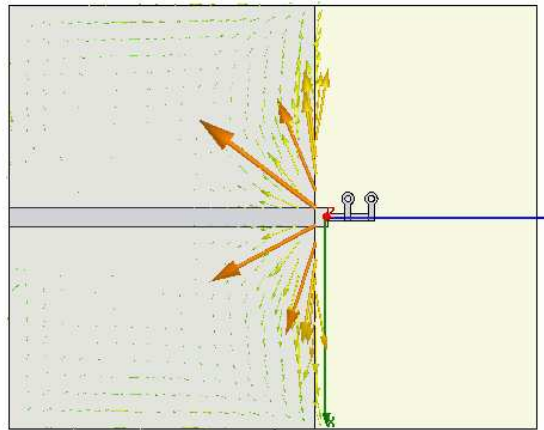
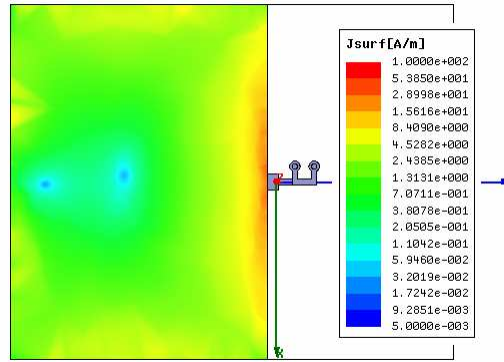
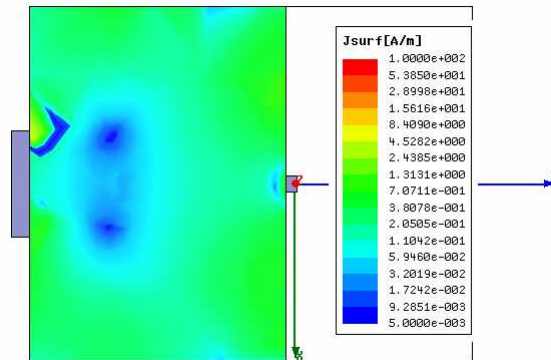


Figure 10.17 Vector surface current plot on the ground plane

As there was a considerable amount of current flowing on the ground plane, it was hard to distinguish between the microstrip mode and the surface wave mode. To try and ascertain the difference in current between the two modes a HFSS model was created with the rectaxial element removed. The surface current magnitude plots for the two cases are shown in Figure 10.18.



(a)



(b)

Figure 10.18. Surface current plot (a) with and (b) without rectaxial element

The plots in Figure 10.18 both have the same scale for surface current magnitude. Figure 10.18 (a) has a peak current maximum of approximately 100 A/m, while the model with no antenna, Figure 10.18 (b), has the peak current value of about 4 A/m. While this is much lower, there is still propagation of waves into free space. The electric field and gain far-field radiation patterns from the HFSS model with no antenna, are shown in Figure 10.19.

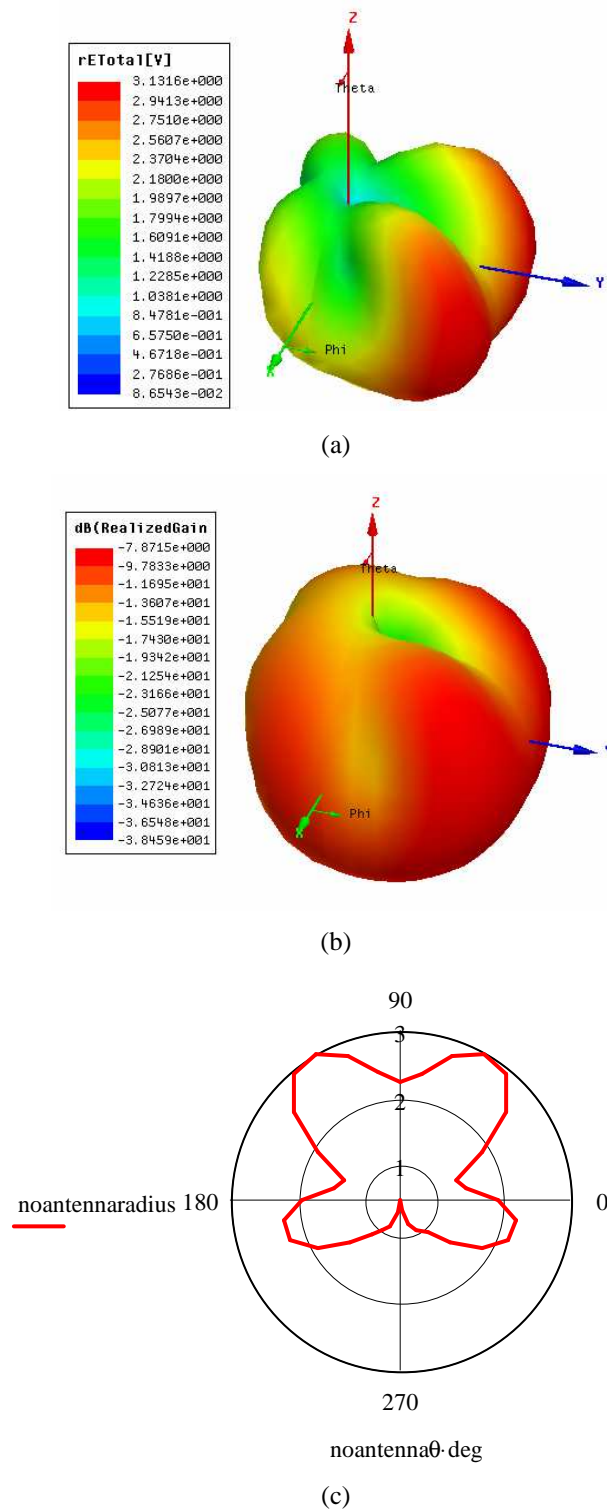
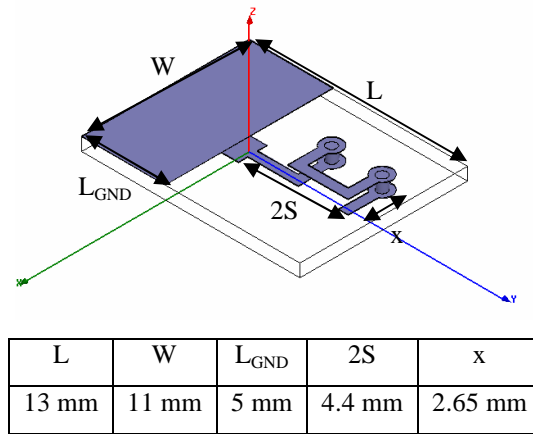


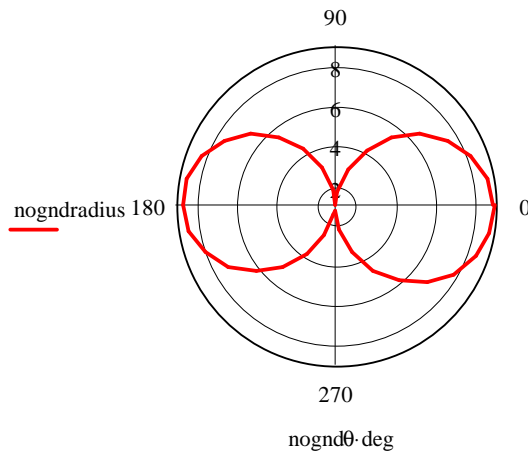
Figure 10.19. Simulated plots for (a) 3D E-field (b) 3D Gain (dBi) (c) x - y cut of E-field

The main radiation mechanism for the board with no antenna is when the current, which is being driven from the stub, meets the corner. This is highlighted by Figure 10.19 (a), which shows two prominent peaks in the y direction. To

highlight the impact the surface waves had on the far-field radiation pattern, a HFSS model was constructed of the rectaxial antenna but with an extremely small ground plane. This is shown in Figure 10.20.



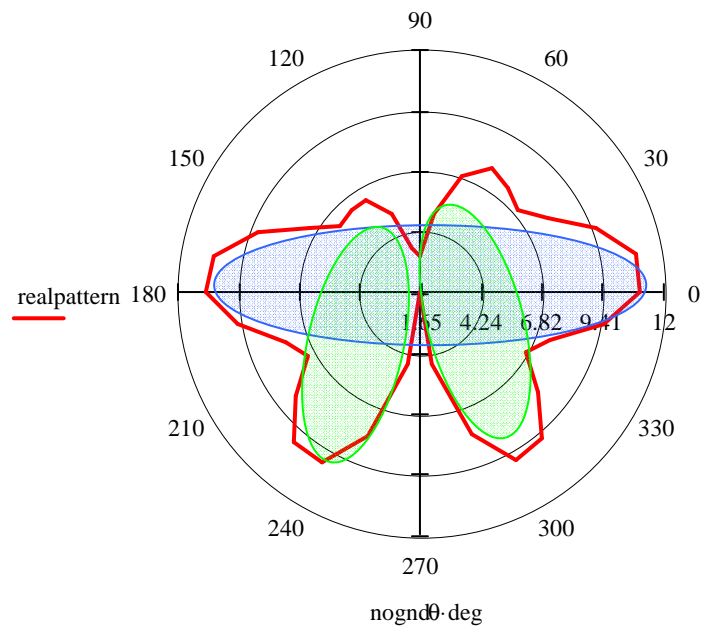
(a)



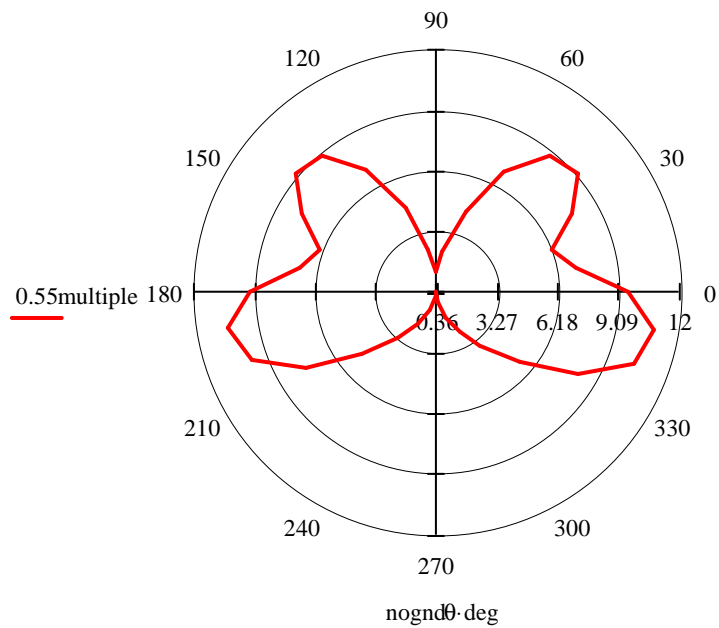
(b)

Figure 10.20. (a) Rectaxial antenna with small ground plane (b) x - y cut of Electric far-field radiation pattern

To help illustrate the impact of surface waves, Mathcad was used to multiply the patterns of Figure 10.19 (c) and Figure 10.20 (b). This is shown in Figure 10.21.



(a)



(b)

Figure 10.21 x-y cuts for (a) 5.8 GHz rectaxial antenna and (b) pattern multiplication of Figure 8.15 (c) and Figure 8.16 (b)

Using Figure 10.21 (a) it could be suggested that the area highlighted by the blue oval is the main pattern produced by the rectaxial element and the areas highlighted in green are a result of the current on ground plane.

Unfortunately, as a result of surface wave propagation degrading the radiation pattern at 5.8 GHz, coupled with need for an even smaller antenna to accommodate active circuitry, within the specification set out by the Speckled Computing Consortium, the rectaxial antenna was deemed unsuitable. Other antennas were therefore investigated as described next.

10.3 Integrated antennas at 5.8 GHz

After identifying the limitations of the rectaxial antenna in the previous section, other antennas were investigated for their potential to fulfil the Specknet requirements. These antennas were designed with the intention of taking up as little space as possible and were designed around the MMIC transceiver circuitry, designed by Ian McGregor and shown in Figure 10.22.

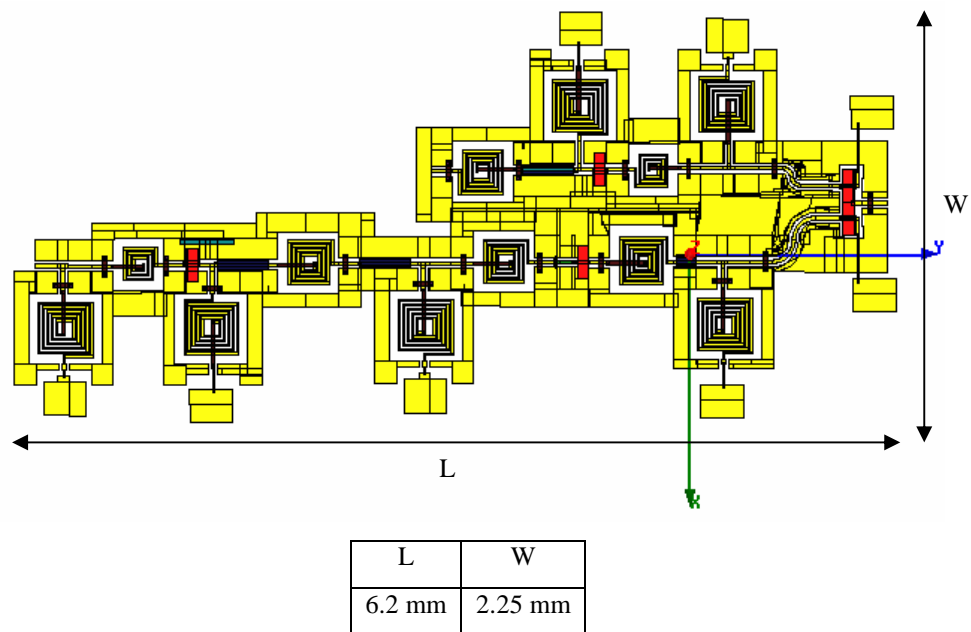


Figure 10.22. A 5.8 GHz MMIC Transceiver.

Two antennas, a compact folded dipole and a 'patch', that were designed to be integrated into and around the transceiver, are discussed in this section. Also considered in this chapter is the approach to feeding the antennas, by the use of a CPW-to-slotline transition to achieve optimal performance. The antennas designed were electrically small and found to be rather inefficient. To understand

this lack of efficiency, this section follows with a discussion on the fundamental limits of antennas.

10.3.1 Quality factor, bandwidth and efficiency

When designing radio frequency systems it is sometimes necessary to try and reduce the area that the device occupies. As previously mentioned, for the class of applications being considered by the Speckled Computing Consortium, there is a desire for the transceiver and the antenna to fit into 5mm^2 . There are many ways to reduce the area that the antenna occupies, such as, folding, meandering and bending. The use of shorting walls, pins and high dielectric constant materials can also be used. However, using these techniques come at a cost, as the bandwidth and efficiency are reduced.

Chapter 3 investigated the fundamental limitations of electrically small antenna as those whose maximum dimension is less than the $1/k$, where k = wave number. This section will investigate the impact on the quality factor, Q , of losses such as radiation, conduction (ohmic), dielectric and surface wave losses. The total quality factor, Q_t , which is influenced by these losses, can be written as [15]:

$$\frac{1}{Q_t} = \frac{1}{Q_{rad}} + \frac{1}{Q_c} + \frac{1}{Q_d} + \frac{1}{Q_{sw}} \quad (10.8)$$

Where:

Q_t = total quality factor

Q_{rad} = quality factor due to radiation losses

Q_c = quality factor due to conductive (ohmic) losses

Q_d = quality factor due to dielectric losses

Q_{sw} = quality factor due to surface waves

For very thin substrates the losses due to surface waves are very small, and can generally be neglected, until the substrate approaches a height large enough for propagation of the higher order modes as discussed in section 10.2.5. For very thin substrates ($d \ll \lambda$) of arbitrary shapes (including rectangular and circular),

approximate formulas can be used to represent the quality factors of the various losses in 10.8. They are as follows [16]:

$$Q_c = d\sqrt{\pi f \mu \sigma} \quad (10.9)$$

$$Q_d = \frac{1}{\tan \delta} \quad (10.10)$$

$$Q_{rad} = \frac{2\omega\epsilon_r}{dG_t/l} K \quad (10.11)$$

Where:

$\tan \delta$ = loss tangent of dielectric substrate

σ = is the conductivity associated with any metallization used

G_t/l = the total conductance per unit length of the radiating aperture

$$K = \frac{\iint_{area} |E|^2 dA}{\oint_{perimeter} |E|^2 dL} \quad (10.12)$$

To help simplify the understanding an example of a rectangular patch antenna, as described in chapter 5, can be used. For a patch antenna operating in the dominant TM_{01} mode the following are given [16]:

$$K = \frac{L}{4} \quad (10.13)$$

$$G_t/l = \frac{G_{rad}}{W} \quad (10.14)$$

The Q_{rad} described by equation 10.11 is inversely proportional to the height of the substrate, and for very thin substrates is the dominant factor. The fractional bandwidth of antenna is inversely proportional to the Q of an antenna. Taking account of all losses it can be defined as:

$$\frac{\Delta f}{f_0} = \frac{1}{Q_t} \quad (10.15)$$

Equation 10.15 can also be modified to take into account the impedance matching at the terminals of the antenna and is described as follows:

$$\frac{\Delta f}{f_0} = \frac{VSWR - 1}{Q_t \sqrt{VSWR}} \quad (10.16)$$

The fractional bandwidth is proportional to the volume, which for a rectangular microstrip antenna at a constant resonant frequency can be expressed as:

BW \propto volume = area x height = length x width x height

$$\propto \frac{1}{\sqrt{\epsilon_r}} \frac{1}{\sqrt{\epsilon_r}} \sqrt{\epsilon_r} = \frac{1}{\sqrt{\epsilon_r}} \quad (10.17)$$

For increasing height of substrate the bandwidth increases, increasing the dielectric constant the bandwidth decreases.

Increasing the dielectric constant also has an impact on the antenna efficiency. To help understand the impact the conduction-dielectric efficiency, η , can be used. It is defined as a ratio of the power delivered to the radiation resistance (R_r), to the power delivered to R_r and the loss resistance (R_L), and is written as follows:

$$\eta = \left[\frac{R_r}{R_L + R_r} \right] \quad (10.18)$$

Equation 10.18 can be expressed in terms of the quality factors described in equation 10.8 as follows:

$$\eta = \frac{1/Q_{rad}}{1/Q_t} = \frac{Q_t}{Q_{rad}} \quad (10.19)$$

Equation 10.19 illustrates that for antenna with constant dimensions but increasing dielectric constant the efficiency is inversely proportional to the permittivity. The following two sections discuss antennas that are electrically small and have associated radiation, conductive and dielectric losses.

10.3.2 A compact folded dipole antenna at 5.8 GHz

Initially, the compact folded dipole was not considered as a candidate to be integrated with the transceiver at 5.8 GHz. This was due to the fact that half a wavelength in free space would not fit the form factor of 5mm. However, after the design of the SRR, the link budget analysis allowed for the antenna to have reduced efficiency i.e. reduced size.

The compact folded dipole was therefore designed and folded around the transceiver, placed over a ground plane, and parasitically loaded by the transceiver body. A geometrical representation of the folded dipole attached to the transceiver body is shown in Figure 10.24.

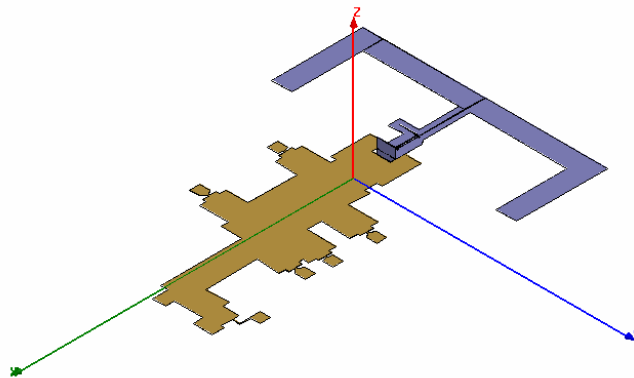


Figure 10.24. Folded dipole with transceiver attached.

To help with the meshing, the transceiver was approximated as a section of metallization. The dipole also had to be fed via slotline to provide a balanced transition. The next section outlines the balun design.

10.3.2.1 Balun design

One of the most important aspects of dipole design is ensuring that there is a balanced feed into the centre of the dipole. For a monolithic design, this can be provided by slotline. Unfortunately, slotline is not the transmission line of choice when designing MMICs. More commonly, CPW or microstrip lines are used, as they allow for easier integration between components.

The transceiver, shown in Figure 10.22, uses CPW lines to connect the discrete components, and as a result there needs to be a transition, which acts as a balun. A balun was designed [17], which allowed for a transition from CPW-to-slotline, and is shown in Figure 10.25.

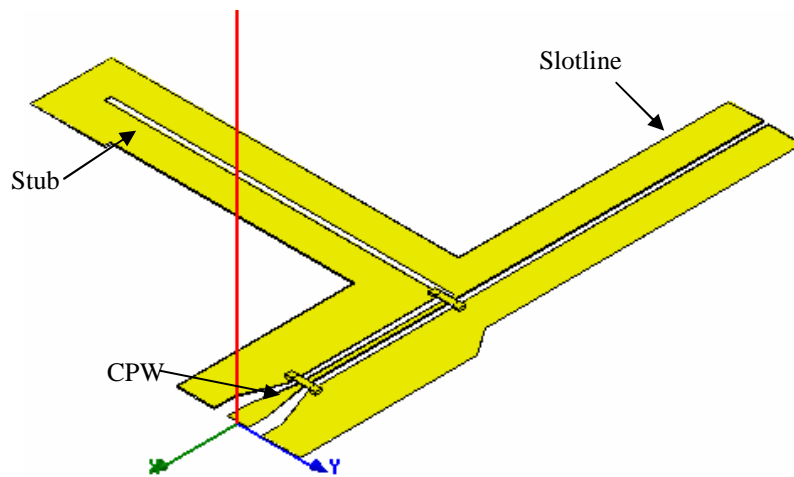


Figure 10.25. A CPW-to-slotline transition

As well as acting as a balun, the 50Ω CPW line to 50Ω slotline transition also gives a certain amount of matching capability. The stub acts as a 180° phase shifter effectively removing half the CPW mode to leave the slotline mode. Figure 10.26 shows simulated results for S_{21} , S_{11} and S_{22} .

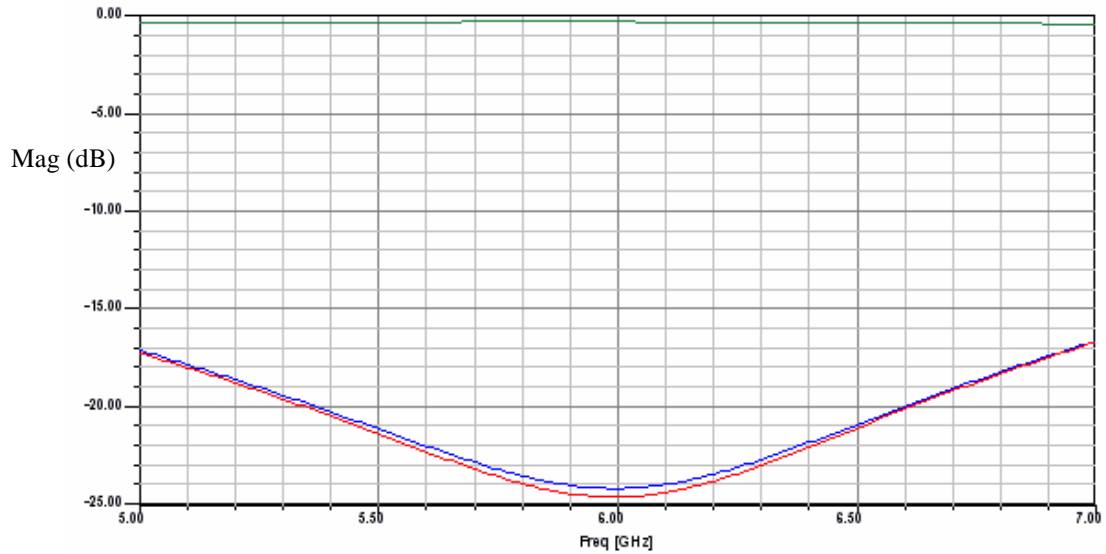


Figure 10.26. Simulated results for S_{21} (green), S_{11} (blue) and S_{22} (red). Stub length=5mm

The transition can give medium bandwidth, as the length of stub corresponds to a quarter of a guided wavelength at the desired frequency of operation. Shown in Figure 10.26, the stub length is 5mm, which approximately corresponds to a quarter of a guided wavelength at 6 GHz.

Further investigation of the transition using Smith Charts [18] yields interesting results. To try and obtain a better understanding of the transition the stub itself was analysed by modelling a slotline termination. Figure 10.27 shows S_{11} for various lengths of stub plotted on a Smith chart.

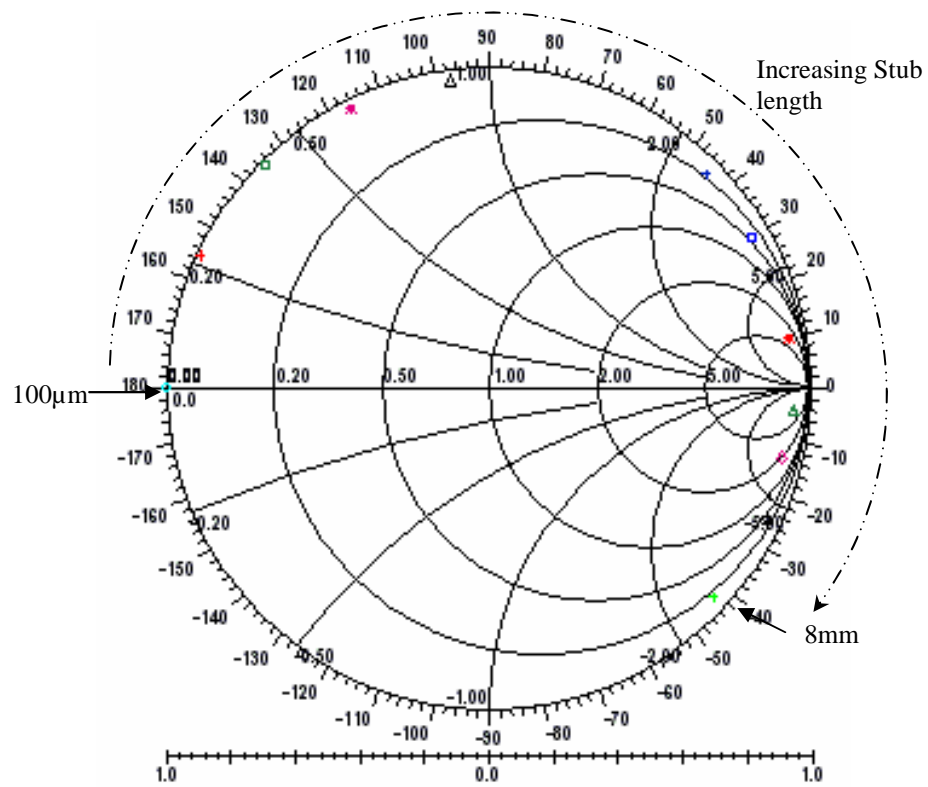


Figure 10.27. Smith chart showing S_{11} at 5.8 GHz for increasing length of Slotline termination

Inspection of Figure 10.27 shows that the stub is short circuit with increasing resistive losses as it gets longer. When it is connected to the CPW and slotline, the behaviour becomes more complex. The simulated result for S_{11} is plotted on a Smith chart and is shown in Figure 10.28.

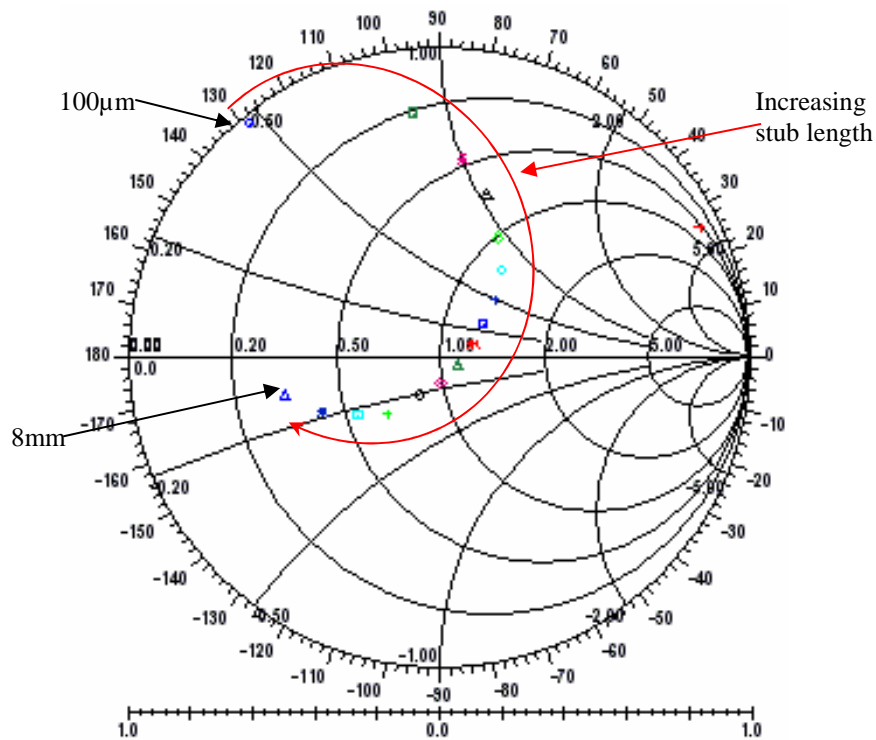


Figure 10.28. Smith chart showing S_{11} at 5.8 GHz for CPW-to-slotline transition for increasing length of stub

Inspection of Figure 10.28 reveals that the full transition is a short-circuit stub with real and complex losses. Although the behaviour is hard to predict, the stub can still be used to match the circuit via optimisation using HFSS.

10.3.2.2 Design of compact-folded dipole antenna

As the dipole was folded around the transceiver, they were then placed over a ground plane and used the transceiver body as a parasitic load to the antenna. This represented an extremely complex 3D electromagnetic structure. This section will consider various parameters of the antenna and their impact on its performance and overall size. The parameters investigated are width of dipole, dielectric loading, placing over a ground plane, and bending the arms.

10.3.2.2.1 Width of dipole

It is well known that a thin dipole with sinusoidal current distribution has a resistance of 73Ω and a inductive reactance component of $j42.5\Omega$ [19]. As the dipole used in this investigation is not thin, the value of input impedance will change as the current can no longer be approximated by a sinusoidal distribution.

Research into cylindrical dipoles is extensive and there are many methods available for calculating the input impedance of an antenna, such as the Method of Moments (MoM). Fortunately, there is a very simple empirical method for calculating the approximate self-impedance of cylindrical centre-fed antennas as demonstrated by Krauss [20]. Using this information the value extracted is approximately $65\text{-}70\Omega$ for the values shown in Figure 10.29.

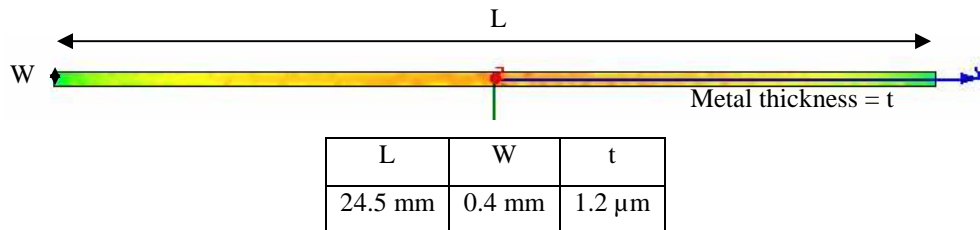


Figure 10.29. Half-wavelength dipole showing current distribution.

As shown in Figure 10.29, the length of the dipole is 25.4mm, this value being approximately 1% less than half the wavelength, in free space, for 5.8 GHz. Adjusting the width of the dipole can be used to remove the reactive component present on the dipole. For the model shown in Figure 10.27 the width was varied between $50\mu\text{m}$ and $400\mu\text{m}$. The resulting input resistance as a function of frequency are shown in Figure 10.30.

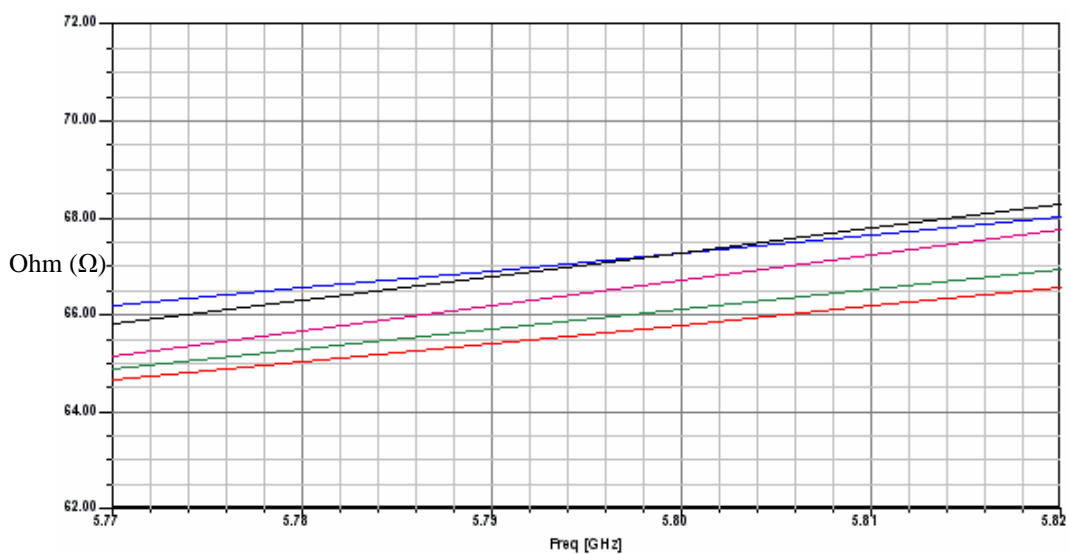


Figure 10.30. Input resistance (Ω) with width variation of $50\mu\text{m}$ (blue), $100\mu\text{m}$ (red), $200\mu\text{m}$ (green), $300\mu\text{m}$ (magenta), $400\mu\text{m}$ (black)

Inspection of Figure 10.30 shows the important point to note is that there is only a variation of approximately 2Ω . The real advantage of increasing the width is the removal of the reactive component. This is shown in Figure 10.31.

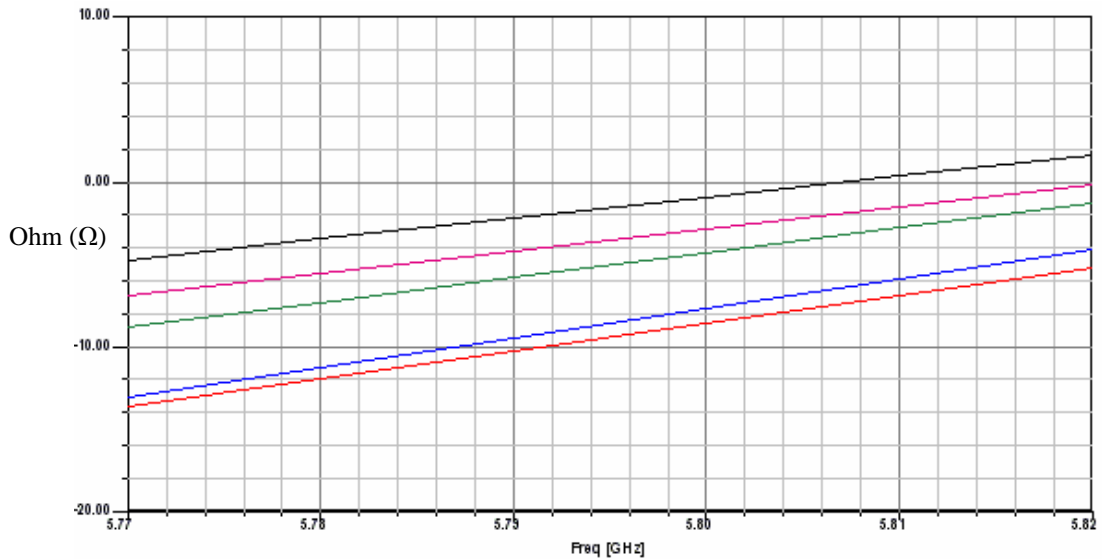


Figure 10.31. Input reactance (Ω) with width variation of 50 μm (blue), 100 μm (red), 200 μm (green), 300 μm (magenta), 400 μm (black)

As shown by Figure 10.31, increasing the width to 400 μm almost completely removes the reactive component at the frequency of operation.

10.3.2.2.2 Printed dipole on substrate

With an understanding of the impact of the geometry of the dipole in free space the next investigation was to analyse the dipole on a substrate. Figure 10.32 shows the layout of a half-wavelength dipole placed on a GaAs substrate.

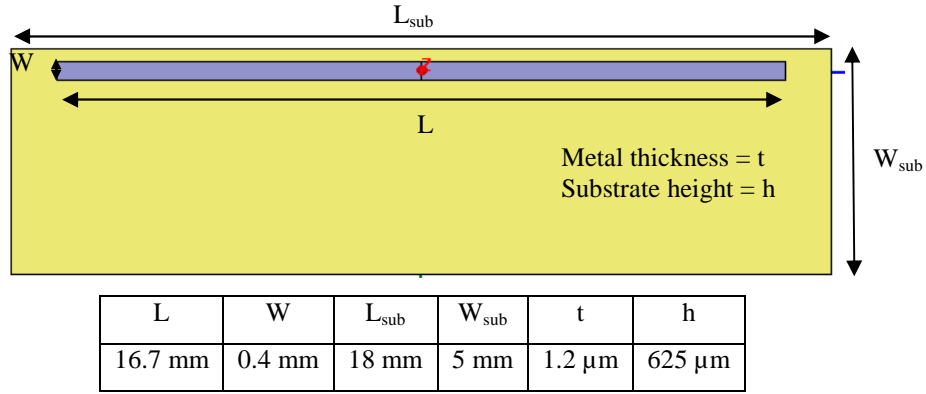


Figure 10.32. Half-wavelength dipole placed on GaAs substrate

One of the advantages of placing the dipole on a high permittivity substrate such as GaAs, is that the length can be reduced due to the dielectric reducing the effective wavelength. As a result of placing the dipole on a GaAs substrate there is approximately a 34% reduction in size compared the dipole in free space. However, the reduction in size comes at a cost, as there are extra losses added to the system as a result of the substrate. Figure 10.33 shows the simulated results for input resistance with respect to variations of width for a dipole length of 16.7mm.

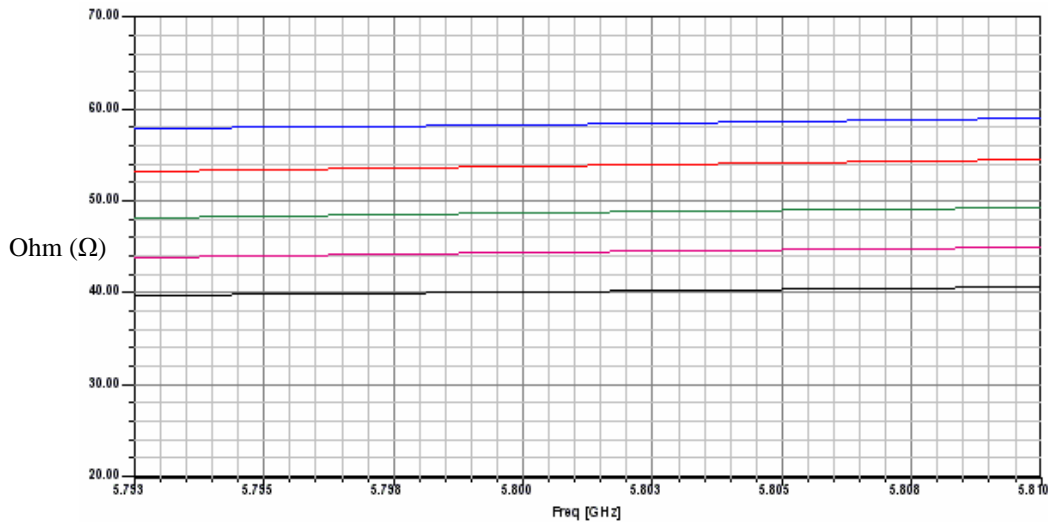


Figure 10.33. Input resistance (Ω) with width variation of 50 μm (blue), 100 μm (red), 200 μm (green), 300 μm (magenta), 400 μm (black)

Comparing Figure 10.33 to the previous Figure 10.30 there is much larger variation in the input resistance. This is to be expected, as the antenna is more

sensitive as a result of its reduction in size. Viewing the input reactance in Figure 10.34 verifies this.

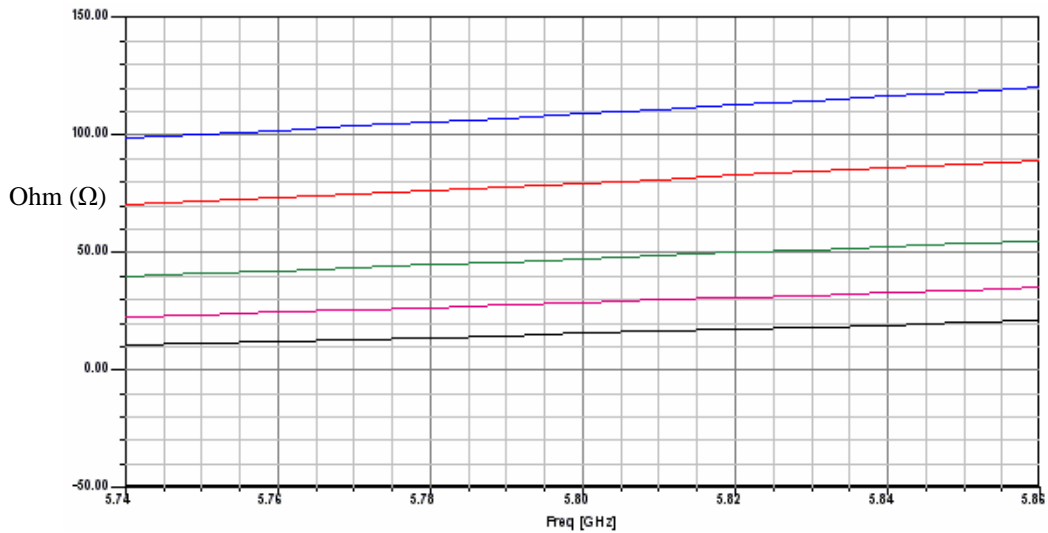


Figure 10.34. Input reactance (Ω) with width variation of 50 μm (blue), 100 μm (red), 200 μm (green), 300 μm (magenta), 400 μm (black)

The extra losses due to the introduction of the substrate are identified by viewing the increased values of reactance at various widths, though they can still be reduced by tuning the width, as shown by Figure 10.34.

10.3.2.2.3 Slotline-fed dipole over a ground plane

It was assumed that the dipole was going to be surrounded by, or very close to, a large section of metal e.g. a battery. An example of this is shown in Figure 10.35.

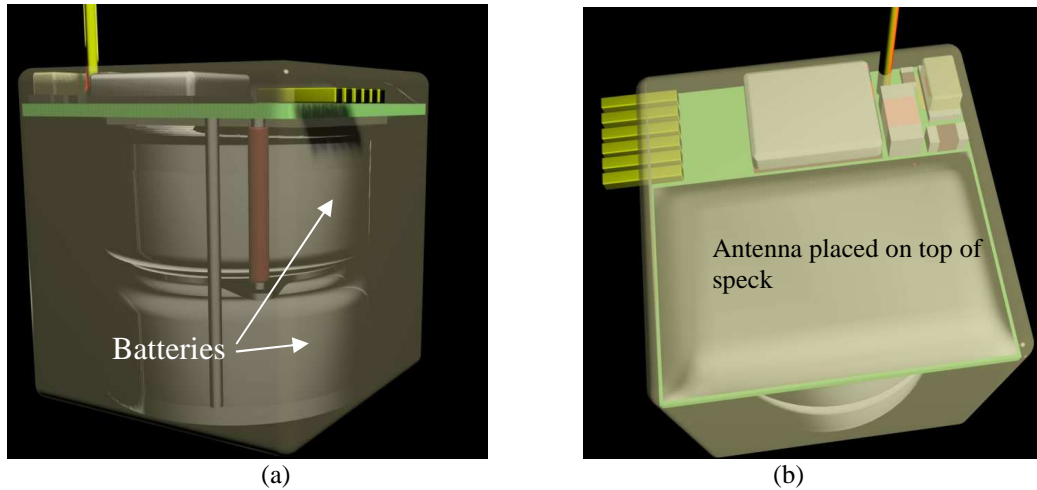
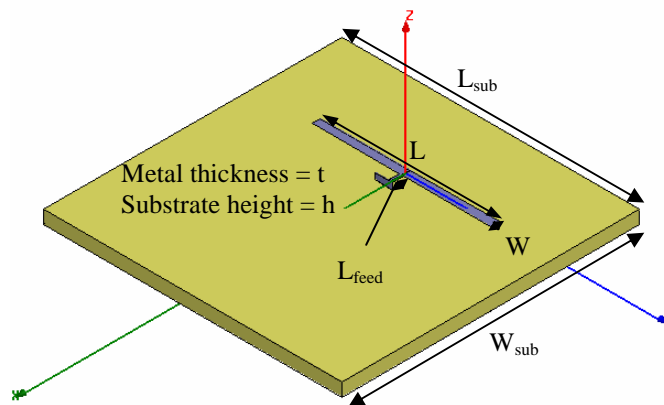


Figure 10.35. Possible configuration of Speck (a) side view (b) plan view.

Integrating the dipole design with a ground plane meant that the ground could then be used as part of the radiation mechanism. The introduction of a ground plane results in the antenna behaving to an approximation like a microstrip transmission line, and having similar operation to that of a patch antenna. The HFSS model used for this analysis is shown in Figure 10.36.



L	W	L_{sub}	W_{sub}	L_{feed}	t	h
8.39 mm	0.4 mm	14 mm	14 mm	0.8 mm	1.2 μm	625 μm

Figure 10.36. Slotline-fed dipole antenna over ground plane

Unfortunately now that the dipole has been greatly reduced in size, the effective aperture has been reduced greatly; as a result the radiation resistance has been reduced dramatically. Figure 10.37 shows the input impedance for the antenna.

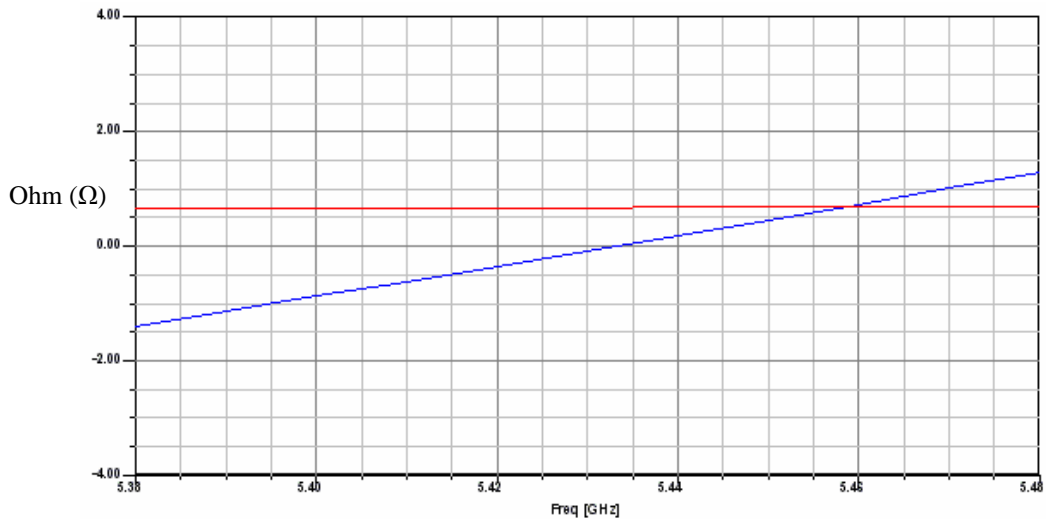


Figure 10.37. Results for real (red) and imaginary (blue) input impedance for a printed dipole antenna over a ground plane

The first resonance occurs at approximately 5.5 GHz with a very low value of input resistance of 2.4Ω . This value of resistance is indicative of a very low value of radiation resistance, which unsurprisingly will affect the antennas efficiency. Evidence of this is shown in Figure 10.41 (b). This also corresponds with the theory discussed in Section 10.3.1 that a reduction in size gives a reduction in efficiency.

10.3.2.2.4 Folded dipole over a ground plane with transceiver

To try and reduce the area further, the arms of the antenna were folded around the transceiver. It has already been reported by Nakano [21] that this has a minimal effect on current and the far-field pattern for a 90 degree bend on a dipole. The layout for a slotline-fed folded dipole with the transceiver body is shown in Figure 10.38.

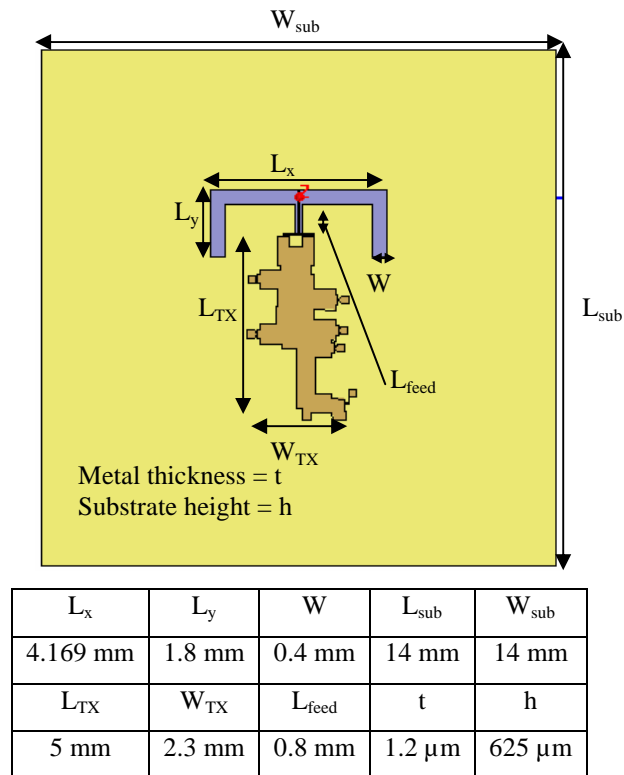


Figure 10.38. Layout for a slotline-fed folded dipole with the transceiver body

The input impedance results, shown in Figure 10.39, for the folded dipole over ground are as expected and similar to those of the straight dipole over a ground plane results, shown in Figure 10.37.

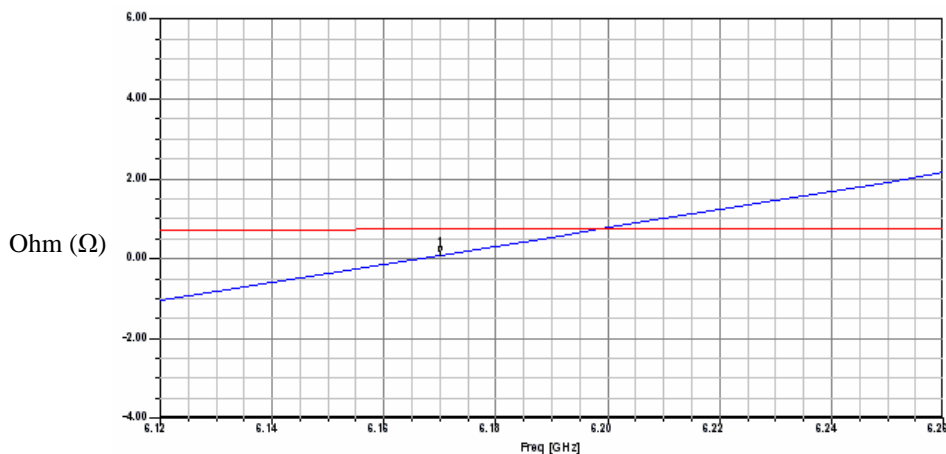
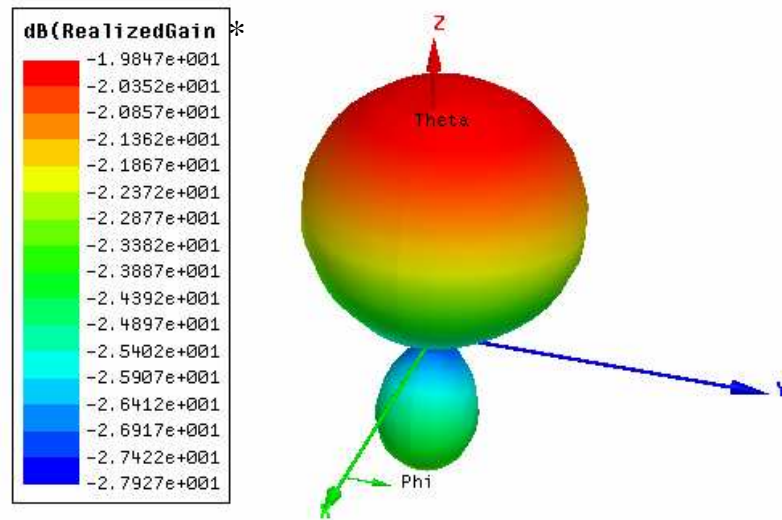
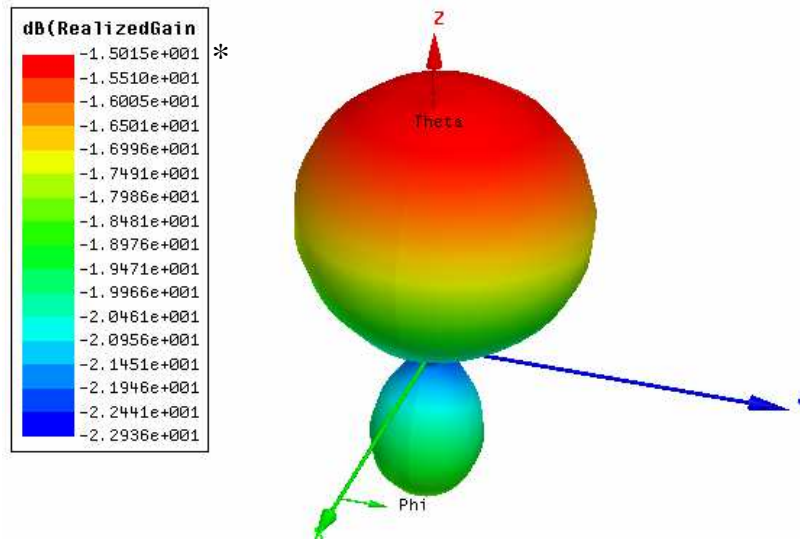


Figure 10.39. Results for real (red) and imaginary (blue) input impedance for a printed dipole antenna over a ground plane

A comparison of the 3D-gain patterns for the antenna in this section, and the previous section 10.3.2.2.3, is shown in Figure 10.40.



(a)



(b)

Figure 10.40. Far-field gain (dB) plots for (a) Folded dipole over a ground plane with transceiver
(b) Slotline fed dipole over a ground plane.

* due to a bug in HFSS V9 and V10 it translates the value as natural logarithm as opposed to the base 10 therefore, $-1.9847e+001 \text{ dB} = -5.39 \text{ dB}$ and $-1.5015 e+001 \text{ dB} = -4.0815$

Analysis of Figure 10.40 shows that the gain for both antennas is very poor with only 1.31 dB improvement for Figure 10.40 (b).

While the overall length of the dipole has not changed, the effective area that the antenna plus transceiver occupies is much smaller. The antenna in the previous section had an effective area of 46mm^2 compared to 26mm^2 . This is

approximately a 44% reduction in size at no cost to the performance of the antenna.

10.3.2.3 Final design of printed dipole folded around transceiver

With an understanding of the factors that had a major impact on antenna performance, appropriate optimisation could take place utilising the geometry of the dipole and the CPW-to-slotline transition. The final design iteration which was fabricated at the James Watt Nano-fabrication Centre (JWNC) using the process outlined in section 5.2. The final geometrical layout is shown in Figure 10.41.

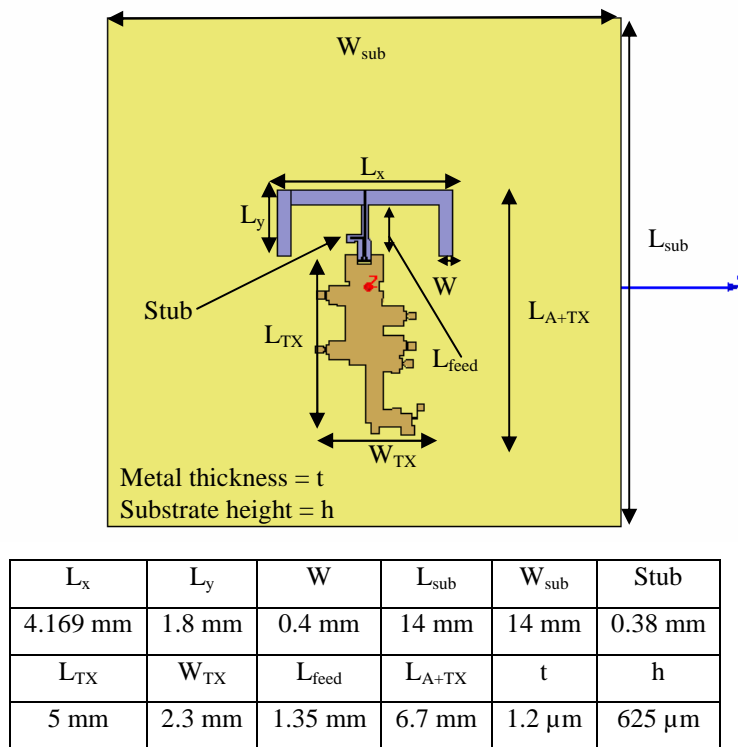


Figure 10.41. Schematic of folded dipole over ground plane with CPW-slotline transition

10.3.2.4 Simulated and experimental results for final design

After the antenna was fabricated, the antenna was tested by using a Wiltron 3622A 40 MHz to 60 GHz VNA with Cascade-Microtech probes. The antenna was placed on a low dielectric material (Styrofoam) to negate any external coupling from the surrounding metallization. The results for S_{11} after optimisation of the feed and dipole geometry are shown in Figure 10.42.

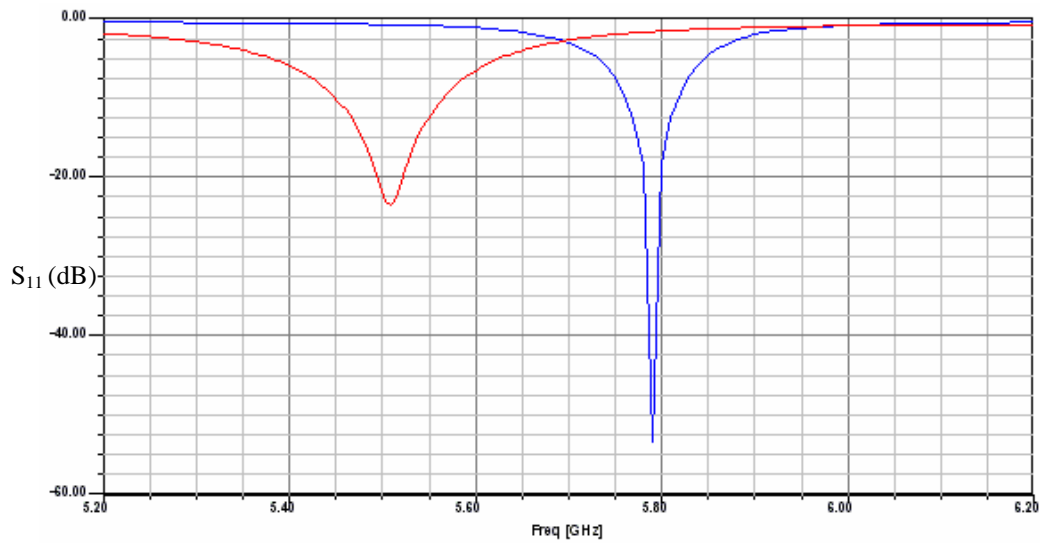


Figure 10.42. Simulated (blue) and experimental (red) results for S_{11}

Analysis of the results in Figure 10.42 shows a discrepancy between the simulated and experimental resonant frequencies. One factor that can be discounted is errors in the size of the antenna and transceiver metallization as it was manufactured in the JWNC, which has a high fabrication precision. A possible cause of error is that the substrate height may be smaller than indicated. Also, to speed up the fabrication process, gold-wire bonds were used instead of standard air-bridges. Another possible explanation for the discrepancy of simulated and practical results is the proximity of the probe pad to the antenna. An interesting point to note about the experimental results is that bandwidth is larger, so lower Q , when compared to the simulated results. This can be attributed to extra external losses occurring, most likely a result of the probe being in close proximity to the antenna.

Analysis of the input impedance, shown in Figure 10.43, shows similar responses for both experimental and simulated results, even though the operating frequency is different.

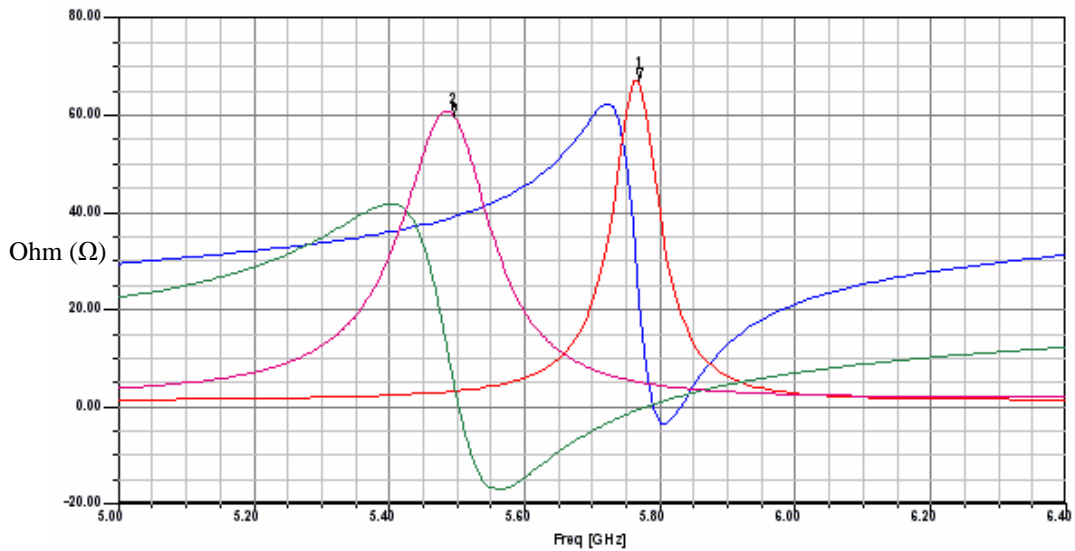


Figure 10.43. Simulated input resistance (red) and reactance (blue). Experimental input resistance (magenta) and reactance (green)

As a point of interest, it is important to note that the input impedance in Figure 10.38 is measured before the CPW-to-slotline transition. As a result of the transition acting as a matching network there appears to be a good match. The antenna, in fact, has an even worse performance after it has been connected to the transceiver body via the transition. Comparing the antenna in this section to the antenna in section 10.3.2.2.4, where there was no transition. The simulated antenna gain as calculated by HFSS has dropped from -5.39 dB to -8.6582 dB is shown in Figure 10.44.

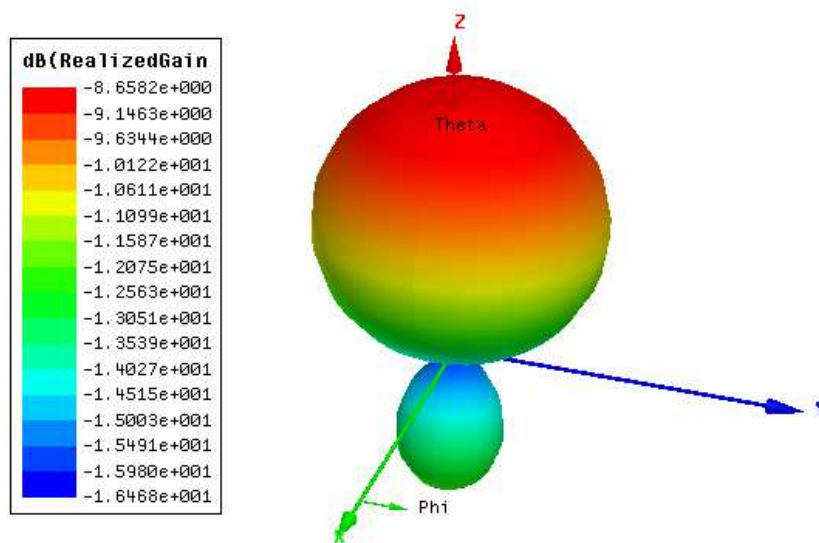


Figure 10.44. Simulated 3D Gain plot for folded dipole

The compact folded dipole at 5.8 GHz is not a good antenna, as it is an inefficient radiator of electromagnetic energy. However, it was during the investigation of the compact folded dipole it was observed that there was a lower order resonance occurring. After further investigation it was discovered there was a patch antenna like mode. The next section describes it.

10.3.3 A 'patch' antenna at 5.8 GHz

While investigating the dipole configurations in section 10.3.2, another mode was identified while shortening the length of the dipole arms. After further investigation it was discovered that it was a fundamental patch antenna-like mode. The geometry of the 'patch' antenna is shown in Figure 10.45.

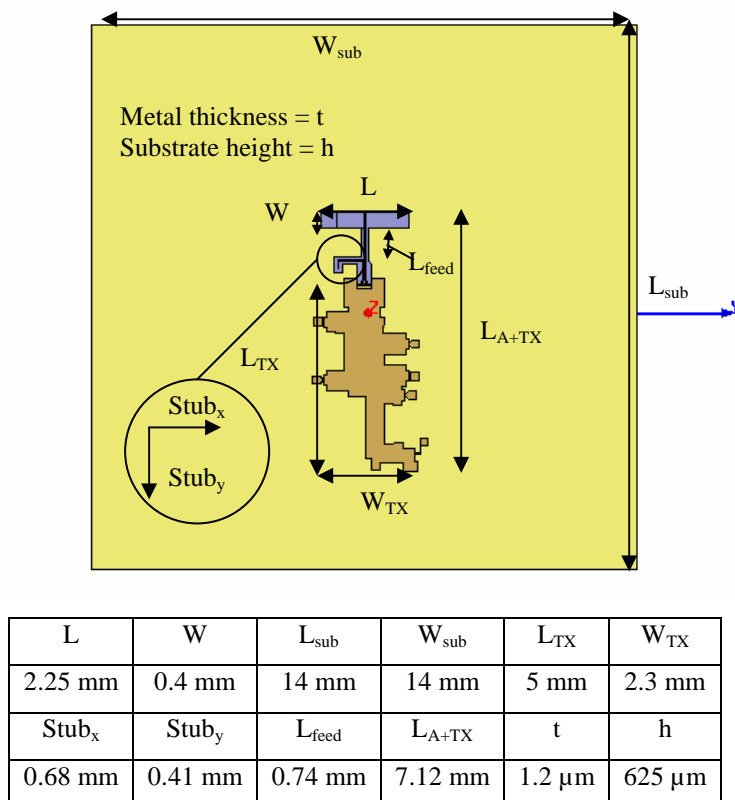
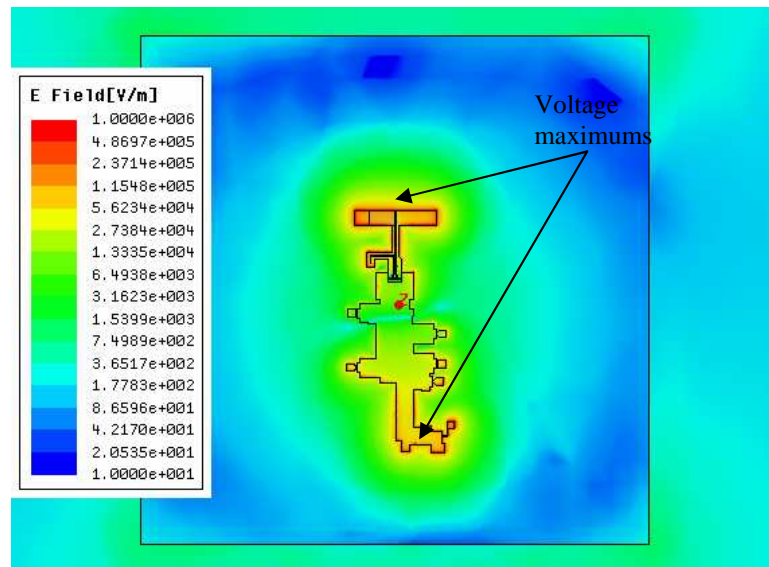


Figure 10.45. Schematic of 'patch' antenna with main dimensions outlined

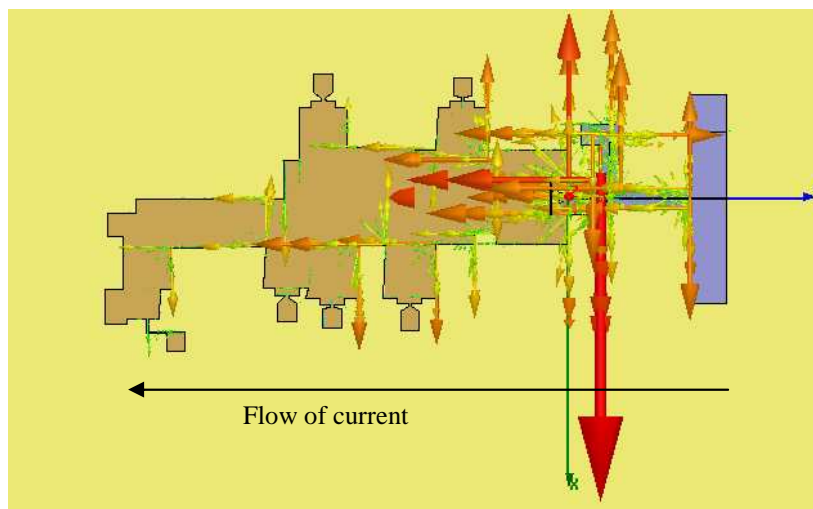
Utilising the design formulas in section 6.2, the length and width of a patch were calculated. It was possible to confirm the length was similar to the theoretically

calculated value. For a 0.625mm thick GaAs substrate and 1.2 μ m thickness of gold, the length and width were found to be 7.06 mm and 9.8mm respectively. Comparing the calculated dimensions with those of Figure 10.45, there is only a 0.84% error between the theoretical and actual value for length, which is the main factor in resonance. As the width is smaller this would result in a reduction of bandwidth.

To validate that the fundamental patch antenna mode, TM_{01} , was occurring, the vector plots for the near E-field and surface current were obtained using HFSS. These are shown in Figure 10.46.



(a)



(b)

Figure 10.46. Vector plots for 5.8 GHz 'patch' antenna (a) E-field (b) Vector surface current

Inspection of Figure 10.46 confirms the type of radiation associated with a patch antenna. Figure 10.46 (a) shows two voltage maximums at the top and bottom of the patch. Unfortunately, due to difficulty in mesh size, it was impossible to obtain a sensible vector current plot for the electric field over the ‘patch’. There is, however, verification that the two maximums are 180° out of phase, as Figure 10.46 (b) shows the surface current flowing in a uniform direction along the length of the antenna, with a current maximum in the middle.

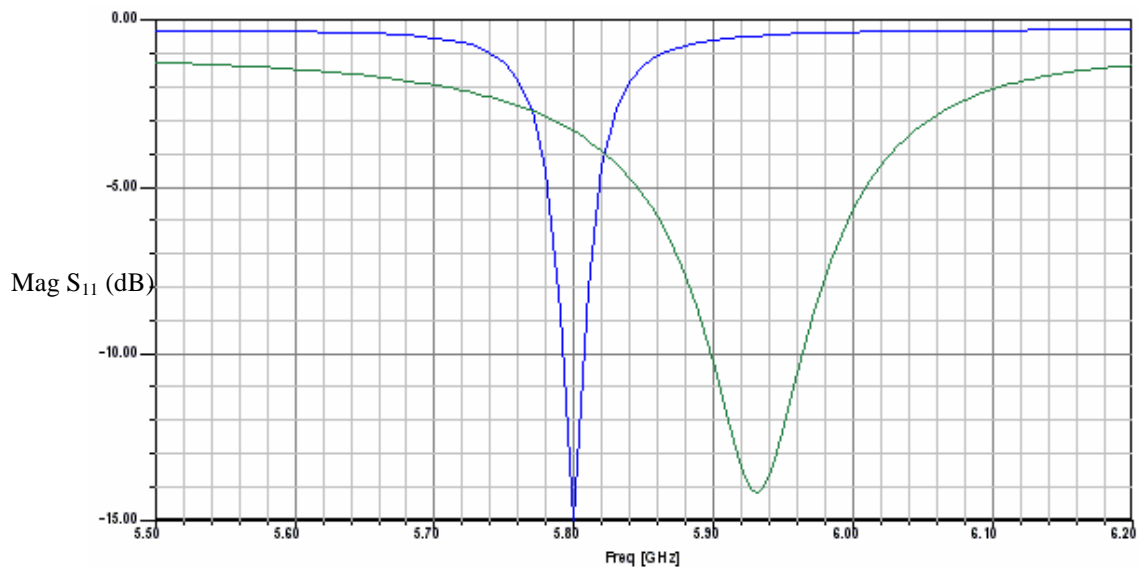


Figure 10.47. Simulated (blue) and experimental (green) S_{11} results for ‘patch’ antenna

Experimental results were obtained for the ‘patch’ antenna using the process described in section 10.3.2.2.6 and are shown in Figure 10.47 along with the simulated results. Inspection of the results in Figure 10.47 shows relatively good agreement between the simulated and experimental results, especially when compared to the compact-folded dipole results. There is a slight mismatch in the operating frequency with the ‘patch’ antenna, which resonates at 5.92 GHz instead of 5.8 GHz. As with the folded dipole discussed in the previous section, there appears to be a wider operational bandwidth for the experimental result, when compared to the simulated response. This can possibly be attributed to extra losses added caused by the close proximity of the probe over the antenna.

Inspection of the simulated radiation pattern, shown in Figure 10.48, shows a marked improvement in gain (-3.13 dBi) compared to the folded dipole (-8.65 dBi).

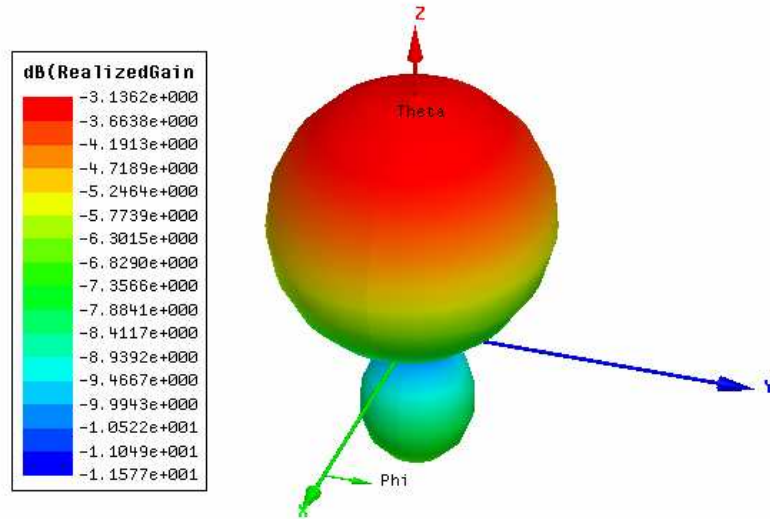


Figure 10.48. Simulated 3D gain plot for 'patch' antenna

The improvement in gain can be attributed to the effective aperture of the antenna being increased. Instead of the dipole acting only as the radiating element the whole transceiver radiates, which results in the antenna filling the 'sphere', as outlined by the theory in chapter 3 and section 10.3.1, hence resulting in improvements for antenna gain. While the improvement in gain is welcome there would be some concern on the impact of the devices within the body of the transceiver. To investigate this HFSS was used to calculate the power flow through the body of the transceiver. The power flow is calculated via the Poynting vector [22], and is calculated by:

$$\vec{P}_{av} = \iint_S \vec{W}_{av} \cdot \hat{n} \cdot da \quad (10.20)$$

Where,

$$\vec{W}_{av} = \frac{1}{2} \text{Re}[\vec{E} \times \vec{H}^*] (W/m^2) \quad (10.21)$$

The $\frac{1}{2}$ factor appears in Equation 10.12 because HFSS uses peak phasor values of \vec{E} and \vec{H} . To calculate the power flow through the transceiver, the body was highlighted as shown in Figure 10.49.

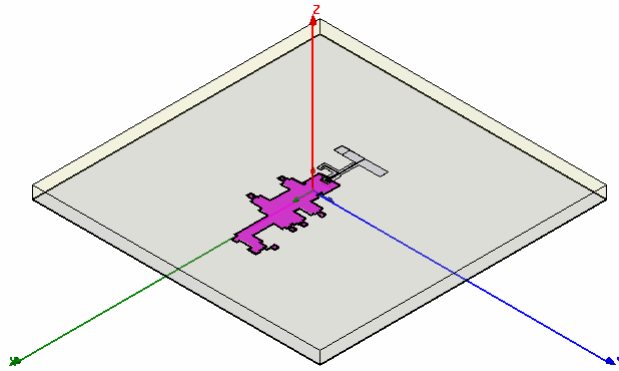


Figure 10.49. Transceiver body highlighted for Poynting vector calculation

Using the field calculator facility in HFSS it is possible to select an arbitrary surface and calculate the power flow through it as follows.

As is standard with HFSS the input power (P_{in}) to the antenna port is 1 Watt. To convert to dBm the following formula is used:

$$P_{in} (dBm) = 10 \text{Log}_{10} \left(\frac{P_{in}}{1 \text{ mW}} \right) = 10 \text{Log}_{10} \left(\frac{1W}{1 \text{ mW}} \right) = 30dBm \quad (10.22)$$

From HFSS, the value of power flow (\vec{P}_{av}) through the transceiver is 0.117 Watts which equates to:

$$P_{av} (dBm) = 10 \text{Log}_{10} \left(\frac{0.117}{1 \text{ mW}} \right) = 20.7dBm \quad (10.23)$$

This means that amount of power flowing through the transceiver is 9.3 dB less than the input power. Using this data it is possible to speculate how much power would flow through the transceiver discussed in section 10.1. For the transceiver in section 10.1 the output power was equal to -10.85 dBm, which means -10.85 dBm inputted at the terminals of the antenna. To calculate the power flow through the transceiver the process of 10.13 and 10.14 is reversed, as follows:

$$P_{av} (dBm) = -10.85dBm - 9.7dBm = -20.55dBm \quad (10.24)$$

$$P_{in} = 1mW \times 10^{\left(\frac{P_{in}(dBm)}{10}\right)} = 1mW \times 10^{\left(\frac{-10.85}{10}\right)} = 82.22\mu W \quad (10.25)$$

$$P_{in} = 1mW \times 10^{\left(\frac{-20.55}{10}\right)} = 8.81\mu W$$

This equates to 82.22 μW input power of which 8.81 μW flows through the body of the transceiver.

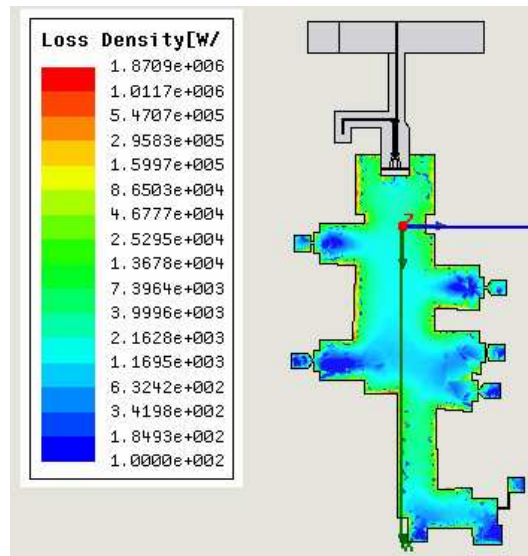


Figure 10.50. Simulated surface loss density on 5.8 GHz transceiver body

To try and understand the impact of the power flow through the transceiver the surface loss density was viewed. The surface loss density in HFSS calculates the impedance loss at every node in the triangle that makes up the mesh on the surface of interest. This can be used to view the power distribution over the surface of the transceiver. Viewing Figure 10.50 it can be seen that most of the power resides around the edges of the transceiver; whether or not this would have an impact on the operation of the transceiver it is uncertain at this stage.

10.3.4 A approximate gain measurement for integrated 5.8 GHz antennas

Both the antennas discussed in this chapter had to be tested by on-wafer probing. However, the position of the feed was close to the centre of the antenna, which precluded strapping the antenna onto a carrier substrate and feeding via wirebonds; and as a result it was impossible to measure them in the anechoic

chamber. To obtain some of measured data on the radiation characteristics, an experiment was set up, as shown in Figure 10.51.

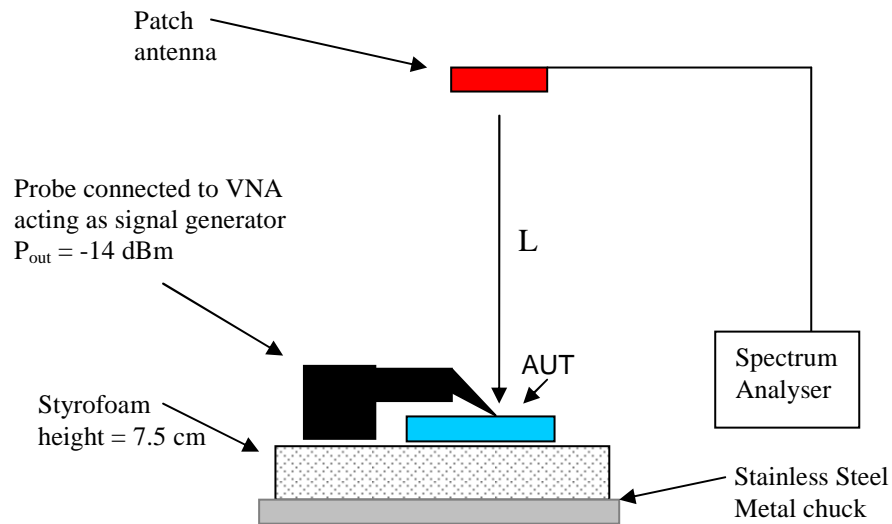


Figure 10.51. Experimental setup for gain measurement

The process for obtaining values of gain for the folded dipole and ‘patch’ antenna was as follows:

- Measure transmission response of patch
- Extrapolate values for approximate gain at 5.5 GHz and 5.92 GHz
- Calculate link budget so the only unknown is the gain of AUT and use the Friis equation to approximate the gain by measuring the power received on the spectrum analyser

The transmission response for the 5.8 GHz patch antenna discussed in chapter seven for various separations is shown in Figure 10.52.

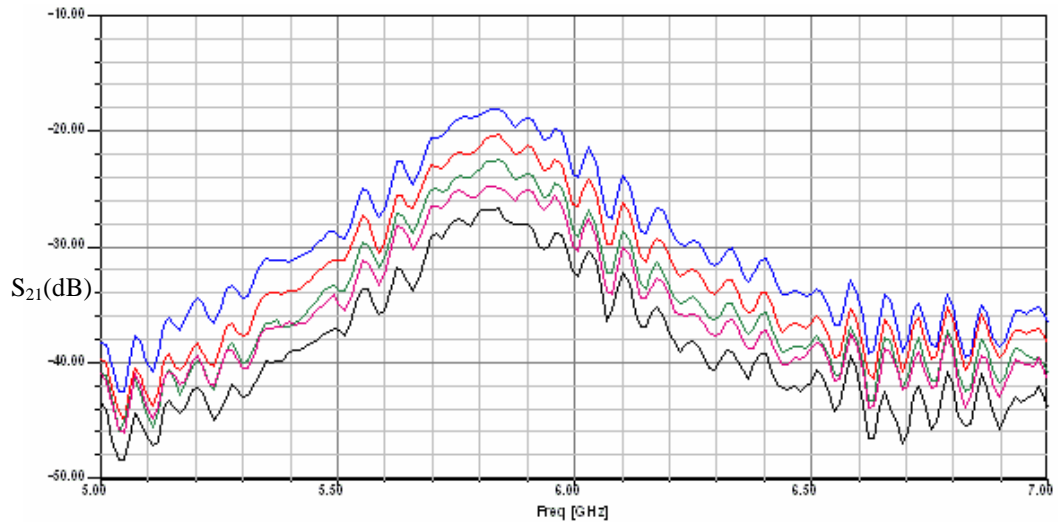


Figure 10.52. Experimental results for S_{21} for 5.8 GHz proximity-coupled patch antenna with separations of 14.5cm (blue), 20cm (red), 25cm (green), 30cm (magenta), and 40cm (black)

Using the transmission response combined with the Friis free space equation, from Equation (10.2), it was possible to calculate the approximate gain of the patch antenna at the operating frequencies of both the folded dipole and the ‘patch’ antenna. Table 10.4 shows the approximated gain of the patch antenna at 5.5 GHz and 5.92 GHz.

Distance separation (cm)	Gain per antenna (dB) 5.5 GHz	Gain per antenna (dB) 5.92 GHz
14.5	0.7	5.6
20	1.1	5.64
25	0.75	5.5
30	0.88	5.54
40	1.05	5
Gain Average (dB)	0.896	5.456

Table 10.4 Calculated values for average gain at 5.5 GHz and 5.92 GHz

Using the calculated values of average gain it was then possible to approximate the gain of the folded dipole and the ‘patch’ antenna by using the approximate gain of the patch antenna as part of a link budget. The results for the compact folded dipole at 5.5 GHz and the ‘patch’ antenna at 5.92 GHz are shown in tables 10.5 and 10.6 respectively.

Distance Separation (cm)	Signal Received (dBm)	Calculated Gain (dB)
10	-54	-14
15	-57	-13.2
20	-59	-12.7
25	-61	-12.7
30	-63	-13.1
35	-61	-9.7

Table 10.5. Folded dipole - Signal received on spectrum analyser via patch antenna for various separations with the calculated value of gain

Distance Separation (cm)	Signal Received (dBm)	Calculated Gain (dB)
10	-49	-12.6
15	-52	-12.1
20	-52	-9.6
25	-52	-7.7
30	-50	-4.1
35	-52	-4.7

Table 10.6. 'Patch' antenna - Signal received on spectrum analyser via patch antenna for various separations with the calculated value of gain

Inspection of the results in table 10.5 and 10.6 show some confirmation of the simulated results. Both antennas gains are a lower than the simulated response but it is clear that the patch antenna has an overall better response. One interesting phenomenon, occurring with both sets of results, is the improvement on the signal level being received the further the antenna is moved from the AUT. The minimum separation of 10 cm (patch maximum diameter = 50 mm) was used to ensure that the patch was in the far-field, so it is unlikely that the phenomena occurs by the antenna being in the near-field. However, there is the possibility that the probe arm used to test the antenna increased the maximum linear dimension of the antenna and as a result the far-field boundary was greater than 10 cm. Another possible explanation is that there is some form of multi-path

constructive/destructive interference as well as absorption occurring because of the presence of the metal chuck in the measurement system. The presence of the probe can explain the lower than expected values of signal received as the maximum attenuation occurring in the cables was about 1dB.

Both the antennas investigated in this chapter have given a useful insight into the problems of miniaturisation. However, the folded dipole can probably be discarded as a possible integrated antenna for the transceiver due to its very poor performance. The 'patch' antenna, however, offers a lot of promise. Gain improvements can be obtained by optimising the shape of the transceiver. It may also be possible to excite a circularly-polarised wave, increasing the suitability of the antenna for wireless sensor networks.

11. Discussion and conclusions

The work in this thesis presents a wide ranging insight into the design, fabrication and testing of antennas that are suitable for wireless sensor networks, and in particular, those required by the Speckled Computing Consortium.

To give an understanding into the research carried out in this project, the essence of what an antenna is, and how it radiates, was outlined. An in-depth study of the dipole provided the fundamental basis of the majority of work carried out in this project. As some of the antennas were defined as electrically small a review of fundamental limitations of antennas was carried out. An antenna does not radiate by itself, so an appreciation had to be gained of the feeding methods; in the case of this project feeds were provided by planar transmission lines such as microstrip, CPW and slotline. Also reviewed were the fundamental parameters used to characterise antennas in this thesis, including impedance bandwidth, S-parameters, radiation pattern, directivity, antenna efficiency, gain and polarisation.

Antennas were designed, manufactured and tested using conventional printed circuit boards (PCB's), and Gallium Arsenide (GaAs) substrates, operating at a range of frequencies from 2.4 GHz to 12 GHz. Available at Glasgow University was a wide range of test equipment and software for an antenna design engineer. The 3D electromagnetic simulation software, HFSS, was used for every antenna designed in this thesis. This software was combined with a powerful PC to increase the design accuracy through finer meshing. Various VNA and spectrum analysers were used to obtain many of the fundamental parameters used to characterise antennas. The anechoic chamber installed at the end of the project allowed for radiation pattern characterisation of the patch and UWB antennas, discussed in chapters six and eight, respectively.

A large part of this research was conducted in the area of UWB antenna design, simulation and testing. Using the fundamental antenna parameters outlined at the start of the thesis, chapters seven and eight highlighted the extra complexity required for UWB antenna design, such as increased impedance band width from

3.1 – 10.16 GHz, group delay and phase. The initial UWB antennas investigated in chapter 8 were used to give an appreciation of the two of the main types of antenna that could be designed for UWB. The Vivaldi antenna, which had a wide bandwidth, was directional and had an excellent pulse response but was electrically very large. Also due to its size it was operating in the reactive near-field and was deemed unsuitable for short-range wireless sensor networks. The CPW-fed monopole was the opposite, as it was compact, omni-directional but had a poor pulse response and impedance bandwidth response compared to the Vivaldi.

As the collaborative channel-modelling project between Strathclyde and Glasgow Universities required an omni-directional antenna, the UWB dipole was proposed as a possible candidate. The main drawback was the need to provide a balanced feed that did not excite leakage current. Four antennas were investigated, a microstrip-fed UWB dipole, a CPW-fed UWB dipole, a hybrid-feed UWB dipole, and a tapered-feed UWB dipole and these were fully characterised using the fundamental antenna parameters and radiation patterns obtained at 3, 6, and 9 GHz. All four antennas satisfied the impedance bandwidth criteria, but there was differing performance in terms of radiation pattern and pulse transmission. The antenna with the best radiation pattern was the CPW-fed UWB dipole with slots, while the tapered feed UWB dipole gave the best performance for pulse transmission.

An anechoic chamber was installed at Glasgow University in 2007, in the latter part of this thesis work. The results for the radiation patterns presented in chapters six and eight were obtained from the near-field data, whilst not ideal the data still provided useful insight. The software supplied by Near-field Systems Inc (NSI) takes the near-field data, which was used in this thesis and applies a Fourier transform to change it to the far-field. The data obtained from far-field transform was at best very noisy, and quite often illogical. Whether this can be attributed to a system error, or human error, is unknown at this stage and further investigation is required.

The hybrid- and tapered-feed UWB dipole radiation pattern responses were disappointing. Further research is required to identify the discrepancy between the simulated and experimental results. A possible and quite likely reason was the manufacturing methods employed, as both antennas were assembled by hand and misalignment was likely. As the hybrid-feed UWB dipole was constructed with multiple substrates, the alignment between the feed and the elements was hard to engineer; further development should be conducted into improving the procedure. For the tapered-feed UWB dipole a more elegant way of inserting the feed needs to be devised.

Chapter 10 focused on the antenna design work directly related to the Speckled Computing Consortium objective of designing a 5mm^3 'Speck'. Discussed in this Chapter 10 was the radio architectures used, such as the diode rectifier method and the super-regenerative receiver, which had low power consumptions that will meet the overall power consumption target of less than $400\ \mu\text{W}$.

This thesis investigated several antennas that were narrowband and electrically small. The 2.45 GHz Rectaxial antenna had excellent matching ($S_{11} = -20\text{dB}$) at the frequency of operation and an omni-directional radiation pattern with a maximum gain of 2.69 dBi, as measured in a far-field anechoic chamber. An attempt was made to reduce the size of the antenna by increasing the frequency of operation to 5.8 GHz. Unfortunately, due to excitation of surface waves along the ground plane this distorted the radiation pattern and, due to the unpredictability of results, the Rectaxial antenna was deemed unsuitable for operation at 5.8 GHz or greater.

After identifying the limitations of the rectaxial antenna at 5.8 GHz, other antennas were investigated. These were the compact-folded dipole and the 'patch' antenna, which were fabricated on GaAs and designed to be integrated around a MMIC transceiver to operating at 5.8 GHz. The compact-folded dipole was found to be an extremely poor radiator of electromagnetic energy, with an experimentally obtained value of gain = -14 dB. This poor gain, coupled with the unpredictability in its resonant frequency (simulated = 5.8 GHz; experimental = 5.5 GHz), made it a poor choice for a integrated antenna. However, the 'patch'

antenna was very promising, with acceptable gain (- 4 to -7 dB) and reasonable correlation between simulated (5.8 GHz) and experimental (5.92 GHz) resonant frequency.

Further research needs to be conducted into improving the gain, and potential impact of crosstalk on the active circuitry due to the entire transceiver radiating. Also, an accurate method of obtaining a radiation pattern for the 'patch' antenna needs to be identified. This would also include an alternative way of feeding the 'patch' antenna so that wafer probes would not interfere with the 'patch'.

12. List of References

12.1 Chapter 1

[1] www.specknet.org

[2] <http://robotics.eecs.berkeley.edu/~pister/SmartDust/>

12.2 Chapter 2

[1] J. C. Maxwell “A treatise on electricity and magnetism” Vol 1 & 2, Mitchell Library copy, Glasgow

[2] Constantine A. Balanis: “Antenna theory, analysis and design” Third edition, John Wiley & Sons, Inc. ISBN 0-471-60639-1. Chapter 1, pg 1.

ISBN 0-07-112240-0, Chapter 6, pp 170

[3] Constantine A. Balanis: “Antenna theory, analysis and design”. Third edition, John Wiley & Sons, Inc. ISBN 0-471-60639-1. Chapter 1, pp 2.

[4] Constantine A. Balanis: “Antenna theory, analysis and design” Third edition, John Wiley & Sons, Inc. ISBN 0-471-60639-1. Chapter 1, pp 9.

[5] Constantine A. Balanis: “Antenna theory, analysis and design” Third edition, John Wiley & Sons, Inc. ISBN 0-471-60639-1. Chapter 1, pp 10.

[6] J. D. Krauss, “Antennas For All Applications”, Third edition, McGraw-Hill, ISBN 0-07-112240-0, Chapter 2, pp 38

[7] Constantine A. Balanis: “Antenna theory, analysis and design” Third edition, John Wiley & Sons, Inc. ISBN 0-471-60639-1. Chapter 1, pp 13.

[8] J. D. Krauss, “Antennas For All Applications”, Third edition, McGraw-Hill,

[9] David M. Pozar, “Microwave Engineering”, 2nd Edition, John Wiley & Sons, Inc, ISBN 0-471-17096-8, Chapter 1 pp 16-17

[10] Constantine A. Balanis: “Antenna theory, analysis and design” Third edition, John Wiley & Sons, Inc. ISBN 0-471-60639-1. Chapter 4, pg 152.

[11] Constantine A. Balanis: “Antenna theory, analysis and design” Third edition, John Wiley & Sons, Inc. ISBN 0-471-60639-1. Chapter 4, pg 152.

[12] J. D. Krauss, “Antennas For All Applications”, Third edition, McGraw-Hill, ISBN 0-07-112240-0, Chapter 6, pg 167

[13] J. D. Krauss, “Antennas For All Applications”, Third edition, McGraw-Hill, ISBN 0-07-112240-0, Chapter 6, pg 168

[14] J. D. Krauss, "Antennas For All Applications", Third edition, McGraw-Hill, ISBN 0-07-112240-0, Chapter 6, pp 177

[15] J. D. Krauss, "Antennas For All Applications", Third edition, McGraw-Hill, ISBN 0-07-112240-0, Chapter 6, pp 177

12.3 Chapter 3

[1] H. A. Wheeler, "Fundamental Limitations of Small Antennas," Proceedings of the IRE, vol. 35, pp. 1479-1484, Dec. 1947

[2] H. A. Wheeler, "Small Antennas", IEEE Antennas & Propagation, AP-23, 4, pp 462-469, 1975

[3] L. J. Chu, "Physical limitations on omni-directional antennas," *J. Appl. Phys.*, vol. 19, pp. 1163-1175, Dec. 1948.

[4] Constantine A. Balanis: "Antenna theory, analysis and design" Third edition, John Wiley & Sons, Inc. ISBN 0-471-60639-1. Chapter 11, pp 638

[5] R.C. Hansen, "Fundamental Limitations in Antennas," IEEE, vol. 69, pgs 170-182, February 1981

[6] J. S. McLean, "A re-examination of the fundamental limits on the radiation Q of electrically small antennas," *IEEE Transaction on Antennas and Propagation*, vol. 44, pp. 672-675, May 1996.

[7] Hans Schantz, "The Art and Science of Ultra Wideband Antennas", Artech House, ISBN 1-58053-888-6, Chapter 5, pp 179

[8] Skrivervik, A.K.; Zurcher, J.-F.; Staub, O.; Mosig, J.R.; "PCS antenna design: the challenge of miniaturization" [Antennas and Propagation Magazine, IEEE](#) Volume 43, [Issue 4](#), Aug. 2001 Page(s):12 - 27

12.4 Chapter 4

[1] David M. Pozar, "Microwave Engineering", 2nd Edition, John Wiley & Sons, Inc, ISBN 0-471-17096-8, Chapter 2 pp 58-59

[2] David M. Pozar, "Microwave Engineering", 2nd Edition, John Wiley & Sons, Inc, ISBN 0-471-17096-8, Chapter 2 pp 62

[3] David M. Pozar, "Microwave Engineering", 2nd Edition, John Wiley & Sons, Inc, ISBN 0-471-17096-8, Chapter 2 pg 119

- [4] David M. Pozar, "Microwave Engineering", 2nd Edition, John Wiley & Sons, Inc, ISBN 0-471-17096-8, Chapter 2 pg 65
- [5] K.C. Gupta, R. Garg, and I. J. Bahl, "Microstrip Lines and Slotlines", Artech House, 1979
- [6] David M. Pozar, "Microwave Engineering", 2nd Edition, John Wiley & Sons, Inc, ISBN 0-471-17096-8, Chapter 3 pg 162
- [7] K.C. Gupta, R. Garg, and I. J. Bahl, "Microstrip Lines and Slotlines", Artech House, 1979
- [8] S. B. Cohn, "Slotline on a dielectric substrate," IEEE Trans. Microwave Theory and Tech., vol. MTT-17, pp. 768-778, Oct. 1969.
- [9] K.C. Gupta, R. Garg, and I. J. Bahl, "Microstrip Lines and Slotlines", Artech House, 1979
- [10] K.C. Gupta, R. Garg, and I. J. Bahl, "Microstrip Lines and Slotlines", Artech House, 1979

12.5 Chapter 5

- [1] David M. Pozar, "Microwave Engineering", 2nd Edition, John Wiley & Sons, Inc, ISBN 0-471-17096-8, Chapter 3 pp 66-68
- [2] IEEE "IEEE Standard Definitions of Terms for Antennas" Published by The Institute of Electrical and Electronics Engineers, Inc 345 East 47th Street, New York, NY 10017, USA, June 22, 1983, pg 24
- [3] Constantine A. Balanis: "Antenna theory, analysis and design" Third edition, John Wiley & Sons, Inc. ISBN 0-471-60639-1. Chapter 2, pg 28.
- [4] IEEE "IEEE Standard Definitions of Terms for Antennas" Published by The Institute of Electrical and Electronics Engineers, Inc 345 East 47th Street, New York, NY 10017, USA, June 22, 1983, pg 12
- [5] J. D. Krauss, "Antennas", Chapter 7, 1st Edition, McGraw-Hill, 1950, Chapter 3, pp 42-43
- [6] IEEE "IEEE Standard Definitions of Terms for Antennas" Published by The Institute of Electrical and Electronics Engineers, Inc 345 East 47th Street, New York, NY 10017, USA, June 22, 1983, pg 15
- [7] IEEE "IEEE Standard Definitions of Terms for Antennas" Published by The Institute of Electrical and Electronics Engineers, Inc 345 East 47th Street, New York, NY 10017, USA, June 22, 1983, pg 23

[8] Constantine A. Balanis: "Antenna theory, analysis and design" Third edition, John Wiley & Sons, Inc. ISBN 0-471-60639-1. Chapter 2, pp 70-75.

12.6 Chapter 6

[1] Park, Y.-J., Herschlein, A., Wiesbeck, W. "A Photonic Bandgap Structure for Guiding and Suppressing Surface Waves in Millimeter Wave Antennas", IEEE Transactions On Microwave Theory and Techniques, Vol. 49, No. 10, October 2001 (Part 2 of 2), pp 1854-1859

[2] S. Wi, J. Kim, N. Kang, J. Kim, H. Yang, Y. Kim, J. Yook, "Package-Level Integrated LTCC Antenna for RF Package Application", IEEE Transactions on Advanced Packaging, Vol. 30, NO. , February 2007, pp 132 – 141

[3] <http://www.ansoft.com/products/hf/hfss/>

[4] Girish Kumar, K.P. Ray, "Broadband Microstrip Antennas", Artech House, ISBN: 1-58053-244-6, Chapter 2, pg 7

[5] Dan Slater, "Near-Field Antenna Measurements", Artech House, ISBN Number: 0-89006-361-3, 1991, Chapter 2, pp 7-25

12.7 Chapter 7

[1] Constantine A. Balanis: "Antenna theory, analysis and design" Third edition, John Wiley & Sons, Inc. ISBN 0-471-60639-1. Chapter 14, pg 28.

[2] Constantine A. Balanis: "Antenna theory, analysis and design" Third edition, John Wiley & Sons, Inc. ISBN 0-471-60639-1. Chapter 14, pg 28.

[3] Constantine A. Balanis: "Antenna theory, analysis and design" Third edition, John Wiley & Sons, Inc. ISBN 0-471-60639-1. Chapter 14, pg 28.

[4] James, J. R., and P.S. Hall, "Handbook of Microstrip Antennas", Vol. 1, London: Peter Peregrinus Ltd., 1989

[5] Girish Kumar, K.P. Ray, "Broadband Microstrip Antennas", Artech House, ISBN: 1-58053-244-6, Chapter 2, pp 36-37

[6] David M. Pozar, "Microwave Engineering", 2nd Edition, John Wiley & Sons, Inc, ISBN 0-471-17096-8, Chapter 2 pp 89-90

12.8 Chapter 8

[1] J.C. Adams et al, "Ultra-wideband for navigation and communications," *IEEE Aerospace Conference Proceedings*, Vol.2, 2001, pp. 785-792

- [2] Ernest R. Kretzmer “Interference Characteristics of Pulse-Time Modulation”, PROCEEDINGS OF THE I.R.E., March 1950, pp 252-255
- [3] Jung N. Lee et al, “Design of a compact frequency-notched UWB slot antenna”, Microwave and Optical Technology Letters Volume 48, Issue 1 , pp 105 – 107
- [4] Seong H. Lee, Jong K. Park, Jung N. Lee, “A novel CPW-fed ultra-wideband antenna design”, Microwave and Optical Technology Letters Volume 44, Issue 5 , pp 393 - 396
- [5] Stanislav Licul et al “A parametric study of time-domain characteristics of possible UWB antenna architectures”, Vehicular Technology Conference, 2003. VTC 2003-Fall. 2003, IEEE 58th, Volume: 5, pp 3110- 3114
- [6] P.J. Gibson, “The Vivaldi Aerial”, 9th *European Microwave Conference Proc.*, 1979
- [7] K. Chung et al, “Wideband CPW-fed monopole antenna with parasitic elements and slots” *Electronics Letters*, Vol. 40, Issue 17, 19 Aug. 2004, pp1038-1040.
- [8] I. McGregor, G.Whyte, E.Wasige and I. Thayne, “UWB TEST SYSTEM” Biennial Analog Signal Processing Conference, Oxford-Brookes College, November 2004
- [9] Mikhnev, V. Vainikainen, P., “Wideband Tapered-Slot Antenna With Corrugated Edges For GPR Applications”, EUROPEAN MICROWAVE CONFERENCE, 2003, VOL 33; VOL 2, pp 727-730
- [10] Aiello, G.R., Rogerson, G.D., “Ultra-wideband wireless systems”, Microwave Magazine, IEEE, June 2003, Volume: 4, Issue: 2
- [11] Narayan Prasad Agrawall, Girish Kumar, and K. P. Ray, Wide-Band Planar Monopole Antennas, IEEE TRANSACTIONS ON ANTENNAS AND PROPAGATION, VOL. 46, NO. 2, FEBRUARY 1998, pp 294 -295

12.9 Chapter 9

- [1] Hans Schantz, "Planar Elliptical Element Ultra-Wideband Dipole Antennas," Proceedings of the IEEE, APS Conference (2002).
- [2] Do-Hoon Kwon, Yongjin Kim, “Suppression of Cable Leakage Current for Edge-Fed Printed Dipole UWB Antennas Using Leakage-Blocking Slots”, IEEE

ANTENNAS AND WIRELESS PROPAGATION LETTERS, VOL. 5, 2006, pp 183-186

[3] Yoon, I.-J.; Hyungrak Kim; Kihun Chang; Young Joong Yoon; Young-Hwan Kim; “Ultra wideband tapered slot antenna with band-stop characteristic” Antennas and Propagation Society International Symposium, 2004. IEEE Volume 2, 20-25 June 2004 Page(s):1780 - 1783 Vol.2

[4] Hyungkuk Yoon; Hyungrak Kim; Kihun Chang; Young Joong Yoon; Young-Hwan Kim; “A study on the UWB antenna with band-rejection characteristic”, Antennas and Propagation Society International Symposium, 2004. IEEE Volume 2, 20-25 June 2004 pp1784 - 1787 Vol.2

[5] Schantz, H.G.; “Bottom fed planar elliptical UWB antennas” Ultra Wideband Systems and Technologies, 2003 IEEE Conference on 16-19 Nov. 2003 pp 219 - 223

[6] Duncan, J.W. and V.P. Minerva, “100:1 Bandwidth Balun Transformer”, Proceedings of the IRE, Vol. 48, 1960, pp. 156-164

[7] www.matchcad.com

12.10 Chapter 10

[1] E. H. Armstrong, “Some recent developments of regenerative circuits”, Proc. Inst. Radio Eng, Vol 10, pp. 244-260 Aug. 1922

[2] I.Mcgregor, I.; Whyte, G.; Elgaid, K.; Wasige, E.; Thayne, I.; “A 700 μ W Tx/400 μ W Rx 2.4GHz Super - Regenerative GaAs Transceiver” Microwave Conference, 2006. 36th European 10-15 Sept. 2006 pp1523 - 1525

[3] Constantine A. Balanis: “Antenna theory, analysis and design” Third edition, John Wiley & Sons, Inc. ISBN 0-471-60639-1. Chapter 2, pp 94-96.

[4] J. D. Krauss, “Antennas”, Chapter 7, 1st Edition, McGraw-Hill, 1950, Chapter 7

[5] J. D. Krauss, “Antennas”, Chapter 7, 1st Edition, McGraw-Hill, 1950, Chapter 7, pg 175

[6] J. D. Krauss, “Antennas”, Chapter 7, 1st Edition, McGraw-Hill, 1950, Chapter 7, pg 180

[7] J. D. Krauss, “Antennas”, Chapter 7, 1st Edition, McGraw-Hill, 1950, Chapter 7, pg 157

- [8] Whyte, G, "An Omnidirectional, Low Cost, Low Profile, 2.45 GHz Microstrip Fed Rectaxial Antenna for Wireless Sensor Network Applications" IEE and IEEE conference, Loughborough Antennas and Propagation Conference, LAPC 2006.
- [9] J. D. Krauss, "Antennas", Chapter 7, 1st Edition, McGraw-Hill, 1950. Chapter 7
- [10] Chien-Jen Wang et al, "Small Microstrip Helical Antenna". Microwave Conference, 1999 Asia Pacific, Volume 2, 30 Nov.-3 Dec. 1999 pp 367 - 370.
- [11] Jung-Ick Moon and Seong-Ook Park, "Small Chip Antenna for 2.4/5.8 GHz Dual ISM-Band Applications", IEEE Antennas and Wireless Propagation Letters 2003, Vol. 2, pp 313-315.
- [12] www.ofcom.org.uk
- [13] David M. Pozar, "Microwave Engineering", 2nd Edition, John Wiley & Sons, Inc, ISBN 0-471-17096-8, Chapter 3 pg 157
- [14] David M. Pozar, "Microwave Engineering", 2nd Edition, John Wiley & Sons, Inc, ISBN 0-471-17096-8, Chapter 3 pg 151
- [15] K. R. Karver and J. W. Mink, "Microstrip Antenna Technology", IEEE Trans. Antennas and Propagation., Vol. AP-29, No. 1, pp.25-27, January 1981
- [16] Constantine A. Balanis: "Antenna theory, analysis and design" Third edition, John Wiley & Sons, Inc. ISBN 0-471-60639-1. Chapter 14, pp 853 - 854.
- [17] Khaled Elgaid Thesis, Dept. Of E & E Engineering, Glasgow University
- [18] David M. Pozar, "Microwave Engineering", 2nd Edition, John Wiley & Sons, Inc, ISBN 0-471-17096-8, Chapter 2 pp 73-79
- [19] J. D. Krauss, "Antennas", Chapter 7, 1st Edition, McGraw-Hill, 1950, Chapter 7, pg 245
- [20] H. Nakano, J. Yamauchi, K. Kawashima, and K. Hirose, "Effects of arm bend and asymmetric feeding on dipole antennae," Int. J. Electron., vol. 55, pp. 353-364, 1983
- [21] Constantine A. Balanis: "Antenna theory, analysis and design" Third edition, John Wiley & Sons, Inc. ISBN 0-471-60639-1. Chapter 2, pg 38-40.